

UNCLASSIFIED

AD NUMBER

AD449435

LIMITATION CHANGES

TO:

Approved for public release; distribution is unlimited. Document partially illegible.

FROM:

Distribution authorized to U.S. Gov't. agencies and their contractors;
Administrative/Operational Use; APR 1964. Other requests shall be referred to Air Force Flight Test Center, 6593rd Test Group, Edwards AFB, CA. Document partially illegible.

AUTHORITY

afrpl ltr 5 mar 1970

THIS PAGE IS UNCLASSIFIED

UNCLASSIFIED

AD. 4 4 9 4 3 5

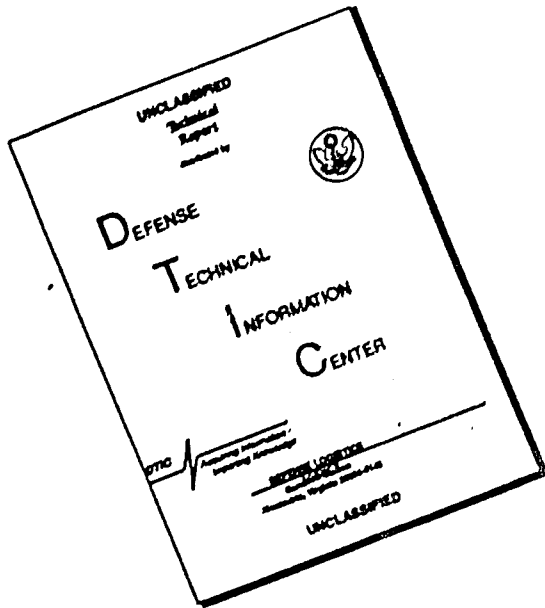
**DEFENSE DOCUMENTATION CENTER
FOR
SCIENTIFIC AND TECHNICAL INFORMATION**

CAMERON STATION ALEXANDRIA, VIRGINIA



UNCLASSIFIED

DISCLAIMER NOTICE



**THIS DOCUMENT IS BEST
QUALITY AVAILABLE. THE COPY
FURNISHED TO DTIC CONTAINED
A SIGNIFICANT NUMBER OF
PAGES WHICH DO NOT
REPRODUCE LEGIBLY.**

NOTICE: When government or other drawings, specifications or other data are used for any purpose other than in connection with a definitely related government procurement operation, the U. S. Government thereby incurs no responsibility, nor any obligation whatsoever; and the fact that the Government may have formulated, furnished, or in any way supplied the said drawings, specifications, or other data is not to be regarded by implication or otherwise as in any manner licensing the holder or any other person or corporation, or conveying any rights or permission to manufacture, use or sell any patented invention that may in any way be related thereto.

449435

RPL-TDR-64-113

449435

The Feasibility of a Rotating Detonation Wave Rocket Motor

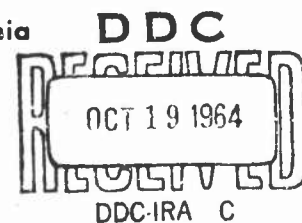
Contract No. DDC

AS NO. NO.

TECHNICAL DOCUMENTARY REPORT NO. RPL-TDR-64-113

April 1964

Air Force Flight Test Center
6593d Test Group (Development)
Air Force Systems Command
United States Air Force
Edwards Air Force Base, California



Project No. 3058, Task No. 305802

(Prepared under Contract No. AF 04(611)-8503 by The University of Michigan, Department of Aeronautical and Astronautical Engineering, Ann Arbor, Michigan; J. A. Nicholls and R. E. Cullen, authors)

When Government drawings, specifications, or other data are used for any purpose other than in connection with a definitely related Government procurement operation, the United States Government thereby incurs no responsibility nor any obligation whatsoever; and the fact that the Government may have formulated, furnished, or in any way supplied the said drawings, specifications, or other data, is not to be regarded by application or otherwise as in any manner licensing the holder or any other person or corporation, or conveying any rights or permission to manufacture, use, or sell any patented invention, that may in any way be related thereto.

Qualified requesters may obtain copies of this report from the Defense Documentation Center (DDC), Cameron Station, Alexandria, Virginia 22314. Department of Defense contractors must be established for DDC services, or have their "need-to-know" certified by the cognizant military agency of their project or contract.

ERRATA SHEET

Page	Line	Comments		
xiii	14	r is extraneous		
xv	15	bunred	should read	burned
8	3rd eq. *	m_{arg}	" "	m_{avg}
11	1st eq	m_p	" "	m_p
11	4th eq	m	" "	m_p
17	1st eq.	\bar{T}_P	" "	\bar{T}_p
24	2nd eq	\bar{T}_P	" "	\bar{T}_p
24	3rd eq.	\bar{T}_P	" "	\bar{T}_p
24	4th eq.	\bar{T}_P	" "	\bar{T}_p
26	7	\bar{T}_P	" "	\bar{T}_p
44	5*	ϕ_{B_0}	" "	ρ_{B_0}
51	1st eq.	(P_e/P_B)	" "	(P_e/P)
51	last eq.	$\sqrt{P\ell + dy + \dots}$	"	$P\ell_t dy \sqrt{\dots} +$
62	7	F_j	" "	F_j
63	footnote	functions	" "	function.
65	7	U_∞^2	" "	U_∞^2
65	7	U_0^∞	" "	U_0^∞
66	17	is 10^{-4} cm, 10^4 cm, and 10^2 cm	should read	
			is 10^{-4} cm, 10^{-4} cm, 10^4 cm, and 10^2 cm	
68	5	delete comma		
72	2	of the order of glycerol	should read	
			of the same order as for glycerol	
72	10	Gorden ²⁹	should read	Gordon ²⁹

*indicates from bottom of page

ERRATA SHEET (cont)

Page	Line		Comments	
168	4	\bar{T}_p	should read	TP
168	4	\bar{T}_P	" "	\bar{T}_p
168	4		the work input is extraneous	
171	11*	\bar{T}_p	should read	TP
171	11*	\bar{T}	" "	\bar{T}_p
172	4*	$\bar{T}_p \approx 540^{\circ}R$	" "	$T_p \approx 537^{\circ}R$
175	9*	\bar{T}_p	" "	TP
		\bar{T}_P	" "	\bar{T}_p
175	11*	m_L	" "	m_ℓ
175	12*	m_G	" "	m_G
Fig. 1(c)	3*	B_η	" "	$B\eta$
Fig. 3(a)	1*	\bar{T}_P^η	" "	\bar{T}_p
Fig. 3(b)	2*	\bar{T}_P	" "	\bar{T}_p
Fig. 4(a)	1*	\bar{T}_P	" "	\bar{T}_p
Fig. 4(b)	1*	\bar{T}_P	" "	\bar{T}_p

*indicates from bottom of page.

RPL-TDR-64-113

THE FEASIBILITY OF A ROTATING DETONATION WAVE ROCKET MOTOR

TECHNICAL DOCUMENTARY REPORT NO. RPL-TDR-64-113

April 1964

Air Force Flight Test Center
6593d Test Group (Development)
Air Force Systems Command
United States Air Force
Edwards Air Force Base, California

Project No. 3058, Task No. 305802

(Prepared under Contract No. AF 04(611)-8503 by The University of Michigan,
Department of Aeronautical and Astronautical Engineering, Ann Arbor,
Michigan; J. A. Nicholls and R. E. Cullen, authors)

TABLE OF CONTENTS

	Page
LIST OF TABLES	v
LIST OF FIGURES	vii
NOMENCLATURE	xi
FOREWORD	xvii
ABSTRACT	xix
I. INTRODUCTION	1
II. ANALYTICAL MODEL OF THE INTERNAL GASDYNAMICS OF THE ROTATING DETONATION WAVE ROCKET MOTOR	3
A. Introduction	3
B. One-Dimensional Model of the Rotating Detonation Wave Rocket Motor	4
C. Results and Conclusions	59
III. DETONATION IN A HETEROGENEOUS, LIQUID-GAS MEDIA	61
A. Literature Review of Heterogeneous Detonation	61
B. Literature Review of the Droplet Breakup Process Behind a Shock Wave and Estimation of Droplet Breakup Times in Heterogeneous H ₂ -O ₂ Detonations	70
C. Experimental Studies of the Droplet Breakup Process Behind Chapman-Jouguet Detonations	82
IV. THEORETICAL STUDY OF HEAT TRANSFER IN THE ROTATING DETONATION WAVE ENGINE	88
A. Theoretical Model for Heat Flux	88
B. Condition of Combustion Gases Outside the Boundary Layer and Behind the Detonation	89
C. Heat Flux Across the Boundary Layer	90
D. Heat Conduction in the Solid Wall	96
E. The Effect of Dissociation and Recombination on Heat Transfer	101
V. EXPERIMENTAL STUDY OF THE EFFECT OF LOW TEMPERATURE AND HIGH PRESSURE ON THE DETONATION VELOCITY OF H ₂ -O ₂ MIXTURES	106
A. Introduction	106
B. Test Equipment	107
C. Methods and Procedures	107
D. Test Results	108
E. Discussion of Test Results	108

TABLE OF CONTENTS (cont)

	Page
VI. EXPERIMENTAL STUDY OF THE EFFECT OF CURVATURE AND CONFINEMENT ON DETONATION WAVES IN ANNULAR CHANNELS	117
A. Introduction	117
B. Experimental Test Equipment	118
C. Experimental Procedure	118
D. Results	119
E. Conclusions	122
VII. EXPERIMENTS ON THE GASEOUS ANNULAR MOTOR AND THE LINEAR MOTOR	123
A. Introduction	123
B. Test Equipment and Instrumentation	124
C. Tests in the Linear Motor	127
D. Tests in the Annular Motor	130
E. Discussion of the Test Results in the Annular Motor	133
VII. COMPARISON OF ANNULAR MOTOR STUDIES WITH EXPERIMENTS OF VOITSEKHOVSKY	137
IX. CONCLUSIONS AND RECOMMENDATIONS	140
REFERENCES	145
APPENDIX A	150
APPENDIX B	165
FIGURES	

LIST OF TABLES

1. Influence Coefficients
2. Computational Results for the Blocked Injector ($d \bar{m}_p = 0$) Equations for $\gamma(k) = 1, 2$
3. Solution of the Complete Mixing Case Equations
4. Solution of the No-Mixing Case Equations—Warm Gaseous Case
5. Solution of the No-Mixing Case Equations—Cold Gaseous Case
6. Rankine Hugoniot Equations for Dilute Sprays and Gaseous Mixtures
7. Characteristic Regions for Spray Detonation
8. Theoretical and Experimental Correlation of Critical Size of Droplets of Different Fluids for Bag-Type Droplet Breakup
9. Theoretical and Experimental Correlation of Critical Size of Burning and Non-Burning Droplets of RP-1 for Shear-Type Droplet Breakup
10. Theoretical Shear-Type Droplet Breakup Times for Burning and Non-Burning Droplets of RP-1 using Experimental Values of Critical Velocity and Critical Size
11. Theoretical Shear-Type Droplet Breakup Times of Liquid Oxygen Droplets in a Stoichiometric H_2-O_2 Detonation
12. The Variation of Detonation Parameters and Heat Flux with Mixture Ratio
13. Experimental Detonation Velocities of H_2-O_2 Mixtures at Reduced Initial Temperatures and Increased Initial Pressures
14. Results of Velocity Deficit Calculations using Theory of Reference 54
15. Results of Diaphragm Tests in Annular Motor with Hydrogen-Oxygen
16. Comparison of Experimental Conditions and Observations with Those of Voitsekhovsky

LIST OF FIGURES

- 1(a) Mach Number, M , as a Function of the $B\eta$ Product for the Case of a Blocked Injector ($d\dot{m}_p = 0$)
- 1(b) Dimensionless Velocity, \bar{v} , as a Function of the $B\eta$ Product for the Case of a Blocked Injector ($d\dot{m}_p = 0$)
- 1(c) Dimensionless Pressure, \bar{P} , as a Function of the $B\eta$ Product for the Case of a Blocked Injector ($d\dot{m}_p = 0$)
- 2(a) Dimensionless Properties \bar{P} , \bar{T} , $\bar{\rho} v$, and μ as Functions of the Dimensionless Circumferential Coordinate, η
- 2(b) Mach Number, M , and Dimensionless Velocity, \bar{v} , as a Function of the Dimensionless Circumferential Coordinate, η
- 3(a) Dimensionless Properties \bar{P} , \bar{T}_A , \bar{T}_B , $\bar{\rho}_B$, ξ , and \bar{m} as Functions of the Dimensionless Circumferential Coordinate, η , for $\bar{T}_p = 537^0R$, Gaseous No Mixing Case
- 3(b) Dimensionless Properties M_A , M_B , \bar{v}_A , \bar{v}_B as Functions of the Dimensionless Circumferential Coordinate, η , for $\bar{T}_p = 537^0R$, Gaseous No Mixing Case
- 4(a) Dimensionless Properties \bar{P} , \bar{T}_A , \bar{T}_B , $\bar{\rho}_B$, ξ , and \bar{m} as Functions of the Dimensionless Circumferential Coordinate, η , for $\bar{T}_p = 270^0R$, Gaseous No Mixing Case
- 4(b) Dimensionless Properties M_A , M_B , \bar{v}_A , \bar{v}_B as Functions of the Dimensionless Circumferential Coordinate, η , for $\bar{T}_p = 270^0R$, Gaseous No Mixing Case
- 5 Theoretical Results Compared with an Experimental Pressure-Time History for the Passage of the Initial Detonation Wave
- 6(a) Schematic Process for Shear Type Breakup
- 6(b) Schematic Process of Bag Type Breakup
- 7 Photograph of the Test Setup for Detonation-Droplet Interaction Studies
- 8 Schlieren Photographs of the Shattering of H_2O Droplets Behind H_2-O_2 Detonation Waves ($X_{H_2} \approx .70$)
- 9 Schlieren Photographs of the Shattering of H_2O Droplets Behind H_2-O_2 Detonation Waves ($X_{H_2} \approx .67$)
- 10 Detonation Moving Over a Flat Plate
- 11 Coordinate System for Heat Transfer Analysis
- 12 Square Pulse Approximation of Surface Heat Flux
- 13 Theoretical Heat Transfer Model—Rotating Detonation Wave Engine
- 14 One Dimensional Conduction Model
- 15 Equilibrium Concentration vs. Initial Hydrogen Content Behind H_2-O_2 Chapman-Jouguet Detonations

LIST OF FIGURES (cont)

- 16 Heat Flux to the Wall of the Rotating Detonation Wave Engine vs. Mixture Ratio with and without Dissociative Recombination
- 17 H₂-O₂ Chapman-Jouguet Detonation and Combustion Chamber Temperatures as a Function of Mixture Ratio
- 18 Photograph of the Test Setup for the Measurement of the Temperature and Pressure Effects on Hydrogen-Oxygen Detonation Velocities
- 19 Schematic View of the Test Setup for the Measurement of the Temperature and Pressure Effect on Hydrogen-Oxygen Detonation Velocities
- 20 Photograph of the Coiled Detonation Tube and the Low-Temperature Vessel
- 21 Schematic View of the Ionization Probe for Detonation Velocity Measurements
- 22 Schematic View of the System for Detonation Velocity Measurements
- 23 Experimental Detonation Velocity, U_D, of Hydrogen-Oxygen Detonations as a Function of the Mole-Fraction of Hydrogen (X_{H₂}) from Data Obtained by Moyle (Reference 38)
- 24 Experimental Detonation Velocity, U_D, of Hydrogen-Oxygen Detonations as a Function of the Initial Temperature, T₁, for X_{H₂} = 0.500
- 25 Experimental Detonation Velocity, U_D, of Hydrogen-Oxygen Detonations as a Function of the Initial Temperature, T₁, for X_{H₂} = 0.667
- 26 Experimental Detonation Velocity, U_D, of Hydrogen-Oxygen Detonations as a Function of the Initial Temperature, T₁, for X_{H₂} = 0.730
- 27 Experimental Detonation Velocity, U_D, of Hydrogen-Oxygen Detonations as a Function of the Initial Temperature, T₁, for X_{H₂} = 0.800
- 28 Experimental Detonation Velocity, U_D, of Hydrogen-Oxygen Detonations as a Function of the Mole-Fraction of Hydrogen, X_{H₂}, for Initial Pressure, P₁ = 10 Atmospheres
- 29 Comparison of Experimental Detonation Velocity, U_D, as a Function of Initial Temperature, T₁, at Various Initial Pressures, P₁, with Results of Other Investigators for Stoichiometric (X_{H₂} = .667) H₂-O₂ Mixtures
- 30 Log of the Detonation Pressure Ratio, P₂/P₁ (obtained from experimental detonation velocity measurements) as a Function of the Initial Temperature, T₁, for Stoichiometric (X_{H₂} = .667) H₂-O₂ Mixtures
- 31 Schematic Drawing of the Curved Detonation Tube Section with Solid Walls
- 32 Photograph of the Curved Detonation Tube with Solid Walls
- 33 Schematic Diagram of the Basic Experimental System for Studying Detonation Waves in Curved Channels

LIST OF FIGURES (cont)

- 34(a) Schlieren Photograph of a Stoichiometric H₂-O₂ Detonation Wave in a Curved Channel Utilizing a Thin, Nitrocellulose Membrane for Inward Radial Relief Employing a Flowing System
- 34(b) Schlieren Photograph of a Stoichiometric H₂-O₂ Detonation Wave in a Curved Channel with Complete Solid Wall Confinement Employing a Flowing System
- 35 Position vs. Relative Time of Stoichiometric H₂-O₂ Detonation Waves Along the Outer Radius of the Curved Channel with Complete Solid Wall Confinement Employing a Flowing System
- 36 Interpretive Sketch of a Stoichiometric H₂-O₂ Detonation Wave in a Curved Channel with Complete Solid Wall Confinement
- 37 Schlieren Photograph of a Stoichiometric H₂-O₂ Detonation Wave in a Curved Channel with the Inner Wall Removed Employing a Flowing System
- 38 Interpretive Sketch of a Stoichiometric H₂-O₂ Detonation Wave in a Curved Channel with the Inner Wall Removed Employing a Flowing System
- 39 Position vs. Relative Time of Stoichiometric H₂-O₂ Detonation Waves Along the Outer Radius of the Curved Channel with Inner Wall Removed Employing a Flowing System
- 40 Schlieren Photograph of a Stoichiometric H₂-O₂ Detonation Wave in a Curved Channel with One Window Removed (Relief in the Axial Direction)
- 41 Schematic Drawing of Annular Motor
- 42 Photograph of Downstream End of Annular Motor
- 43 High Speed Photographs of Colliding Detonation Waves in Annular Motor Taken by 8 mm Fastax Camera
- 44 Schematic Diagram of Propellant Feed System and Instrumentation
- 45 Photograph of Solenoid Valves and Injector Manifold Arrangement
- 46 Typical Oscillograph Record of Sequence of Events
- 47 Calibration of Kistler 603 Pressure-Transducer in Detonation Tube
- 48 Photograph of Instrumentation Setup Outside Test Cell
- 49 Photograph of the Linear Motor on the Test Stand
- 50 Photograph of the Components of the Linear Motor
- 51 Schematic Drawing of Test Configurations for the Linear Motor
- 52 Spark Schlieren Photograph of Test in Linear Motor Configuration (a)
- 53 Photograph of Plexiglas Window from Linear Motor After Test
- 54 Pressure Recording of Starter Tube Fired into Stagnant Air—Linear Motor
- 55 Pressure Recording of Linear Motor Configuration (b) Tests 15 and 16
- 56 Photograph Showing Diaphragm in Annular Motor
- 57 Photograph of Nozzle End of Annular Motor

LIST OF FIGURES (concluded)

- 58 Station Locations for Pressure-Transducers in Annular Motor
- 59 Pressure Recordings of Annular Motor Tests, Hydrogen-Oxygen,
 $A_c/A_t = 2.0$
- 60 Pressure Recordings of Annular Motor Tests Hydrogen-Oxygen,
 $A_c/A_t = 1.0$
- 61 High Speed Photographs of Annular Motor Tests, Hydrogen-Oxygen
- 62 Pressure Recordings of Annular Motor Tests, Methane-Oxygen,
 $A_c/A_t = 2.0$
- 63 Pressure Recordings of Annular Motor Tests, Methane-Oxygen,
 $A_c/A_t = 1.0$
- 64 High Speed Photographs of Annular Motor Tests, Methane-Oxygen
- 65 Chapman-Jouguet Detonation Velocity for Methane-Oxygen in Closed Tube
- 66 Displacement vs. Time Plots for Initial Detonation Wave in Annular Motor,
Hydrogen-Oxygen
- 67 Displacement vs. Time Plots for Initial Detonation Wave in Annular Motor,
Methane-Oxygen
- 68 Summary of Initial Detonation Wave Velocity vs. Mixture Ratio in
Annular Motor

NOMENCLATURE

Part II

a (ft/sec)	local speed of sound
A (ft ²)	cross-sectional area
B	area ratio parameter, $(\ell_t L/A_c)[2/(\gamma + 1)]^{(\gamma + 1)/2(\gamma - 1)}$
c^* (ft/sec)	rocket motor characteristic velocity, $P_c A_t / \dot{m}_p$
C_F	thrust coefficient, $F/P_c A_t$
C_p (ft-lb slug ⁻¹ R)	specific heat at constant pressure
C_{p_ℓ}	injector orifice pressure loss coefficient
F (lb)	rocket motor thrust
g_0 (lbf slug)	unit conversion constant (32.174)
G	mass flow parameter, $\dot{m}_p/\rho_0 v_0 A_c N$ or $\dot{m}_G/\rho_0 v_0 A_c N$
h (ft-lb slug)	specific enthalpy
$h^{(0)}$ (ft-lb slug)	specific enthalpy at absolute zero temperature
I_{sp} (sec)	theoretical specific impulse
ℓ_c (ft)	radial width of the chamber
ℓ_i (ft)	injector orifice length
ℓ_t (ft)	radial width of the RDWE throat
L (ft)	distance between successive detonation waves in the RDWE, $2\pi R/N$
m (mole ⁻¹)	molecular weight
\dot{m} (slugs/sec)	mass flow rate
M	Mach number, v/a
n (ft)	radial coordinate in the RDWE chamber
N	number of waves in the RDWE chamber
N_i	number of injector orifices

NOMENCLATURE (cont)

P (lbs/ft ²)	absolute pressure
P_a (lbs/ft ²)	atmospheric pressure
P_D (lbs/ft ²)	injector plenum pressure
Q (ft-lb/slug)	heat added per unit mass of propellant
R (ft)	radius of the RDWE
R_0 (ft-lb/slug-mol-°R)	universal gas constant
S (ft ²)	surface of control volume
t (sec)	time
T (°R)	absolute temperature
u, v (ft/sec)	axial and circumferential velocity components in the RDWE chamber
V (ft/sec)	magnitude of the velocity
x, y (ft)	axial and circumferential coordinates in the RDWE chamber
X	mole fraction
γ	specific heat ratio
η	dimensionless circumferential coordinate in the RDWE chamber, y/L
μ	relative mass concentration of the unburned propellant
ξ	dimensionless axial coordinate of the unburned-burned gas interface, x/x_n
ρ (slugs/ft ³)	mass density
τ (sec)	stay time of a fluid particle in the convergent section of the RDWE nozzle
Subscripts	
0	refers to condition at $y = 0$ ($\eta = 0$)
1	refers to condition at $y = L$ ($\eta = 1$)
a	refers to absolute velocity
avg	refers to mean value

NOMENCLATURE (cont)

A	refers to unburned propellant
B	refers to burned propellant
C	refers to chamber condition in a conventional rocket motor
e	refers to nozzle exit condition
G	refers to gaseous propellant
i	refers to injector orifice
l	refers to liquid propellant
n	refers to condition at beginning of nozzle convergent section
p	refers to initial propellant condition
S. L.	refers to condition for sea level operation
t r	refers to condition at rocket nozzle throat
vac	refers to condition for vacuum operation
f	denotes f/f_0
l	denotes a vector quantity

Part III

D	diameter of the droplet
f_j	spray distribution function type j
h	enthalpy per unit mass
L_B	distance traversed by the detonation wave front during droplet breakup time
L_C	distance between the initial shock wave front and the zone of significant chemical reaction
M	liquid species
p	pressure
r	radius of the droplet
Re	Reynolds number

NOMENCLATURE (cont)

S	surface tension
t	time
t_b	droplet breakup time
T	temperature
<u>u</u>	velocity of the gas
U	relative velocity between the gas and the droplets
<u>V</u>	velocity vector of droplet
W	molecular weight
We	Weber number
$(We)_{cr}$	critical Weber number
<u>x</u>	position vector in phase space
Y	mass fraction of a component of the gas
Z	mass flux fraction of spray
μ_l	viscosity of the liquid
ρ	density
ρ_g	density of the gas
ρ_g'	mass per unit volume of space available to the gas
ρ_l	density of the liquid

Part IV

c	ratio of heat pulse width to wavelength
C_s	specific heat of wall material
D	binary diffusion coefficient
e	conditions downstream of the detonation
h	enthalpy per unit mass
h_r	adiabatic recovery enthalpy
k	thermal conductivity

NOMENCLATURE (cont)

ℓ	thickness of combustion chamber walls
Le	Lewis number = $\bar{C}_p D\rho/k$
M	Mach number
p	pressure
Pr	Prandtl number = $(C_p \mu)/k$
\bar{q}_w	heat flux per unit area at wall
$\bar{\bar{q}}_w$	average heat flux per unit area during pulse
Q_w	total heat flux during heat pulse
\bar{Q}_w	overall average heat flux per unit area to walls of chamber
R_0	universal gas constant
T	temperature
T_c	temperature in conventional combustion chamber
V	velocity
V_c	velocity of burned gas relative to detonation
V_D	detonation velocity
\bar{W}	average molecular weight of a mixture
w_i	molecular weight of species i
x	distance from the detonation wave
X_i	mole-fraction of species i
$0()$	means order of
1	conditions upstream of the detonation
α	thermal diffusivity $k/\rho C_s$
μ	viscosity
ν	kinematic viscosity
ρ_1	density of unburned gas
τ_w	shear stress at the wall
ρ	density

FOREWORD

This is the final report on Contract AF 04(611)-8503 between Edwards Air Force Base and The University of Michigan covering the period 1 June 1962 to 31 January 1964. The aim of this contract is to investigate the feasibility of a rotating detonation wave rocket motor. The project was directed by Professors J. A. Nicholls and R. E. Cullen of the Aeronautical and Astronautical Engineering Department of The University of Michigan. The Air Force Project Engineer was Richard Weiss (DGRR), 6593d Test Group (Development) Edwards, California

Personnel contributing to the various phases of the project are listed below next to the corresponding section number of the report.

- II T. C. Adamson, Jr., G. Olsson
- III J. Fu, E. Kurath
- IV M. Sichel, T. David
- V K. Ragland, G. L. Cosens
- VI F. Cheslak, G. L. Cosens, S. Schmidt
- VII K. Ragland, G. L. Cosens, J. Brown, S. Schmidt

ABSTRACT

A study has been conducted which deals with the feasibility of utilizing exclusively the detonative mode of combustion in a rocket motor rather than the deflagrative mode used in conventional, chemical rocket motors. The configuration adopted consists of an annular combustion chamber wherein detonation wave(s) completely fill the chamber cross-section and propagate steadily in the same circumferential direction. This configuration leads to the descriptive term "Rotating Detonation Wave Engine" (RDWE).

Several separate studies pertinent to the feasibility of such a device have been made. These include:

1. Detonation in a two phase (liquid droplet gaseous) media.
2. Detonation at low temperatures and high pressures for H₂-O₂ gaseous mixtures.
3. Heat transfer associated with the detonative process.
4. Detonation in curved partially confined channels utilizing premixed hydrogen and oxygen.
5. Detonation in annular and linear motor configurations with separate gaseous fuel (hydrogen or methane) and gaseous oxidizer (oxygen) injection.
6. A simplified analytical model of the idealized gas dynamics in the annular chamber of the RDWE.

From the studies conducted the following conclusions are drawn:

1. The droplet shattering process is of extreme importance in stabilized two phase detonations. Experiments show that the droplet shattering times might be sufficiently short to support this type of detonation.
2. Experimental detonation velocities with gaseous mixtures at elevated initial pressures (15 atmospheres) and at initial temperatures down to the vapor saturation line of oxygen (~ 112°K) are somewhat higher than those predicted theoretically. Presumably this is due to imperfect gas effects at these conditions.
3. Theoretical heat transfer to the wall of the RDWE is of the same order (~ 10 BTU/in²-sec) as it is at the throat of a conventional small rocket motor operating on H₂-O₂.
4. Detonation velocities in curved, partially confined channels utilizing premixed H₂ and O₂ suffer a degradation of about 7% compared to detonations in straight, confined tubes.
5. Although a maintained detonative process (multiple passages of the wave) was not achieved in the experiments with the annular motor utilizing a separate, fuel and oxidizer injection system, it is concluded that nothing fundamental stands in the way of this accomplishment. This conclusion is supported by the independent experiments

- of Voitsekhovsky wherein maintained detonation was achieved in a similar annular configuration using premixed reactants (acetylene oxygen). This leads to the conclusion that the method of separate injection must be reexamined more critically.
6. Solutions to the differential equations describing the idealized gas dynamics in the chamber of the RDWE reveal that the chamber properties are essentially parabolic functions of the circumferential coordinate. Expressions are developed comparing the theoretical specific impulse of the RDWE to the conventional rocket motor. It is concluded that there is no significant degradation in the sea level specific impulse for the RDWE (assuming an idealized one-dimensional expansion) as long as the average chamber pressure is higher than 500 psia. The vacuum specific impulse of both devices is essentially identical.

It is concluded finally that due to the complexities of the problems encountered that further conclusions regarding the feasibility of the RDWE cannot be made at this time. Recommendations for further study are made.

I. INTRODUCTION

Conventional chemical jet propulsion devices rely on the deflagrative mode of combustion. The possibility exists, however, of utilizing detonating waves which yield extremely high values of energy release per unit volume per unit time. Consideration has been given in earlier studies to the use of detonation waves in a pulse jet¹, in a hypersonic ramjet^{2,3} and to a steady-state process in the divergent portion of the exhaust nozzle of a conventional rocket motor⁴. This report is concerned with the feasibility of applying detonative combustion to a rocket motor wherein the detonation wave(s) move steadily in a circumferential direction in an annular chamber leading to the term "rotating detonation wave" used in this study to describe the process. It might be noted that one of the disadvantages of detonative combustion in air breathers is the relatively high stagnation pressure loss sustained. In rocket motors at high altitude this would be of no consequence in that the pressure ratio across the nozzle approaches infinite values. Possibly one of the greatest reasons foreseen for detonation wave rocket engines (RDWE) is associated with scaling. The occurrence of combustion instability in large scale conventional rocket motors has plagued the development of new engines. To date, due to combustion instability, it has not been possible to systematically scale up in thrust level from successful operations of small motors. Many, but certainly not all, engineers believe that detonation occurs in some form as a part of this instability. The thought behind the RDWE is to deliberately force the occurrence of detonation (the extreme case of an instability), design the engine for it, and operate the engine in a controlled fashion. In this way it is believed that the scaling problem would be very minimal. Other possible advantages foreseen include, (1) lower engine weight per unit thrust, (2) more flexibility of engine design, such as a very flat engine, and (3) less massive interstage structural components.

In 1961 Professor R. B. Morrison and Mr. G. L. Cossens of the Department of Aeronautical and Astronautical Engineering, obtained limited funds from the Institute of Science and Technology of The University of Michigan to conduct exploratory studies on the rotating wave motor. They effected a simplified analysis of the concept and some preliminary experiments. Subsequently, a contract between the university and the Air Force was effected, aimed at determining feasibility of the RDWE. The report herein describes those facets studied and results obtained pertinent to the question of feasibility.

A few different aspects of the overall problem were identified as being particularly important to the question of feasibility. These facets and their significance are described below.

- (1) It was deemed essential that a rather elaborate, but certainly approximate, theoretical analysis of the internal gas dynamics of the RDWE be effected so that information regarding scaling factors and potential performance could be obtained.
- (2) High rates of heat transfer to the wall would be expected, therefore an approximate theoretical analysis was desired.
- (3) In a liquid bipropellant system the question arises as to whether a detonation wave can propagate steadily in a gaseous-liquid droplet environment. This phase was treated briefly, theoretically as well as experimentally.
- (4) Some propellants of interest would be cryogenic and hence properties of detonation in an environment at elevated pressures and very low temperatures are important. Hence the detonation velocities of gaseous hydrogen-oxygen mixtures at initial pressures up to 15 atmospheres and temperatures down to the vapor saturation temperature of oxygen (≈ 112 °K) were measured.
- (5) The motor envisaged consisted of a detonation wave traversing an annular combustion chamber with an annular exhaust nozzle. Measurements of detonation velocity were made under these conditions.
- (6) Experimental results from an actual RDWE were deemed essential and such experiments were conducted on a small scale annular motor and on a linear motor.

The explorations enumerated above are described in detail in the subsequent sections of this report. Most of these results are also described in earlier progress reports of the project⁵⁻⁹ but this final report is complete in itself.

It will be readily apparent that much of the material herein is also pertinent to conventional rocket motor combustion instability problems. In this regard it is well to mention some very closely related work done in Russia by Voitsekhovsky^{10, 11}. He succeeded in obtaining a rotating detonation wave as well as oscillating waves in a premixed gaseous system, thereby circumventing injector problems experienced in this work. Presumably the Russian work relates to combustion instability. In view of the pertinence of this work, a translation of Reference 11 has been included as Appendix A of this report.

II. ANALYTICAL MODEL OF THE INTERNAL GASDYNAMICS OF THE ROTATING DETONATION WAVE ROCKET MOTOR

A. INTRODUCTION

It is highly desirable to establish theoretically the effects of the various design parameters (motor geometry, propellant flow rate, etc.) on the performance of the rotating detonation wave rocket motor. To accomplish this it is necessary to formulate an analytical model of the motor internal gasdynamics. This model, while retaining the essential physical features, should be simple enough to permit insight into motor operation so that it can be used as a design tool and as a basis for comparison of theoretical performance with that of other types of propulsion devices.

The first attempt to investigate the phenomena associated with a maintained rotating detonation wave appears to be due to Voitsekhovsky^{10,11} (see Appendix A for a translation of Reference 11). Because of the presence of many oblique waves in his detonation chamber (see Figure 5 of Appendix A) the flow field is very complicated and difficult to describe analytically. But Voitsekhovsky's experimental results (see Figure 3 in Appendix A) indicate the feasibility of maintaining stabilized rotating detonation waves in an annular channel with side relief. Interest in utilizing such a device for rocket propulsion began with the work of Morrison and Cossens⁵⁻⁹ and the studies initiated under the present contract.

In the present analysis a simplified description of an idealized rotating wave rocket motor is sought. It is assumed that the detonation waves completely fill the chamber cross-section and no reflected oblique shock waves are present. The chosen level of sophistication of the analytical model developed here is equivalent to that of the quasi-one dimensional, frozen specific heat, steady, isentropic flow model of conventional rocket motors. Thus

a system of mathematical equations is obtained that may be solved numerically to provide a description of the details of the flow field within the chamber. Also, expressions for the theoretical specific impulse and thrust coefficient of the rotating detonation wave rocket motor are derived.

B. ONE-DIMENSIONAL MODEL OF THE ROTATING DETONATION WAVE ROCKET MOTOR

1. Basic Hypotheses and Assumptions

The object here is to formulate an analytical model of the rotating detonation wave rocket motor which, while retaining the essential physical features of engine operation, is simple enough to permit insight into the internal gas-dynamics of the motor. However, the fluid flow field in the motor is quite complex; it is three-dimensional and unsteady with heat and mass addition and turbulent mixing taking place. As a result, simplifying assumptions must be made to achieve a solvable mathematical model of the motor. The key simplifying condition is that the detonation wave velocity is stabilized, so the fluid flow field is steady and quasi-one dimensional with respect to a frame of reference moving with the rotating detonation waves

The following is a list of the hypotheses and assumptions related to the establishment of a simplified analytical model of the rotating detonation wave rocket motor

- (a) The detonation wave velocity has reached a steady state, constant value.
- (b) The detonation waves are to be treated as plane discontinuities, that is, they are considered to be shock waves with heat addition. Otherwise, the flow is assumed to be in frozen chemical equilibrium
- (c) The detonation waves completely fill the motor chamber cross-section; there are no oblique waves present

- (d) Shear forces and heat transfer effects are negligible.
- (e) The propellant mass flow rate through the injector is constant and uniform in distribution. This condition is satisfied if the injector to chamber pressure ratio is always at or above the critical value and if the injector design is axially symmetric.
- (f) The pressure variations across the chamber in the axial and radial directions are negligible. From order of magnitude estimates this condition implies the rocket motor chamber dimensions are small compared to the overall motor radius. For a curved streamline

$$\frac{dP}{dn} = \frac{\rho V_a^2}{R}$$

and to have a negligible pressure variation in the radial direction it is required that

$$\frac{dP}{dn} \ll \frac{P}{l_c}$$

Noting that

$$\frac{P}{\rho V_a^2} = \frac{1}{\gamma M_a^2},$$

which is of order unity, the condition for the radial pressure variation to be small becomes

$$\frac{l_c}{R} \ll 1$$

For the axial pressure variation to be small the time for an acoustic wave to cross the chamber in the axial direction must be much less than the time the detonation wave takes to travel the distance between successive waves. Therefore, the condition is

$$\frac{x_n}{a_1} << \frac{2\pi R}{NV_w}$$

where a_1 is the minimum value of the sound speed in the chamber (the value just ahead of the detonation wave). Now since

$$\frac{V_w}{a_1} = M_w ,$$

where M_w is the detonation wave Mach number (which is of the same order of magnitude as 2π), the resulting condition for the axial pressure variation to be small is

$$\frac{x_n}{R} << \frac{1}{N}$$

where N is the number of detonation waves in the rocket motor.

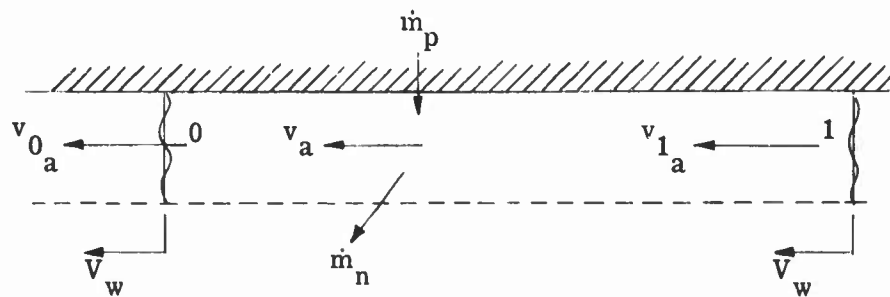
- (g) The fluid flow through the convergent section of the nozzle is assumed to be quasi-one-dimensional in the axial direction. The axial component of velocity at the throat is equated to the local speed of sound and the circumferential velocity component is invariant for a fluid particle passing through the convergent section of the nozzle. Also, the "stay time" of a fluid particle in the nozzle convergent section is small.
- (h) Both the unburned and burned propellants are thermally and calorically perfect gases.
- (i) The phenomenon of turbulent mixing between the burned and unburned propellants is treated by assuming alternatively complete instantaneous mixing or no mixing between the burned and unburned propellants. Either of these assumptions avoids the necessity of considering any axial gradients in the fluid properties and permits the establishment of a quasi-one-dimensional model of the rocket motor gasdynamics.

2. Derivation of the Equations for the Analytical Model

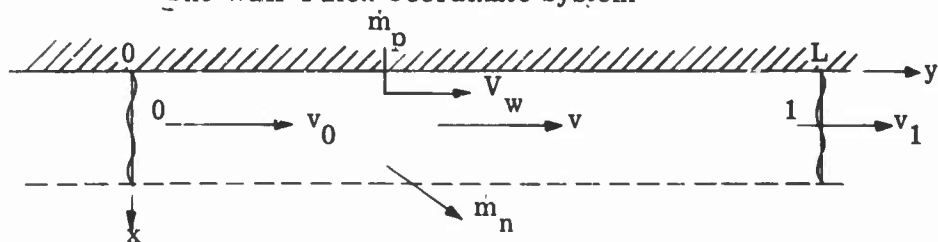
The first case to be analyzed is the gaseous "complete mixing" case where complete instantaneous mixing is assumed to occur between the burned and unburned propellants. The reason for considering this case is the relative simplicity of the analysis; in actual rocket motor operation mixing between the burned and unburned propellants should be avoided because it degrades the performance.

Definition of Coordinate Systems

Because the radial width of the chamber is considered to be small compared with the radius of curvature the rocket motor chamber can be "unrolled" and stretched out for purposes of analysis. Then the problem is one wherein a long tube of constant cross-sectional area has unburned mass entering one side and burned mass being ejected through the other. In this tube detonation waves occur periodically a distance L apart, each moving at a constant velocity, V_w . From the viewpoint of an observer moving with a detonation wave the flow field becomes steady and quasi-one-dimensional.



The Wall-Fixed Coordinate System



The Wave-Fixed Coordinate System

Note: arrows define the direction of positive velocity.

The two coordinate systems are related by the transformation

$$y = V_w t$$

$$v = V_w - v_a$$

with $t = 0$ when a reference point on the rocket motor chamber wall is coincident with a detonation wave.

Jump Relations Across a Detonation Wave

The fluid flow properties at $y = 0$ and $y = L$ are related by the hydrodynamic jump conditions across a detonation wave:

$$\rho_1 v_1 = \rho_0 v_0$$

$$P_1 + \rho_1 v_1^2 = P_0 + \rho_0 v_0^2$$

$$C_{P_1} T_1 + \frac{1}{2} v_1^2 + \mu_1 Q = C_{P_0} T_0 + \frac{1}{2} v_0^2$$

where μ_1 is the relative mass concentration of unburned propellant at $y = L$.

With the ideal gas assumption the thermal and caloric equations of state are

$$P = \frac{\rho R_0 T}{m_{avg}}$$

$$C_P = \frac{\gamma}{\gamma - 1} \frac{R_0}{m_{avg}}$$

and the speed of sound is given by

$$a^2 = \frac{\gamma P}{\rho}$$

Introducing the non-dimensional quantities

$$\bar{P} = \frac{P}{P_0}, \quad \bar{v} = \frac{v}{v_0}, \quad \bar{a} = \frac{a}{a_0}, \quad M = \frac{v}{a}, \quad \bar{Q} = \frac{Q}{C_P T_0}$$

the above equations, when solved for \bar{P}_1 , \bar{v}_1 , and M_1 in terms of M_0 and \bar{Q} , yield

$$\bar{v}_1 = b + \sqrt{b^2 + c}$$

$$\bar{P}_1 = 1 - \gamma_0 M_0^2 (\bar{v}_1 - 1)$$

$$M_1 = \sqrt{\frac{\gamma_0 \bar{v}_1}{\gamma_1 \bar{P}_1}}$$

where

$$b = \frac{\gamma_1}{\gamma_0} \left[\frac{1 + \gamma_0 M_0^2}{(\gamma_1 + 1) M_0^2} \right],$$

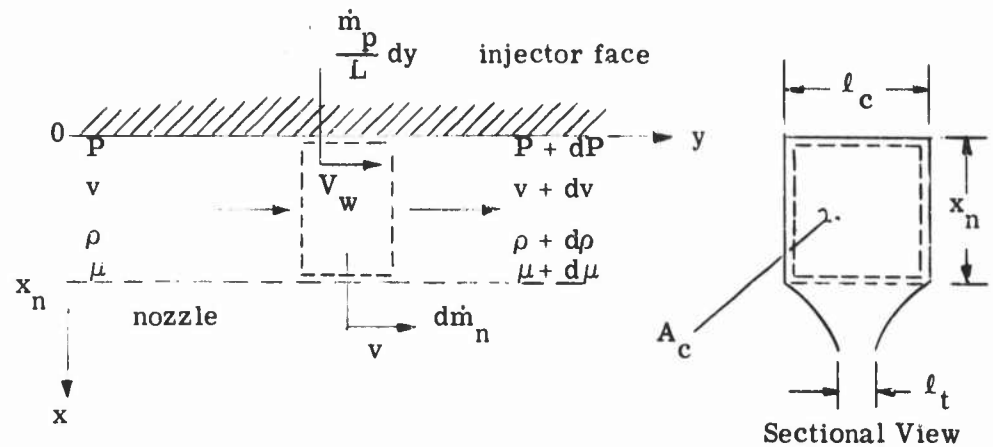
$$c = \frac{2}{\gamma_0 - 1} \left(\frac{\gamma_1 - 1}{\gamma_1 + 1} \right) \frac{1}{M_0^2} \left[\mu_1 \bar{Q} - \left(1 + \frac{\gamma_0 - 1}{2} M_0^2 \right) \right].$$

If $\gamma_1 = \gamma_0 = \gamma$ and $M_0 = 1$ then

$$\bar{v}_1 = 1 + \sqrt{\frac{2 \mu_1 \bar{Q}}{\gamma + 1}}.$$

Conservation Equations for a Fluid Element in the "Complete Mixing" Case

The conservation equations are written for the fluid flow through a small increment of the rocket motor chamber, of length dy .



Definition of the Control Volume

The conservation equations for steady inviscid, and adiabatic flow of a fluid through a given control volume with surface S are:

$$\iint_S \rho \mathbf{v} \cdot \hat{\mathbf{n}} dS = 0 \quad \text{continuity equation}$$

$$\iint_S \rho \mu \mathbf{v} \cdot \hat{\mathbf{n}} dS = 0 \quad \text{continuity of unburned species equation}$$

$$\iint_S \rho (\mathbf{v} \cdot \hat{\mathbf{n}}) \mathbf{v} dS = - \iint_S P \hat{\mathbf{n}} dS \quad \text{momentum equation}$$

$$\iint_S \rho (\mathbf{v} \cdot \hat{\mathbf{n}}) \left(h + \frac{1}{2} v^2 \right) dS = 0 \quad \text{energy equation}$$

Application of these relations to the control volume in question yields (after some manipulation):

$$\frac{d}{dy} (\rho v A_c) = \frac{\dot{m}_P}{NL} - \frac{1}{N} \frac{d\dot{m}_n}{dy}$$

$$\rho v A_c \frac{d\mu}{dy} = (1 - \mu) \frac{\dot{m}_p}{NL}$$

$$\rho v A_c \frac{dv}{dy} + A_c \frac{dP}{dy} = \frac{\dot{m}_p}{NL} (V_w - v)$$

$$\rho v A_c \frac{d}{dy} \left(h + \frac{1}{2} v^2 \right) = \frac{\dot{m}}{NL} \left[h_p + \frac{1}{2} V_w^2 - \left(h + \frac{1}{2} v^2 \right) \right]$$

Now for a mixture of unburned and burned propellants the enthalpy, h , is given by

$$h = \mu h_A + (1 - \mu) h_B$$

$$= \mu \left[\int_0^T C_{P_A} dT + h_A^{(0)} \right] + (1 - \mu) \left[\int_0^T C_{P_B} dT + h_B^{(0)} \right]$$

Since in this "complete mixing" case $C_{P_A} = C_{P_B} = C_P$ and since Q is defined by the relation

$$h_A^{(0)} = Q + h_B^{(0)}$$

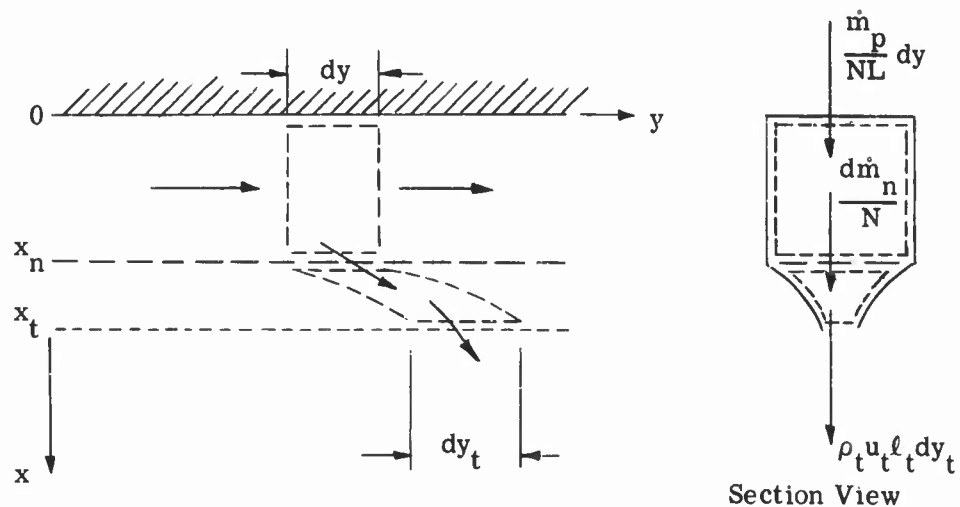
the enthalpy of the mixture is

$$h = C_P T + \mu Q + h_B^{(0)}$$

Combination of this relation with the energy and conservation of unburned species equations gives

$$\rho v A_c \frac{d}{dy} \left(C_p T + \frac{1}{2} v^2 \right) = \frac{\dot{m}_p}{NL} \left[C_p T_p + \frac{1}{2} v_w^2 - \left(C_p T + \frac{1}{2} v^2 \right) \right] .$$

It is now required to relate the incremental mass flow from the rocket motor chamber into the nozzle, $d\dot{m}_n$, to the local flow properties in the chamber. Consider a control volume in the convergent section of the nozzle bounded by two adjacent streamlines:



Then the equations governing this control volume are

$$\frac{1}{N} \frac{d\dot{m}_n}{dy} = \rho_t u_t l_t \frac{dy_t}{dy} \quad \text{continuity equation}$$

$$h_t + \frac{1}{2} (u_t^2 + v^2) = h + \frac{1}{2} v^2 \quad \text{energy equation}$$

$$\frac{P_t}{P} = \left(\frac{\rho_t}{\rho} \right)^\gamma \quad \text{isentropic process equation}$$

To estimate the relative displacement of two adjacent streamlines, dy_t/dy , consider the stay time, τ , of a fluid particle in the convergent section of the rocket nozzle.

$$\tau = \int_{x_n}^{x_t} \frac{dx}{u}$$

Then

$$\begin{aligned} dy_t &= dy + \left(v + \frac{dv}{dy} \cdot dy \right) \tau - v\tau + \dots \\ &\approx dy \left(1 + \tau \frac{dv}{dy} \right) \\ &\approx dy \end{aligned}$$

for a small stay time, τ , of a fluid particle in the convergent nozzle section; that is, $dy_t \approx dy$ for relatively short convergent nozzle sections. Thus

$$\frac{1}{N} \frac{dm_n}{dy} = \rho a \left(\frac{2}{\gamma + 1} \right)^{\frac{\gamma + 1}{2(\gamma - 1)}} \ell_t$$

provides the desired relation for dm_n in terms of local rocket motor chamber conditions.

Then the equations for a fluid element in the rocket motor chamber for the "complete mixing" case are

$$\frac{d}{dy} (\rho v A_c) = \frac{m_p}{NL} - \rho a \left(\frac{2}{\gamma + 1} \right)^{\frac{\gamma + 1}{2(\gamma - 1)}} \ell_t$$

$$\rho v A_c \frac{d\mu}{dy} = (1 - \mu) \frac{m_p}{NL}$$

$$\rho v A_c \frac{dv}{dy} + A_c \frac{dp}{dy} = \frac{\dot{m}_p}{NL} (v_w - v)$$

$$\rho v A_c \frac{d}{dy} \left(C_p T + \frac{1}{2} v^2 \right) = \frac{\dot{m}_p}{NL} \left[C_p T_p + \frac{1}{2} v_w^2 - \left(C_p T + \frac{1}{2} v^2 \right) \right]$$

It should be noted that the model of the flow in the motor chamber is a special case of the generalized (steady) one-dimensional flows discussed by Shapiro¹².

It is convenient to adopt the following non-dimensional notations:

$$\bar{P} = \frac{P}{P_0}, \quad \bar{v} = \frac{v}{v_0}, \quad \bar{a} = \frac{a}{a_0}, \quad \bar{\rho} = \frac{\rho}{\rho_0}, \quad M = \frac{v}{a} = M_0 \frac{\bar{v}}{\bar{a}}, \quad \eta = \frac{y}{L},$$

$$\bar{m} = \bar{\rho} \bar{v} = \frac{\bar{P} M^2}{\bar{v} M_0^2}, \quad \frac{d\bar{m}_p}{d\eta} = \frac{\bar{m}_p}{\rho_0 v_0 A_c N} = G,$$

$$\frac{d\bar{m}_n}{d\eta} = \frac{d\bar{m}_n}{\rho_0 v_0 A_c N} = \frac{B M \bar{P}}{\bar{v} M_0^2}, \quad B = \frac{\ell_t L}{A_c} \left(\frac{2}{\gamma + 1} \right)^{\frac{\gamma + 1}{2(\gamma - 1)}}$$

Also, note that

$$\frac{d\bar{m}_p}{\bar{m}} = \frac{\bar{v} M_0^2 G}{\bar{P} M^2} d\eta, \quad \frac{d\bar{m}_n}{\bar{m}} = \frac{B}{M} d\eta, \quad \frac{dM}{M} = \frac{d\bar{v}}{\bar{v}} - \frac{da}{a}.$$

Then, writing the equations in logarithmic differential form with M , \bar{v} , \bar{P} as the dependent variables, one obtains

$$2 \frac{dM}{M} - \frac{dv}{\bar{v}} + \frac{d\bar{P}}{\bar{P}} = \frac{\bar{m}_p}{\bar{m}} - \frac{\bar{m}_n}{\bar{m}}$$

$$\frac{dv}{\bar{v}} + \frac{1}{\gamma M^2} \frac{d\bar{P}}{\bar{P}} = \left(\frac{\bar{V}_w - \bar{v}}{\bar{v}} \right) \frac{\bar{m}_p}{\bar{m}}$$

$$- 2 \frac{dM}{M} + 2 \left(1 + \frac{\gamma - 1}{2} M^2 \right) \frac{dv}{\bar{v}} = \left[\frac{M^2}{\bar{v}^2 M_0^2} \left(\bar{T}_p + \frac{\gamma - 1}{2} M_0^2 \bar{V}_w^2 \right) - \left(1 + \frac{\gamma - 1}{2} M^2 \right) \right] \frac{\bar{m}_p}{\bar{m}}$$

$$\frac{d\mu}{1 - \mu} = \frac{\bar{m}_p}{\bar{m}}$$

By applying Cramer's rule the differential quantities dM/M , dv/\bar{v} , and $d\bar{P}/\bar{P}$ are found in terms of Mach number and the quantities on the right hand side of the equations. It is convenient to present the results in the form of a table of influence coefficients. (See Table 1.) As an example of the use of this table of influence coefficients, $d\bar{P}/\bar{P}$ is given by

$$\frac{d\bar{P}}{\bar{P}} = \frac{\gamma M^2}{M^2 - 1} \left\{ \left(1 - \frac{\bar{V}_w - \bar{v}}{\bar{v}} \left[1 + (\gamma - 1) M^2 \right] + \frac{M^2}{M_0^2 \bar{v}^2} \left(\bar{T}_p + \frac{\gamma - 1}{2} M_0^2 \bar{V}_w^2 \right) \right. \right. \\ \left. \left. - \left(1 + \frac{\gamma - 1}{2} M^2 \right) \right) \frac{\bar{v} M_0^2 G}{PM^2} - \frac{B}{M} \right\} d\eta .$$

Evaluation of the Mach Number of the Flow Just Behind the Detonation Wave

It is to be demonstrated here that the rocket motor flow model employed results in the detonation waves satisfying the Chapman-Jouguet condition; that is, the Mach number, M_0 , of the flow just behind the detonation wave is unity relative to a wave-fixed coordinate system.

TABLE I. INFLUENCE COEFFICIENTS

$$\frac{d\bar{m}_p}{\bar{m}} = \frac{\left(\bar{V}_w - \bar{V}\right) d\bar{m}_p}{\bar{m}} = \left[\frac{M^2}{M_0^2} \frac{2}{\gamma - 2} \left(\bar{T}_p + \frac{\gamma - 1}{2} M_0^2 \bar{V}_w^2 \right) - \left(1 + \frac{\gamma - 1}{2} M^2 \right) \right] \frac{d\bar{m}_p}{\bar{m}}$$

$$\frac{dM}{M} = - \frac{1 + \frac{\gamma - 1}{2} M^2}{M^2 - 1} \frac{1 + \frac{\gamma - 1}{2} M^2}{M^2 - 1} - \frac{\gamma M^2 \left(1 + \frac{\gamma - 1}{2} M^2 \right)}{M^2 - 1} - \frac{\frac{1}{2} (1 + \gamma M^2)}{M^2 - 1}$$

$$\frac{d\bar{v}}{\bar{v}} = - \frac{1}{M^2 - 1} - \frac{1}{M^2 - 1} - \frac{\gamma M^2}{M^2 - 1} - \frac{1}{M^2 - 1}$$

$$\frac{d\bar{P}}{\bar{P}} = \frac{\gamma M^2}{M^2 - 1} - \frac{\gamma M^2}{M^2 - 1} - \frac{\gamma M^2 [1 + (\gamma - 1) M^2]}{M^2 - 1} - \frac{\gamma M^2}{M^2 - 1}$$

$$\frac{da}{a} = \frac{\frac{\gamma - 1}{2} M^2}{M^2 - 1} - \frac{\frac{\gamma - 1}{2} M^2}{M^2 - 1} - \frac{\frac{\gamma (\gamma - 1)}{2} M^4}{M^2 - 1} - \frac{\frac{1}{2} (\gamma M^2 - 1)}{M^2 - 1}$$

$$0 \quad 0 \quad 0 \quad 0$$

The derivative of the pressure at $\eta = 0$ is

$$\left(\frac{d\bar{P}}{d\eta} \right)_{\eta=0} = \frac{\gamma M_0^2}{M_0^2 - 1} \left\{ \left[\bar{T}_P + \frac{\gamma - 1}{2} M_0^2 \left(\bar{V}_w^2 - 1 \right)^2 - (\bar{V}_w - 1) \right] G - \frac{B}{M_0} \right\}$$

From experimental evidence and physical reasoning (in the region between successive detonation waves the pressure must decrease to meet the initial condition for the next wave) one obtains the restriction

$$\left(\frac{d\bar{P}}{d\eta} \right)_{\eta=0} \leq 0 .$$

Consideration of the possible values of the various parameters results in the order estimates

$$\frac{\gamma - 1}{2} = \mathcal{O}(.1) , \quad B/G = \mathcal{O}(1) , \quad \bar{V}_w - 1 = \mathcal{O}(1) ,$$

$$T_p = \mathcal{O}(.1) , \quad M_{0c} = \mathcal{O}(5)$$

where M_{0c} is the lowest positive root of the equation $\left\{ \right\} = 0$. Therefore, noting that the quantity in braces, $\left\{ \right\}$, is a steadily increasing function of M_0 , $\left\{ \right\} \leq 0$ for a range of values of M_0 including the interval $0 \leq M_0 \leq M_{0c}$. Thus, since both $(dP/d\eta)_{\eta=0}$ and $\left\{ \right\}$ are negative

$$\frac{\gamma M_0^2}{M_0^2 - 1} \geq 0$$

when $0 \leq M_0 < \mathcal{O}(5)$. Hence

$$M_0 \geq 1 .$$

However, the detonation wave is considered to be a shock wave followed closely by a chemical reaction resulting in the release of energy in the form of heat. For such a wave

$$M_0 \leq 1$$

(see, for example, Courant and Friedrichs¹³ for a discussion of this matter).

Comparison of the two restrictions on M_0 demonstrates that

$$M_0 = 1$$

and according to the analytical model the detonation waves in the rocket motor are indeed Chapman-Jouguet waves.

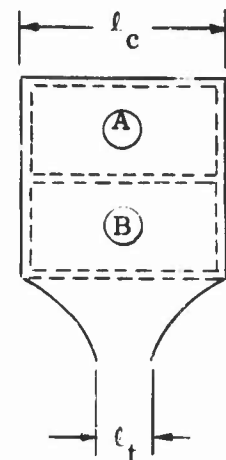
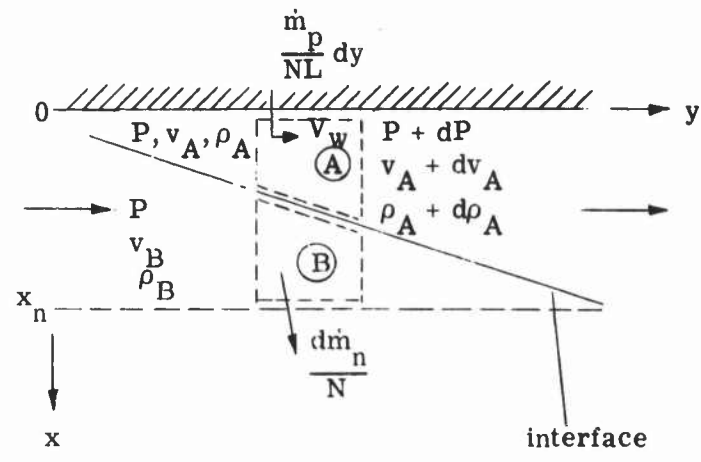
The Gaseous "No Mixing" Case

To achieve a more realistic model of the rotating detonation wave rocket motor account is taken of the differences in properties of the burned and unburned propellants. This is accomplished within the limitation of a quasi-one-dimensional model of the flow field by assuming no mixing to occur between the burned and unburned propellants; that is, they are separated by an interface which is stationary with respect to the rotating detonation waves and across which no mass or energy transfer takes place. In other respects the treatment follows that of the "complete mixing" case. The control volume is split by the interface into two sections, A and B, corresponding to the unburned and burned propellants, respectively. In each section the flow is assumed to be quasi-one-dimensional in the circumferential direction with the pressure gradient across the interface taken to be zero. Since the interface is a streamline, assuming the slope of the interface

$$\frac{dx}{dy} = \frac{u}{v}$$

to be small is consistent with the condition that the flow is quasi-one-dimensional in the circumferential direction, namely, that

$$\frac{u}{v} \ll 1 .$$



Sectional View

Definition of Control Volumes

As in the "complete mixing" case the incremental mass flow rate into the convergent section of the nozzle is given by

$$\frac{dm_n}{N} = \rho_B a_B \left(\frac{2}{\gamma_B + 1} \right)^{\frac{\gamma_B + 1}{2(\gamma_B - 1)}} l_t dy .$$

Note that in this "no mixing" case the gases exhausting through the rocket nozzle are considered to be completely burned and, hence, this model will predict the ideal performance of a rotating detonation wave rocket motor.

Conservation Equations for a Fluid Element in the "No Mixing" Case

Application of the conservation equations for steady, adiabatic and inviscid fluid flow to control volumes A and B results in the relations

$$\frac{d}{dy} (\rho_A v_A \ell_c x) = \frac{\dot{m}_p}{NL}, \quad (A) \text{ continuity equation}$$

$$\rho_A v_A \ell_c x \cdot \frac{dv_A}{dy} + \ell_c x \frac{dP}{dy} = \frac{\dot{m}_p}{NL} (v_w - v_A), \quad (A) \text{ momentum equation}$$

$$\frac{d}{dy} \left[\rho_A v_A \ell_c x \left(h_A + \frac{1}{2} v_A^2 \right) \right] = \frac{\dot{m}_p}{NL} \left(h_p + \frac{1}{2} v_w^2 \right), \quad (A) \text{ energy equation}$$

$$\frac{d}{dy} \left[\rho_B v_B \ell_c (x_n - x) \right] = - \rho_B a_B \left(\frac{2}{\gamma_B + 1} \right)^{\frac{\gamma_B + 1}{2(\gamma_B - 1)}} \ell_t \quad (B) \text{ continuity equation}$$

$$\rho_B v_B \frac{dv_B}{dy} + \frac{dP}{dy} = 0, \quad (B) \text{ momentum equation}$$

$$\frac{d}{dy} \left(h_B + \frac{1}{2} v_B^2 \right) = 0, \quad (B) \text{ energy equation}$$

Note that here x is the axial coordinate to the interface separating the unburned and burned propellants.

Four of these equations can be integrated, yielding the system of equations for the "no mixing" case:

$$\rho_A v_A \ell_c x = \frac{\dot{m}_p}{NL} y$$

$$\frac{\dot{m}_p}{NL} y \frac{dv_A}{dy} + \ell_c x \frac{dP}{dy} = \frac{\dot{m}_p}{NL} (v_w - v_A)$$

$$C_{P_A} T_A + \frac{1}{2} v_A^2 = C_{P_A} T_p + \frac{1}{2} v_w^2$$

$$\frac{d}{dy} [\rho_B v_B \ell_c (x_n - x)] = - \rho_B a_B \left(\frac{2}{\gamma_B + 1} \right)^{\frac{\gamma_B + 1}{2(\gamma_B - 1)}} \ell_t$$

$$\frac{P}{(\gamma_B - 1) \rho_B} + \frac{1}{2} v_B^2 = \frac{P_0}{(\gamma_B - 1) \rho_{B_0}} + \frac{1}{2} v_{B_0}^2$$

$$C_{P_B} T_B + \frac{1}{2} v_B^2 = C_{P_B} T_{B_0} + \frac{1}{2} v_{B_0}^2$$

It is again convenient to transform to non-dimensional variables:

$$\eta = \frac{y}{L}, \quad \xi = \frac{x}{x_n}, \quad \bar{P} = \frac{P}{P_0}, \quad \bar{v}_A = \frac{v_A}{v_{B_0}}, \quad \bar{\rho}_A = \frac{\rho_A}{\rho_{B_0}}, \quad \bar{a}_A = \frac{a_A}{a_{B_0}},$$

$$\bar{v}_B = \frac{v_B}{v_{B_0}}, \quad \bar{\rho}_B = \frac{\rho_B}{\rho_{B_0}}, \quad \bar{a}_B = \frac{a_B}{a_{B_0}}, \quad M_A = \frac{\bar{v}_A}{\bar{a}_A}, \quad M_B = \frac{\bar{v}_B}{\bar{a}_B}.$$

Note that, as in the "complete mixing" case, $M_{B_0} = 1$, and therefore, $a_{B_0} = v_{B_0}$. In the non-dimensionalization of the equations the following non-dimensional parameters will appear:

$$G = \frac{\dot{m}_p}{\rho_{B_0} v_{B_0} N A_c}, \quad B = \frac{\ell_t L}{A_c} \left(\frac{2}{\gamma_B + 1} \right)^{\frac{\gamma_B + 1}{2(\gamma_B - 1)}}, \quad \bar{C}_{P_A} = \frac{C_{P_A}}{C_{P_B}},$$

$$\bar{T}_p = \frac{T_p}{T_{B_0}}, \quad \bar{Q} = \frac{Q}{C_{P_B} T_{B_0}}, \quad \bar{V}_w = \frac{V_w}{v_{B_0}}.$$

Note that in the "no-mixing" case the mass flow parameter G (equal to the ratio of the propellant mass flow rate to the mass flow rate through the detonation waves) is unity, and the relation

$$G = \frac{\dot{m}_p}{\rho_{B_0} v_{B_0} N A_c} = 1$$

defines A_c , which in this case is the effective frontal area of the detonation waves.

The equations are simplified somewhat when the various dependent variables are expressed in terms of the Mach numbers, M_A and M_B . The logarithmic differential relations are

$$\frac{d\bar{v}_A}{\bar{v}_A} = \frac{1}{1 + \frac{\gamma_A - 1}{2} M_A^2} \frac{dM_A}{M_A},$$

$$\frac{d\bar{a}_A}{\bar{a}_A} = - \frac{\frac{\gamma_A - 1}{2} M_A^2}{1 + \frac{\gamma_A - 1}{2} M_A^2} \frac{dM_A}{M_A},$$

$$\frac{d\bar{P}}{\bar{P}} = - \frac{\gamma_B M_B^2}{1 + \frac{\gamma_B - 1}{2} M_B^2} \frac{dM_B}{M_B} ,$$

$$\frac{d\bar{v}_B}{\bar{v}_B} = \frac{1}{1 + \frac{\gamma_B - 1}{2} M_B^2} \frac{dM_B}{M_B} ,$$

$$\frac{d\bar{a}_B}{\bar{a}_B} = - \frac{\frac{\gamma_B - 1}{2} M_B^2}{1 + \frac{\gamma_B - 1}{2} M_B^2} \frac{dM_B}{M_B} ,$$

$$\frac{d\xi}{\xi} = \frac{d\eta}{\eta} - \frac{1 + (\gamma_A - 1) M_A^2}{1 + \frac{\gamma_A - 1}{2} M_A^2} \frac{dM_A}{M_A} + \frac{\gamma_B M_B^2}{1 + \frac{\gamma_B - 1}{2} M_B^2} \frac{dM_B}{M_B} .$$

Then the integrated relationships are

$$\bar{P} = \left[\frac{\frac{\gamma_B + 1}{2}}{1 + \frac{\gamma_B - 1}{2} M_B^2} \right]^{\frac{\gamma_B}{\gamma_B - 1}} ,$$

$$\bar{v}_B = M_B \left[\frac{\frac{\gamma_B + 1}{2}}{1 + \frac{\gamma_B - 1}{2} M_B^2} \right]^{\frac{1}{2}} ,$$

$$\bar{\rho}_B = \left[\frac{\frac{\gamma_B + 1}{2}}{1 + \frac{\gamma_B - 1}{2} M_B^2} \right]^{\frac{1}{\gamma_B - 1}},$$

$$\bar{v}_A = M_A \left[\frac{\frac{\gamma_A - 1}{\gamma_B - 1} \bar{C}_{P_A} \bar{T}_P + \frac{\gamma_A - 1}{2} \bar{V}_w^2}{1 + \frac{\gamma_A - 1}{2} M_A^2} \right]^{\frac{1}{2}},$$

$$\bar{\rho}_A = \frac{\gamma_A}{\gamma_B} \left[\frac{\frac{\gamma_B + 1}{2}}{1 + \frac{\gamma_B - 1}{2} M_B^2} \right]^{\frac{\gamma_B}{\gamma_B - 1}} \left[\frac{1 + \frac{\gamma_A - 1}{2} M_A^2}{\frac{\gamma_A - 1}{\gamma_B - 1} \bar{C}_{P_A} \bar{T}_P + \frac{\gamma_A - 1}{2} \bar{V}_w^2} \right]^{\frac{1}{\gamma_B - 1}},$$

$$\xi = \left[\frac{\frac{\gamma_A - 1}{\gamma_B - 1} \bar{C}_{P_A} \bar{T}_P + \frac{\gamma_A - 1}{2} \bar{V}_w^2}{1 + \frac{\gamma_A - 1}{2} M_A^2} \right]^{\frac{1}{2}} \left[\frac{1 + \frac{\gamma_B - 1}{2} M_B^2}{\frac{\gamma_B + 1}{2}} \right]^{\frac{\gamma_B}{\gamma_B - 1}} \frac{\gamma_B G \eta}{\gamma_A M_A}.$$

The non-dimensional form for the differential equations in the "no mixing" case is

$$\frac{\xi}{1 + \frac{\gamma_A - 1}{2} M_A^2} \frac{dM_A}{M_A} - \left(\frac{\gamma_B M_B^2}{\gamma_A M_A^2} \right) \frac{\xi}{1 + \frac{\gamma_B - 1}{2} M_B^2} \frac{dM_B}{M_B} = \left(\frac{\bar{V}_w - \bar{v}_A}{\bar{v}_A} \right) \frac{G d\eta}{\bar{\rho}_A \bar{v}_A},$$

$$\frac{\xi [1 + (\gamma_A - 1) M_A^2] dM_A}{1 + \frac{\gamma_A - 1}{2} M_A^2} - \frac{M_B^2 - 1 + \xi [1 + (\gamma_B - 1) M_B^2] dM_B}{1 + \frac{\gamma_B - 1}{2} M_B^2} = \left(\frac{G}{\bar{\rho}_A \bar{v}_A} - \frac{B}{M_B} \right) d\eta .$$

Solving these equations by Cramer's rule for the derivatives dM_A/M_A and dM_B/M_B gives two simultaneous first order quasi-linear ordinary differential equations for M_A and M_B :

$$\frac{1}{1 + \frac{\gamma_A - 1}{2} M_A^2} \cdot \frac{1}{M_A} \frac{dM_A}{d\eta} = \frac{\frac{\gamma_B M_B^2}{\gamma_A M_A^2} \left(\frac{G}{\bar{\rho}_A \bar{v}_A} - \frac{B}{M_B} \right) - \left(\frac{\bar{v}_w - \bar{v}_A}{\bar{v}_A} \right) \frac{G}{\bar{\rho}_A \bar{v}_A} \left[1 + (\gamma_B - 1) M_B^2 + \frac{M_B^2 - 1}{\xi} \right]}{\xi \left\{ \frac{\gamma_B M_B^2}{\gamma_A M_A^2} \left[1 + (\gamma_A - 1) M_A^2 \right] - \left[1 + (\gamma_B - 1) M_B^2 \right] \right\} - (M_B^2 - 1)} ,$$

$$\frac{1}{1 + \frac{\gamma_B - 1}{2} M_B^2} \cdot \frac{1}{M_B} \frac{dM_B}{d\eta} = \frac{\frac{G}{\bar{\rho}_A \bar{v}_A} - \frac{B}{M_B} - \left(\frac{\bar{v}_w - \bar{v}_A}{\bar{v}_A} \right) \frac{G}{\bar{\rho}_A \bar{v}_A} \left[1 + (\gamma_A - 1) M_A^2 \right]}{\xi \left\{ \frac{\gamma_B M_B^2}{\gamma_A M_A^2} \left[1 + (\gamma_A - 1) M_A^2 \right] - \left[1 + (\gamma_B - 1) M_B^2 \right] \right\} - (M_B^2 - 1)} ,$$

Hence, the problem in the "no mixing" case consists of finding a solution to this pair of differential equations consistent with the jump conditions across the detonation wave, which take the form

$$\bar{v}_{A_1} = b + \sqrt{b^2 + c} ,$$

$$\bar{P}_1 = 1 - \gamma_B \left(\bar{v}_{A_1} - 1 \right) ,$$

$$M_{A_1} = \sqrt{\frac{\gamma_B \bar{v}_{A_1}}{\gamma_A \bar{P}_1}} ,$$

with

$$b = \frac{\gamma_A}{\gamma_B} \left(\frac{\gamma_B + 1}{\gamma_A + 1} \right) ,$$

$$c = \frac{2}{\gamma_B - 1} \left(\frac{\gamma_A - 1}{\gamma_A + 1} \right) \left(\bar{Q} - \frac{\gamma_B + 1}{2} \right) .$$

Note that this system of equations is an eigenvalue problem. Of the parameters G , \bar{T}_p , \bar{C}_{pA} , γ_A , γ_B , B , \bar{V}_w and \bar{Q} , the first five are to be specified while the latter three are unknown eigenvalues. The number of unknown eigenvalues is reduced to two when the integrated energy equation in (A) is evaluated at $\eta = 1$:

$$\bar{v}_{A_1} = M_{A_1} \left[\frac{\frac{\gamma_A - 1}{\gamma_B - 1} \bar{C}_{pA} \bar{T}_p + \frac{\gamma_A - 1}{2} \bar{V}_w^2}{1 + \frac{\gamma_A - 1}{2} M_{A_1}^2} \right]^{\frac{1}{2}} .$$

The eigenvalues are correctly determined when the solution of the differential equations also satisfies the jump relations across the detonation waves.

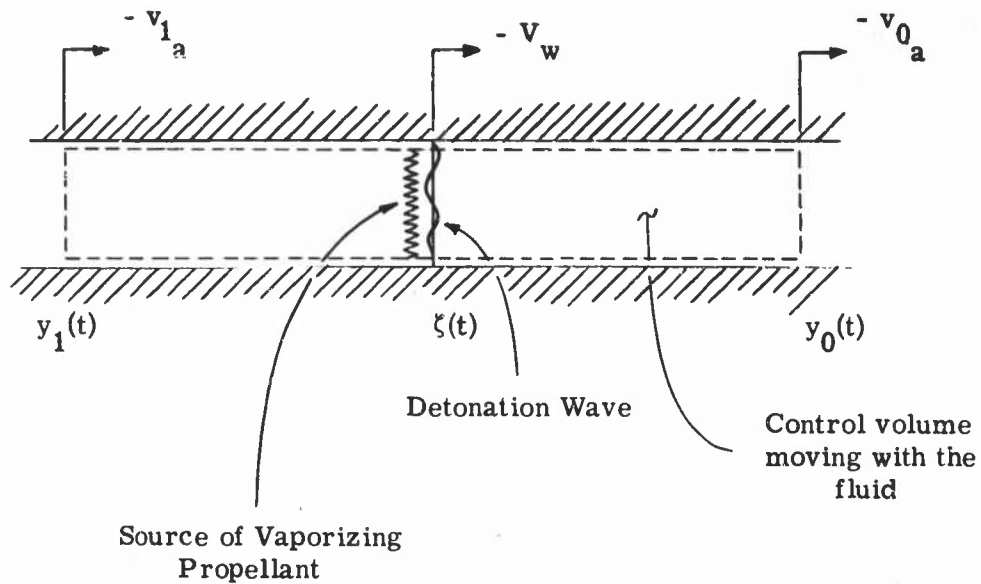
The Liquid-Gaseous "No-Mixing" Case

A practical situation to consider is when one propellant is injected into the rocket motor chamber in the liquid state (for example, the case of liquid oxygen and gaseous hydrogen as propellants). A quasi-one dimensional steady flow model of the rotating detonation wave rocket motor gasdynamics is obtained in this case when the "no mixing" model is adopted with the following additional assumptions:

- (a) The volume of the liquid propellant is negligible as compared with the volume of the gaseous propellant.
- (b) The liquid propellant evaporates and reacts instantaneously at the plane of the detonation wave, no consideration is given here to the problem of the propagation of detonation waves through heterogeneous media—only gross gasdynamic effects are considered.
- (c) There is no interaction between the liquid drops and the gaseous propellant, and hence the circumferential coordinate of the drops remains stationary with respect to the chamber walls. In control volume (A) the liquid drops have the velocity V_w relative to the detonation waves.

Control volume (A) now effectively will contain only gaseous propellant since the liquid occupies negligible volume and is assumed not to interact with the gaseous propellant. Therefore, the differential equations derived for the all-gaseous "no-mixing" case are still valid here, except that the parameters γ_A , \bar{C}_{P_A} , G , and \bar{T}_p now only refer to properties of the gaseous propellant component. At the detonation wave there is a source of vaporizing propellant, however, and the jump conditions across the detonation wave need modification.

It is required to re-derive the jump conditions across a detonation wave with the following picture in mind



The derivation of the jump relations given here follows the method presented in Courant and Friedrichs¹³. The conservation equations of mass and momentum for a control volume moving with the fluid are

$$\frac{d}{dt} \int_{y_1(t)}^{y_0(t)} \rho dy = \frac{\dot{m}_\ell}{NA_c},$$

$$\frac{d}{dt} \int_{y_1(t)}^{y_0(t)} \rho (-v_a) dy = P_1 - P_0.$$

Note that these integrals are of the form

$$J = \int_{y_1(t)}^{y_0(t)} \psi(y, t) dt$$

and therefore,

$$\frac{dJ}{dt} = \frac{d}{dt} \int_{y_1(t)}^{\xi(t)} \psi(y, t) dy + \frac{d}{dt} \int_{\xi(t)}^{y_0(t)} \psi(y, t) dy$$

Then, by Liebnitz' rule for differentiation under the integral,

$$\frac{dJ}{dt} = \int_{y_1(t)}^{y_0(t)} \frac{\partial \psi}{\partial t} dy + \psi(\xi^(-), t) \dot{\xi} - \psi(y_1, t) \dot{y}_1 + \psi(y_1, t) \dot{y}_0 - \psi(\xi^(+), t) \dot{\xi}$$

But

$$\dot{\xi} = V_w, \quad y_0 = -v_{1a}, \quad y_1 = -v_{0a}$$

Utilizing the velocity transformation from the wall fixed coordinate system to the coordinate system moving with the detonation waves,

$$v = V_w - v_a$$

one obtains

$$\lim_{(y_0 - y_1) \rightarrow 0} \left(\frac{dJ}{dt} \right) = \psi_0 v_{B_0} - \psi_1 v_{A_1}$$

The continuity equation becomes, with $\psi = \rho$,

$$\rho_{A_1} v_{A_1} + \frac{\dot{m}_\ell}{NA_c} = \rho_{B_0} v_{B_0}$$

For the momentum equation $\psi = -\rho v_a$ and hence,

$$-\rho_{B_0} v_{B_0} (V_w - v_{B_0}) + \rho_{A_1} v_{A_1} (V_w - v_{A_1}) = P_1 - P_0$$

Combination with the continuity equation yields

$$P_1 + \rho_{A_1} v_{A_1}^2 + \frac{\dot{m}_l V_w}{NA_c} = P_0 + \rho_{B_0} v_{B_0}^2$$

In non-dimensional form the jump relations are expressed as

$$\bar{\rho}_{A_1} \bar{v}_{A_1} + \bar{\dot{m}}_l = 1$$

$$\bar{P}_1 + \gamma_B \bar{\rho}_{A_1} \bar{v}_{A_1}^2 + \gamma_B \bar{\dot{m}}_l \bar{V}_w = \gamma_B + 1$$

where $\bar{\dot{m}}_l$ is defined by

$$\bar{\dot{m}}_l = \frac{\dot{m}_l}{\rho_{B_0} v_{B_0} NA_c}$$

Now the total propellant mass flow rate, \dot{m}_p , equals the sum of the mass flow rates of gaseous and liquid propellants

$$\dot{m}_p = \dot{m}_G + \dot{m}_l$$

Then, defining G by

$$G = \frac{\dot{m}_G}{\rho_{B_0} v_{B_0} NA_c}$$

one obtains the relations

$$\bar{\rho}_{A_1} \bar{v}_{A_1} = G$$

$$\bar{m}_l = 1 - G$$

and the momentum jump relation in non-dimensional form becomes:

$$\bar{P}_1 + \gamma_B G \bar{v}_{A_1} + \gamma_B (1 - G) \bar{V}_w = \gamma_B + 1$$

Note that here G is the ratio of the mass flow rate of gaseous propellant to the total propellant mass flow rate and is always less than unity.

Thus the jump conditions across the detonation wave for the liquid-gaseous "no-mixing" case lead to the relations

$$\bar{v}_{A_1} = r + \sqrt{r^2 - s},$$

$$\bar{P}_1 = 1 - \gamma_B [G \bar{v}_{A_1} + (1 - G) \bar{V}_w - 1],$$

$$M_{A_1} = \sqrt{\frac{\gamma_B G \bar{v}_{A_1}}{\gamma_A \bar{P}_1}},$$

where

$$r = \frac{\gamma_A}{\gamma_B G} \left\{ \frac{1 - \gamma_B [(1 - G) \bar{V}_w - 1]}{\gamma_A + 1} \right\},$$

$$s = \frac{2}{\gamma_A + 1} \left(\frac{\gamma_A - 1}{\gamma_B - 1} \bar{C}_{P_A} \bar{T}_p + \frac{\gamma_A - 1}{2} \bar{V}_w^2 \right).$$

3. Solution of the Equations

Series Solution of the Equations for the Gaseous "Complete Mixing" Case

Consideration of the "complete mixing" case model of the rotating detonation wave rocket motor leads to the problem of obtaining solutions to a system of four simultaneous, quasi-linear, first order ordinary differential equations of the form

$$\frac{dM}{d\eta} = \frac{f_1}{M - 1}$$

$$\frac{d\bar{v}}{d\eta} = \frac{f_2}{M - 1}$$

$$\frac{d\bar{P}}{d\eta} = \frac{f_3}{M - 1}$$

$$\frac{d\mu}{d\eta} = (1 - \mu) f_4$$

where

$$f_i = f_i(M, \bar{v}, \bar{P}; \gamma, G, \bar{T}_p, B, \bar{V}_w)$$

and where

$$f_i(1, 1, 1, \gamma, G, \bar{T}_p, B, \bar{V}_w) \neq 0, i = 1, 2, 3, 4 .$$

The initial conditions are

$$M(0) = \bar{v}(0) = \bar{P}(0) = 1 .$$

These equations admit the series solutions

$$M = 1 + \sum_{k=1}^{\infty} a_k \eta^{k/2}$$

$$\bar{v} = 1 + \sum_{k=1}^{\infty} b_k \eta^{k/2}$$

$$\bar{P} = 1 + \sum_{k=1}^{\infty} c_k \eta^{k/2}$$

The coefficients are found by substitution into the differential equations, giving

$$M = 1 + \sqrt{\frac{\gamma+1}{2}} K \eta + \dots$$

$$\bar{v} = 1 + \sqrt{\frac{2}{\gamma+1}} K \eta + \dots$$

$$\bar{P} = 1 - \gamma \sqrt{\frac{2}{\gamma+1}} K \eta + \dots$$

with

$$K = B + G \left[\gamma \bar{V}_w - \frac{\gamma+1}{2} - \left(\bar{T}_p + \frac{\gamma-1}{2} \bar{V}_w^2 \right) \right]$$

Although the infinite series illustrates the nature of the solution to the differential equations, especially in the neighborhood of the singularity at $\eta = 0$, because of convergence difficulties it does not provide values of M , \bar{v} and \bar{P} at $\eta = 1$ for evaluation of the unknown eigenvalues B , \bar{V}_w and \bar{Q} .

Integration of the Differential Equations for the Special Case $\bar{d}m_p = 0$

In a practical detonation wave rocket motor the propellant injection pressure might be somewhat lower than the peak chamber pressure, P_0 , behind the detonation wave. Then, if one neglects the details of the dynamics of the flow of propellant through the injector orifices, $\bar{d}m_p$ would be zero until the

local chamber pressure at an injector drops below the propellant injection pressure. In this case the differential equation for the Mach number M is

$$\frac{\frac{M^2 - 1}{\gamma - 1} M^2}{1 + \frac{\gamma - 1}{2} M^2} \frac{dM}{d\eta} = B .$$

The initial condition is $M = 1$ at $\eta = 0$, and integration leads to

$$B\eta = \frac{2(M - 1)}{\gamma - 1} - \frac{\gamma + 1}{\gamma - 1} \sqrt{\frac{2}{\gamma - 1}} \arctan \left(\frac{\sqrt{\frac{\gamma - 1}{2}} (M - 1)}{1 + \frac{\gamma - 1}{2} M} \right) .$$

Note that in this instance the flow is isentropic and the non-dimensional velocity and pressure are given in terms of the Mach number by

$$\bar{v} = M \sqrt{\frac{\frac{\gamma + 1}{2}}{1 + \frac{\gamma - 1}{2} M^2}}$$

$$\bar{P} = \left[\frac{\frac{\gamma + 1}{2}}{1 + \frac{\gamma - 1}{2} M^2} \right]^{\frac{\gamma}{\gamma - 1}}$$

Figures 1(a), 1(b) and 1(c) display the Mach number M , velocity \bar{v} , and pressure \bar{P} as functions of $B\eta$ for several values of the specific heat ratio. For given values of the geometric parameter B and the specific heat ratio γ , the Mach number, velocity and pressure as functions of η can be determined. Note that this exact solution provides a convenient check for any numerical methods utilized to solve the equations. (The computer program utilized to obtain the results presented in Figure 1 and Table 2 is described in Appendix B. 1.)

Series Solution of the Equations for the Gaseous "No Mixing" Case

In an analogous manner to the analysis for the "complete mixing" case a series solution to the "no-mixing" equations can be obtained. The results are

$$M_A = M_{A_0} + \frac{\gamma_B \left[1 + \frac{\gamma_A - 1}{2} M_{A_0}^2 \right]}{\gamma_A M_{A_0}} \sqrt{\frac{2}{\gamma_B + 1} B - \frac{G}{\bar{\rho}_{A_0} \bar{V}_w}} \eta^{1/2} + \dots ,$$

$$M_B = 1 + \sqrt{\frac{\gamma_B + 1}{2} \left(B - \frac{G}{\bar{\rho}_{A_0} \bar{V}_w} \right)} \eta^{1/2} + \dots .$$

where

$$M_{A_0} = \bar{V}_w \left(\frac{\gamma_A - 1}{\gamma_B - 1} \bar{C}_{P_A} \bar{T}_p \right)^{-\frac{1}{2}},$$

$$\bar{\rho}_{A_0} = \frac{\gamma_A (\gamma_B - 1)}{\gamma_B (\gamma_A - 1) \bar{C}_{P_A} \bar{T}_p}.$$

Numerical Solutions of the Equations

To obtain complete solutions to the systems of equations developed from the analytical model of the rotating wave motor internal gasdynamics it is necessary to employ numerical techniques. Because of their complexity and due to the availability of a computer facility* the problems have been programmed for machine solution. The various digital computer programs developed are reproduced in Appendix B [the MAD¹⁴ (Michigan Algorithmic Decoder) procedural language is utilized in the programming]. The calculated results appear in Tables 2, 3, 4, and 5 and Figures 1, 2, 3, and 4.

*The University of Michigan Computing Center IBM 7090 digital computer.

TABLE 2. COMPUTATIONAL RESULTS FOR THE BLOCKED INJECTOR
 $(d\dot{m}_p = 0)$ EQUATIONS FOR $\gamma(k) = 1, 2$.

SOLUTION FOR THE BLOCKED INJECTOR CASE WITH $K = 1.200$

B-ETA	M	V	P	M - 1
.00000000	1.00000000	1.00000000	1.00000000	.00000000
.00229643	1.05000000	1.04514188	.94586992	.05026000
.00927700	1.09999999	1.08964798	.89273483	.10101832
.02107115	1.14999999	1.13350388	.84081832	.15224410
.03779824	1.19999999	1.17669679	.79031457	.20390700
.05956751	1.24999999	1.21921550	.74138813	.25597707
.08647838	1.29999998	1.26105036	.69417509	.30842538
.11862063	1.34999998	1.30219325	.64878402	.36122388
.15607432	1.39999998	1.34263752	.60529769	.41434495
.19891024	1.44999997	1.38237792	.56377461	.46776196
.24719030	1.49999997	1.42141061	.52425136	.52144925
.30096734	1.54999997	1.45973296	.48674407	.57538167
.36028576	1.59999996	1.49734369	.45125104	.62953501
.42518181	1.64999996	1.53424264	.41775466	.68388594
.49568385	1.69999996	1.57043077	.38622339	.73841196
.57181287	1.74999996	1.60591009	.35661388	.79309151
.65358210	1.79999995	1.64068364	.32887301	.84790347
.74099809	1.84999995	1.67475528	.30293932	.90282772
.83406162	1.89999995	1.70812982	.27874521	.95784538
.93276584	1.94999994	1.74081279	.25621799	1.01293752
1.03709960	1.99999994	1.77281047	.23528159	1.06808686
1.14704502	2.04999992	1.80412987	.21585765	1.12327623
1.26257968	2.09999990	1.83477846	.19786652	1.17848955
1.38367641	2.14999989	1.86476441	.18122848	1.23371148
1.51030278	2.19999987	1.89409629	.16586426	1.28892708
1.64242363	2.24999985	1.92278317	.15169592	1.34412275
1.77999854	2.29999983	1.95083444	.13864727	1.39928496
1.92298400	2.34999982	1.97825991	.12664447	1.45440103
2.07133353	2.39999980	2.00506961	.11561628	1.50945911
2.22499716	2.44999978	2.03127387	.10549436	1.56444778
2.38392293	2.49999976	2.05688328	.09621351	1.61935641
2.54805529	2.54999974	2.08190843	.08771175	1.67417467
2.71733773	2.59999973	2.10636029	.07993044	1.72889312
2.89171052	2.64999971	2.13024971	.07281423	1.78350259
3.07111347	2.69999969	2.15358779	.06631111	1.83799477
3.25548339	2.74999967	2.17638558	.06037238	1.89236140
3.44475698	2.79999965	2.19865414	.05495247	1.94659513
3.63886940	2.84999964	2.22040460	.05000895	2.00068894
3.83775437	2.89999962	2.24164799	.04550233	2.05463615
4.04134583	2.94999960	2.26239532	.04139601	2.10843077
4.24957514	2.99999958	2.28265756	.03765606	2.16206673
4.46237516	3.04999956	2.30244556	.03425115	2.21553889
4.67967772	3.09999955	2.32177007	.03115236	2.26884231
4.90141392	3.14999953	2.34064177	.02833306	2.32197225
5.12751508	3.19999951	2.35907111	.02576876	2.37492454
5.35791254	3.24999949	2.37706858	.02343694	2.42769516
5.59253754	3.29999948	2.39464441	.02131698	2.48028049
5.83132195	3.34999946	2.41180864	.01938997	2.53267726
6.07419705	3.39999944	2.42857128	.01763859	2.58488232
6.32109475	3.44999942	2.44494203	.01604702	2.63689288
6.57194853	3.49999940	2.46093053	.01460079	2.68870661
6.82669044	3.54999939	2.47654617	.01328672	2.74032104
7.08525419	3.59999937	2.49179822	.01209275	2.79173416

TABLE 2. CONCLUDED.

7.34757447	3.64999935	2.50669575	.01100793	2.84294420
7.61358476	3.69999933	2.52124766	.01002227	2.89394939
7.88322163	3.74999931	2.53546259	.00912666	2.94474849
8.15642047	3.79999930	2.54934907	.00831284	2.99534011
8.43311834	3.84999928	2.56291550	.00757327	3.04572320
8.71325350	3.89999926	2.57616988	.00690112	3.09589708
8.99676299	3.94999924	2.58912027	.00629017	3.14586061
9.28358698	3.99999923	2.60177436	.00573477	3.19561347
9.57366586	4.04999918	2.61413980	.00522982	3.24515522
9.86694002	4.09999913	2.62622398	.00477063	3.29448536
10.16335154	4.14999908	2.63803414	.00435300	3.34360382
10.46284270	4.19999903	2.64957723	.00397309	3.39251041
10.76535773	4.24999989	2.66086021	.00362743	3.44120523
11.07084131	4.29999894	2.67188978	.00331285	3.48968843
11.37923884	4.34999889	2.68267247	.00302651	3.53796023
11.69049597	4.39999884	2.69321463	.00276580	3.586C2086
12.0C456166	4.44999880	2.70352238	.00252837	3.63387087
12.32138252	4.49999875	2.71360186	.00231209	3.68151066
12.64090800	4.54999870	2.72345898	.00211502	3.72894067
12.96308780	4.59999865	2.73309931	.00193541	3.77616158
13.28787398	4.64999861	2.74252856	.00177105	3.82317421
13.61521792	4.69999856	2.75175211	.00162233	3.86997926
13.94507146	4.74999851	2.76077518	.00148611	3.91657737
14.27738953	4.79999846	2.76960298	.00136181	3.96296963
14.61212611	4.84999841	2.77824053	.00124835	4.00915682
14.94923615	4.89999837	2.78669265	.00114477	4.05513990
15.28867650	4.94999832	2.79496405	.00105015	4.10091990
15.63040376	4.99999827	2.80305931	.00096371	4.14649779
15.97437620	5.04999822	2.81098297	.00088471	4.19187468
16.32055211	5.09999818	2.81873935	.00081249	4.23705173
16.66889119	5.14999813	2.82633272	.00074644	4.28202993
17.01935387	5.19999808	2.83376712	.00068600	4.32681048
17.37190175	5.24999803	2.84104666	.00063071	4.37139469
17.72649574	5.29999799	2.84817514	.00059008	4.41578364
18.08309855	5.34999794	2.85515636	.00053371	4.45997846
18.44167447	5.39999789	2.86194900	.00049125	4.50398064
18.80218744	5.44999784	2.86869174	.00045232	4.54779130
19.16460156	5.49999779	2.87525293	.00041664	4.59141171
19.52888298	5.54999775	2.88168094	.00038391	4.63484317
19.89499855	5.59999770	2.88797924	.00035389	4.67808700
20.26291394	5.64999765	2.89415085	.00032634	4.72114450
20.63259768	5.69999760	2.90019900	.00030105	4.76401693
21.00401807	5.74999756	2.90612665	.00027782	4.80670571
21.37714386	5.79999751	2.91193670	.00025647	4.84921205
21.75194478	5.84999746	2.91763207	.00023686	4.89153749
22.12839103	5.89999741	2.92321557	.00021882	4.93368322
22.50645328	5.94999737	2.92868990	.00020224	4.97565055
22.88610363	5.99999732	2.93405762	.00018698	5.01744092

TABLE 3. SOLUTION OF THE COMPLETE MIXING CASE EQUATIONS.

RUNGE-KUTTA SOLUTION, COMPLETE MIXING CASE

K = 1.250 KA = 1.250 KB = 1.250 TP = .743E-01

G = 1.000 B = 2.362 VH = .155E 01

X	M - 1	V - 1	1 - P	F1	F2	F3	MU
.00000000	.00000000	.00000000	.00000000	.000E 00	.000E 00	.000E 00	.000000
.00099999	.05616070	.0492062	.06240077	.269E 02	.231E 02	.281E 02	.001002
.00110000	.05891269	.05228525	.065280215	.256E 02	.220E 02	.267E 02	.001102
.00121000	.06179917	.05476099	.068295252	.244E 02	.202E 02	.254E 02	.001213
.00133099	.064822676	.05735285	.07144651	.233E 02	.199E 02	.241E 02	.001334
.00146410	.06800245	.06006606	.07474095	.222E 02	.189E 02	.229E 02	.001467
.00161050	.07133352	.06290606	.07818886	.212E 02	.180E 02	.218E 02	.001614
.00177155	.0748276	.06587848	.08178444	.202E 02	.171E 02	.207E 02	.001776
.00194871	.07849295	.06898919	.085554611	.193E 02	.163E 02	.197E 02	.001954
.00214358	.08233785	.07244426	.08947648	.184E 02	.155E 02	.187E 02	.002149
.00235794	.08637124	.07565001	.093588233	.175E 02	.147E 02	.177E 02	.002364
.00259374	.09060248	.07921296	.09787064	.167E 02	.140E 02	.168E 02	.002601
.00285311	.09504138	.08293989	.10234859	.159E 02	.133E 02	.160E 02	.002861
.00313842	.09969824	.086837779	.10702351	.152E 02	.127E 02	.151E 02	.003147
.00345226	.10458391	.09091390	.11190292	.145E 02	.120E 02	.144E 02	.003462
.00379749	.10970978	.09517568	.11699450	.138E 02	.114E 02	.136E 02	.003808
.00417724	.11508781	.09963084	.12230466	.132E 02	.109E 02	.129E 02	.004190
.00459497	.12073061	.10428730	.12784558	.126E 02	.103E 02	.122E 02	.004609
.00505447	.12665141	.10915322	.133626111	.120E 02	.980E 01	.116E 02	.005070
.00555991	.13286414	.11423697	.13964086	.115E 02	.931E 01	.110E 02	.005577
.00611591	.13938365	.11954712	.14591307	.109E 02	.884E 01	.104E 02	.006135
.00672749	.14622476	.12509246	.1524465	.104E 02	.839E 01	.984E 01	.006749
.00740024	.15340432	.13088194	.15924814	.995E 01	.796E 01	.931E 01	.007425
.00814027	.16093920	.13692469	.16632766	.949E 01	.755E 01	.880E 01	.008168
.00895429	.16884743	.14322996	.17369287	.906E 01	.715E 01	.832E 01	.008985
.00984973	.17714796	.14980713	.18135198	.864E 01	.678E 01	.786E 01	.009884
.01083470	.18586082	.15666566	.1893103	.825E 01	.642E 01	.742E 01	.010873
.01191817	.19500709	.16381503	.19758388	.787E 01	.608E 01	.700E 01	.011961
.01310999	.20460902	.17126475	.20617215	.751E 01	.576E 01	.660E 01	.013158
.01442099	.21469010	.17902425	.21508512	.717E 01	.545E 01	.623E 01	.014474
.01586308	.22527514	.18710283	.22432974	.685E 01	.516E 01	.586E 01	.015922
.01744939	.23639035	.1950964	.23391246	.654E 01	.487E 01	.552E 01	.017514
.01919433	.24800343	.20425351	.24383930	.624E 01	.460E 01	.519E 01	.019266
.02111377	.2603237C	.21334293	.25411527	.596E 01	.435E 01	.488E 01	.021192
.02322514	.27320220	.22278589	.26474521	.569E 01	.410E 01	.459E 01	.023310
.02554765	.28673178	.23258980	.27573274	.544E 01	.387E 01	.430E 01	.025640
.02810242	.30094729	.24276131	.28708065	.520E 01	.364E 01	.434E 01	.028201

TABLE 3. CONCLUDED.

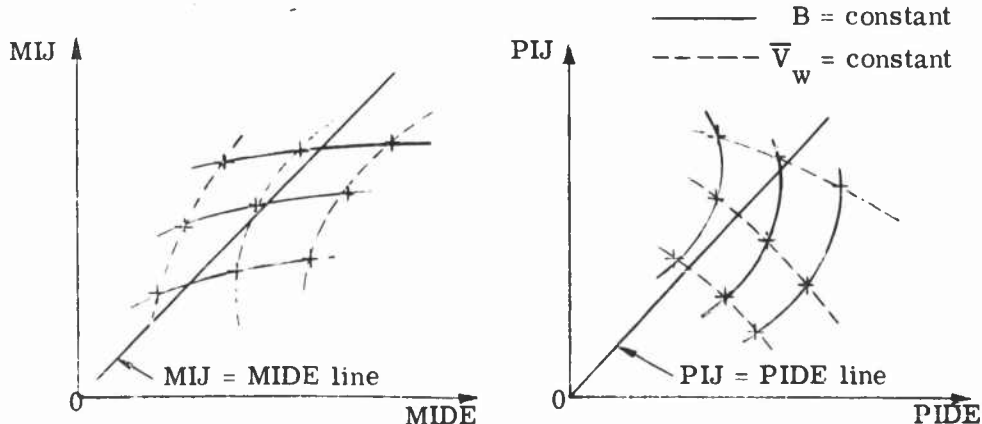
*03091267	*31588573	*25330615	*29879065	*497E C1	*343E C1	*378E 01	*031017
*03400394	*33158634	*26422896	*31086325	*475E 01	*322E 01	*354E 01	*034112
*03740433	*31809086	*27553309	*32329766	*454E 01	*303E 01	*331E 01	*037515
*04114476	*36544368	*28722035	*33609160	*434E C1	*284E 01	*309E 01	*041254
*04525924	*38369211	*29929075	*34924123	*415E 01	*266E 01	*288E 01	*045361
*04978516	*4C288654	*31174221	*36274095	*397E 01	*249E 01	*268E 01	*049874
*05476367	*42308079	*32457023	*37659327	*380E 01	*233E 01	*250E C1	*054829
*06024C04	*44433236	*33776754	*39075870	*363E 01	*217E 01	*232E 01	*06268
*06626404	*46670280	*35132372	*40525558	*348E 01	*202E 01	*215E 01	*066237
*07289045	*49025800	*36522471	*42005995	*333E 01	*188E 01	*199E 01	*072784
*08017949	*51506872	*37945241	*43515547	*319E 01	*175E 01	*184E 01	*079961
*08819744	*54121095	*39398415	*45052326	*306E 01	*162E 01	*170E 01	*087825
*097C1718	*56876647	*40879218	*46614186	*293E C1	*149E 01	*157E 01	*096434
*10671890	*59782342	*42384308	*48198716	*281E 01	*137E 01	*144E 01	*105853
*11739079	*62847692	*43909727	*49803233	*270E 01	*126E 01	*132E 01	*116148
*12912986	*66082979	*45450840	*51424786	*259E 01	*115E 01	*121E 01	*127388
*14204285	*69499338	*47002284	*53060166	*249E 01	*104E 01	*111E 01	*139645
*15624713	*731C8847	*48557921	*54705679	*240E 01	*946E 00	*101E 01	*152993
*17187185	*769224618	*50110796	*5635826	*230E 01	*851E 00	*918E 05	*167507
*18905903	*80965920	*51653115	*58013256	*222E 01	*762E 00	*833E 00	*183259
*20796493	*85233290	*53176230	*59666821	*214E 01	*677E 00	*754E 00	*203220
*22876142	*89758665	*54670662	*61314598	*206E 01	*597E 00	*680E 00	*218757
*25163756	*94555528	*56126136	*62952127	*199E 01	*522E 00	*612E 00	*238627
*27680132	*99644049	*57531667	*57531667	*192E 01	*451E 00	*549E 00	*259980
*30448145	*1.05046234	*58875688	*66178121	*185E 01	*385E 00	*499E 00	*282850
*33492959	*1.10786070	*60146217	*67757330	*179E 01	*324E 00	*437E 00	*307253
*36842254	*1.16889647	*61331095	*69307870	*174E 01	*268E 00	*388E 00	*333185
*40526479	*1.23385234	*62418262	*70825223	*168E 01	*216E 00	*344E 00	*36615
*45579126	*1.30303311	*63396110	*72305001	*163E 01	*170E 00	*303E 00	*389481
*49037038	*1.3766476	*64253864	*73742984	*158E 01	*128E 00	*265E 00	*419687
*54037C37	*1.45691256	*64994349	*75160751	*153E 01	*937E -01	*234E 00	*451717
*59237037	*1.53470926	*65545101	*76408171	*150E 01	*662E -01	*209E 00	*481771
*64037037	*1.61042665	*65942587	*77513958	*146E 01	*438E -01	*187E 00	*509952
*69037037	*1.68427178	*66215751	*78500503	*143E 01	*256E -01	*168E 00	*536365
*74037037	*1.75640371	*66387810	*79385565	*140E 01	*108E -01	*152E 00	*561115
*79037036	*1.82694519	*66477547	*80183435	*137E 01	*-129E -02	*138E 00	*584366
*84037036	*1.89599119	*66500253	*80905764	*134E 01	*-111E -01	*125E 00	*606035
*89037035	*1.96361534	*66468450	*81562158	*131E 01	*-190E -01	*114E 00	*626400
*94037035	*2.02987462	*66392434	*82160622	*129E 01	*-254E -01	*105E 00	*645491
*99037035	*2.09481320	*66280703	*82703878	*128E 01	*-265E -01	*123E 00	*663394
M1J = 3.110880 PIJ = 1.7180 MDE = 3.10717 PDE = .17192 QBAR = .74081E 00							

TABLE 4. SOLUTION OF THE NO-MIXING CASE EQUATIONS—WARM GASEOUS CASE.

TABLE 5. SOLUTION OF THE NO-MIXING CASE EQUATIONS—COLD GASEOUS CASE.

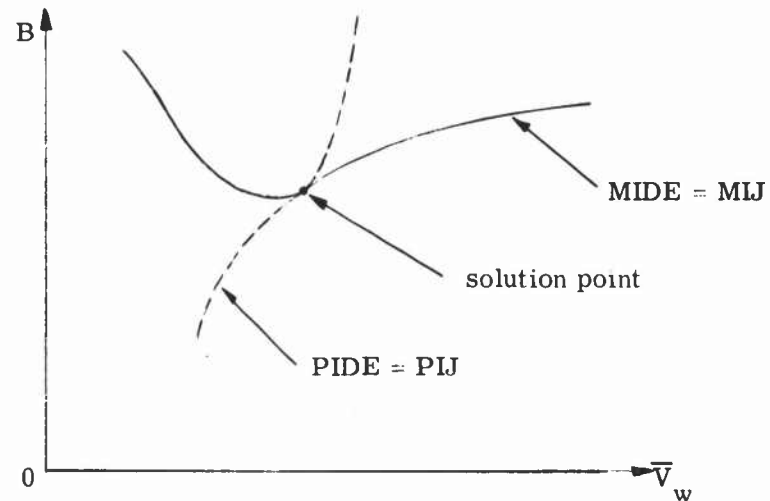
The RKDEQ (Runge-Kutta fourth order method) computer subroutine^{15, 16} is used to carry out the numerical integration of the differential equations derived in the analytical model. One difficulty encountered in applying the Runge-Kutta procedure in the present case is starting the numerical integration, since the values of $dM/d\eta$, $d\bar{V}/d\eta$, etc., are unbounded at $\eta = 0$. This difficulty is overcome by representing the dependent variables by the first terms in their series expansions in the neighborhood of $\eta = 0$ and initiating the numerical integration at some small but finite value of η .

For given values of the parameters G , \bar{T}_p , γ , B , \bar{V}_w (in the complete mixing case; for the no mixing case the parameters are G , \bar{T}_p , \bar{C}_{PA} , γ_A , γ_B , B , \bar{V}_w) the computer program integrates the differential equations from $\eta = 0$ to $\eta = 1$. A correct solution to the problem (i. e., the correct values of B and \bar{V}_w for given values of G , \bar{T}_p and γ) is obtained when the values of \bar{v}_1 , M_1 , and \bar{P}_1 calculated from the differential equations agree with the values calculated from the jump conditions. An iteration procedure is used in the search for the correct solution. MIDE, MIJ, PIDE and PIJ* are calculated for various values of B and \bar{V}_w chosen by "intelligent guesses" and the following plots are made.



*See Appendix B. 2 for definitions of the symbols MIDE, MIJ, PIDE, and PIJ.

By interpolation the values of B and \bar{V}_w for which $M_{IJ} = M_{IDE}$ and $P_{IJ} = P_{IDE}$ are obtained and the solution to the problem corresponds to the intersection of these lines on a plot of B versus \bar{V}_w :



It should be noted that obtaining numerical solutions to these equations proved fairly tedious. To obtain a single solution 20 to 50 trial integrations may be required, depending upon the experience of the operator in making "intelligent guesses" of the unknown parameters, B and \bar{V}_w .

Numerical Solution for the "Complete Mixing" Case

A numerical solution to the system of equations for the "complete mixing" case was obtained for the following values of the parameters

$$G = 1.0, \quad \bar{T}_p = 0.0743, \quad \gamma = 1.25$$

which correspond to a stoichiometric mixture of gaseous hydrogen and oxygen as the propellant, injected at ambient temperature. $G = 1.0$ means that the mass flow rate through the detonation waves equals the propellant mass flow

rate. However, in the complete mixing case some of the unburned propellant mixes with the burned gases and does not pass through the detonation waves, and in this particular case only $2/3$ of the unburned propellant passes through the detonation waves (i. e., $\mu_1 = 0.67$). The numerical solution is tabulated in Table 3 and plotted in Figures 2(a) and 2(b). The values obtained for the dependent parameters are

$$B = 2.36, \quad \bar{V}_w = 1.55, \quad \bar{Q} = 0.741$$

One interesting quantity is the absolute velocity, v_{1a} , of the gas just ahead of the detonation wave. It is given by the relation

$$v_{1a} = v_0 (\bar{V}_w - \bar{v}_1)$$

and can be estimated since $v_0 \sim 5 \times 10^3$ ft/sec and from the numerical solution, $\bar{V}_w = 1.55$ and $\bar{v}_1 = 1.66$. Hence

$$v_{1a} \sim -500 \text{ ft/sec}$$

The minus sign indicates that this velocity is directed into the wave. The predicted magnitude of this velocity seems reasonable, that is, not too large.

Because one result of complete instantaneous mixing of the burned and unburned propellants is that one third of the unburned propellant does not pass through the detonation wave it is hoped that actual motor operation would correspond more closely to the assumption of no mixing between the burned and unburned propellants.

Numerical Solutions for the "No Mixing" Case

Numerical solutions to the system of equations for the gaseous no mixing case were obtained for the following values of the parameters.

(1)	(2)
$G = 1.0$	$G = 1.0$
$\bar{T}_p = 0.081$	$\bar{T}_p = 0.04075$
$\bar{C}_{P_A} = 0.5497$	$\bar{C}_{P_A} = 0.4923$
$\gamma_A = 1.401$	$\gamma_A = 1.5$
$\gamma_B = 1.15$	$\gamma_B = 1.15$

These values correspond to a stoichiometric mixture gaseous hydrogen and oxygen as the propellant, injected in the first case (1) at ambient temperature ($\sim 537^{\circ}\text{R}$) and in the second case (2) at a low temperature ($\sim 270^{\circ}\text{R}$). The values of the specific heats and specific heat ratios corresponding to the given initial propellant temperatures were obtained from the results of theoretical calculations of detonation properties by Zeleznik and Gordon^{17, 18}. The speed of sound immediately behind a detonation wave propagating through a stoichiometric mixture of gaseous hydrogen and oxygen is about 5300 ft/sec over a fairly wide range of initial temperatures and pressures. $G = 1.0$ means that all of the injected propellant passes through the detonation wave, and this theoretical model represents idealized operation of the rotating detonation wave rocket motor. The values obtained for the dependent parameters are

(1)	(2)
$B = 5.76$	$B = 608$
$\bar{V}_w = 1.7966$	$\bar{V}_w = 1.8303$
$\frac{\bar{Q}}{Q} = 0.788$	$\frac{\bar{Q}}{Q} = 0.8037$

The solutions are tabulated in Tables 4 and 5 and plotted in Figures 3 and 4. It can be seen from the figures as well as the series expansions that M_B , \bar{P} , \bar{v}_B , etc., are approximately parabolic functions of η .

In a manner similar to the "complete mixing" case described earlier the values of the wave velocity, V_w , and the absolute velocity of the unburned gas ahead of the wave, v_{A1a} , can be evaluated. Since $a_{B0} \approx 5300$ ft/sec and since in case (1)

$$\bar{V}_w = 1.7966$$

$$\bar{v}_{A1a} = -0.372$$

then

$$V_w = 9520 \text{ ft/sec}$$

$$v_{A1a} \approx -197 \text{ ft/sec}$$

which seem to be reasonable values for these quantities. That is, the determined value of the eigenvalue, \bar{V}_w , in the mathematical problem corresponds to the assumptions involved in the development of the analytical model.

Although a computer program for the liquid-gaseous "no mixing" case has been developed (see Appendix B.4) the numerical solution of this case has not been carried to completion.

4. Similarity Considerations for Rotating Detonation Wave Rocket Motors

The condition for the similarity of different rotating wave rocket motor configuration is for the non-dimensional formulation of the differential equations, boundary conditions, and other pertinent relations to be identical; then one motor may be said to be a scale model of another. In the following the non-dimensional parameters that occur in the simplified flow model are identified and the similarity rules for the internal gasdynamics of rotating detonation wave rocket motors are indicated. It is shown that for the gaseous "no-mixing" case there are four independent similarity parameters

When no mixing is assumed to occur between the burned and unburned propellants the non-dimensional parameters that occur in the equations are

$$B = \frac{\ell_t L}{A_c} \left(\frac{2}{\gamma_B + 1} \right)^{\frac{\gamma_B + 1}{2(\gamma_B - 1)}} = \text{area ratio parameter.}$$

$\bar{C}_{P_A} = \frac{C_{P_A}}{C_{P_B}}$ = ratio of the specific heat at constant pressure for the unburned propellants to that for the burned propellants.

$G = \frac{\dot{m}_p}{\rho_{B_0} v_{B_0} A_c N}$ = mass flow parameter, which is unity for the gaseous "no mixing" case flow model.

$M_{B_0} = \frac{v_{B_0}}{a_{B_0}}$ = Mach number behind the detonation wave, which is unity.

$\bar{Q} = \frac{Q}{C_{P_B} T_{B_0}}$ = heat addition parameter.

$\bar{T}_p = \frac{T_p}{T_{B_0}}$ = dimensionless propellant injection temperature.

$\bar{V}_w = \frac{V_w}{v_{B_0}}$ = dimensionless wave velocity.

γ_A, γ_B = specific heat ratios of the unburned and burned propellants, respectively.

Four of the dimensionless quantities may be specified independently while the three jump relations, the Chapman-Jouguet condition, $M_{B_0} = 1$, and the requirement $G = 1$ provide equations for determining solutions of the form

$$B = B(\bar{T}_p, \bar{C}_{P_A}, \gamma_A, \gamma_B) ,$$

$$\bar{V}_w = \bar{V}_w(\bar{T}_p, \bar{C}_{P_A}, \gamma_A, \gamma_B) ,$$

$$\bar{Q} = \bar{Q}(\bar{T}_p, \bar{C}_{P_A}, \gamma_A, \gamma_B) ,$$

$$M_A = M_A(\eta; \bar{T}_p, \bar{C}_{P_A}, \gamma_A, \gamma_B) ,$$

$$M_B = M_B(\eta; \bar{T}_p, \bar{C}_{P_A}, \gamma_A, \gamma_B) .$$

Hence the rotating detonation wave rocket motor similarity parameters are

$$\bar{T}_p, \bar{C}_{P_A}, \gamma_A, \gamma_B .$$

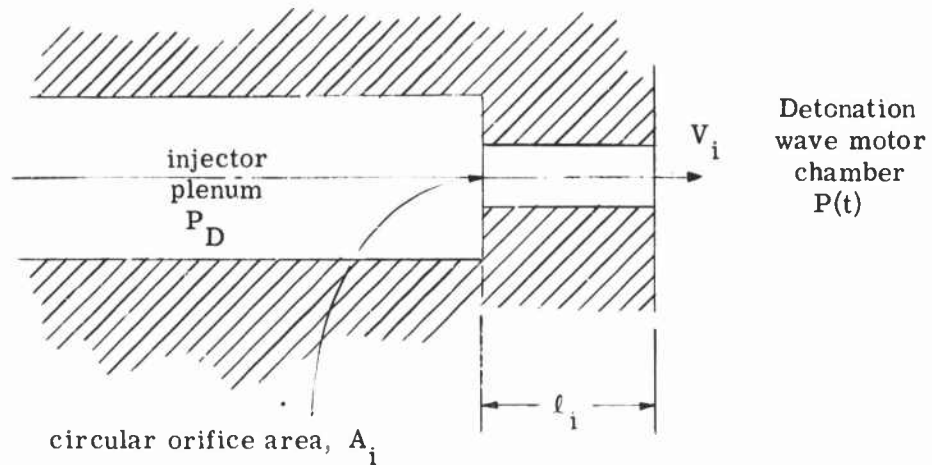
Thus the numerical results obtained from the rocket motor analytical model (see Tables 4 and 5 and Figures 3 and 4) describe classes of rotating wave rocket motors for which the parameters \bar{T}_p , \bar{C}_{P_A} , γ_A and γ_B are identical.

5. Injection Dynamics for a Liquid Propellant in a Rotating Detonation Wave Rocket Motor

An important aspect of engine design for the rotating detonation wave rocket motor is the injection of liquid propellant. It is necessary to insure the injector design will provide the necessary mass flow rate of liquid propellant and also distribute the liquid across the axial dimension of the detonation chamber. An approach used by Morrison* is applied to obtain some crude injector design criteria.

*Unpublished analysis made at this laboratory by Professor R. B. Morrison.

The injector is assumed to consist of a large number of holes of the form



For steady flow through this system the pressure loss coefficient, C_{P_ℓ} , is given by

$$C_{P_\ell} = \frac{\Delta P}{\frac{1}{2} \rho_\ell V^2}$$

where ΔP is the loss in total pressure across the orifice and V is a characteristic velocity. Choosing the injection velocity V_i to be the characteristic velocity,

$$C_{P_\ell} = \frac{P_D - P - \frac{1}{2} \rho_\ell V_i^2}{\frac{1}{2} \rho_\ell V_i^2}$$

for steady flow.

The momentum contained in the orifice at some instant in time is $\rho_\ell A_i \ell_i V_i$. Hence the pressure head due to the inertia of the fluid is $\rho_\ell \ell_i dV_i/dt$, and the pressure loss coefficient for the unsteady flow case can be written as

$$C_{P_\ell} = \frac{P_D - P - \frac{1}{2} \rho_\ell V_i^2 - \rho_\ell \ell_i dV_i/dt}{\frac{1}{2} \rho_\ell V_i^2}$$

to a crude approximation. To proceed further it is assumed that C_{P_ℓ} is constant in time. (Note that the only justification of the assumptions employed here is that they provide a basis for obtaining a simple solution to the problem.) Also, P_D is constant while P fluctuates very rapidly with time. Thus, the differential equation for V_i is

$$\frac{dV_i}{dt} + \frac{1 + C_{P_\ell}}{2\ell_i} V_i^2 = \frac{P_D - P}{\rho_\ell \ell_i}$$

To put this equation in non-dimensional form introduce

$$\bar{P} = P/P_0, \quad \bar{P}_D = P_D/P_0, \quad \eta = V_w t/L,$$

$$\bar{V}_i = V_i/v_{B_0}, \quad \bar{\rho}_\ell = \rho_\ell/\phi_{B_0}, \quad \bar{\ell}_i = \ell_i/L,$$

resulting in the non-linear differential equation

$$\frac{d\bar{V}_i}{d\eta} + \frac{1 + C_{P_\ell}}{2 \bar{V}_w \bar{\ell}_i} \bar{V}_i^2 = \frac{\bar{P}_D - \bar{P}}{\nu_B \bar{\rho}_\ell \bar{\ell}_i \bar{V}_w}$$

The boundary condition is

$$\bar{V}_i(0) = \bar{V}_i(1)$$

Since the equation is non-linear an exact solution would require numerical integration, for example by the Runge-Kutta procedure. To obtain some insight into the effects of injection dynamics a perturbation solution to the differential equation is obtained.

Define $\phi(\eta)$ as the fluctuation in \bar{V}_i from the mean value $\bar{V}_{i \text{ avg}}$:

$$\phi = \bar{V}_i - \bar{V}_{i \text{ avg}}$$

Assume $\phi/\bar{V}_{i \text{ avg}} \ll 1$ (this is equivalent to assuming $\bar{P}_D \gg 1$). If \bar{P} is represented by the first two terms of its infinite series,

$$\bar{P} = 1 - K_1 \eta^{1/2}$$

where

$$K_1 = \gamma_B \sqrt{\left(\frac{2}{\gamma_B + 1}\right)} \left(B - \frac{G}{\rho_A \bar{V}_w}\right)$$

then the linearized differential equation for ϕ is

$$\frac{d\phi}{d\eta} + \omega \phi = \alpha + \beta \eta^{1/2}$$

where

$$\omega = \frac{\left(1 + C_{P_\ell}\right) \bar{V}_{i \text{ avg}}}{\bar{\ell}_i \bar{V}_w}$$

$$\alpha = - \frac{\left(1 + C_{P_\ell}\right) \bar{V}_{i \text{ avg}}}{2 \bar{\ell}_i \bar{V}_w} + \frac{\bar{P}_D - 1}{\gamma_B \bar{\rho}_\ell \bar{\ell}_i \bar{V}_w}$$

$$\beta = \frac{K_1}{\gamma_B \bar{\rho}_\ell \bar{\ell}_i \bar{V}_w}$$

This differential equation can be solved by the method of variation of parameters, resulting in

$$\phi(\eta) = \frac{\alpha}{\omega} + \beta e^{-\omega\eta} \int_0^\eta \xi^{1/2} e^{\omega\xi} d\xi + \frac{\beta e^{-\omega\eta}}{e^\omega - 1} \int_0^1 \xi^{1/2} e^{\omega\xi} d\xi$$

where ξ is a dummy variable of integration.

From the definition of $\bar{V}_{i \text{ avg}}$

$$\int_0^1 \phi d\eta = 0$$

giving the restriction on the parameters

$$\alpha + \frac{2}{3} \beta = 0$$

or

$$\bar{V}_{i \text{ avg}} \approx \sqrt{\frac{2 (\bar{P}_D - \bar{P}_{\text{avg}})}{\gamma_B \bar{\rho}_l \left(1 + C_{P_l}\right)}}$$

where

$$\bar{P}_{\text{avg}} = \int_0^1 \bar{P} d\eta \approx 1 - \frac{2}{3} K_1$$

Note that in this linearized dynamic analysis the mean injection velocity obtained does not differ from the steady flow value and that P_{avg} , the mean pressure in the rotating detonation wave rocket motor chamber, is equivalent, for purposes of comparison, to the chamber pressure, P_c , of conventional rocket motors.

Sizing Relations Derived from the Liquid Injection Analysis

Using the derived relation for $\bar{V}_{i \text{ avg}}$ one can express the following approximate rotating wave rocket motor chamber sizing relations in quantitative form.

- (a) The total mass flow rate of liquid through the injector should equal (in the liquid-gaseous "no mixing" case) the mass flow rate of liquid propellant reacting at the detonation waves in the rocket motor chamber. Now

$$\dot{m}_l = \rho_l N_i A_i V_{i \text{ avg}}$$

where N_i is the number of injector orifices for the liquid propellant and A_i is the cross-sectional area of each orifice. In non-dimensional form this becomes

$$\bar{m}_l = \bar{\rho}_l \bar{V}_{i \text{ avg}} \left(\frac{N_i A_i}{N A_c} \right)$$

From the liquid-gaseous "no mixing" case analysis the relation

$$\dot{m}_l = \frac{m_l (1 - X_G)}{m_G X_G + m_l (1 - X_G)}$$

is obtained, and thus the total injector orifice area is related to the non-dimensional plenum pressure, \bar{P}_D , by

$$\frac{N_i A_i}{N A_c} = \sqrt{\frac{\gamma_B (1 + C_{P_l})}{2 (\bar{P}_D - \bar{P}_{avg})}} \left(\frac{m_l (1 - X_G)}{m_G X_G + m_l (1 - X_G)} \right)$$

- (b) To fill the rotating wave rocket motor chamber the injected liquid should move a distance x_n in the same time duration the detonation waves travel a distance L . Hence

$$\frac{x_n}{V_{i \text{ avg}}} = \frac{L}{V_w} .$$

Thus,

$$\frac{x_n}{L} = \frac{1}{\bar{V}_w} \sqrt{\frac{\sum (\bar{P}_D - \bar{P}_{\text{avg}})}{\gamma_B \bar{\rho}_l (1 + C_{P_l})}}$$

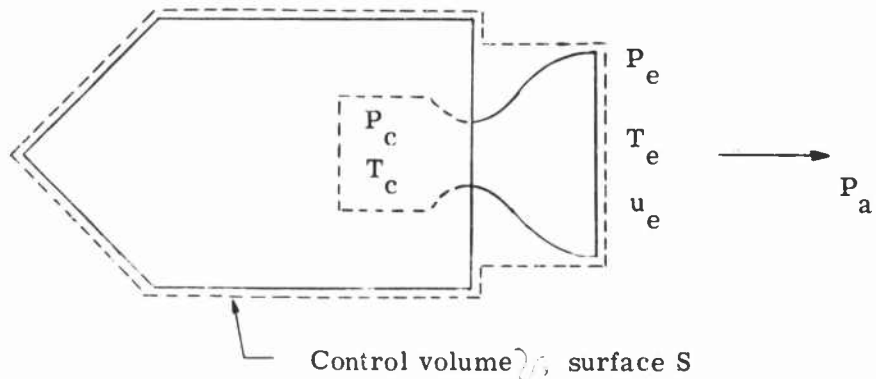
provides a rough sizing relation for the axial rocket motor chamber dimension, x_n .

6. Theoretical Performance of a Rotating Detonation Wave Rocket Engine (RDWE)

To derive the relations describing the performance of the RDWE the steady flow analysis for conventional rocket motors is applied to calculate the thrust of an infinitesimal segment of the engine. This quantity is integrated over the circumference of the RDWE to yield an expression for the overall thrust. It is assumed that the flow expands isentropically through the rocket nozzle to a given nozzle exit pressure, P_e .

Performance of a Conventional Rocket Motor

Consider a rocket motor mounted on a test stand:



From the momentum theorem for steady, inviscid flow,

$$\oint_R \rho \vec{V} (\vec{V} \cdot \hat{n}) dS = - \oint_R P \hat{n} dS$$

where \hat{n} is the local outward unit normal vector and R is some specified closed control surface, one obtains for the magnitude of the thrust of a conventional rocket motor

$$F = \rho_e u_e^2 A_e + (P_e - P_a) A_e .$$

From the continuity, energy and isentropic flow relations

$$\rho_e u_e A_e = \rho_t u_t A_t = \dot{m}_p ,$$

$$C_p T_e + \frac{1}{2} u_e^2 = C_p T_t + \frac{1}{2} u_t^2 = C_p T_C ,$$

and

$$\frac{T_e}{T_C} = \left(\frac{P_e}{P_C} \right)^{\frac{\gamma - 1}{\gamma}}$$

expressions for the thrust coefficient, C_F , and specific impulse, I_{sp} , are derived:

$$C_F \equiv \frac{F}{P_C A_t} = \sqrt{\frac{2\gamma}{\gamma - 1} \left(\frac{2}{\gamma + 1} \right)^{\frac{\gamma + 1}{\gamma - 1}} \left[1 - \left(\frac{P_e}{P_C} \right)^{\frac{\gamma - 1}{\gamma}} \right] + \left(\frac{P_e - P_a}{P_C} \right) \frac{A_e}{A_t}} ,$$

$$I_{sp} \equiv \frac{F}{\dot{m}_p g_0} = \frac{a_C}{g_0} \left\{ \sqrt{\frac{2}{\gamma - 1} \left[1 - \left(\frac{P_e}{P_C} \right)^{\frac{\gamma - 1}{\gamma}} \right] + \left(\frac{P_e - P_a}{P_C} \right) \frac{A_e}{A_t} \cdot \frac{1}{\gamma} \left(\frac{\gamma + 1}{2} \right)^{\frac{\gamma + 1}{2(\gamma - 1)}}} \right\}$$

In the case of ideal expansion in a vacuum these relations simplify to

$$C_{F_{vac}} = \sqrt{\frac{2\gamma^2}{\gamma - 1} \left(\frac{2}{\gamma + 1} \right)^{\frac{\gamma + 1}{\gamma - 1}}},$$

$$I_{sp_{vac}} = \frac{a_C}{g_0} \sqrt{\frac{2}{\gamma - 1}}$$

The characteristic velocity, c^* , is given by

$$c^* \equiv \frac{P_C A_t}{m_p} = \frac{a_C}{\gamma} \left(\frac{\gamma + 1}{2} \right)^{\frac{\gamma + 1}{2(\gamma - 1)}}$$

Performance of a Rotating Detonation Wave Rocket Engine (RDWE)

To determine the performance of a RDWE consider the flow field with reference to the wave-fixed coordinate system. The flow field is steady and the nozzle flow can be represented as consisting of a large number of infinitesimal conventional rocket motors. Note that the axial velocity component, u , has the same value in both the wall-fixed and the wave-fixed coordinate systems and hence the thrust calculation can be performed in either reference system. Consider one such incremental segment of the rocket motor. The energy equation relating the temperature of a fluid particle at the nozzle exit to the temperature existing locally in the rocket motor chamber is

$$C_{P_B} + \frac{1}{2} u_e^2 = C_{P_B} T_B$$

Note that T_B depends upon the detonation chamber circumferential coordinate, η . For isentropic nozzle flow

$$\frac{T_e}{T_B} = \left(\frac{P_e}{P_B} \right)^{\frac{\gamma_B - 1}{\gamma_B}}$$

and hence

$$u_e = a_B \sqrt{\frac{2}{\gamma_B - 1} \left[1 - \left(\frac{P_e}{P_B} \right)^{\frac{\gamma_B - 1}{\gamma_B}} \right]}.$$

The mass flow rate through an infinitesimal nozzle segment is

$$\frac{dm_t}{N} = \rho_B a_B \ell_t \left(\frac{2}{\gamma_B + 1} \right)^{\frac{\gamma_B + 1}{2(\gamma_B - 1)}} dy ,$$

so the thrust of this nozzle segment is

$$dF = \sqrt{\frac{2\gamma_B^2}{\gamma_B - 1} \left(\frac{2}{\gamma_B + 1} \right)^{\frac{\gamma_B + 1}{\gamma_B - 1}} \left[1 - \left(\frac{P_e}{P_B} \right)^{\frac{\gamma_B - 1}{\gamma_B}} \right]} P \ell + dy + (P_e - P_a) \ell_e dy .$$

By integrating over the circumference of the rocket motor one obtains for C_F and I_{sp} the relations

$$C_F = \sqrt{\frac{2\gamma_B^2}{\gamma_B - 1} \left(\frac{2}{\gamma_B + 1} \right)^{\frac{\gamma_B + 1}{\gamma_B - 1}} \left\{ \frac{1}{0} \int_{\frac{1}{\bar{P}}}^{\frac{\gamma_B - 1}{\bar{P}}} \left[1 - \left(\frac{1}{\bar{P}} \frac{P_e}{P_0} \right)^{\frac{\gamma_B}{\gamma_B - 1}} \right] d\eta \right\} + \left(\frac{P_e - P_a}{P_{avg}} \right) A_e A_t},$$

$$I_{sp} = \frac{a_{B0}}{g_0} \left(B \int_0^1 \bar{P} d\eta \right) \left(\sqrt{\frac{2}{\gamma_B - 1}} \left\{ \frac{\int_0^1 \bar{P} \left[1 - \left(\frac{1}{\bar{P}} \frac{P_e}{P_0} \right)^{\frac{\gamma_B}{\gamma_B - 1}} \right] d\eta}{\int_0^1 \bar{P} d\eta} \right\} + \left(\frac{P_e - P_a}{P_{avg}} \right) \frac{A_e}{A_t} \cdot \frac{1}{\gamma_B} \left(\frac{\gamma_B + 1}{2} \right)^{\frac{\gamma_B + 1}{2(\gamma_B - 1)}} \right).$$

The characteristic velocity, c^* , for a rotating detonation wave rocket motor is given by

$$c^* = \frac{a_{B0}}{\gamma_B} \left(\frac{\gamma_B + 1}{2} \right)^{\frac{\gamma_B + 1}{2(\gamma_B - 1)}} \left(B \int_0^1 \bar{P} d\eta \right).$$

For ideal expansion in a vacuum $I_{sp_{vac}}$ and $C_{F_{vac}}$ are

$$C_{F_{vac}} = \sqrt{\frac{2\gamma_B^2}{\gamma_B - 1} \left(\frac{2}{\gamma_B + 1} \right)^{\frac{\gamma_B + 1}{\gamma_B - 1}}},$$

$$I_{sp_{vac}} = \frac{a_{B_0}}{g_0} \sqrt{\frac{2}{\gamma_B - 1}} \left[B \int_0^1 \bar{P} d\eta \right]$$

Comparison of Theoretical Performance

To facilitate the comparison of the theoretical performance of a RDWE with a conventional rocket motor consider a particular rocket motor operating point. Let the mean chamber pressure (P_{avg} or P_C) be 560 psia (this corresponds to a pressure of 10 atm ahead of the detonation waves for a stoichiometric mixture of hydrogen and oxygen, that is, $X_{H_2} = 2/3$).

The numerical solution to the gaseous "no mixing" case (see Table 4 and Figure 3) provides the following necessary information. (Note that the "no mixing" case solution is employed here instead of the "complete mixing" case solution because it represents the ideal operating configuration of the RDWE.)

$$B \approx 5.76$$

$$\gamma_B = 1.15$$

$$\int_0^1 \bar{P} d\eta = 0.157$$

$$\bar{P}_1 = 0.0412$$

Thus P_0 is 3567 psia. From thermochemical computations of Zeleznik and Gordon* the speed of sound immediately behind the detonation waves, a_{B_0} ,

*Some thermochemical computer program¹⁷ numerical results were received in a private communication from Mr. Sanford Gordon.

is 5300 ft/sec, and thus, all the data required for computing the performance of an RDWE in this special case are at hand.

The performance data for the conventional rocket motor is obtained from the calculations of Gordon and McBride¹⁹

The results are as follows.

	RDWE Performance	Conventional Rocket Motor Performance	
		frozen equilibrium calculation	shifting equilibrium calculation
c^*	7000 ft/sec	7080 ft/sec	6940 ft/sec
$(C_F)_{S.L.}$	1.59	1.56	1.49
$(I_{sp})_{S.L.}$	347 sec	342 sec	321 sec
$\left(C_F \text{ vac} \right)_{\frac{A_e}{A_t} = 100}$	2.03	2.07	1.94
$\left(I_{sp} \text{ vac} \right)_{\frac{A_e}{A_t} = 100}$	442 sec	455 sec	417 sec

Note: $P_{avg} = P_C = 560 \text{ psia}$, stoichiometric H_2 - O_2 mixture.

From an examination of the table of results and the theoretical expressions for c^* , C_F and I_{sp} the following comparisons can be made of the frozen equilibrium calculations for the two rocket motors

The characteristic velocity, c^* , is slightly higher for the RDWE because of the higher temperature at the detonation waves. This is compensated

somewhat by the factor

$$B \int_0^1 \bar{P} d\eta = 0.904$$

which appears in the formula for c^* for the RDWE. Thus one might define, for purposes of comparison with conventional rocket motors, a mean speed of sound, a_{avg} , in the rotating wave motor chamber by

$$a_{avg} = a_{B_0} B \int_0^1 \bar{P} d\eta$$

Then the expressions for c^* (frozen equilibrium value) for both rotating wave and conventional rocket motors will have the same form.

The discrepancy in the results for the thrust coefficient, C_F , of the two rocket motors is explained by the difference in the values of specific heat ratio used in the calculations. For the conventional rocket motor the frozen equilibrium specific heat ratio, γ , is 1.22 while the value employed for the RDWE, γ_B , is 1.15, and the factor $\sqrt{2/(\gamma - 1)}$ occurring in the expressions for C_F is sensitive to small differences in specific heat ratio. Utilizing a higher value of γ_B would bring the results for C_F of the RDWE in line with the values of the thrust coefficient, C_F (frozen equilibrium calculation), for the conventional motor, and would be more consistent with the idea of a frozen equilibrium analysis of the RDWE. The factors expressing the degradation in thrust due to finite rocket motor nozzle area ratio are found to be almost numerically identical for the two rocket motors for mean chamber pressures greater than about 500 psia. Thus, for ease of calculation the expression

$$\left\{ \frac{\int_0^1 \bar{P} \left[1 - \left(\frac{1}{\bar{P}} \frac{P_e}{P_0} \right)^{\frac{\gamma_B - 1}{\gamma_B}} \right]^{\frac{1}{2}} d\eta}{\int_0^1 \bar{P} d\eta} \right\}$$

appearing in the formula for C_F of the RDWE could be replaced by

$$\left[1 - \left(\frac{P_e}{P_{avg}} \right)^{\frac{\gamma_B - 1}{\gamma_B}} \right]^{\frac{1}{2}}$$

Then the relations for C_F for both rotating wave and conventional rocket motors have the same form

Since for both conventional and rotating wave rocket motors

$$I_{sp} = \frac{c * C_F}{g_0}$$

the variations in the results for I_{sp} are just due to the differences in the calculated values of the characteristic velocity, c^* , and the thrust coefficient, C_F . If the definition of a_{avg} is used and the factor expressing the degradation in thrust due to finite rocket nozzle area ratio for the RDWE is replaced by the equivalent expression for conventional rocket motors the formula for the specific impulse, I_{sp} , of both conventional and rotating wave rocket motors assumes the form

$$I_{sp} = \frac{a_{avg}}{g_0} \left\{ \sqrt{\frac{2}{\gamma_B - 1} \left[1 - \left(\frac{P_e}{P_{avg}} \right)^{\frac{\gamma_B}{\gamma_B - 1}} \right] + \left(\frac{P_e - P_a}{P_{avg}} \right) \frac{A_e}{A_t}} \right\}$$

Note that this expression is only valid when the mean chamber pressure, P_{avg} , of the RDWE is greater than about 500 psia. It can be concluded from this result that there are no essential differences between the theoretical performances of rotating detonation wave and conventional rocket motors.

A more practical comparison of rotating wave and conventional motors as rocket propulsion systems should include some of the following considerations:

- (a) an evaluation of the experimental performance of the RDWE,
- (b) a weight comparison of the systems (relative weights of nozzles, chambers, pumps, feed lines, structural supports, etc.,), relative lengths of the motors to find the necessary rocket vehicle interstage structure weight, rocket motor performance corresponding to the propellant mixture ratio for minimum propellant tankage weight, and
- (c) an evaluation of special features such as ease of thrust vector control, throttling and restarting capabilities of the RDWE

Because of the lack of experimental data such considerations at this time appear to be beyond the scope of the present analysis

7. Comparison of Theoretical Results With an Experimental Pressure-Time History for the Passage of the Initial Detonation Wave

In Figure 5, theoretical results from solutions to the warm gaseous "no mixing" case equations are compared with an experimental pressure-time history for the passage of the initial detonation wave in the annular motor. The theoretical results are for $G \approx 1.0$, $\bar{T}_p = 0.081$, $\bar{C}_{P_A} = 0.54968$, $\gamma_A = 1.401$, $\gamma_B = 1.15$, $\bar{V}_w = 1.80$ with $B = 3.0, 3.7$, and 5.76 . The latter case (see Figure 3

and Table 4) corresponds to a solution of both the differential equations and the jump conditions across the detonation wave, while the values for $B = 3.0$ and 3.7 , which were obtained in trial solutions to the equations, correspond roughly to the experimental operating conditions and should be used for purposes of comparison with the experimental results. The areas under the pressure-time curves for roughly corresponding experimental and theoretical values of B agree within the expected margin for engineering approximations, even though several hypotheses of the analytical model are violated in the experimental configuration.

- (a) The theory presumes the establishment of steady and continued propagation of the detonation waves, which is not achieved in this experiment.
- (b) In the theoretical development it is assumed that

$$\frac{\ell}{R} \ll 1, \quad \frac{Nx_n}{R} \ll 1$$

while experimentally the values are 0.133 and 0.533 , respectively.

(The agreement between experiment and theory should improve for larger radius motors)

- (c) Another possible source of error is the finite thickness of the zone of chemical reaction following the detonation wave. The theory assumes all chemical reactions go to completion instantaneously and occur only at the wave front

A source of experimental error may be a time lag in the recorded pressure due to inability of the instrumentation to follow the rapid decay behind the initial pressure pulse of the detonation wave

Within the spirit of a frozen chemical equilibrium, quasi-one dimensional analytical model of the RDWE internal gasdynamics there appears to be at least a qualitative agreement between the theoretical and the experimental results.

C. RESULTS AND CONCLUSIONS

An analytical model representing an ideal gas, frozen chemical equilibrium, quasi-one dimensional analysis has been developed which provides a description of the internal gasdynamics of an idealized rotating detonation wave rocket motor. From this model of the RDWE the following results and conclusions have been ascertained.

- (1) The detonation waves travelling around the annular rocket motor chamber of the RDWE satisfy the Chapman-Jouguet condition,
 $M_{B0} = 1$
- (2) A series solution of the equations developed from the analytical model indicates that the chamber flow properties (Mach number, velocity, pressure, etc.,) are approximately parabolic functions of the circumferential coordinate in the rocket motor.
- (3) Extensive mixing between the unburned and burned propellants would degrade the performance of the RDWE.
- (4) The numerical values obtained from the solution to the analytical model equations in the gaseous "no mixing" case for the detonation wave velocity ($V_w = 9520$ ft/sec) and the absolute velocity of the gas just ahead of the detonation wave ($v_{A1a} = -197$ ft/sec) appear qualitatively correct and hence tend to justify the assumptions made in the development of the analytical model
- (5) For purposes of comparison with conventional rocket motors the effective chamber pressure of the RDWE is the mean value, P_{avg} .
- (6) A comparison of the theoretical specific impulses (frozen chemical equilibrium calculation) of conventional and rotating detonation wave rocket motors indicates that the theoretical performances of these two types of propulsion devices are essentially identical. In terms of average chamber conditions the specific impulse relation in both instances assumes the form

$$I_{sp} = \frac{a_{avg}}{g_0} \left\{ \sqrt{\frac{2}{\gamma_B - 1}} \left[1 - \left(\frac{P_e}{P_{avg}} \right)^{\frac{\gamma_B - 1}{\gamma_B}} \right] + \left(\frac{P_e - P_a}{P_{avg}} \right) \frac{A_e}{A_t} \right\}$$

where

$$P_{avg} = P_0 \int_0^1 \bar{P} d\eta ,$$

$$a_{avg} = a_{B_0} B \int_0^1 \bar{P} d\eta$$

- (7) Although possibilities for comparison with experimental results are limited, there is at least qualitative agreement between theoretical pressure-time histories and an experimental pressure-time history for the passage of the initial detonation wave.

III. DETONATION IN A HETEROGENEOUS, LIQUID-GAS MEDIA

A. LITERATURE REVIEW OF HETEROGENEOUS DETONATION

To date only a few studies of detonation waves in sprays have been made. Williams²⁰ has thoroughly investigated detonation waves in dilute sprays by applying a statistical method to spray combustion²¹. Webber²² has found, through experimentation, that most of the cases of spray combustion in a shock tube lead to a high amplitude wave. Also, Cramer's²³ experiments have shown that droplet shattering can enable a detonation wave to propagate through a heterogeneous medium.

A brief review of these studies shall be presented in the following discussion.

In a dilute spray* with $W_e \ll W_{e_{cr}}$, ** F. A. Williams has employed the spray distribution function^{21, 24},

$$f_j(r, x, V, t) dr dx dV \quad (1)$$

*The mass of fluid per unit spatial volume, ρ_f , is related to the actual mass of fluid per unit volume of space available to the gas, ρ_g , through the equation

$$\frac{\rho_f}{\rho_g} = 1 - \sum_{j=1}^M \iiint \frac{4}{3} \pi r^3 f_j dr dV$$

The last term of the equation is the fraction of the total spatial volume occupied by the droplets. A dilute spray implies $\rho_f \approx \rho_g$.

**The Weber number is defined as

$$W_e = \frac{2r\rho_g |V - U|}{S}$$

where U is the gas velocity and S is the surface tension. Hinze²⁷ found that if the Weber number exceeds some critical value, $W_{e_{cr}} \approx 20$, the aerodynamic forces will cause the droplet to break up. Also, it was found that for $W_e \ll W_{e_{cr}}$ the droplets are nearly spherical.²⁸

which gives the probable number of droplets of composition j at time t , with a radius between r and $r + dr$, located in the position range $d\underline{x} = dx_1 dx_2 dx_3$ about \underline{x} , and with a velocity in the range $d\underline{V} = dV_1 dV_2 dV_3$ about \underline{V} .

The change of f_j with time can be represented by

$$\frac{\partial f_j}{\partial t} = - \frac{\partial}{\partial r} (R_j f_j) - \nabla_{\underline{x}} \cdot (\underline{V} f_j) - \nabla_{\underline{V}} \cdot (\underline{F}_j f_j) + Q_j + \Gamma_j \quad (2)$$

where Q_j is a droplet source term, Γ_j is a droplet collision term,

$$\underline{F}_j = \frac{d\underline{V}}{dt} \Big|_j \quad \text{and} \quad R_j = \frac{dr}{dt} \Big|_j$$

are the total forces on the droplet per unit droplet mass and the rate of droplet growth respectively. It is apparent that Equation (2) must play the same role in spray combustion as the Boltzmann equation does in the mathematical theory of non-uniform gases, and that the $f_j(r, \underline{x}, \underline{V}, t)$ is a function similar to the molecular distribution function

In accordance with the assumption of dilute sprays, the equations governing the propagation of a detonation wave through a spray are the ordinary fluid dynamic equations with suitable modifications to account for the average effect of the droplets²¹. The spray distribution function is coupled with the equations of motion for the gaseous medium by the total force on the droplet per unit droplet mass and the rate of droplet growth. Then the general equations relating the change of fluid properties across a detonation wave, assuming uniform conditions at stations 0 and ∞ , are written as follows

$$\begin{aligned} \rho_{f_\infty} U_\infty + \sum_{j=1}^M \iint \rho_{f_j} j_\infty \frac{4}{3} \pi r^3 V f_{j_\infty} dr dV &= \rho_{f_0} U_0 \\ + \sum_{j=1}^M \iint \rho_{f_j} j_0 \frac{4}{3} \pi r^3 V f_{j_0} dr dV \end{aligned} \quad (3)$$

$$\rho_{f_\infty} U_\infty^2 + \sum_{j=1}^M \iint \rho_{\ell, j_\infty} \frac{4}{3} \pi r^3 V^2 f_{j_\infty} dr dV + p_\infty = \rho_{f_0} U_0^2 \quad (4)$$

$$+ \sum_{j=1}^M \iint \rho_{\ell, j_0} \frac{4}{3} \pi r^3 V^2 f_{j_0} dr dV + p_0$$

$$\rho_{f_\infty} U_\infty h_{f_\infty} + \frac{U_\infty^2}{2} + \sum_{j=1}^M \iint \rho_{\ell, j_\infty} \frac{4}{3} \pi r^3 V \left(h_{\ell, j_\infty} + \frac{V^2}{2} \right) f_{j_\infty} dV dr = \rho_{f_0} U_0 h_{f_0} + \frac{U_0^2}{2}$$

$$+ \sum_{j=1}^M \iint \rho_{\ell, j_0} \frac{4}{3} \pi r^3 V \left(h_{\ell, j_0} + \frac{V^2}{2} \right) f_{j_0} dr dV \quad (5)$$

$$\frac{p_\infty}{\rho_{f_\infty} T_{f_\infty} \sum_{k=1}^N \frac{Y_{k_\infty}}{W_k}} = \frac{p_0}{\rho_{f_0} T_{f_0} \sum_{k=1}^N \frac{Y_{k_0}}{W_k}} \quad (6)$$

In order to derive the Rankine-Hugoniot equations for dilute sprays, Williams²⁰ proposed the following assumptions: (a) there are no droplet sources or sinks and no collisions between drops in the control volume being considered, (b) all droplets will disappear downstream of the detonation wave, $f_{j_\infty} = 0$, (c) initially all the droplets have the same velocity as the gas, $f_{j_0} \propto \delta(V - U_0)$, * (d) the initial enthalpy per unit mass, $h_{\ell, j}$, of the droplets

* δ \equiv Dirac delta functions.

is independent of the drop diameter, (e) the initial and final average molecular weights of the gas are equal,

$$\sum_{k=1}^N \frac{Y_{k\infty}}{W_k} = \sum_{k=1}^N \frac{Y_{k0}}{W_k},$$

(f) the specific heats of all gaseous species are constant and equal over a temperature range including T_{f0} , $T_{f\infty}$ and a standard reference temperature T^0 . Williams derived the Rankine-Hugoniot equations for dilute sprays by using the above assumptions and Equations (2), (4), (6)

Comparison of Williams' results with classical theory, Table 6, shows that the Rankine-Hugoniot equations for detonations in dilute sprays differ from those in gaseous media only in the effective heat of reaction and in the equation of state.

The Chapman-Jouguet case for dilute sprays and gaseous media having the same amount of actual heat release and the same initial conditions were found, by Williams, to differ on the following points: (a) a Chapman-Jouguet detonation wave in a dilute spray propagates at a slightly higher Mach number, (b) the downstream pressure is slightly higher, about 10% for the case of the dilute spray, and c) the dilute spray case has a slightly higher downstream temperature. Since the above comparison is based on constant actual total heat release, the differences must be the result of change in the equation of state and in the effective heat of reaction caused by the presence of the droplets. If a comparison is made between two systems, dilute spray and gaseous media, having the same initial temperature and comprised of the same fuel and oxidizer, the decrease in the total heat release caused by the latent heat of vaporization of the droplet will tend to erase the above differences.

TABLE 6 RANKINE-HUGONIOT EQUATIONS FOR DILUTE SPRAYS AND GASEOUS MIXTURES

Williams' theory for dilute sprays	Classical theory for gaseous mixtures
$\rho_\infty U_\infty = \rho_0 U_0$	$\rho_\infty' U_\infty' = \rho_0' U_0'$
$\rho_\infty U_\infty^2 + p_\infty = \rho_0 U_0^2 + p_0$	$\rho_\infty' U_\infty'^2 + p_\infty' = \rho_0' U_0'^2 + p_0'$
$C_p T_{f_\infty} + \frac{U_\infty^2}{2} = C_p (1 - Z_0) T_{f_0} + \frac{U_0^2}{2} + Q$	$C_p' T_{\infty'} + \frac{U_\infty'^2}{2} = C_p' T_0' + \frac{U_0'^2}{2}$
$\frac{p_\infty}{\rho_\infty T_\infty} = \frac{p_0}{\rho_0 (1 - Z_0) T_{f_0}}$	$\frac{p_\infty'}{\rho_\infty' T_\infty'} = \frac{p_0'}{\rho_0' T_0'}$

where

$$Q \equiv Z_0 C_p T_{f_0} + \sum_{j=1}^M Z_{j_0} h_{f_j, j_0} + \sum_{k=1}^M \left\{ \left[h_k^0 + C_p (T_{f_0} - T^0) \right] \left[Y_{k_0} (1 - Z_0) - Y_{k_\infty} \right] \right\}$$

or

$$Q \equiv Z_0 C_p T_{f_0} + \hat{Q}$$

where \hat{Q} is the total heat released per unit mass of mixture and Z_0 is the mass flux fraction of spray in front of the detonation wave.

In analyzing the steady, one-dimensional spray detonation structure,²⁵ additional assumptions are made for simplification: (a) all droplets are the same size and travel with the same velocity, i. e., $f(x, r, v) = n(x)\delta(r - \bar{r})\delta x(v - \bar{v})$, (b) the system is composed of non-volatile sprays in a gaseous atmosphere so that the burning processes are completed in the surface layer of the droplet, i. e., homogeneous reactions are negligible in comparison to the heterogeneous processes, (c) diffusion in the gas can be neglected, (d) the overall stoichiometry of the reactions occurring in the immediate neighborhood of each droplet does not change, and (e) the radial mass flux fraction at the outer edge of the surface layer of a droplet is independent of x . Using these additional assumptions Williams²⁵ found that the von Neumann detonation structure for gaseous detonations* would be a valid approximation to the structure of a heterogeneous detonation wave. This conclusion was obtained by examining the characteristic length for such properties as gas temperature, gas velocity, droplet velocity, and the mass flux fraction of sprays. The order of magnitude of these characteristic lengths, for a spray composed of 30μ fuel droplets in air is 10^{-4} cm, 10^4 cm, and 10^2 cm respectively.

Due to the thickness of the reaction zone in a pure heterogeneous detonation process²⁵, the interaction of the deflagration zone with the walls seems stronger than its interaction with the shock wave. Therefore, it is questionable whether the heterogeneous combustion could release sufficient heat to afford the wall losses and to support the shock front. Hence the stability of a spray-detonation must involve both the heterogeneous and homogeneous types of combustion.²⁵

*A gaseous shock wave followed by a heterogeneous deflagration wave.

Due to the various assumptions in Williams theory, its application might be limited. In order to ascertain the extent of applicability, Williams theory will be compared with some experimental results.

Investigating heterogeneous combustion at high Reynolds numbers in a shock tube, Webber²² found that an overly fine spray or a volatile fuel could produce a spontaneous explosion. Sprays of fairly coarse droplets or of relatively nonvolatile liquid fuels might burn rapidly enough to sustain and amplify a pressure wave. These experiments show that at high Reynolds numbers the specific combustion rates depend on the rate at which atomized particles are torn off the droplet, and this specific combustion rate influences the stability of the pressure wave.

Cramer²³ continued Webber's work by studying the onset of detonations in a two-phase medium. The gross pattern of the structure of spray-detonation waves superficially appears similar to that found by Williams; it is approximately like the von Neumann detonation structure for a gaseous mixture. However, the detailed mechanism showed that shattering of large drops into small droplets by the high velocity gas behind the shock wave had a great influence on the stability of the detonation wave. Williams' analysis of spray combustion does not consider this shattering phenomenon because it was assumed that the droplets had the property $W_e \ll W_{e\ cr}$. This is one reason why Williams found the stabilization of spray detonation waves doubtful.*

It is possible to generalize Williams' theory to include the case when droplet breakup phenomenon is prevailing. The necessary assumptions are (a) the droplets retain their spherical shape until they arrive at a critical flow condition

*Also, the heterogeneous reaction assumption, non-volatile fuels, contributes to this conclusion.

at which time they instantly breakup, (b) a source term, Q , describing this instantaneous disappearance and creation of particles be introduced into the governing equations. *

The sequence of events observed by Cramer** in the development of a "detonation like" wave from an accelerating hot gas piston, are as follows: (a) the high velocity gas behind the initial shock wave has a displacement as well as a shattering effect on the droplets, (b) the heterogeneous non-uniform spray is subjected to a transient redistribution behind the shock wave because of the displacement phenomenon, (c) the redistribution of droplets causes the combustion process to pass through three zones. The first zone has a high number density while the second zone contains particles with nearly the original size distribution. The third zone is composed of very small droplets. At about the time the leading edge of the flame reaches the third zone, the majority of the large droplets in zones one and two will begin to shatter into extremely fine droplets. Consequently, the combustion of these small droplets will cause an explosive heat release capable of supplying sufficient energy to enable the flame to overtake the shock front. The detonation wave is apparently sustained by the burning of these microdrops immediately behind the shock front. Therefore, Cramer concluded that some shattering mechanism is providing sufficient fuel vapor to sustain a detonation front.

From the previous discussion it is obvious that the drop size and the relative velocity between the droplet and the gaseous stream strongly influence the

*The addition of the source term makes the equations difficult, if not impossible, to solve

**Cramer used two detonation tubes in his experiment, one transparent tube for taking pictures and one steel tube for measuring p - t - x relations.

shattering phenomenon, and hence, the combustion mechanism. Burgoyne and Cohen²⁶ found that drops whose diameters were less than 10 microns behaved like a vapor, and drops with diameters greater than 40 microns burn individually.

Therefore, it is reasonable to expect the existence of two critical radii, $r_{cr\ 1}$ and $r_{cr\ 2}$, such that the area for spray detonation is divided into three regions, see Table 7.

TABLE 7. CHARACTERISTIC REGIONS FOR SPRAY DETONATION

I	II	III
Drop diameters are small enough so that the classical gaseous detonation theory is applicable.	The droplets remain spherical and do not breakup. Therefore Williams' theory is valid, and detonation waves are sustained by both homogeneous and heterogeneous reactions.	Drop shattering is dominant. Williams' theory with the addition of a source term can be applied in principle. Detonation waves are stabilized by shattering phenomenon.

According to Burgoyne and Cohen²⁶, it is reasonable to let $r_{cr\ 1} \approx 5 \mu$. The determination of $r_{cr\ 2}$ is not as obvious because of its strong dependence on the relative velocity between the gas and droplets.

The previous discussion implies that a droplet combustion driven shock front differs from gaseous detonation in at least four points, (a) the burning droplets add mass to the gaseous stream, (b) the droplet burning zone seems

thicker, (c) the wave model is now a shock wave following by droplet shattering and combustion, (d) a true detonation wave in sprays seems doubtful, if the droplet shattering time is not exceedingly short.

Since the droplet shattering phenomenon plays an important role in detonations through sprays, it is felt that the mechanism of breakup, the breakup time, and the critical velocity and droplet size are fundamental parameters in the two-phase detonation process. It has been found that the disintegration phenomenon is due to the interaction between the droplet and the flow field behind the shock wave, and is not due to the interaction between the droplet and the shock front itself^{27, 28, 29, 30, 31}.

B. LITERATURE REVIEW OF THE DROPLET BREAKUP PROCESS BEHIND A SHOCK WAVE AND ESTIMATION OF DROPLET BREAKUP TIMES IN HETEROGENEOUS H₂-O₂ DETONATIONS

1. Some Experimental Observations Concerning the Droplet Breakup Process

Experimental results^{30, 32, 33} show that two types of droplet breakup exist in the zone behind a shock wave front: the bag-type breakup and the shear-type breakup. The successive stages of a droplet breakup process can be described phenomenologically and are shown schematically in Figures 6(a) and 6(b).

(1) For a bag-type breakup, the increased pressure on the droplet surface, due to the high convective velocities following the wave front, flatten the droplet into a disk-shape, having its face perpendicular to the direction of the flow. Then the center portion is blown out into a thin hollow bag anchored to a heavy rim.* Finally the thin bag bursts into small droplets, while the rim breaks into fragments. Photographic evidence on this phenomenon appears in References 32 and 33. (2) For a shear-type breakup, in contrast, the droplet is

*Lane³³ states that up to 70% of the liquid remains in the rim.

distorted into a saucer-shaped disk with its convex surface facing to the gas flow. Then a thin ring layer is drawn out from the edges of the disk. Finally, the thin layer is stripped off the droplet and breaks up completely into micro-droplets. Engel³⁴ showed that the mechanism of micro-droplet formation is due to mechanical effects only and is not due to vaporization of liquid. Photographic details of this process may be found in References 30, 33, and 34.

2. Various Theories on Breakup of Droplets

However complex the phenomenon, it is highly desirable to treat it from both the experimental and theoretical aspects. The following is a discussion of pertinent theoretical analyses concerning the shattering processes of a droplet:

- a) Hinze's Theory. One of the earliest mathematical analyses on this subject was presented by Hinze²⁷. The theory is based on linearized hydrodynamical equations for slight deformations of a droplet in an air flow. The main emphasis was in the derivation of the relation between critical speed and critical size. Considering the influence of the aerodynamic pressure on a droplet and the surface tension of the droplet, Hinze found the criterion for determining breakup of a droplet to be the relevant value of the Weber number. By using the experimental data of Merrington and Richardson³⁵, Hinze indicated the critical Weber number, $(W_e)_{cr} = 10$. * However, the critical Weber number can be derived theoretically by using the critical radius $(r)_{cr}$ (see Equation 9 of Section b) and the definition of the Weber number. It shows the critical Weber number, $(W_e)_{cr} = 8$, which agrees closely with Hinze's value. Hinze also found that the

*Hinze²⁷ defined $W_e = (\rho_g U^2 r)/S$ but Williams²¹ defined $W_e = [\rho_g U^2 (2r)]/S$. In this report, Hinze's definition will be adopted.

effect of viscosity of liquid on deformation appears small except for large values of viscosity, e. g., viscosities of the order of glycerol. In this case, the viscosity effect tends to retard the breakup. The effect of viscosity on breakup has been studied in more detail by Hanson³⁶. He found that when the viscosity of a liquid is less than about 10 centistokes, the effect on droplet breakup is negligible; while if it is between 10 and 100 centistokes, the breakup process is retarded.

- (b) Mathematical Model for Bag Type Breakup of a Droplet. This mathematical analysis was proposed by Gorden²⁹. In the analysis, it is assumed that a cylindrical plug of diameter r and length $2r$ (where r is the radius of the droplet) is extruded from a droplet around the cylinder remains at rest. This deformation is caused by the air pressure in front of the droplet, but is retarded by surface tension, viscosity, and inertial forces of the droplet. Estimating the magnitude of the pressures caused by these forces, and combining them with the inertial effect, a differential equation for the extruded cylinder is obtained, i. e.,

$$\frac{dv}{dt} = \frac{1}{\rho_\ell D} \left(\frac{1}{2} \rho_g U^2 - \frac{16 \mu_\ell v}{D} - \frac{8S}{D} \right) \quad (7)$$

where v = velocity of the extruded cylinder. Equation 7 is solved for the instantaneous velocity, v , and the resulting equation is in turn solved for the instantaneous displacement of the cylinder as a function of time. The displacement is then set equal to the droplet diameter D to determine the total breakup time, t_b . The result is:

$$\frac{2 (16 \mu_\ell)^2}{\rho_\ell D^2 \left(\rho_g U^2 - \frac{16S}{D} \right)} = \frac{16 \mu_\ell t_b}{\rho_\ell D^2} - 1 + \exp \left(- \frac{16 \mu_\ell t_b}{\rho_\ell D^2} \right) \quad (8)$$

where t_b is the breakup time. The breakup time approaches infinity if a droplet is stable. Hence it is obvious from Equation 8 that the critical condition occurs at

$$\left(\rho_g U^2 - \frac{16S}{D} \right) = 0$$

which implies the critical radius is given by

$$(r)_{cr} = \frac{8S}{\rho_g U^2} \quad (9)$$

Equation 9 is formally identical with Lane's³³ empirical formula, which has been used in correlating experimental results^{32,33} between critical speed and critical size. However, Equation 9 will be used in this report for the same purpose.

Since Equation 8 cannot be solved analytically for the breakup time, a useful approximate solution is

$$t_b = \frac{2D\rho_\ell^{1/2}}{\left(\rho_g U^2 - \frac{16S}{D} \right)^{1/2}} + \frac{32\mu_\ell}{\left(\rho_g U^2 - \frac{16S}{D} \right)} \quad (8-a)$$

Hanson³⁶ and Domich showed experimentally that the effect on breakup can be neglected when the viscosity, $\mu_\ell \leq 10$ centistokes. For this case the bag-type breakup time is approximately

$$t_b = \frac{2D\rho_\ell^{1/2}}{\left(\rho_g U^2 - \frac{16S}{D} \right)^{1/2}} \quad (8-b)$$

It should be noted that according to this theory, Eq. (8-b) can predict the breakup time of droplets larger than critical size, and for droplets of critical sizes the breakup time is infinite.

(c) Mathematical Model for Shear-Type Breakup of a Droplet. This mathematical model is attributed to Dodd²⁸. The basic considerations of this theory are as follows: The tangential frictional aerodynamic forces cause an internal circulation in the surface layer of a droplet. In turn, the centrifugal effect resulting from the circulation causes bulges to form on the surface. On the other hand, the surface tension of the droplet has a retarding effect on bulge formation. If the pressure due to the centrifugal effect equals a fraction, F , of the surface tension pressure, then breakup occurs. The assumptions used in Dodd's analysis are: 1. the circulation velocity is uniform across the thin surface layer; 2. inside the moving layer the liquid is at rest; 3. the frictional force on the surface of the droplet is equal to $0.332 \sqrt{(U^3 \mu_g \rho_g)}/r$ and this force acts over a region of length r (see Figure 6(a) of this report); 4. the thickness of the moving layer is "fr"; where $0 < f < 1$. Based upon the balance of the energy transfer rate between the gas flow behind the shock front and the droplet, a breakup time for a droplet is derived:

$$t_b = \frac{2r}{(1.5U)^{3/2}} \cdot 0.332 \cdot \sqrt{\frac{Sp_f}{\mu_g \rho_g}} \cdot \sqrt{\frac{F}{f}}$$

or

$$t_b = \frac{3.28r}{U^{3/2}} \cdot \sqrt{\frac{Sp_f}{\mu_g \rho_g}} \cdot \sqrt{\frac{F}{f}}$$

By using Engel's³⁴ experimental data, with $\sqrt{F/f} = 0.5$

$$t_b = \frac{1.64r}{U^{3/2}} \cdot \sqrt{\frac{Sp_f}{\mu_g \rho_g}} \quad (10)$$

Due to the inequality of pressure on the upstream and downstream sides, each bulge is subjected to an aerodynamic drag tending to move the bulge off the surface of the droplet. Dodd²⁸ has pointed out that the effect of the aerodynamic force which reinforces the frictional force on the droplet surface, will decrease the breakup time. Therefore, the breakup time given by Equation 10 is too high, and some modification factor is needed to give the correct breakup time. Inasmuch as Dodd did not attempt to evaluate this factor, an attempt will be made to estimate this factor approximately by comparing the order of magnitude of the aerodynamic force and the frictional force.

$$\text{Let } p = \text{the aerodynamic pressure} = \frac{1}{2} \rho_g U^2$$

p_f = the frictional force per unit area

$$= 0.332 \sqrt{(U^3 \mu_g \rho_g) / r}$$

$$\frac{p_f + p}{p_f} = 1 + \frac{p}{p_f} = 1 + \frac{\frac{1/2 \rho_g U^2}{U^3 \mu_g \rho_g}}{0.332 \sqrt{\frac{U^3 \mu_g \rho_g}{r}}} = 1 + 1.5 \sqrt{\frac{\rho_g U r}{\mu_g}} = 1 + 1.5 \sqrt{Re}$$

$$\frac{p_f + p}{p_f} = 1 + 1.5 \sqrt{Re}$$

Since the impulse on the droplet due to the gas is equal to product of the force and the time over which it acts, it implies the breakup time is inversely proportional to the force. Hence breakup time given by Equation 10 should be modified by a factor $1/(1 + 1.5 \sqrt{Re})$, i.e.,

$$t_b = \frac{1.64r}{U^{3/2}} \sqrt{\frac{Sp_f}{\mu g \rho}} \left[\frac{1}{1 + 1.5 \sqrt{Re}} \right] \quad (10-a)$$

In investigating the disintegration of water drops in an air stream, where the relative velocity between air and the drop increases gradually, Dodd found the critical radius for a droplet is

$$(r)_{cr} = \frac{6.67 S}{\rho_g \beta U^2}$$

where β is a correction factor $0 < \beta < 1$. Lane³⁷, using Taylor's loading spring concept suggests that:

$$\frac{\text{Velocity for bursting by suddenly applied blast}}{\text{Velocity of bursting in steady stream}} = 0.71$$

In Reference³⁷, Lane found this factor agrees reasonably well with experimental data. Using this value, the correlation between critical relative velocity and critical size becomes

$$(r)_{cr} = 13S/(\rho_g U^2) \quad (11)$$

3. Comparison Between Theories and Experiments

In order to estimate the validity of these mathematical models, some calculations have been made. The results are listed in Tables 8, 9, 10 and 11. Since it has been pointed out by Rabin³⁰ that small droplets undergo a bag-type breakup while the large droplets experience a shear-type breakup, Equation 9 is used to correlate the critical conditions for small droplets, while Equation 11 is used for large droplets. When applying Gorden's correlation, Equation 9 to the experimental data, in Reference 30, for $(r)_{cr} = 500 \mu$, the deviation between theoretical and experimental critical radii is over 50%. It is felt that Equation 9 is valid only for $r < 500 \mu$, while Equation 11 applied for $r > 500 \mu$.

TABLE 8. THEORETICAL AND EXPERIMENTAL CORRELATION OF CRITICAL SIZE OF DROPLETS OF DIFFERENT FLUIDS FOR BAG-TYPE DROPLET BREAKUP

Liquid	Surface Tension dyne/cm S	Experimental Critical Velocity ft/sec U	Experimental Critical Size micron (r) _{cr}	Calculated Critical Size by Using Eq. (9) and Values of Experimental Critical Velocity micron (r) _{cr}
Group (A)				
Burning RP-1	11	92	100	75
Burning RP-1	11	85	100	87.5
Burning RP-1	11	82	100	98.5
Non-Burning RP-1	38	95	100	240
Non-Burning RP-1	38	125	100	140
Group (B)				
Dow Corning 200-A Fluid	21.14	73.5	213	246
Dow Corning 200-A Fluid	21.14	93.0	143	156
Dow Corning 200-A Fluid	21.14	121.3	90	103
Dow Corning 200-A Fluid	21.14	148.5	59	60.5
Water	71.97	121.3	200	321
Water	71.97	198.8	90	119
Water	71.97	282.0	53	59.5
Methyl Alcohol	22.2	74.4	235	263
Methyl Alcohol	22.2	121	93	101
Group (C)				
Water	72.75	84.3	300	665
Water	72.75	109.5	205	377
Water	72.75	157.3	135	180
Water	72.75	238.5	60	73.5
Methyl Alcohol	22.6	60	317	415
Methyl Alcohol	22.6	84.3	165	208
Methyl Alcohol	22.6	109.5	125	120
Methyl Alcohol	22.6	157.3	99	55

Experimental data for Group (A) are taken from Ref. 30.

Experimental data for Group (B) are taken from Ref. 36.

Experimental data for Group (C) are taken from Ref. 32.

TABLE 9. THEORETICAL AND EXPERIMENTAL CORRELATION OF CRITICAL SIZE OF BURNING AND NON-BURNING DROPLETS OF RP-1 FOR SHEAR-TYPE DROPLET BREAKUP

Liquid	Surface Tension dyne/cm S	Experimental Critical Velocity ft/sec U	Experimental Critical Size micron (r) _{cr}	Calculated Critical Size by Using Eq. (11) micron (r) _{cr}
Burning RP-1	11	83	500	152
Burning RP-1	11	55	500	345
Non-Burning RP-1	38	93	500	411
Non-Burning RP-1	38	80	500	550

Experimental data are taken from Ref. 30

TABLE 10 THEORETICAL SHEAR-TYPE DROPLET BREAKUP TIMES FOR BURNING AND NON-BURNING DROPLETS OF RP-1 USING EXPERIMENTAL VALUES OF CRITICAL VELOCITY AND CRITICAL SIZE

Liquid	Surface Tension dyne/cm S	Experimental Critical Velocity ft/sec U	Experimental Critical Size micron (r) _{cr}	Breakup Times Calculated by Using Eq. 10-a sec
Burning RP-1	11	83	500	0.489×10^{-3}
Burning RP-1	11	55	500	1.16×10^{-3}
Non-Burning RP-1	38	93	500	0.925×10^{-3}
Non-Burning RP-1	38	80	500	1.29×10^{-3}

Experimental data are taken from Ref. 30

TABLE 11. THEORETICAL SHEAR-TYPE DROPLET BREAKUP TIMES OF LIQUID OXYGEN DROPLETS IN A STOICHIOMETRIC H₂-O₂ DETONATION

Radius of the Droplets r (microns)	Reynolds Number Re	Breakup Time Calculated by Using Eq. 10-a t_b (sec)
500	30.8	0.89×10^{-7}
600	37	0.99×10^{-7}
700	43.1	1.0×10^{-7}
800	49.2	1.15×10^{-7}
900	55.6	1.22×10^{-7}
1000	61.6	1.25×10^{-7}

Surface tension of liquid oxygen = 13.2 dyne/cm (at T = 90°K)

= 9400 ft/sec

Mole-fraction of hydrogen

= 0.667

Viscosity of gas mixture

= 0.894×10^{-3}

Density of gas mixture

= 5.2×10^{-4} gm/cm³

Density of liquid oxygen

= 0.4299 gm/cm³ (at T = 154.3°K)

*Corresponding to the condition behind the detached shock.

Equation 10-a gives the breakup time for the shear-type breakup for droplets of critical size as well as for droplets larger than critical size. Some calculated results, by using Equation 10-a and the experimental data given by Reference 30 are listed in Table 10. It indicates the breakup time for droplets of $r > 500 \mu$ and relative air flow velocities of the range $55 \text{ ft/sec} < U < 95 \text{ ft/sec}$, is about 1 millisecond. The velocities used in the above experiments were much lower in comparison to the velocity occurring behind the strong normal shock wave associated with the detonation process. Hence, the breakup time in the zone behind the detonation wave front would be expected to be much smaller than the values listed in Table 10. In order to estimate the order of the droplet breakup time in the detonation case, the following analysis is made utilizing Equation 10-a and the detonation characteristics of hydrogen-oxygen mixtures calculated by Moyle³⁸. For a mixture having a mole-fraction of 0.667 hydrogen, a detonation velocity of about 9400 ft/sec is obtained. Assuming that the structure of a spray detonation consists of a normal shock wave followed by combustion, the gas velocity immediately behind the normal shock front is supersonic and causes a detached shock wave in front of the droplet. It is the gas flow behind the detached shock that is responsible for droplet breakup. Using the conservative minimum value of the sub-sonic velocity behind the detached shock, the breakup time for oxygen droplets having a size range of $500 \leq r \leq 1000 \mu$ have been calculated. The results are shown in Table 11. The breakup times are in order of 0.1 $\mu\text{-sec}$. In this time interval the detonation wave front will travel a distance approximately equal to 1×10^{-2} in. This distance will be denoted by L_B . Dabora³⁹, using experimental data on the detonation velocity decrement of an explosive gas confined by an inert gaseous medium, has made estimations of the length of the reaction zone in stoichiometric $\text{H}_2\text{-O}_2$ and $\text{CH}_4\text{-O}_2$ mix-

tures of .14 inches and .325 inches respectively. Denoting this distance by L_C , it follows that for H_2-O_2 detonations in stoichiometric gaseous mixtures, $L_C = 0(1)$ and therefore $L_B \ll L_C$.

4. Conclusions

The Weber number appears to be an important criterion concerning the droplet-shattering phenomenon. Hinze has shown there exists a critical Weber number of a dilute spray, $(We)_{cr} = 10$. When the Weber number is larger than this value, the droplets tend to break up.

Utilizing a theoretical relation developed by Dodd, the breakup times for oxygen droplets in a H_2-O_2 spray detonation have been calculated. For oxygen droplets within a size range of $500 \leq r \leq 1000\mu$, the breakup time is of the order of $0.1 \mu\text{sec}$. In this time interval the detonation wave front will travel a length, $L_B = 1 \times 10^{-2}$ in. In comparing this order of L_B , with the order of L_C , the length between the shock wave front and the zone of significant chemical reaction, it follows that $L_B \ll L_C$. Thus it is indicated that large droplets will be shattered into microdroplets in a zone sufficiently small behind the shock wave front, that if the subsequent evaporation and combustion of these microdroplets occur rapidly enough, a heat release sufficient to sustain a Chapman-Jouguet detonation wave is possible. Thus it appears that the droplet breakup process occurring behind the shock wave can be an important mechanism in stabilizing a detonation wave in a dilute spray.

In the following section an experimental study is described showing droplet breakup phenomena behind strong shock waves, i. e., H_2-O_2 detonations.

C. EXPERIMENTAL STUDIES OF THE DROPLET BREAKUP PROCESS BEHIND CHAPMAN-JOUQUET, H₂-O₂ DETONATIONS

In order that a rotating detonation wave engine will function properly, the fuel and the oxidizer must be in a form which will support a steady-state detonation process with the detonation wave presumably of the Chapman-Jouguet type. If part of the reactive mixture is present in the form of liquid droplets, any information regarding the effect of the two-phase (liquid-gas) nature of the initial reactants on the detonation process would be very important. A few considerations can be mentioned, e.g., injector design, combustion instability, and combustion efficiency. These considerations are of course of paramount importance to the proper operation of a conventional liquid-propellant rocket engine operating on the deflagrative-mode of combustion. It is believed that these considerations can be even of more importance to the proper design of a rocket engine operating on the detonative mode of combustion due to the extremely high reaction rates and short residence times associated with the detonative process.

It has been pointed out in the above sections, A and B, that if the liquid droplets are large enough in size, it is quite probable that the detonative process could not be supported if the evaporation process is the only mechanism available to accelerate the change of phase of the propellant involved from liquid to gas. Another mechanism, the droplet shattering phenomenon, was suggested as a possible means of accelerating this change of phase process. It is the purpose of this section to report on some preliminary experiments performed to shed some light on this phenomenon, or indeed to see if this phenomenon occurs at all in the time necessary to support a Chapman-Jouguet detonation wave.

The experimental study has been performed in the facility (see Figure 7) described as follows

Detonation Tube

The tube is built in sections, each section flanged and readily dismountable. The test section is fabricated of mild steel of 1 in. x 1 in. square

inside cross section, 6 feet long, with a number of windows. A 4 foot detonation induction section is attached and the tube is mounted horizontally. Extra sections can readily be added, and diaphragms inserted between sections. Thus, sections can be used for expansion chamber, detonation driver or constant volume combustor, or shock tube. For this study it is set up as a detonation tube with glow plug ignition.

Charging System

This system contains the plumbing, valves, etc., to evacuate and charge the tube, and to premix the combustible mixtures.

Schlieren System for Optical Observation

This system utilizes 6-inch diameter, 54-inch focal length mirrors in a conventional single pass arrangement, auxiliary lenses to produce a magnified image (these are inside the shroud on the photograph of Figure 7) and a spark-discharge light source. The latter under favorable conditions will operate up to a voltage of 32 KV, with spark durations of about $0.1 \mu\text{sec}$. The light source has an auxiliary lens mounted in front to increase the light intensity. The system is mounted on a bench and can be moved as desired to observe various locations in the test section.

Electronics

This system consists of a thyratron sensing circuit and a CMC Model 757 BN time-interval counter for wave velocity measurements. These are actuated by ionization probes in the top wall of the test section. In addition a time delay unit and power supply for the light source is required.

For this study, $\text{H}_2\text{-O}_2$ detonations rather than shock waves have been utilized because their properties are well known and they are most convenient to handle. In addition, the detection equipment, utilizing ionization probes, was more suitable to the detonation phenomenon. It is evident that the flow conditions associated with the convective gases immediately behind a gaseous $\text{H}_2\text{-O}_2$, Chapman-Jouguet detonation do not simulate exactly those conditions behind the strong

normal shock wave associated with a detonation propagating through a droplet field. Due to the qualitative nature of this study, it is believed that this simplification is justified.

The detonation waves utilized in these experiments are obtained in approximately stoichiometric mixtures of H₂ and O₂. The waves are initiated by means of a miniature glow plug. Velocity measurements indicate that the detonation waves are fully developed, i. e., Chapman-Jouguet detonations, within approximately 5 1/2 feet of the point of ignition at the closed end of the tube. Therefore, the wave-droplet collision process is photographed at a point 9 feet from the closed end of the tube. In addition, at this position, conditions imposed on the droplets are approximately constant for the time after collision of interest.

The water droplets are introduced into the top of the tube and fall vertically into a drain hole in the bottom wall of the tube. The larger droplets (~ 1000 μ diameter) and the smaller droplets (220-580 μ diameter) utilized in this study were produced by employing standard hypodermic tubing of No. 22 and No. 30 size respectively. Nitrogen pressure of approximately one inch Hg was utilized to obtain the desired droplet spacing for the larger droplets with somewhat higher pressures employed for the smaller droplets. The velocity of the droplets is the order of a few feet per second which is near the terminal velocity for the droplet size involved.

Photographs are taken on 4 in. x 5 in. polaroid film (ASA-3000) with approximately 15% of the light cut-off at the schlieren knife-edge.

Included in this report is a sequence of spark-schlieren photographs taken of the detonation-droplet collision process utilizing different detonation waves for each photograph. The detonation waves are moving toward the right on the photographs. Figure 8 is a sequence of photographs taken under the following conditions:

Droplet diameter	1000 μ
Droplet spacing	3/32 - 1/8 inch
H ₂ -O ₂ mixture	X _{H₂} ≈ .70
Detonation wave velocity	9800 ft/sec
Initial pressure	One atmosphere
Initial temperature	Room temperature
Scale size	2.51

Figure 9 is one of a sequence of photographs taken of the smaller droplets under the following conditions:

Mean droplet diameter	400-500 μ
Range of droplet diameter	220-580 μ
Droplet spacing	3/32 - 1/8 inch
H ₂ -O ₂ mixture	X _{H₂} ≈ 2/3
Detonation wave velocity	9300 ft/sec
Initial pressure	One atmosphere
Initial temperature	Room temperature
Scale size	2.751

The closely spaced parallel wires on the photographs of both figures are reference wires located just outside of the windows of the test section. The photographs labeled (c) and (a) on Figure 8 and Figure 9 respectively are representative of the undisturbed droplet stream. In Figures 8 (4) and 9 (b) the detonation wave is just outside the field of view to the right. Any other droplets appearing outside the vertical droplet row on the photographs (especially apparent on photograph 4 of Figure 8) are caused by extraneous accumulations of water while the injector was being adjusted and should be disregarded. The weak normal shock wave, visible just upstream of the row of droplets in photograph (b) of Figure 9 is not predicted from one-dimensional theory. The predicted convective Mach number of the gases immediately behind a stoichiometric H₂-O₂ Chapman-Jouguet detonation is subsonic (~ .82) with respect to the tube walls. It is possible that due to the blockage effect of the shattering row of droplets, the convective Mach number of the flow has exceeded unity. This effect is not observed, however, in the sequence of photographs utilizing the larger droplets. The photographs of both figures, however,

do show an interesting series of interconnecting shock waves between the individual droplets during the shattering process. These are most evident on photograph (1) of Figure 8 and on photograph (b) of Figure 9.

The conclusions reached concerning the droplet shattering process obtained from the series of photographs are as follows:

The droplets shatter significantly in the time interval of from 5 to 10 μ -sec after the passage of the wave for both sizes of droplets studied. This conclusion is arrived at due to the observed increase in the apparent droplet diameter by a factor of three or more in this time interval. It is believed that this apparent increase is due to the shear-type breakup process observed by other investigators in which the opaque zone is actually a region occupied mainly by a very dense population of micro-droplets surrounding the remains of the parent droplet. It is not possible to establish conclusively whether a portion of the parent droplet still remains after the observed time interval of about 10 μ -sec. Measurements indicate, however, that the location of the upstream edge of the opaque region is unchanged from the original position of the row of droplets up to about 10 μ -sec after the passage of the wave. In the time interval of from 10 to 15 μ -sec after the passage of the wave, however, a measurable change in the upstream position has occurred for the smaller droplets (originally $\sim 300 \mu$ diameter). This indicates that the upstream position of the opaque zone has accelerated to an average velocity in this time interval of the order of 30 to 60 ft/sec. While this is quite low compared to the theoretical gas velocity of about 4200 ft/sec behind a stoichiometric H_2-O_2 detonation wave, it represents the same order of acceleration as that observed in the shorter time interval (0 to 10 μ -sec) for the downstream edge of the opaque zone—a zone which is believed to be made up of a dense population of micro-droplets. While this is not conclusive proof that the parent droplet has completely shattered, it is supporting evidence that most of the original mass has been stripped off in the form of micro-droplets within a time interval of about 10-15 μ -sec after the collision of the detonation wave with the droplet.

In this connection, a recent shockwave-droplet interaction study has been made by Morrell⁴⁰ utilizing cylindrical water jets as small as 457μ in diameter with convective velocities behind the shock wave as high as 1135 ft/sec. He concludes that there is fair agreement between the jet breakup times he observes experimentally and those predicted theoretically for a shear-type breakup process. It is interesting that using the relation suggested by Morrell for the dependence of the breakup time t_b on the initial radius of the jet, R_0 , and the convective velocity of the gas behind the shock wave u ,

$$t_b \sim \left(\frac{R_0}{u} \right)^{1.25}$$

we obtain for the case of a detonation with $u = 4200$ ft/sec and $R_0 = 150 \mu$, a breakup time of $15 \mu\text{-sec}$ compared to the breakup time of $130 \mu\text{-sec}$ for $R_0 = 228 \mu$ and $u = 1135$ ft/sec observed by Morrell.

While it is evident that Morrell's study utilized cylindrical jets rather than droplets with some other different conditions present (such as differences in shocked gas density and viscosity), it is interesting to note the order of agreement between the breakup times predicted using Morrell's relation extrapolated to the higher convective velocities behind detonation waves utilized in the present study.

It is apparent that more refined measurements would be required to establish conclusively the shattering process and droplet breakup times behind the strong shock wave associated with an actual detonation passing through a heterogeneous, liquid-gas media. It is also apparent that since observed breakup times of droplets appear to be in the order of magnitude of that required to support heterogeneous detonation, i.e., $10-15 \mu\text{-sec}$, that the droplet shattering process in this connection is of extreme importance.

IV. THEORETICAL STUDY OF HEAT TRANSFER IN THE ROTATING DETONATION WAVE ENGINE

As in conventional rocket motors, heat transfer to the walls of the rotating detonation wave engine (RDWE) is a key factor in determining the feasibility and design of various engine configurations. A preliminary study of the heat transfer problem has been made and is described below.

An analysis of the temperature distribution in the wall of the RDWE breaks down into the problems of '1' determining the magnitude and time variation of the heat flux from the hot gases behind the detonation wave to the walls of the combustion chamber, and '2' computing the heat conduction in the chamber wall. A detailed discussion of these problems follows below.

A. THEORETICAL MODEL FOR HEAT FLUX

To determine the heat flux it is necessary to have some understanding of the processes which occur in the RDWE. The rotating detonation is followed by a region of high pressure and high temperature gases where the heat flux will be a maximum. After the detonation passes, the combustion products expand through the annular nozzle of the wave engine and fresh fuel and oxidant enter the combustion chamber. During this process the temperature and pressure and consequently the heat flux decrease until at some distance behind the wave the heat flux becomes negligible. Since the flow described above is quite complex the simplified theoretical model described below has been adopted for the initial heat transfer calculations.

It is assumed that the detonation wave is plane and moves past a flat plate and through a combustible mixture which is initially at rest as shown in Figure 10. The velocity induced by the passage of the detonation results in the formation of a boundary layer. Pressure, temperature, and velocity behind the

detonation are assumed constant and equal to the Chapman-Jouguet values for some distance x_p behind the wave. Beyond this point it is assumed that heat transfer will be negligible so that x_p represents a heat pulse width. Since the flow appears steady to an observer moving with the detonation wave a coordinate system which is fixed to the wave as shown in Figure 11 has been adopted. In this coordinate system the wall moves with detonation velocity V_D .

B. CONDITION OF COMBUSTION GASES OUTSIDE THE BOUNDARY LAYER AND BEHIND THE DETONATION

To determine the velocity, pressure, and temperature of the fluid outside the boundary layer induced by the detonation, it is necessary to use the one dimensional conservation equations which are as follows.

$$\text{Mass:} \quad \rho_1 V_D = \rho_e V_e \quad (1)$$

$$\text{Momentum:} \quad p_1 + \rho_1 V_D^2 = p_e + \rho_e V_e^2 \quad (2)$$

$$\text{Energy:} \quad h_1 + \frac{V_D^2}{2} + Q = h_e + \frac{V_e^2}{2} \quad (3)$$

where h = enthalpy and Q is the heat released by the chemical reaction. In addition to the conservation equations it is assumed that the perfect gas approximation holds so that

$$p = \frac{R_0}{\bar{W}} \rho T \quad (4)$$

where R_0 = universal gas constant

$$\bar{W} = \text{average molecular weight of a mixture} = \sum x_i \bar{w}_i$$

Finally it is assumed that the wave in question is a Chapman-Jouguet detonation so that V_e is the local speed of sound, i. e.,

$$\frac{V_e^2 \bar{W}_e}{\gamma_e R_0 T_e} = M_e^2 = 1 \quad (5)$$

Equations 1 to 5 have been extensively discussed, e. g., see Morrison⁴¹. Unfortunately the heat released, Q , can only be computed by laborious iterative, chemical equilibrium calculations. Fortunately both theoretical calculations and experimental measurements for various H_2 - O_2 mixtures, which is the fuel oxidant combination used by the wave engine, have been made by Moyle³⁸ and so his results will be used to determine V_e , T_e , p_e , and ρ_e .

Moyle has calculated the ratio V_D/V_e , the detonation velocity V_D , and \bar{W}_e , the molecular weight of the equilibrium mixture behind the detonation, for various mixture ratios and initial conditions. Moyle's calculated values are in close agreement with experimental results. Assuming that γ_e , the ratio of specific heats behind the wave, has the value 1.22, which from Moyle's results appears to be valid for initial mixtures ranging from 78% H_2 by volume to 35% H_2 by volume, all quantities behind the detonation can be calculated.

For example for an initial H_2 - O_2 mixture of 60% H_2 by volume and an initial pressure and temperature of 1 atmosphere and 300°K it is found that

$$V_D = 8620 \text{ ft/sec}$$

$$T_e = 6322^\circ R$$

$$V_D/V_e = 1.77$$

$$V_e = 4851 \text{ ft/sec}$$

$$\rho_e = .0630 \frac{\text{lb mass}}{\text{ft}^3}$$

C. HEAT FLUX ACROSS THE BOUNDARY LAYER

It has been assumed that the boundary layer formed by the detonation is turbulent throughout. The presence of a combustion zone within the detonation,

which in itself tends to be turbulent⁴², provides a reasonable basis for this assumption.

To obtain an initial estimate of the heat flux Mirels' analysis of the turbulent boundary layer behind a moving shock wave in air has been applied to the present problem. The free stream conditions in Mirels' analysis are constant as is the case in the model adopted for the present analysis. Using a Reynolds analogy Mirels developed the following relation between the heat flux q_w and shear τ_w at the wall:

$$q_w = \frac{(h_r - h_w) \tau_w}{(V_D - V_e) Pr_m^{2/3}} \quad (6)$$

where h_w is the wall enthalpy, and Pr_m is the Prandtl number evaluated at some mean or reference condition within the boundary layer. h_r is the recovery enthalpy and is given by

$$h_r = h_e + \left(\frac{V_D}{V_e} - 1 \right)^2 \frac{V_e^2}{2} Pr_m^{1/3} \quad (7)$$

For mean conditions in the boundary layer Mirels uses fluid properties based on Eckert's⁴⁴ mean enthalpy which is defined as

$$h_m = 0.5(h_w + h_e) + 0.22(h_r - h_e) \quad (8)$$

The shear stress at the wall, τ_w , was determined by a solution of the momentum integral equation, which incorporates the moving wall boundary condition that differentiates the shock tube and conventional boundary layers. Mirels obtained the result

$$\frac{\tau_w}{\rho_e V_e^2} = .0460 \left(\frac{\theta}{\delta} \right) \left[\phi \left(1 - \frac{V_D}{V_e} \right) \frac{\delta}{\theta} \right]^{4/5} \left(\frac{V_D}{V_e} - 1 \right)^{3/5} \left(\frac{\nu_e}{V_e} \right)^{1/5} \left(\frac{1}{x} \right)^{1/5} \quad (9)$$

where

$$\phi = \left(\frac{\mu_m}{\mu_e} \right)^{1/4} \left(\frac{\rho_m}{\rho_e} \right)^{3/4},$$

ν_e is the kinematic viscosity in the free stream, and δ and θ are the boundary layer and momentum thicknesses respectively. The ratio θ/δ is given as a complicated function of h_r , h_w , h_e and V_D/V_e by Mirels; however, in the present case the formula

$$\frac{\theta}{\delta} = 0.317 \left(1 - \frac{V_D}{V_e} \right) \quad (10)$$

given by Hartunian⁴⁵, et al., for shock Mach numbers above 5.0 will be used. Mirels analytical results are in good agreement with the experimental results of Hartunian and this provides some assurance that the formulas above will yield reasonable results. The experimental results also fit the formula

$$St \sqrt{Re} = 3.7 \times 10^{-2} \quad (11)$$

where

$$St = \text{Stanton No.} = \frac{q_w}{\rho_e (V_D - V_e) (h_r - h_w)}$$

$$Re = \text{Reynolds No.} = \frac{\rho_e (V_D - V_e) x}{\mu_e}$$

Throughout the work of Mirels and Hartunian equilibrium air properties are used. Since the boundary layer equations used by Mirels did not include a term for diffusive transport, it would appear that Mirels has assumed equilibrium flow with the Lewis number, $Le = (C_p D_p)/k$, equal to unity, although this fact is never explicitly stated. In the preliminary calculations described below the effects of dissociation have been ignored. Computations based on equilibrium properties of the combustion gases is presented in Section E.

For the 60% H₂ mixture considered above, Equations 6 through 10 yielded the following result for the heat flux:

$$q_w = 1986 \left(\frac{1}{x} \right)^{1/5} \frac{\text{Btu}}{\text{ft}^2 \text{sec}} \quad (12)$$

where x is distance behind the detonation in feet. Moyle's³⁸ results were used for the composition behind the detonation wave and in the present calculation it was assumed that this composition remains fixed throughout. Enthalpies were obtained from NBS tables⁴⁶, and transport properties of the gas mixture behind the detonation were calculated using the charts and formulae given in Barrere⁴⁷. q_w is infinite at the foot of the detonation where x = 0 because of the leading edge singularity of the boundary layer, however, the total or integrated heat flux remains finite.

In general

$$q_w = Kx^{-1/5}$$

where K depends on the properties of the detonation. The total heat flux, Q_w , over a pulse of length x_p is

$$Q_w = K \int_0^{x_p} x^{-1/5} dx = \frac{5}{4} K x_p^{4/5} \text{ Btu} \quad (13)$$

for the unit width of the flat plate. \bar{q}_w , the average heat flux, is given by

$$\bar{q}_w = \frac{Q_w}{x_p} = \frac{5}{4} K x_p^{-1/5} \frac{\text{Btu}}{\text{ft}^2 \text{sec}} . \quad (14)$$

A stationary observer sees a periodic free stream variation of heat flux of period τ . If there are n equally spaced waves rotating in an annulus of diameter D then

$$\tau = \frac{\pi D}{n V_D} . \quad (15)$$

The ratio c of the pulse width to the wavelength will be given by

$$c = \frac{n x_p}{\pi D} = \frac{t_p}{\tau} . \quad (16)$$

where t_p is the pulse duration, and is related to x_p by

$$x_p = V_D t_p = c \tau V_D . \quad (17)$$

During the passage of each detonation a stationary observer will see a time varying heat flux $q_w(t)$ given by

$$q_w(t) = K (V_D t)^{-1/5} . \quad (18)$$

To simplify the conduction problem discussed below the actual variation (Equation 18) has been replaced by a series of square pulses of width $c\tau$ and amplitude \bar{q}_w as shown in Figure 12.

The overall combustion chamber cooling problem depends on the average heat transfer, \bar{Q}_w , to the walls of the chamber per unit time per unit area. \bar{Q}_w is given by

$$\bar{Q}_w = c \bar{q}_w = \frac{5}{4} K c^{4/5} \left(\frac{n}{\pi D} \right)^{1/5} . \quad (19)$$

Equation 19 shows that the dimensionless heat pulse width, c , is of crucial importance in determining the overall chamber heat transfer. If Equation 16 is combined with Equation 19 the following expression for \bar{Q}_w is obtained:

$$\bar{Q}_w = \frac{5}{4} K \frac{n x_p^{4/5}}{\pi D} . \quad (20)$$

Equation 20 shows that for a given pulse width x_p , \bar{Q}_w varies directly with the number of detonations rotating about the chamber and inversely with the diameter of the annular combustion chamber. Either c or x_p depends on the complex flow behind the detonation, an approximate solution of which is presented in Section II of this report.

As a specific example, the case of the 7 in. ID, 8 in. OD, annular experimental engine operating with a 60% H_2 mixture has been considered. It has been assumed that $c = 1/3$. Pressure traces obtained during the tests of this engine indicate that this assumption for c is quite reasonable for the high pressures behind the detonation seem to persist for less than 1/3 of the first cycle. From Equations 12, 14, 15 and 17 it follows that

$$\tau = 2.28 \times 10^{-4} \text{ sec} = 228 \text{ sec}$$

$$\bar{q}_w = 2700 \text{ Btu/ft}^2 \text{ sec} = 18.8 \text{ Btu/in.}^2 \text{ sec}$$

and from Equation 19 it follows that with $c = 1/3$

$$\bar{Q}_w = 900 \text{ Btu/ft}^2 \text{ sec} = 6.25 \text{ Btu/in.}^2 \text{ sec} .$$

\bar{Q}_w is of the same order of magnitude as the heat flux near the throat of a conventional rocket motor.

The calculation of \bar{Q}_w involves numerous approximations. First it should be mentioned that heat flux due to radiation has been neglected. Experience with conventional rocket motors indicates that radiation may increase the heat flux

10-20%. Conditions behind the detonation wave are not constant, but rather because of expansion through the nozzle and admission of fresh unburnt fuel and oxidant there will be a rapid drop in temperature and pressure. In ignoring this factor the calculations above are quite conservative. Consideration of the fact that the dissociated combustion products may recombine near the cool wall of the combustion chamber may cause some increase in \bar{Q}_w .

The combustion chamber surface temperature depends upon the conduction within the chamber walls and this problem is discussed below.

D. HEAT CONDUCTION IN THE SOLID WALL

To solve the combustion chamber heat transfer problem it is necessary to consider the conduction through the cylindrical inner and outer walls of the chamber as shown in Figure 13. On one surface of each cylinder the boundary condition consists of a series of equally spaced heat pulses moving past the surface with velocity V_D . The other surface is in contact with coolant. An exact solution of this two dimensional, unsteady conduction problem is very difficult. It has been found possible to make two simplifications which greatly simplify the analysis.

If $d_i/R_c \ll 1$ and $d_e/R_c \ll 1$, where R_c is average combustion chamber radius and d_i and d_e are inner and outer wall thickness, then the cylindrical walls can be replaced by an infinite flat plate with heat pulses moving past one side and coolant on the other side. If the width x_p of the heat pulse is sufficiently great and the period T of the heat pulse is sufficiently small then the effects of the periodicity of the heat pulse will be confined to a thin region near the surface of the flat plate. In such case the work of Jaeger⁴⁸ indicates that for purposes of determining the maximum surface temperature two dimensional effects can be neglected. Thus one can replace the combustion chamber conduction problem by the conduction through a one dimensional flat plate with periodic surface conditions.

The above approximation has been applied by Phillips⁴⁹ to the problem of heat transfer from a moving arc to an electrode, and his results are directly applicable to the present problem. Phillips determined the temperature within an infinite flat plate of thickness ℓ with a periodic heat flux on one surface and heat transfer across a coolant film on the other surface, as shown in Figure 14. Phillips obtained the solution of the heat equation

$$\frac{\partial^2 T}{\partial y^2} - \frac{1}{\alpha} \frac{\partial T}{\partial t} = 0 \quad (21)$$

subject to the boundary conditions

$$\begin{aligned} -k \frac{\partial T}{\partial y} &= \bar{q}_w; & m\tau \leq t \leq (m+c)\tau \\ -k \frac{\partial T}{\partial y} &= 0; & (m+c)\tau \leq t \leq (m+1)\tau \\ m &= 0, 1, 2, 3 \end{aligned} \quad (22)$$

at $y = 0$, and

$$-k \frac{\partial T}{\partial y} = h(T - T_0); \quad y = \ell \quad (23)$$

where α is the thermal diffusivity, $k/\rho c_s$, h is the coolant film coefficient, k the conductivity, and c_s the specific heat. Equation 22 is an analytical representation of square pulse heat flux shown in Figure 12. Initial conditions are

$$T(y, 0) = T_0 \quad (24)$$

The solution of the problem above consists of a steady state part and a transient part which dies out as $t \rightarrow \infty$. In the present case only the steady state value of the surface temperature is of interest, and is given by

$$(T_s - T_0) = \frac{2\bar{q}_w \ell}{k} \sum_{n=1}^{\infty} p_n \left(\left\{ 1 - \exp \left[-\frac{\beta_n^2 \alpha}{\ell^2} (t - m\tau) \right] \right\} + \exp \left[-\frac{\beta_n^2 \alpha}{\ell^2} (t - m\tau) \right] \left[\frac{1 - \exp \left(\frac{c\tau\alpha\beta_n^2}{\ell^2} \right)}{1 - \exp \left(\frac{\tau\alpha\beta_n^2}{\ell^2} \right)} \right] \right) - \frac{\bar{q}_w c}{h} (1 + h'\ell) , \quad (25)$$

where β_n are eigenvalues determined from the equation

$$\beta_n \tan \beta_n = h'\ell \quad (26)$$

and

$$p_n = \frac{[\beta_n^2 + (h'\ell)^2]}{\beta_n^2 [\beta_n^2 + h\ell (1 + h'\ell)]} \quad (27)$$

where $h' = h/k$. Equation 25 is valid only during intervals

$$m\tau \leq t \leq (m + c)\tau$$

$$m = 0, 1, 2, 3, \dots$$

when $q = \bar{q}_w$. Only this part of the solution is of interest for it is during this interval that the surface temperature reaches its maximum value. The maximum surface temperature, which occurs at the end of the square heat pulse is according to Equation 25 given by

$$(T_{s_{\max}} - T_0) = \frac{2\bar{q}_w \ell}{k} \sum_{n=1}^{\infty} p_n \left[\frac{1 - \exp\left(-\frac{c\alpha\tau\beta_n^2}{\ell^2}\right)}{1 - \exp\left(-\frac{\alpha\tau\beta_n^2}{\ell^2}\right)} \right] - \frac{\bar{q}_w c}{h} (1 + h^\ell), \quad (28)$$

while the minimum surface temperature, which occurs at the start of the heat pulse is

$$(T_{s_{\min}} - T_0) = \frac{2\bar{q}_w \ell}{k} \sum_{n=1}^{\infty} p_n \left[\frac{1 - \exp\left(\frac{c\alpha\tau\beta_n^2}{\ell^2}\right)}{1 - \exp\left(\frac{\alpha\tau\beta_n^2}{\ell^2}\right)} \right] - \frac{\bar{q}_w c}{h} (1 + h^\ell) \quad (29)$$

The amplitude of the surface temperature fluctuation, i.e., $T_{s_{\max}} - T_{s_{\min}}$ depends upon the dimensionless pulse width c and the factor $\alpha\tau/\ell^2$. For $c = 1$, i.e., continuous heat flux, $T_{s_{\max}} = T_{s_{\min}}$ as is to be expected. From Equation 26 it is readily shown that

$$\beta_n < (2n - 1) \frac{\pi}{2}$$

so that

$$\frac{\alpha\tau}{\ell^2} \beta_n^2 < (2n - 1)^2 \frac{2}{4} \frac{\alpha\tau}{\ell^2} \quad (30)$$

From Equations 28 and 29 it thus follows that if $(\alpha\tau/\ell^2) \ll 1$ then surface temperature fluctuations also will be quite small. This is evident if the exponentials in Equations 28 and 29 are expanded so that the following equation is obtained

$$\frac{T_{s_{\max}} - T_{s_{\min}}}{(cq_w \ell / k)} = \frac{2}{c} \sum_{n=1}^{\infty} p_n \left[\frac{\alpha \tau}{\ell^2} \beta_n^2 c (1 - c) + \left(0 \frac{\alpha \tau}{\ell^2} \beta_n^2 \right)^3 \right] \quad (31)$$

where $cq_w \ell / k$ is the temperature drop through the plate if the heat pulses are replaced by a steady heat flux cq_w . The series (Equation 31) is only carried to n_ℓ such that for $n \leq n_\ell$, $\alpha \tau \beta_n^2 / \ell^2 \ll 1$. For $n > n_\ell$ the series expansion of the exponentials in Equations 28 and 29 no longer will be valid. If n_ℓ is sufficiently large the portion of the series (Equations 28 and 29) with $n > n_\ell$ will be negligible since $p_n \sim 1/\beta_n^2$. In that case Equation 31 provides a good approximation of the amplitude of the temperature fluctuation.

A specific example will be considered. Assuming, somewhat arbitrarily, that it is necessary that

$$\frac{\alpha \tau \beta_n^2}{\ell^2} < 0.01$$

for Equation 31 to be valid, and that n_ℓ is such that $\beta_n^2 \approx 10$ it follows that the condition

$$\frac{\alpha \tau}{\ell^2} < 0.01$$

must be satisfied. In such case the dimensionless temperature fluctuation given by Equation 31 will be approximately .025 since

$$p_n \sim \frac{1}{\beta_n^2} : \quad n_\ell \sim 2$$

Thus the surface temperature fluctuation is essentially negligible. Now assuming a brass plate with $\alpha = 3.6 \times 10^{-4} \text{ ft}^2/\text{sec}^2$ and using the value of τ found in Section C,

$$\alpha^* = 8.2 \times 10^{-8} \text{ ft}^2$$

so that for

$$l \geq 2.87 \times 10^{-3} \text{ ft} = .034 \text{ in.}$$

surface temperature fluctuations will be negligible.

Phillips analysis leads to the conclusion that in most cases the time varying heat flux may be replaced by an average steady value. The only exception to this result will arise if cooling system designs with very thin chamber walls are considered. If temperature fluctuations are neglected the surface temperature is given by

$$T_s - T_0 = \bar{q}_w \left(\frac{l}{k} + \frac{1}{h} \right) \quad (32)$$

where the film coefficient h reflects the cooling system design.

Assuming a steady heat input, the time required for the combustion chamber surface of an uncooled engine to reach the melting temperature was computed. For this purpose the solution for the semi-infinite solid with a constant surface heat flux, which is given by Carslaw and Jaeger⁵⁰, was used. Using the average heat flux

$$c\bar{q}_w = \frac{1}{3} (2700) = 900 \text{ Btu/ft}^2 \text{ sec}$$

calculated in Section C it was found that the surface temperature rises from 540°R to 2160°R , the melting temperature of brass, in 2 seconds.

E. THE EFFECT OF DISSOCIATION AND RECOMBINATION ON HEAT TRANSFER

In this section the effects of dissociation and recombination and of fuel-oxidizer mixture ratio upon the heat transfer have been investigated. As mentioned earlier, the recombination of dissociated species which are present behind the detonation can result in an appreciable increase in the heat flux across the boundary layer

In a dissociating gas, energy is transported not only by conduction but also by the diffusion of atomic species. The heat flux across a boundary layer in a dissociated gas may be increased by the recombination of atomic species within the boundary layer and by diffusion of atomic species from the free stream to the cold wall where, in most cases, recombination with heat release occurs. When the Lewis number, $Le = (C_p D\rho)/k$, is unity the heat transfer across a boundary layer in contact with a cold, catalytic wall is proportional to the difference between the free stream and wall enthalpies regardless of the energy transfer mechanism⁵¹. The enthalpy of course must include the chemical heat of formation.

For a preliminary estimate of the increase in heat transfer due to dissociation it has been assumed that $Le = 1.0$. Consequently, it has been possible to use the boundary layer heat flux results used earlier, the only change being in the calculation of the enthalpy difference across the boundary layer.

The heat flux to the wall also depends upon the ratio of hydrogen to oxygen in the explosive mixture into which the detonation propagates. Consequently, calculations of wall heat flux have been made for $0.40 \leq X_{H_2} \leq 0.80$ where X_{H_2} is the mole fraction of molecular hydrogen. The composition of the combustion products at the Chapman-Jouguet plane have been computed by Moyle³⁸ and his results, which were used in the calculations, are reproduced in Figure 15.

The heat flux, q_w , as computed earlier is evaluated by means of Equation 6 with τ_w , the shear stress at the wall given by Equation 9, where the subscript in indicates that ρ and μ are calculated at the temperature corresponding to the Eckert reference enthalpy, h_m , obtained by Equation 8.

The free stream enthalpy per unit mass of gas consisting of the constituents of the equilibrium mixture at the Chapman-Jouguet plane was computed according to the equation

$$h = \frac{1}{\bar{W}} \sum_{i=1}^n X_i \left[H_i, T_e - H_i, 298.16^\circ K + \Delta H_f^0 \right] \quad (33)$$

where \bar{W} is the average molecular weight of the mixture given by

$$\bar{W} = \sum X_i W_i$$

and the enthalpies and standard heats of formation have been taken from the tables in Penner⁴⁶. The recovery enthalpy of the turbulent boundary layer was once again computed according to Equation 7. In computing the reference temperature from h_m it was assumed that the fluid composition was the same as in the free stream. The validity of this assumption is somewhat questionable and must be studied further.

A wall temperature of $900^\circ R$ was assumed. Since dissociation is negligible at this temperature the gas at the wall will consist of H_2 and H_2O for the rich mixtures and O_2 and H_2O for the lean mixtures.

The results of the calculations described above are presented in Table 12 and in Figure 16. It can be seen that the heat flux values computed by taking dissociation into account are about 35% more than the non-dissociative value. The maximum heat flux occurs for a fuel-rich mixture with $X_{H_2} = 0.75$ or a ratio of oxidant to fuel weight of 5.3. Again assuming that the heat pulse lasts for only one third of the period between the passage of successive waves, the maximum value of the overall heat flux, \bar{Q}_w , to the walls of the annular motor at $X_{H_2} = 0.75$ becomes

$$\bar{Q}_w|_{max} = 1660 \text{ Btu/ft}^2 \text{ sec} = 11.5 \text{ Btu/in}^2 \text{ sec}$$

TABLE 12. THE VARIATION OF DETONATION PARAMETERS
AND HEAT FLUX WITH MIXTURE RATIO

X_{H_2}	V_D	T_e	q_w , No Dissociation	q_w , With Dissociation
	ft/sec	o_R	Btu/ft ² sec	Btu/ft ² sec
0.40	6,879	5893	1493 $\frac{1}{x}^{1/5}$	1902 $\frac{1}{x}^{1/5}$
0.50	7,672	6314	1819	2589
0.60	8,620	6510	2135	3298
0.76	10,758	6484	2723	3776
0.80	11,262	6267	2683	3337

X_{H_2} = mole-fraction of H_2
 V_D = detonation velocity
 T_e = temperature behind the detonation
 q_w = heat flux at the wall
 x = distance behind detonation (ft)

For the mixture with $X_{H_2} = 0.60$, which was used earlier the overall heat flux density would be

$$\bar{Q}_w|_{X_{H_2}=0.60} = 1480 \text{ Btu/ft}^2 \text{ sec} - 10.2 \text{ Btu/in.}^2 \text{ sec}$$

It is interesting to compare the above values of \bar{Q}_w to the nozzle throat heat flux of $9.95 \text{ Btu/in.}^2 \text{ sec}$ computed by Curran, et al⁵² for a conventional H_2-O_2 1000-lb thrust rocket for a mixture with $X_{H_2} \approx 0.84$ (corresponding to maximum specific impulse). Thus the heat flux of the RDWE is of the same order as the throat heat flux of a small conventional engine, and this is still in essential agreement with the conclusion reached in Section C.

Nevertheless, the calculations above indicate basic differences between the RDWE and conventional rocket motors. For a given mixture ratio the temperature behind a detonation is higher than in a conventional combustion chamber with a corresponding increase in the dissociation of the combustion products. This can be seen from Figure 17 which shows the variation of T_e , the temperature behind the detonation and T_c , the temperature in a conventional 300 psia combustion chamber⁵⁹ with X_{H_2} . At the mixture ratio for which I_{SP} , the specific impulse of a conventional engine is a maximum, T_c is about 1000°F lower than T_e . The dissociation behind the detonation is thus sufficient to cause an appreciable increase in the heat flux, as is shown by the calculations above. Even though the temperature T_e reaches a maximum value near the stoichiometric composition with $X_{H_2} = 0.667$, the velocity difference, $(V_D - V_e)$, across the wave continues to increase as X_{H_2} increases. Since heat flux increases with both $(V_D - V_e)$, and $(h_r - h_w)$, the maximum heat flux occurs with a rich mixture, $X_{H_2} \approx 0.75$, rather than occurring near the stoichiometric mixture ratio, $X_{H_2} = 0.667$.

V. EXPERIMENTAL STUDY OF THE EFFECT OF LOW TEMPERATURE AND HIGH PRESSURE ON THE DETONATION VELOCITY OF H₂-O₂ MIXTURES

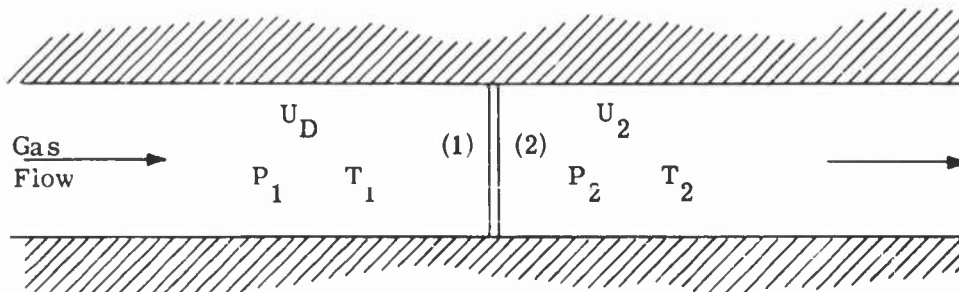
A. INTRODUCTION

The propellants of the rotating detonation wave engine can be injected into the combustion chamber in a gaseous state with temperatures near the oxygen vapor saturation point. However the detonation velocity of the hydrogen-oxygen propellants have never been determined at such low temperatures (110°K). Furthermore the velocity of detonation is a critical parameter in the design of the rotating detonation wave engine. Theoretical calculations of detonation velocity at these low temperatures and high pressures can conceivably be in error because of imperfect gas effects and lack of thermodynamic data. Experimentally, Moyle³⁸ obtained data on detonation velocities for hydrogen-oxygen mixtures at one atmosphere initial pressure and initial temperatures of 160°K to 500°K. Gealer⁵³ obtained data for room temperature H₂-O₂ mixtures over an initial pressure range of 1 to 68 atmospheres.

The purpose of this experiment is to obtain the detonation velocity of hydrogen-oxygen mixtures for use in the rotating detonation wave engine design over a range of initial temperatures from room temperature to the oxygen vapor saturation point (~ 110°K) and initial pressures of 1 to 15 atmospheres. Stoichiometric and hydrogen-rich mixtures were considered of primary interest.

The design of this experiment has been greatly facilitated by Moyle³⁸ who showed that the detonation velocity for a mixture in a coiled tube is essentially the same as that for a straight tube (if the experiment is at ambient temperature and pressure).

The notation used throughout this section will be as shown below, utilizing a wave-fixed coordinate system with (1) representing the undisturbed gas and (2) the conditions behind the detonation wave (at the Chapman-Jouguet plane, i. e., $M_2 = 1$).



B. TEST EQUIPMENT

A photograph of the test setup is shown in Figure 18 and a schematic of the test setup is presented in Figure 19. Mixing reservoirs were located in a blast proof pit outside the test room. The experiments were performed in a coiled tube shown in Figure 20. A straight tube was used to check the mixture ratio during the tests.

The velocity of the detonation wave was measured electronically by utilizing the ionized gases behind the detonation wave to trigger a time interval counter. This was accomplished by means of an ionization probe (Figure 21) as an input to a thyratron circuit. A schematic view of the velocity measurement system is shown in Figure 22.

The detonation coil was made of stainless steel tubing, 0.25 in. I.D., 0.50 in. O.D., 20 feet long and coiled in a 10 in. diameter. Three ionization probes were spaced 6 feet apart with 8 feet of coil before the first ionization probe. The straight detonation tube was also 0.25 in. I.D. stainless-steel tubing.

The hydrogen-oxygen mixtures were cooled to low temperatures in the following way. A double-walled stainless steel vessel was fabricated. This vessel was filled with a liquid with the lowest freezing point commercially available—isopentane (112°K). The isopentane was then cooled by bubbling liquid nitrogen through it, and then the detonation coil was immersed in the bath. Originally it was planned to obtain temperatures below 112°K by using liquid nitrogen under pressure as the liquid for the bath. This turned out not to be feasible because the detonation coil had to be removed from the bath after each run for reasons discussed later.

The temperature of the bath and the mixture were measured by four thermocouples in the bath and three thermocouples located in the detonation coil as shown in Figure

A model airplane type glow plug was used to ignite the mixtures.

C. METHODS AND PROCEDURES

The procedure for obtaining a single data point consisted of first bringing the detonation coil to room temperature, purging it with gaseous nitrogen, replacing the blow-out diaphragm and drawing a vacuum long enough to insure that the detonation coil was completely dry. Then the coil was immersed in the bath and allowed to come to the temperature of the bath. Finally the desired $\text{H}_2\text{-O}_2$ mixture was cooled to the bath temperature in a matter of seconds. Then the mixture was ignited.

This procedure had to be followed for each run; thus the test procedure was rather time consuming. It was found that the combustion products (water) froze on the walls of the detonation coil, and that unless the water was removed, erroneous results were obtained on the next run. Several methods were tried to eliminate the ice without removing the coil from the bath including a helium shock tube driver (gaseous piston), but due to the extremely rapid freezing process and the minute vapor pressure of ice at low temperatures these attempts were not successful.

A critical part of the experiment was the determination of the actual mixture ratio of H_2 - O_2 used for a test. This was done by measuring the detonation velocity of a given mixture at one atmosphere and 20°C in a straight detonation tube and comparing the result with the extensive data compiled by Moyle³⁸ and verified for stoichiometric mixtures in this experiment by partial pressure mixing; see Figure 23.

D. TEST RESULTS

The results of the experiments are presented in Table 13. The results of detonation velocities for fully developed (Chapman-Jouguet) waves versus initial temperature of the mixture for initial pressures of 1, 5, 10, 15 atmospheres and 0.500, 0.667, 0.730 and 0.800 mole-fractions of hydrogen are plotted in Figures 24, 25, 26 and 27. The emphasis was placed on mixture ratios of 0.667 and 0.730 for motor design considerations. A cross-plot of detonation velocity versus mole-fraction of hydrogen is shown in Figure 28 for 10 atmospheres initial pressure. The data for stoichiometric mixtures was taken over an extended period of time and with mixtures slightly different than stoichiometric. This data was corrected as shown in Table 13 in order to base these runs on a true stoichiometric mixture. The data for mole-fractions of $H_2 = 0.80$ has a somewhat higher variation in mixture ratio ± 0.01 because at one atmosphere initial pressure the mixture could not be detonated; therefore, the extensive data of Moyle³⁸ at 1 atmosphere initial pressure could not be utilized to determine the more exact mixture ratio.

E. DISCUSSION OF TEST RESULTS

The test results indicate that for a given initial pressure the detonation velocity increases at a slightly greater than linear rate as the initial temperature is lowered down to the saturation point of oxygen. The results for stoichiometric H_2 - O_2 mixtures are compared with the theoretical results³³ of Zeleznik and Gordon¹⁸ and with the previous data of Gealer³³ and Moyle³⁸ in Figure 29.

TABLE 13

EXPERIMENTAL DETONATION VELOCITIES OF H₂ - O₂ MIXTURES
AT REDUCED INITIAL TEMPERATURES AND INCREASED INITIAL PRESSURES

Tube I. D. = 1/4 in.

Coil I. D. = 1/4 in.

$$X_{H_2} = 0.500 \pm .005$$

Run No.	P ₁ (atm)	T ₁ (°K)	Time in Tube (μ-sec)	Time in Coil (μ-sec)	U _D (ft/sec)
41	1	293	399		7519
42	1	293	398		7538
43	1	293	400		7500
45	1	113		778	7712
46	1	126		781	7682
47	1	134		785	7643
48	1	148		784	7653
50	1	178		792	7575
51	1	197		795	7547
52	1	293		806	7444
53	1	293		808	7425
54	1	293		807	7434
55	1	217		798	7518
56	1	228		799	7509

TABLE 13 (continued)

$$X_{H_2} = 0.667 \pm .0025$$

(Note: Corrected data based on 330 μ -seconds in straight tube (9090 ft/sec) as the correct time for $X_{H_2} = 0.667$.)

Run No.	P_1 (atm)	T_1 (°K.)	Time in Tube (μ -sec)	Time in Coil (μ -sec)	U_D (ft/sec)	Corrected Time (μ -sec)	Corrected U_D (ft/sec)
1	1	293	327		9174		
2	1	293	328		9146		
3	1	293	327		9147		
5	1	293		656	9146	662	9063
6	1	293		656	9146	662	9063
7	1	293		656	9146	662	9063
8	1	293		654	9176	660	9091
9	1	293	323		9288		
10	1	293	323		9288		
11	1	197		642	9345	656	9146
12	1	293	324		9259		
13	1	208		642	9345	654	9176
14	1	293	325		9231		
15	1	217		643	9331	653	9188
16	1	225		644	9316	654	9176
17	1	220		645	9302	655	9160
18	1	293	324		9259		
19	1	169		638	9404	650	9231
20	1	111		623	9630	635	9449
21	1	130		629	9538	641	9360
22	1	169		639	9389	651	9217
23	1	186		641	9360	653	9188
24	1	199		641	9360	653	9188
28	1	263		652	9202	664	9036
33	1	113		625	9600	637	9419
73	1	293	325		9231		
74	1	293	325		9231		
77	1	293	326		9202		
78	5	284		615	9756	625	9600
79	5	284		616	9740	626	9585

TABLE 13 (continued)

Run No.	P ₁ (atm)	T ₁ (°K)	Time in Tube (μ-sec)	Time in Coil (μ-sec)	U _D (ft/sec)	Corrected Time (μ-sec)	Corrected U _D (ft/sec)
83	5	251		613	9787	623	9631
84	5	116		597	10,050	607	9884
85	5	140		600	10,000	610	9834
86	5	155		605	9917	615	9756
87	5	165		605	9917	615	9756
88	5	115		596	10,066	606	9900
90	5	184		605	9917	615	9756
91	5	217		610	9834	620	9677
57	1	293	327		9174		
58	1	293	327		9174		
59	1	293	327		9174		
60	10	183		593	10,118	599	10,017
66	1	293	326		9202		
67	1	293	327		9174		
68	10	173		592	10,135	599	10,017
69	10	143		590	10,169	597	10,050
70	10	122		587	10,221	594	10,101
71	10	289		608	9868	615	9756
72	10	114		588	10,204	595	10,084
73	1	293	325		9230		
74	1	293	326		9230		
80	10	284		604	9933	614	9772
81	10	284		603	9950	613	9788
82	10	246		602	9966	612	9804
89	10	117		585	10,256	595	10,084
126	1	293	327		9174		
127	1	293	326		9202		
128	1	293	327		9174		
129	1	293	326		9202		
130	15	288		601	9983	608	9868
131	15	288		601	9983	608	9868
132	15	125		584	10,274	591	10,152
133	15	134		586	10,239	593	10,118
134	15	153		590	10,160	597	10,050
135	15	164		588	10,204	595	10,084
136	15	209		594	10,101	601	9983

TABLE 13 (continued)

$$X_{H_2} = 0.730 \pm .005$$

Run No.	P ₁ (atm)	T ₁ (°K)	Time in Tube (μ-sec)	Time in Coil (μ-sec)	U _D (ft/sec)
25	1	293	301		9967
26	1	293	300		10,000
27	1	293	299		10,033
29	1	293		602	9966
30	1	293		604	9934
31	1	293		604	9934
32	1	293		604	9934
34	1	129		578	10,381
35	1	152		583	10,201
36	1	158		587	10,221
37	1	174		589	10,186
38	1	193		591	10,152
39	1	203		591	10,152
40	1	222		595	10,084
44	1	113		572	10,489
92	1	291	300		10,000
93	1	291	299		10,033
94	1	291	299		10,033
95	1	291	300		10,000
96	5	291		578	10,381
97	5	291		578	10,381
104	5	113		559	10,733
105	5	118		559	10,733
106	5	137		561	10,695
107	5	155		563	10,657
109	5	203		567	10,582
98	10	291		563	10,657
99	10	291		563	10,657
100	10	138		549	10,929
101	10	161		552	10,861
102	10	120		548	10,949
103	10	118		547	10,969
108	10	197		556	10,791

TABLE 13 (concluded)

$$X_{H_2} = 0.80 \pm .01$$

Run No.	P ₁ (atm)	T ₁ (°K)	Time in Tube (μ-sec)	Time in Coil (μ-sec)	U _D (ft/sec)
110	10	291	263	11, 407	
111	10	291	264	11, 364	
112	5	291	267	11, 236	
113	5	291	267	11, 236	
114	5	291	267	11, 236	
115	10	291	263	11, 407	
116	10	288		527	11, 385
117	10	288		527	11, 385
118	10	288		526	11, 407
119	10	116		516	11, 628
120	10	119		516	11, 628
121	10	133		516	11, 628
122	10	148		520	11, 538
123	10	163		520	11, 538
124	10	203		521	11, 516

In comparing theory with experiment it should be noted that the size of the detonation tube has a significant effect on the velocity so that the measured velocity is less than that predicted by the Chapman-Jouguet plane wave theory. Fay⁵⁴ has proposed that this velocity deficit is caused by a viscous boundary layer on the tube wall within the reaction zone. On the basis of a two-dimensional analysis, Fay obtains the following expression for the velocity deficit, ΔU_1 :

$$\frac{\Delta U_1}{U_1} = \frac{2.1 \sigma^*}{D}$$

where

$$\sigma^* = 0.22 (t)^{0.8} \left(\frac{\mu_e}{\rho_1 U_1} \right)^{0.2}$$

and where

D = diameter of tube in centimeters

σ^* = boundary layer displacement thickness

U_1 = propagation velocity of the detonation wave

t = thickness of reaction zone

μ_e = viscosity of the gas in the combustion zone at outer edge of boundary layer

ρ_1 = initial (upstream) density

For the stoichiometric hydrogen-oxygen reaction at one atmosphere pressure and room temperature Fay suggests the values $t = 0.35$ cm and $\mu_e = 12.3 \times 10^{-4}$ gm cm⁻¹ sec⁻¹. For application to this experiment we assume that the thickness of the reaction zone (t) is primarily determined by a recombination reaction so that t is inversely proportional to the square of the initial pressure. Also we assume that μ_e does not vary significantly with initial pressure and temperature.

The results of the velocity deficit calculations are shown in Table 14. With this correction good agreement between theory and experiment is obtained at low pressures. At higher pressures a significant variation between theory and experiment is apparent that cannot be accounted for by the tube size effect. It is possible that imperfect gas effects (not considered in the theoretical calculations of Ref. 18) can be the major cause of this discrepancy.

The predicted experimental pressure rise across a Chapman-Jouguet detonation wave may be calculated very simply once the detonation velocity is known by using the following well-known momentum relation developed from one-dimensional perfect-gas considerations:

TABLE 14. RESULTS OF VELOCITY DEFICIT CALCULATIONS
USING THEORY OF REFERENCE 54

P_1 (ATM)	T_1 ($^{\circ}$ K)	$\frac{\Delta U_1}{U_1}$ (%)	U_1 (ft/sec)
1	293	3. 1	280
	200	2. 9	265
	110	2. 6	240
5	293	0. 17	17
	200	0. 16	16
	110	0. 14	14
10	293	0. 049	5
	200	0. 046	5
	110	0. 040	4
15	293	0. 024	2
	200	0. 022	2
	110	0. 019	2

$$\frac{P_2}{P_1} = \frac{1 + \frac{U_D^2 \bar{m}}{R_0 T_1}}{1 + \gamma_2}$$

where \bar{m} is the average molecular weight of the undisturbed gas

R_0 is the universal gas constant

and γ_2 is the ratio of specific heats behind the detonation wave (which from theory¹⁸ is nearly constant)

The results of this calculation, shown in Figure 30 for stoichiometric H₂-O₂ mixtures indicate that a mixture initially at 10 atmospheres and 120°K will produce a peak pressure of 7,900 psia behind the wave.

VI. EXPERIMENTAL STUDY OF THE EFFECT OF CURVATURE AND CONFINEMENT ON DETONATION WAVES IN ANNULAR CHANNELS

A. INTRODUCTION

Inasmuch as the detonation waves moving around the chamber of the RDWE have certain geometrical effects imposed on them that are different than the system effects imposed on detonations in straight tubes it was decided that a study of some of these effects be made in an idealized experimental system wherein other more complex phenomena would be eliminated. Two of these effects that were chosen to be studied separately and in combination were

- (1) The effect of curvature. Detonations moving in a channel with a finite radius of curvature have in addition to centrifugal forces imposed on the high velocity gases behind the waves, a longer distance to travel around the outer radius of the annulus than along the inner radius. Due to this effect, the stability of Chapman-Jouguet type detonation normally measured in straight tubes might be affected.
- (2) The effect of confinement. Detonations moving in channels without complete confinement, i. e., with one of the walls removed allowing a lateral expansion of the high pressure gases immediately behind the wave simulate to some degree the actual confinement occurring in the actual annular chamber of the RDWE. This problem was studied in this laboratory by Sommers⁵⁵ and Dabora³⁹ in straight tubes and it exhibited such a significant effect on the detonation process in straight tubes that it was believed necessary to assess its effect, at least qualitatively, on detonations in curved channels.

To this end experiments were performed using the three following different geometrical configurations all possessing the same radius of curvature (3.75 inches) as the small annular motor described in Section VII of this report:

- (1) A curved channel with the cross-sectional dimensions of $1/2 \times 3/8$ inch with a radius of curvature of 3.75 inches having complete confinement, i. e., solid walls.
- (2) A curved channel with the same dimensions as in (1) above except with the elimination of the inner wall allowing a two-dimensional expansion (lateral relief) of the burned gases behind the wave in the inward, radial direction. Provision is made for the placement of a thin nitrocellulose film along this inner wall separating the unburned gases from the atmosphere

- (3) The same channel dimensions as in (1) and (2) above with one window removed so that the relief is in the axial direction.

The majority of the experiments utilized a stoichiometric mixture of hydrogen and oxygen.

B. EXPERIMENTAL TEST EQUIPMENT

A schematic diagram of the basic test section with solid walls is shown in Figure 31. A photograph of the test section is shown in Figure 32. The curved section includes 270°. Provision is made for the removal of the inner wall for the full 270°.

A different section including only 90° was utilized for some of the studies of detonations with inward, radial relief. This section has provision for a thin membrane. Details of the construction and film preparation is given in References 7 and 39.

Each curved test section, when used, is attached to a straight detonation tube driver section of the same cross-sectional dimensions as the curved sections. The straight driver section is nine feet long to insure a fully developed detonation wave before entry into the curved section. A miniature glow plug is used for ignition purposes. A schematic diagram of the basic system appears in Figure 33.

C. EXPERIMENTAL PROCEDURE

The experiments performed in the test section with the solid walls is obtained in the following manner. A diaphragm is used to seal the end of the test section, and the tube and test section are evacuated by means of a vacuum pump. Then the H₂-O₂ mixture is introduced into the tube and test section from a vessel containing the pre-mixed combustible gases. This vessel is not shown in Figure 33. The mixture is then ignited.

The experiments performed in the sections employing lateral relief are made in either of two ways

- (1) The H₂-O₂ mixture from the vessel containing the pre-mixed gases is allowed to flow slowly through the straight tube and test section for at least one minute to purge the air and other gases completely. The valve to the pre-mixed gas vessel is closed and the end of the test section is sealed immediately with masking tape. The mixture is then ignited.
- (2) A flowing system of H₂-O₂ is introduced continually through a mixing tee (Figure 33) and metered by means of sonic orifices in each line. The mixture is ignited with the system flowing. This method was also employed when utilizing the test section with solid walls for reasons discussed later.

For each method, the detonation velocity is measured in the straight tube by means of ionization probes. In addition, the time interval to the spark light discharge is also measured. Two CMC, Model 757 BN time interval counters are employed for the two measurements. To photograph the waves, a schlieren system is used employing six inch diameter mirrors instead of the lens system shown (for simplicity) in Figure 33. The effective exposure time for the high-voltage, capacitor-discharge light source is approximately $0.1 \mu\text{-sec}$.

D. RESULTS

Because of the presence of small leaks, the final experiments utilizing the test section with solid walls employed the flowing system for consistency of results.

In addition, for the experiments employing lateral relief, the method of charging the tube by first purging and then sealing the end was found undesirable because it was determined that the unburned mixture partially diffuses through the thin membrane in the time interval of about three seconds between the closing of the valve and ignition. This effect was determined by noting that the degree of wave curvature could be changed by varying the aforementioned time interval.

For this reason the following experiments were performed employing the flowing system. Figure 34(a) shows a typical schlieren photograph of a detonation wave with inward radial relief provided by utilizing a thin nitrocellulose membrane on the inner wall. The wave curvature is quite similar to a wave shown in Figure 34(b) propagating in the curved channel with solid walls. Note that the direction of travel is different for the two waves, i.e., the wave in Figure 34(b) is moving counter-clockwise. On the premise that the degree of wave curvature near the relief boundary is a measure of the degree of confinement of the wave³⁹, it is concluded that the confinement provided by the thinnest nitrocellulose membrane successfully employed is essentially the same as that provided by the solid walls. It is for this reason that the experiments performed utilizing the membrane were not carried out to a more definitive conclusion *

*The reader is referred to the work of Dabora³⁹ for a comprehensive study of this confinement effect utilizing extremely thin (230 Å) membranes.

A composite distance versus relative time plot of stoichiometric H₂-O₂ detonation waves in the solid walled curved section employing a flowing system is shown in Figure 35. The distance as shown is obtained by measuring the wave position along the outer wall. It is apparent due to the linear nature of the average of the experimental data that the wave velocity is constant throughout the curved section. The wave velocity obtained from the slope of the average line is 9762 ft/sec. From similar plots the velocity on the inner wall and on the center line are 8541 ft/sec and 9152 ft/sec respectively. The average wave velocity measured in the straight tube before the curved test section is 9159 ft/sec, a value very close to that observed along the center line of the curved section.

A schematic drawing showing the essential features of a typical detonation wave in a curved channel is shown in Figure 36, obtained from typical schlieren photographs similar to Figure 34(b). Two interesting effects are shown in addition to the curvature of the wave from the radial direction. First, it is noted that stria exist in the burned gases behind the wave, a characteristic typical of detonations. Also observable are multiply-reflecting shock waves emanating initially from the outer wall intersection with the detonation wave front. It is apparent that such a reflected wave must accompany an oblique shock wave in steady flow. Upon close scrutinization of many original photographs it appears that the observed stria indicate the approximate direction of the streamlines in the burned gases because they are deflected in the same manner as that predicted by two dimensional oblique shock theory. It is concluded therefore that the observed shock system (which does not dissipate with the distance travelled by the wave in the curved tube) is a characteristic of a steady state detonation in a curved channel.

It is of interest to calculate the theoretical pressure gradient in the radial direction. This quantity is represented by the following relation:

$$\frac{\partial P_2}{\partial r} = \frac{\rho_2 V_2^2}{r} \quad (1)$$

where P₂, ρ₂ and V₂ are the pressure, density and absolute gas velocity in burned gases immediately behind a detonation wave. Using theoretical values for the properties behind a stoichiometric, C-J detonation (initially at 1 atmosphere and room temperature), a value of 63.5 psi/inch is obtained using relation (1). Utilizing the experimental distance of 1/2 inch between the outer and inner wall, a value of about 32 psi is obtained for the overall radial pressure differential theoretically predicted using the 1/2 inch section. It is to be noted that this differential is about 12% of the theoretically predicted pressure, P₂, of 276 psia immediately behind a one-dimensional detonation.

Another method can also be used to predict the radial pressure gradient behind a detonation in a curved channel by utilizing the momentum equation across the wave,

$$\frac{P_2}{P_1} = \frac{1 + \gamma_1 M_1^2}{1 + \gamma_2 M_2^2} \quad (2)$$

where M_1 and M_2 are the Mach number in the unburned and burned cases respectively for a one-dimensional wave. The Mach number normal to the wave which is required by this relation can be obtained from measurements of the wave angle at points along the wave. It was determined from the experiments that the angular deviation of the wave from the radial direction varied from zero at the inner wall to 16.4° at the outer wall. Using relation (2) above, the pressure differential across the channel is calculated to be about 47 psi which compares favorably with the value of 32 psi predicted by Equation 1.

Other tests were made utilizing the 270° curved test section with the inner wall removed and using a flowing stoichiometric mixture of H_2-O_2 . Figure 37 is a schlieren photograph of a typical detonation wave in this system. The wave is approximately 250° from the beginning of the curved section. Because of the lack of detail on the photograph, Figure 38 is included as a sketch of the essential details. With the flowing system utilized, a high concentration of combustible mixture is maintained apparently due to centrifugal effects allowing the detonation wave to be sustained. Although some mixing must be occurring between the unburned mixture and the atmosphere, the effect must be small, at least near the beginning of the curved section. Also just visible in Figure 37 is the first reflected wave originating from the intersection of the detonation wave and the outer wall. Multiple reflected shock waves are not observed due to the absence of a reflection from the gaseous interface between the burned gases and the atmosphere.

Figure 39 shows a distance versus relative time plot from a limited number of waves. Again, in a manner similar to the case with the tube having solid walls, the velocity (slope) of the average curve seems to be linear. However, in comparing the detonation velocity at the channel centerline with the velocity obtained previously with a solid wall inner boundary, the velocity obtained with the inner wall removed appears to be about 7.5% lower over the complete length of the curved section. This is rather surprising inasmuch as it would appear that the mixing effect between the unburned gases and the atmosphere would become progressively more noticeable as the wave moves into the curved section. From the experiments, apparently this effect is not

measurable over the distance involved, and the degradation of about 7.5% in the detonation wave velocity is actually due primarily to the relief effect of the unconfined gases behind the detonation wave. It is to be noted that certain theoretical and experimental results of the related study³⁹ tend to support these observations.

Figure 40 shows a schlieren photograph of a detonation wave propagating in a channel with one window removed so that in effect an expansion of the burned gases takes place in the axial direction. The wave has passed through the first four inches of the curved section. It is apparent from the photograph that the detonation wave has degenerated into a curved shock front followed by the combustion zone (indicated by the turbulent region beginning about 1/4 inch behind the initial shock wave). It is quite possible that the detonation wave is in the process of being quenched due to the mixing processes which could be more pronounced for this case where centrifugal effects are not encountered in the same stabilizing manner as in the case with the inner wall removed.

E. CONCLUSIONS

- (1) In general it can be stated that in curved channels of rectangular crosssection (of the same approximate dimensions as that utilized here) detonation waves will propagate at velocities (measured at the channel centerline) equal to that observed in straight tubes, i. e., velocities very nearly those predicted theoretically for Chapman-Jouguet detonations.
- (2) With lateral relief on the inner wall, measured detonation velocities in the curved channel, utilizing nearly stoichiometric H₂-O₂ mixtures, appear to suffer a degradation of no more than 7.5% compared to the measured velocities of completely confined waves.

VII. EXPERIMENTS ON THE GASEOUS ANNULAR MOTOR AND THE LINEAR MOTOR

A. INTRODUCTION

A schematic diagram of the annular motor showing critical dimensions is presented in Figure 41 and a photograph of the nozzle end of the motor is shown in Figure 42. The propellants are injected at the upstream end of the combustion chamber and mixed by impingement. The ignitor (either a spark plug or a small detonation tube) generates a detonation wave which progresses around the annular combustion chamber and the burned gases are exhausted through the nozzle. The pressure at any given position in the chamber is thus time varying.

The design and initial testing of the annular motor was carried out at The University of Michigan in 1961. At that time funds allowed only a preliminary examination of the concept. The instrumentation utilized for diagnostic purposes was one Photocon pressure transducer with a $30 \mu\text{-sec}$ rise time and a 16 mm Fastax motion picture camera with a minimum framing period of 140 microseconds per frame. These early tests indicated that a detonation wave could be initiated in this annular test section. On the basis of the test data it was also believed that successive rotations of the wave occurred.

The design of the annular motor was based on the assumption that the detonation wave would propagate around the annulus with nearly the same characteristics as a Chapman-Jouguet detonation in a closed tube. The propellant was to be supplied from standard 2000 psi, 300 cubic feet cylinders, and the motor was to be operated within the laboratory. Hydrogen and oxygen were chosen as propellants in that they are convenient to handle and much is known about their detonation characteristics so that theory and experiment could be readily compared. The detonation velocity of near-stoichiometric mixtures of hydrogen and oxygen is about 10,000 ft/sec. The ideal operating condition of the detonation motor is such that the combustion chamber will always be filled with unburned gas just ahead of the detonation wave. Thus the propellant flow rates per cross-section of combustion chamber must be much greater than in a conventional rocket motor. And furthermore, if designed properly, the axial velocity of the unburned gas in the chamber will be greater than the turbulent flame speed (100-200 fps) so that theoretically deflagration after the detonation wave is minimized. In this regard there should be no protrusions in the combustion chamber which would tend to act as flame-holders. For safety reasons it was decided not to premix the hydrogen and oxygen, but rather to use discrete impinging injectors. The nozzle was designed to partially confine the detonation wave but still allow the combustion chamber to blow down to near ambient atmospheric pressure just ahead of the wave to minimize the mass flow requirements.

During the first part of this study the equipment used in the preliminary tests was completely reworked. The motor was mounted on a new test-stand. The propellant feed lines were modified and the propellant supply banks enlarged. Control equipment associated with the motor and with high-speed cameras was fabricated and installed. New pressure instrumentation for the motor was incorporated into the test setup.

The first part of the test program consisted of attempting to duplicate the earlier tests. In these tests it became apparent that multiple rotations of the wave were not occurring in spite of running all possible combinations which had been used in the earlier tests. These tests, utilizing either the detonation starter tube or a spark plug initiator, resulted in two detonation waves originating at the point of initiation in the annular combustion chamber of the motor. These waves propagated in opposite directions in the annulus and hence collided at a position approximately 180° from the point of ignition. The collision resulted in reflected shock waves which were rapidly attenuated and no subsequent pressure disturbances were observed. Photographs of this collision process taken with an 8 mm Fastax motion picture camera at approximately 70 microseconds per frame are shown in Figure 43. It should be mentioned that attempts to shield the spark plug and to place a thin metal diaphragm on a hinged mount across the combustion chamber near the point of initiation were not successful in stopping the generation of the "backward" propagating wave.

In view of these difficulties it was apparent that nothing could be learned from the annular motor until a unidirectional wave could be initiated. In order to investigate the starting problem more fully a linear model of the annular motor was built. The tests in this linear motor and subsequent tests in the annular motor will now be described in detail after first describing the test equipment, procedure, and instrumentation.

B. TEST EQUIPMENT AND INSTRUMENTATION

Two basic test configurations were used and are referred to here as the annular motor and the linear motor. Both test models used the same propellant sequencing system and similar instrumentation.

The annular motor, which was made of brass, consisted of five separate sections (as shown in Figure 41) for ease in changing geometry. Each section was sealed by means of "O" rings. The fuel and oxidizer were kept separate in the manifold and injected through small discrete orifices, impinging (like on unlike) in the combustion chamber. These injector orifices were removable and various sizes were used. For the majority of the tests the hole diameter of the fuel injectors was 0.017 inches and the hole diameter of the oxygen

injectors was 0.024 inches. Seventy-two injector pairs spaced 5° apart (0.326 inches apart along a 7.5 inch diameter circle) were used. The fuel and oxygen injectors were offset to the axial direction at 40° and $7\frac{1}{2}^{\circ}$ respectively so that the momentum balance upon impingement would yield a nearly axial velocity. The discharge coefficient for an individual injector was measured by allowing the gas to flow from a high pressure source through the injector and into an evacuated tank of known volume. Six tests of one hydrogen injector using hydrogen at 500 psi indicated that the discharge coefficient was 0.74 based on nominal hole size. Two tests of one oxygen injector using oxygen at 500 psi indicated a discharge coefficient of 0.80. It is felt that tests of the entire injector assembly should be made to obtain accurate results, but the above results indicate approximate values. All the mass flow rates and mixture ratios given in the section on test results are based on a discharge coefficient of unity.

Two different initiators were tried: a detonation tube starter and a spark plug. The detonation tube starter consisted of a 3/8 inch steel tube which was inserted through the wall of the combustion chamber and curved in a circumferential direction in the annulus. Gases were drawn from the propellant supply lines and mixed before passing a small spark plug as shown in Figure 42. The other method of initiation utilized was a flush mounted spark plug in the wall of the combustion chamber. The energy of the spark was less than 30 millijoules (due to line losses) obtained by discharging a 1 microfarad capacitor at 250 volts. The spark plug was used in all the later tests because it did not protrude into the combustion chamber.

A schematic diagram of the propellant feed system is shown in Figure 44. The fuel supply and oxygen supply consisted of six 300 cubic foot cylinders each at 2000-2400 psi. One-half inch steel tubing (3/8 inch inside diameter) led from the supply tanks through the Grove Powreactor Dome pressure controller (Model GBX-206-03) to the solenoid operated propellant valves (Marotta Model MV 36) and finally to the manifold of the motor (Figure 45). The desired manifold pressure level was set manually on the Grove pressure regulator before the run. The time that the solenoid valves were open and the timing of the spark were controlled by electronic time delay units. A typical oscillograph record of the sequence of events is shown in Figure 46. When the sequence button is pushed the propellant solenoid valves open and time delay units for the spark and valve shut-off events are initiated. The spark is timed to fire as soon as the manifold pressures in the motor have reached steady state values. The closing of the propellant valves is adjusted to allow about 10 milliseconds (approximately 50 rotations of a detonation wave) of steady state manifold pressure before shut-off.

It should be noted that with the injectors mentioned above and the oxygen supply cylinders at 2000 psi, a 700 psi drop from the oxygen supply bank to the oxygen manifold of the inotor was measured during a test run. This rather

large loss was traced to a 200 psi drop across the valves of the six supply bottles, a 400 psi drop due to friction in the 1/2 inch supply lines and a 100 psi drop across the Grove pressure regulator. Only about a 200 psi drop was measured in the hydrogen supply system.

The manifold pressure measuring (and thus mass flow and mixture ratio) instrumentation consisted of two Norwood, bonded-strain-gauge pressure transducers (Model 104) mounted in the inlet manifolds. The signals were dc amplified and displayed on a Visicorder type oscillograph.

The pressure-time history in the combustion chamber was measured with several high response Kistler quartz pressure transducers flush-mounted in the walls of the combustion chamber. The signals were amplified by electrostatic charge amplifiers and fed to an oscilloscope where they were again amplified and then displayed on the face of the scope. Polaroid pictures of the face of the scope were taken to record the data. A Model 601 Kistler transducer was used with a Kistler amplifier-calibrator as an indication of the position of the wave at a given time, but not to indicate the actual pressure level. Two Kistler 603 pressure transducers were used with Kistler charge amplifiers (Model 566 M) to determine the actual pressure-time history of the motor. The response and calibration of the 603 pickups was checked by testing them in a straight detonation tube. The results are presented in Figure 47. Figure 47a) shows an unmodified response to a Chapman-Jouguet detonation of a 40% hydrogen-60% oxygen mixture by volume. The second rise in the signal is due to a reflected shock off the closed end of the tube. The unmodified signal was unsatisfactory for diagnostic purposes because of the large oscillations and therefore a 27,000 ohm resistor was added in series to the input side of the charge amplifier in addition to a high frequency filter. As shown in Figure 47 the rise time of the modified signal is about 10 microseconds and the amplitude of the initial response has been reduced. Using the theoretical peak pressure behind the detonation wave of 250 psi, a sensitivity for the modified signal of 0.160 picocoulombs/psi was calculated (compared to the advertised sensitivity of 0.405 pCb/psi). It was found that the signal from a Kistler 603 pickup which was flush mounted in the motor or in the detonation tube would drift below the zero point several hundred microseconds after the passage of the wave. It was believed that this was a temperature effect and to eliminate the problem either scotch tape (.0005 in. thick) or silicone grease over the exposed end of the pickup was successfully used without changing the sensitivity. The grease would ablate and was replaced before each run in the motor tests.

High speed motion pictures of the exit plane of the motor were taken with two different cameras. During the earlier part of the studies an 8 mm Wolensak Fastax camera in conjunction with a Goose control unit (Model J-515) was utilized. The maximum framing rate was ~ 14,000 pictures per second.

Most of the photographic data was obtained with a Beckman and Whitley Dynafax camera, Model 326, using 35 mm Tri-X film which was developed in either Rodinol or Baumann Diafine. This camera obtained 224 frames with a frame separation time of 38.4 μ -sec, which was measured by means of a Computer Measurements counter-timer (Model 727 BN) with the input signal from a magnetic pickup. The effective exposure time used was four microseconds per picture. The open time of the capping-shutter was controlled with an electronic time delay unit sequenced to the motor operations. The available light from the detonation was sufficient with hydrogen rich mixtures and methane-oxygen mixtures, but was insufficient for lean hydrogen runs.

The motor tests were conducted in an isolation room which had one foot thick concrete walls with a glass viewing port. The instrumentation and propellant sequencing equipment were located outside the isolation room as shown in Figure 48. Since the propellant valves employed (particularly the oxygen valve) required about 200 milliseconds to fully open (see Figure 46), a considerable amount of propellant diffused into the test room before ignition. This excess propellant would then explode in the test room at the time of ignition of the motor thereby creating a brief but violent over-pressure in the room which was also hard on the equipment in the isolation cell. A large portion of the roof was removed before each run to minimize this problem.

As stated above the linear motor utilizes the same propellant feed system, test stand and instrumentation as the annular motor. The construction of the linear motor is similar to the annular motor, and may be visualized by cutting the annular motor along a radial line and forming it into a straight test section. The walls of the test section were removable so that metal or plexiglas could be used. A photograph of the linear motor on the test stand is shown in Figure 49, and an exploded view is shown in Figure 50. It was originally hoped that spark-schlieren photographs taken through the windows would be employed; however, two difficulties became apparent. First the plexiglas windows had to be changed after each run. Second, the test section was forced out of alignment due to the repeated detonations and thus high temperature glass such as Vycor could not be used. One condition not simulated in the linear motor was the injector spacing. The linear motor had 36 injector pairs spaced \sim 5/8 inch apart. The annular motor originally had 36 injector pairs but was modified to 72 injector pairs for the later portion of the tests described in this report.

C. TESTS IN THE LINEAR MOTOR

The purpose of the tests in the linear motor was to study methods of achieving a unidirectional wave which could be utilized in the annular motor. More specifically, the propagation of a detonation wave from the starter tube into the

motor was studied, and the idea of blocking several injectors adjacent to the initiator as a means of achieving a unidirectional wave was investigated. Finally, the use of a frangible diaphragm across the combustion chamber to confine the detonation wave was studied. One advantage of the linear motor over the annular motor was that the starting problem could be separated from the wave propagation problem. That is, by igniting the linear motor at one end a unidirectional wave is insured, and if a second wave is started from the same end about 200 microseconds after the first, it should be possible to simulate grossly the conditions for a "second rotation" of the wave in the annular motor. This experiment was also tried and will be described later.

The propagation of a detonation wave from the starter to the chamber was studied in linear motor configuration shown in Figure 51(a). Hydrogen and oxygen gas was conducted from the manifold to two small mixing orifices at the upstream end of the starter tube and the mixture was ignited with a spark plug. Optical studies of the wave propagation were conducted by means of spark-schlieren photographs. One of these photographs is shown in Figure 52. The detonation wave propagated out of the starter in a somewhat spherical fashion so that for a stoichiometric mixture in both the starter and the motor, a detonation wave is started readily in both directions. Notice that the forward moving wave has travelled approximately twice as far as the backward moving wave at the time of the photograph. No significant time delay was observed in transition from starter to motor. Also the bright areas in the left side of Figure 52 indicate that the starter tube may act as a flame holder. Schlieren studies were severely limited because the optical quality of the windows was destroyed after each run (e. g., Figure 53).

The propagation of a second wave down the linear motor at a distance of one test section length (24 inches) behind the first wave in order to simulate the second rotation of the detonation wave in the annular motor was studied in configuration b) of Figure 51. The starting tubes, which in this case were flush with the end of the test section, had thin diaphragms on the end and were filled with a premixed hydrogen-oxygen mixture. A spark was used to initiate the detonation wave. Ionization probes and a Kistler 603 pressure transducer were used to establish the wave patterns. (Optical study was not attempted because of difficulty with the windows.) Typical results from the linear motor configuration (b) tests are shown in Figures 54 and 55. Figure 54 is a modified Kistler 603 pressure recording of the starting pulses alone. In all of the tests a dc drift of the transducer occurred. Figure 55 shows pressure recordings of runs 15 and 16 which were conducted under the same conditions but with the pressure transducer in two different positions. If the second wave did detonate in the combustion chamber a sharp rise should be evident at 200 μ -sec, which is not indicated in Figures 55a or 55b. In Figure 55a a very weak pulse (from the starter tube) appears at about 200 μ -sec, while in Figure 55b the reflected shock off the end of the combustion chamber appears at about 625 μ -sec. A criticism

of these tests is that the second wave is emitted from a 1/4 inch ID tube, whereas in the annular motor the wave would start its second rotation filling the entire chamber. Also measurements of the detonation wave velocity in the combustion chamber were made with ionization probes. These measurements indicated that the first detonation wave travelled at nearly the same speed in the motor as in the starter tube. No significant time delay due to transition from starter to motor was observed.

The method of obtaining a unidirectional start by blocking injectors adjacent to the starter was investigated in the linear motor by blocking five injector pairs in the center of the test section. It was found that a detonation wave started at the edge of the blocked injector region was delayed from passing through the blocked injector region by 100 microseconds for a stoichiometric mixture with a mass flow of 0.45 pounds per second, while a detonation wave starting at the end of the test section was delayed about 50 microseconds by the blocked injector region. Since the blocked injector region must 'hold' for about 200 microseconds (in the annular motor) the number of blocked injectors must be increased. However since it is obvious that the number of blocked injectors must be increased even more as the mass flow is increased, it was felt that this method would not be satisfactory. It should be noted, however, that if an inert gas could be injected in a small region adjacent to the spark plug, this method might be successful. This was not attempted due to the complexities involved.

The final method of starting a unidirectional detonation wave which was investigated was to place a frangible diaphragm across the combustion chamber adjacent to the spark plug (configuration c) of Figure 51. The diaphragm should be strong enough to contain the wave from propagating 'backwards' for 200 microseconds but weak enough to burst rapidly when struck by a full strength detonation wave from the other side. The linear motor greatly simplified the initial study of the diaphragm burst problem because it insured a controlled experiment. The first problem encountered was the extreme difficulty in sealing the diaphragm to the combustion chamber. It was found that a detonation wave could be transmitted through even the smallest of leaks. The method used was to machine two 1/8 x 1/8 inch grooves in the walls of the combustion chamber and nozzle. The diaphragm material was glued or soldered to two steel diaphragm holders which were 1/16 inch thick and inserted in the grooves. A clearance of about 0.002 inch was allowed and cracks sealed with silicone grease. It was further observed that it was not sufficient just to block the combustion chamber but that the nozzle and the area outside the nozzle must be blocked also. This is the case because the spark ignition must be delayed to allow the solenoid valves to fully open thereby allowing propellant to flow out of the nozzle (i.e., into the room) and the detonation wave propagates in and outside the nozzle also. After it was established with pressure transducers and 8 mm Fastax motion pictures that the wave could be contained for at least

300 microseconds with a 1/8 inch plate, several thin diaphragm materials were tried. For example, cellulose acetate film 0.006 inch thick contained the detonation waves about 200 microseconds. The next step was to obtain a diaphragm suitable for the annular motor.

D. TESTS IN THE ANNULAR MOTOR

All of the tests described in this section used a frangible diaphragm across the combustion chamber adjacent to the spark. The spark plug initiator was used rather than the detonation tube starter because the spark plug was less of a protrusion into the combustion chamber. In all of these tests 72 injector pairs were used and the propellant mass flow was approximately one pound per second. The first phase of the tests was to choose the proper diaphragm material and thickness. After the diaphragm was chosen the ability of the annular motor to sustain multiple rotations of the detonation wave was investigated using hydrogen-oxygen mixtures and methane-oxygen mixtures and with several nozzle geometries.

Photographs of the diaphragm and external plate mounted in the annular motor are shown in Figures 56 and 57. In a manner similar to the linear motor, the diaphragm was secured to a diaphragm holder and the assembly inserted in grooves in the walls of the combustion chamber and sealed with silicone grease. Motion pictures with the Beckman and Whitley camera and Kistler pressure transducers were used to determine the behavior of the diaphragm after ignition. The cellulose acetate film diaphragm, which was strong enough in the linear motor, ruptured in less than 100 microseconds in the annular motor. Various materials and thicknesses were tested in the annular motor in order to find the proper design to contain the "backward" propagating wave, and the results are shown in Table 15. Difficulty was experienced in bonding the diaphragm material to the diaphragm holder; soft solder produced the only consistent bond. For hydrogen-oxygen mixtures 0.0015 inch brass and 0.0010 inch steel exhibited the best characteristics and this result was not affected significantly by variation of the mixture ratio. The 0.0010 steel diaphragm was chosen for the remainder of the testing with hydrogen-oxygen. When methane-oxygen was used it was found that the diaphragm thickness had to be changed for different mixture ratios due to the variation of the pressure ratio of CH₄-O₂ detonations with mixture ratio. For mixtures of less than 16% methane by volume the 0.0010 inch steel diaphragm was utilized and for mixtures of more than 33% methane the 0.0020 inch steel diaphragm was most satisfactory, while for all mixtures in between the 0.0015 inch steel diaphragm was selected.

TABLE 15. RESULTS OF DIAPHRAGM TESTS IN ANNULAR MOTOR
WITH HYDROGEN-OXYGEN

Diaphragm Material	Bond Material	Thickness (inch)	Remarks
Cellulose Acetate	Epoxy	0.0060	Too weak
Mylar	Epoxy	0.0075	Would not bond
Mylar	Epoxy	0.0050	Would not bond
Mylar	Epoxy	0.0030	Would not bond
Brass	Solder	0.0010	Too weak
Brass	Solder	0.0015	Satisfactory
Brass	Solder	0.0020	Too strong
Aluminum	Epoxy	0.0010	Too weak
Steel	Solder	0.0010	Satisfactory
Steel	Solder	0.0015	Too strong
Stainless Steel	Epoxy	0.0010	Would not bond
Stainless Steel	Epoxy	0.0008	Would not bond
Stainless Steel	Epoxy	0.0006	Would not bond
Titanium	Epoxy	0.0006	Too weak

Note: Unsupported diaphragm area $1\frac{1}{2} \times 2\frac{1}{2}$ inches. Diaphragm supported $\frac{1}{8}$ inch around all edges.

The tests to determine the characteristics of the transmission of the diaphragm were conducted over a wide range of mixture ratios and nominal mass flow rates of 1.0 to 1.25 lbs per second. Also two different nozzle geometries were investigated. In one case the nozzle was as shown in Figure 41 with the ratio of the area of the combustion chamber* to area of nozzle throat (A_c/A_t) equal to two. In the other case $A_c/A_t = 1$, i.e., nozzle section becomes an extension of the combustion chamber. Originally it was planned to test just hydrogen-oxygen mixtures, however as the problems became more evident it was decided to test methane-oxygen mixtures also because the latter has lower deflagration velocities, has a higher detonation pressure ratio, and has better photographic characteristics because of a luminous flame. Some of the results from the tests are shown in Figures 59 to 64. Figures 59, 60 and 62, 63 are Kistler pressure transducer records of the combustion chamber, while Figures 61 and 64 are typical photographs of the nozzle end of the motor (i.e., the view shown in Figure 57) taken with the Beckman and Whitley camera. The frames alternate between the strips; time between each frame is 38.4 microseconds. Pressure transducers were located at various positions around the channel as shown in Figure 58. Station location 6 was used primarily to indicate that the diaphragm held for the full rotation of the first wave and does not indicate the magnitude of the pressure. Since only two Kistler 603 transducers and amplifiers were available, they were placed in various positions on succeeding runs.

A point to be noted is that the transducer located at station 1 is very close to the diaphragm and it is possible that pieces of the ruptured diaphragm can strike this transducer. This phenomena is shown, for example, in Figure 63 runs 221, 222, 223. The large deflection which occurs at 520 microseconds is interpreted as the diaphragm striking the transducer. (Note zero time occurs when the upper beam is first deflected by the passage of the detonation wave.) This large deflection occurs only on some of the runs and is of varying amplitudes, it is never evident at station 2. It should be noted that the rupturing of the steel diaphragm occurs in general as a shearing out of the whole unsupported diaphragm piece which can usually be found on the floor after the run. On several of the runs it was possible to observe the ruptured diaphragm on photographs taken with the Beckman and Whitley camera. It is therefore felt that this large deflection is definitely the mechanical action of the diaphragm striking the transducer and not a gasdynamic effect.

*As used here A_c represents the combustion chamber area in a plane normal to the axial direction.

E. DISCUSSION OF THE TEST RESULTS OF THE ANNULAR MOTOR

First, a detailed interpretation of Figure 63 run 221 will be given to indicate the method of analysis. Referring to Figure 63 run 221 and the station location diagram (Figure 58) the following interpretation is made; the combustion is initiated at zero degrees, passes the 20° point (station 1) with a pressure level of the order of 150 psi, moves between stations 1 and 2 with an average velocity of 5500 ft/sec, moves between stations 2 and 6 with an average velocity of 6150 ft/sec and strikes the sealed diaphragm. The diaphragm ruptures quite rapidly and a pressure pulse is transmitted past station 1 at 360 microseconds with an amplitude of about one-third the original wave. The pressure pulse continues to station 2 with an average velocity of 5500 ft/sec but with decaying amplitude, and eventually decays to ambient, atmospheric pressure. Note that the velocity of the wave in the chamber agrees within a few percent with the Chapman-Jouguet detonation in a closed tube for a 61.5% methane-oxygen mixture as given in Figure 65.

Examination of the data reveals that in all cases the pressure pulse which is transmitted through the diaphragm does not generate a detonation wave, but rather it decays. The magnitude of this transmitted pressure pulse is greater for the nozzle $A_c/A_t = 2$. However when $A_c/A_t = 2$ the pressure in the chamber has not "blown down" to a pressure of one atmosphere so that the pressure ratio across the transmitted pulse is about 2. When $A_c/A_t = 1$ the pressure in the chamber is about one atmosphere as the transmitted pressure pulse starts so that the pressure ratio is much higher. In either case the gases expanding into the combustion chamber as a result of the diaphragm burst cause a strong enough shock wave to initiate a detonation wave if the fresh propellant was in the proper condition, i.e., sufficiently mixed but yet unburned. Variation of the mixture ratio over a wide range does not seem to affect the transmitted pulse noticeably. The Beckman and Whitley photographs (Figures 61 and 64) indicate that the hot luminous gases are carried about 60° around the annulus due to the diaphragm burst.

From the data taken another phenomenon is noticed particularly in Figures 60 and 62. Namely, the pressure transducer located at station 4 (220°) indicates a second pressure rise following the first passage of the detonation wave. This second pressure rise occurs too soon in time to be associated with the pressure pulse transmitted from the rupture of the diaphragm (clockwise) and also too soon to be caused by a counterclockwise reflection off the diaphragm before the diaphragm ruptures. Additional measurements shown in Figure 60 help to clarify the situation. In these tests a 1/8 in. steel plate was placed across the combustion chamber instead of the frangible diaphragm. These tests indicate that a second pressure wave is following the initial detonation wave by about 100 microseconds. This second following wave increases in amplitude and steepens in slope as it progresses around the annulus. In the

methane runs (Figure 62) the interpretation of pressure trace 4 is felt to be the same although the second following wave is 220 microseconds behind the initial wave.

From the available data a possible explanation of the second wave is offered. As the initial, clockwise detonation wave moves around the annular chamber, it propagates into a zone that is bounded by the unburned mixing region between the H₂ and O₂ streams in the upstream (injector) side and by the exit nozzle on the downstream side. It is obvious that since mixing between the H₂ and O₂ streams is not completed instantaneously, a mixing zone not capable of supporting a detonation wave must exist near the injector face. Thus the detonation wave must degenerate into a shock wave in this region. As this complex detonation wave moves around the annulus an instability apparently arises in the mixing region between the shocked but unburned mixture and the burned gases behind the detonating front. It is evident that this instability grows and steepens as it moves about the annulus behind the initial wave reaching an amplitude in pressure ratio of two or more. Whether this instability is a characteristic of the conditions associated with only the first clockwise detonation moving into a completely unburned mixture or would still be present on subsequent rotations of the wave cannot be established because apparently conditions in the unburned zone after rupture of the diaphragm do not allow subsequent rotations of the initial wave.

It appears that there are several reasons why maintained detonations are not achieved in the annular motor. It is believed that the frangible diaphragm is a convenient method to start a unidirectional wave in the annular motor but that sufficient unburned propellant is not available to maintain the second rotation of the detonation wave after the diaphragm bursts. It is very possible that local deflagration is occurring after the passage of the detonation wave due to the large scale turbulence and recirculation in the combustion chamber. In this regard the choice of injector design may be a very critical factor in the successful operation of the annular motor. The limitation in propellant mass flow rates to about 1 pound per second was another factor which severely influenced the performance of the annular chamber. Assuming no combustion behind the initial detonation wave and assuming that the combustion chamber "blows down" to ambient pressure at the time of diaphragm burst, ideally only approximately 2/3 of the combustion chamber would be filled with fresh propellant at the beginning of the second passage of the wave. Of course secondary combustion, mixing between the burned and unburned gas, and a chamber pressure at the time of diaphragm burst above atmospheric pressure tend to decrease the available volume of fresh propellant in the chamber to sustain multiple rotations of the detonation wave.

Several interesting features of detonation in initially turbulent mixtures were brought out by the test data. First, by triggering the oscilloscope with the signal to the spark plug, the transition time of the detonation wave from

spark to station 1 could be observed. It was found that for hydrogen-oxygen mixtures of 46 to 70% hydrogen by volume and for spark energies of the order of < 30 millijoules, the transition time from spark to station 1 was 80-90 microseconds. This is over an order of magnitude faster than the transition times measured in premixed quiescent, stoichiometric hydrogen-oxygen mixtures⁵⁶.

An additional observation related to the performance of the annular motor was the velocity with which initial detonation waves moved around the annular channel. Distance versus time plots of the visible light associated with the detonation front as it progresses around the annulus (measured along the centerline) are shown in Figures 66 and 67 as derived from the Beckman and Whitley photographs. It should be remembered that during the first rotation of the detonation wave the unburned propellant gases extend through and outside the nozzle. The main effect therefore, is the initial turbulence level rather than axial relief and an inert boundary gas as would be the case occurring for subsequent rotations of the wave. The results of 21 runs indicate the detonation front is formed very rapidly and moves at a nearly constant (possibly slightly accelerating) velocity during the first rotation. The average detonation velocity during the first rotation versus mixture ratio is summarized for 21 test runs in Figure 68*. It appears that the detonation velocity is about 7% higher (for a given mixture ratio) than the theoretical Chapman-Jouguet detonation velocities calculated for H₂-O₂ mixtures by Moyle³⁸ and Zeleznik and Gordon¹⁸. Also, for the methane-oxygen runs in the annular motor, the measured velocities appear higher by about the same increment, 7%, than the detonation velocities determined experimentally by Morrison⁵⁷ and Bone⁵⁸ in straight completely confined tubes utilizing initially quiescent mixtures**. Also, from the results of the 21 runs there appears to be no significant correlation between the measured detonation velocities and the chamber to nozzle area ratio employed.

The reason for the high values for the measured detonation velocities in the annular motor as shown in Figure 68 has not been resolved. Although the difference is not great it does represent a much greater difference than can be explained in the very slight scatter of the points on the displacement time plots obtained from the Beckman and Whitley photographs. In addition, the same time interval counter used to measure the framing rate of the Beckman and Whitley camera was used to measure H₂-O₂ detonation velocities in straight tubes. These measurements agreed very closely with the theoretically predicted values modified for the tube

*The detonation velocities plotted for the H₂-O₂ runs were obtained from the mean slopes shown in Figure 66 utilizing all of the measured points. The detonation velocities for the CH₄-O₂ runs were obtained as shown in Figure 67 utilizing the final points where the slope appears constant.

**The experimental results of Morrison and Bone were utilized for comparison because of the lack of recent theoretical calculations utilizing the methane-oxygen system.

velocity deficit which is significant for small tubes (see Section V of this report). Furthermore, average wave velocity measurements obtained from the pressure transducer records for these same 21 runs indicate the same general trend. A more questionable experimentally determined quantity, the propellant mixture ratio, was mentioned earlier as a possible source of error due to the uncertainty in the actual overall orifice coefficient utilizing 72 injectors for both the fuel and the oxygen. However, in the few calibrations of the individual injectors that were made, it was determined that a fuel injector (.017 inch orifice diameter) had a 7 1/2% lower discharge coefficient than an oxygen injector (.024 inch orifice diameter) based on nominal hole size. Since this effect, if present in all 72 injector pairs, would tend to make the corrected mixture ratios more fuel-lean, this would tend to make an even greater difference between the values of the initial detonation wave velocities measured in the annular motor and those predicted theoretically (or measured in confined tubes) as indicated in Figure 68.

If the hypothesis that the actual detonation wave velocity is indeed actually higher than the predicted theoretical Chapman-Jouguet detonation velocities, two possibilities remain. One, that these are not Chapman-Jouguet detonations, i.e., that a distance of only two feet from ignition is not long enough for the usually observed overdriven wave to decay to Chapman-Jouguet velocities. Due to the very short run-up distances of about two inches, and due to the evidence from the displacement-time plots, it is believed that this wave is not in the process of decaying and is a stable, fully developed detonation for the conditions involved. The other possibility is the high turbulence level associated with the unburned mixture in the annular channel. This is an effect that has not been systematically studied by other investigators to the knowledge of the authors. It is possible that if the turbulence level of the impinging fuel and oxygen streams is sufficiently high, the overall energy level of the reactants would be raised due to the contribution of the velocity fluctuation energy. In order to ascertain whether this effect could be responsible for the measured increase in detonation velocity, an assessment of the order of magnitude of the scale and intensity of turbulence in these impinging streams would have to be made.

VIII. COMPARISON OF ANNULAR MOTOR STUDIES WITH EXPERIMENTS OF VOITSEKHOVSKY

In view of the similarity of the studies by Voitsekhovsky^{10, 11} and those reported in section VII of this report, it is in order to make comparison and draw conclusions where possible. Toward this end, a full translation of Reference 11 (which contains all of the information of Reference 10) appears as Appendix A of this report. It is natural to speculate as to the motivation underlying the Russian work. The motivation behind the subject of this present report is one of propulsion application although with full recognition of the importance to rocket motor combustion instability problems. Presumably, then, the Russian motivation might be along similar lines with the additional possibility of a desire to attain a "maintained detonation" and study interaction processes.

A tabulation of the experimental schemes and observations for the two independent studies is given in Table 16.

We note from the table and from Appendix A that Voitsekhovsky was able to attain a single detonation as well as multiple detonation waves rotating steadily in one direction whereas in the work described herein only the first traverse of the annular channel was possible. It is believed that the major consideration accountable for this difference is a pre-mixed system versus a discrete injector system. In section VII attention was called to the fact that detonation was developed extremely rapidly in the highly turbulent mixture from the discrete fuel-oxidizer injectors. Unfortunately, this extreme turbulence occurring after the passage of the first wave probably causes residual, undesired deflagration and extensive mixing between burned and unburned propellants; all of which is detrimental to the passage of subsequent waves. The difficulty with pre-mixed systems centers around the problem of preventing detonation back to the feed lines and mixing chamber. After indicated difficulties, Voitsekhovsky seems to have overcome this problem.

An interesting observation made by Voitsekhovsky is that multiple waves could be formed, the actual number being dependent on the propellant flow rate and the mixture ratio employed. Evidently, for any given operating condition, the number of waves may fluctuate some but will tend to stabilize around a certain value. Probably the explanation of this self-stabilizing property involves the "side relief" influence studied by Dabora³⁹. Briefly, this would apply as follows. In the case of multiple waves the unburned propellant at the wave location will not fill the entire width of the annulus. Thus, the

TABLE 16. COMPARISON OF EXPERIMENT CONDITIONS AND OBSERVATIONS WITH THOSE OF VOITSEKHOVSKY

Experimental Conditions or Observation	Experiments in Apparatus of Voitsekhovsky (Appendix A)	Experiments in Annular Motor (Section VII of this Report)
1. Scale size of apparatus	Not indicated but presumably of laboratory scale of same order as annular motor described in Section VII of this report.	Diameter of annulus, 7.5 inches at mid-point: radial width of annulus 1/2 inch. Combustion chamber cross sectional area normal to propagation of wave, $A_c = 1$ inch ² .
2. Fuel-oxidizer	Acetylene-oxygen mixtures.	Hydrogen-oxygen and methane-oxygen mixtures.
3. Method of propellant injection	Annular slot - premixed.	72 injector pairs (impinging like on unlike) spaced uniformly around annular chamber.
4. Direction of propellant injection and exhaust	Outward - radial.	Axial.
5. Method of ignition	Spark	Capacitance spark or small detonation tube.
6. Method of annular channel closure for unidirectional propagation of detonation wave(s)	Explosive shutter sequenced to begin opening at moment of ignition allowing opening for passage of successive waves in same direction.	Frangible diaphragm holding for first passage of wave and rupturing upon collision of first wave allowing transmitted wave in same direction.
7. Chamber pressure at ignition	Subatmospheric pressure (exhaust into low pressure) reservoir.	Slightly greater than atmospheric pressure (exhaust to atmosphere).
8. Propellant flow rate	Variable - blowdown from supply tank, flow rates not indicated.	Constant - delivered through pressure regulators from fuel and oxygen supply cylinders. Flow rate ~ 1 lb/sec.
9. Pressure measurements in annular chamber	Not indicated.	Pressure-time measurements during first passage of wave at two different locations around annulus by Kistler 603 pressure transducers (rise time ~ 10 μ sec).
10. Photographic record of wave(s)	Continuous drum camera record in form of hypocycloid utilizing visible light from detonation wave(s).	Beckman and Whitley Dynafax framing camera used at a framing period of 38.4 μ sec per frame utilizing visible light from detonation wave (4-6 pictures during first passage of wave).
11. Number of passages of detonation wave(s)	Not available from report but detonation process maintained for 1-1.5 seconds.	One passage of wave with subsequent decay of detonation process during second passage.
12. Number of stable detonation waves moving in same direction	One to at least five waves.	Initially one wave during first passage with following wave growing during passage.
13. Wave velocities	One wave moving at Chapman-Jouguet velocity up to at least 5 waves moving at speed of sound of burned gases immediately behind wave (i.e., about $1/2 C_J$ velocity).	Approximately 7% greater than calculated (and observed) one-dimensional Chapman-Jouguet detonations for first passage of wave.

detonation will extend over only a portion of the annulus and the high pressure gases behind the detonation will expand transversely to the direction of propagation of the wave. This causes a reduction in the wave velocity and if the relief is pronounced enough the detonation will degenerate into a shock wave and a separate deflagration wave. With this view, then, if there are too many waves an individual wave will have a relatively narrow width of unburned propellant which may lead to quenching and thus reduce the number of waves. Conversely, if there are too few waves, the relief on an individual wave is less so that the velocity is higher. Fewer waves imply also that an element of unburned propellant will be in the annular chamber a longer period of time before being detonated. Evidently this longer time allows other combustion fronts to develop which eventually lead to the correct number of detonating fronts.

Another interesting phenomenon found by Voitsekhovsky is that the velocity of wave propagation of a multiple wave system (five waves) is equal to the speed of sound of the burned gases immediately behind a detonation wave. This velocity is close to one half the normal Chapman-Jouguet velocity. His quoted value of 1.4 km/sec for this velocity is in agreement with the speed of sound of the burned gases behind Chapman-Jouguet detonation waves in $C_2H_2 - O_2$ mixtures as calculated by Morrison and Weir⁴¹. This abnormally low detonation velocity defies the normal limits of velocity defect possible before quenching occurs, but is strikingly similar to an observation of Dabora³⁹. The latter noted this unusual behavior when the detonation was bounded by an inert gas of a very high sound speed. In those cases the detonation generated a shock in the inert gas which was of the detached type and which moved ahead of the detonation. This in turn caused a series of oblique shocks which extended into and thus, "prepared" the unburned propellants for the unusual detonation. Presumably, then, the explanation for these unusual waves lies in the strong two-dimensional effects.

IX. CONCLUSIONS AND RECOMMENDATIONS

A. ANALYTICAL MODEL OF THE INTERNAL GAS DYNAMICS OF THE RDWE

The physical model treated consisted of a gaseous detonation wave propagating at steady velocity in the circumferential direction of an annular combustion chamber. Fresh propellants were continuously introduced and the combustion products exhausted through an annular nozzle. The detonation was assumed to completely fill the cross section of the annulus. The limiting cases of complete versus no mixing between the burned and fresh propellants were considered. The resultant system of quasi-linear, first order, ordinary differential equations were solved on a digital computer. The following major conclusions were drawn.

1. The values of the flow properties (Mach number, pressures, etc.) are approximately parabolic functions of the circumferential coordinate of the chamber.
2. The detonation wave(s) moving steadily around the chamber must be Chapman-Jouguet detonations.
3. The solution to the complete mixing case reveals a fundamental degradation to the performance of an RDWE. This is due primarily to the complete mixing assumption which allows unburned propellant to pass out the chamber through the exit nozzle between successive waves. It is concluded that this case should be avoided if possible in a real application.
4. The numerical values obtained from the solution to the no mixing case equations for the absolute detonation wave velocity of stoichiometric H₂-O₂ mixtures (9520 ft/sec) and the absolute velocity of the unburned gas immediately ahead of each wave (197 ft/sec directed into the wave) appear reasonable from practical considerations and tend to justify the assumptions made in the analysis.
5. For the purposes of comparison with conventional rocket motors the effective chamber pressure of the RDWE is the time average value.
6. A comparison of the theoretical specific impulse (frozen chemical equilibrium) of the RDWE and the conventional rocket motor are essentially identical for the case of an ideal expansion into a vacuum. For the case of an ideal expansion at sea level the specific impulse of the two devices is essentially the same as long as the average chamber pressure of the RDWE is greater than about 500 psia (compared to a conventional rocket motor operating at the same chamber pressure)

7. Although comparison with the results of the annular motor studies presented in Section VII are limited, good qualitative agreement is obtained between the theoretical pressure-time dependence obtained from solutions to the no-mixing case equations and the experimental pressure-time dependence measured from the passage of the first detonation wave in the annular motor.
8. The analysis assumed that the nozzle flow was isentropic and perfectly expanded. It is recognized that this is highly idealized but the magnitude of the error incurred is not known.

B. ANALYTICAL PREDICTIONS OF HEAT TRANSFER RATES IN THE RDWE

This study treated the case of a number of detonation waves traversing a plane wall wherein the distance and time spacing between any two waves was a constant. Limiting cases of zero versus complete recombination at the wall were considered, the latter leading to approximately 30% higher rates in the case of H₂-O₂. The predicted rates appear to be of the same order as current high performance propellants (approximately 11 BTU/in²-sec). Consequently there appears to be no fundamental limitation to the RDWE principle on the basis of heat transfer.

C. IMPLICATIONS OF HETEROGENEOUS DETONATION

While the studies actually conducted under this program assumed a gas-gas system, many possible propellant combinations would include the liquid-gas case. The question arises as to whether detonations are possible in a gaseous-liquid drop environment. An extensive literature search and some calculations indicates that detonation waves in a heterogeneous media can only be expected if either the drops are very small (less than about 10 μ) or if convective velocities behind the shock can shatter the larger drops into very small drops in a very short period of time (of the order of 10 μ sec). The results of some drop shattering experiments conducted as part of this program as well as work done at NASA on the breakup of liquid jets would indicate the shattering is about of this order of time but nothing is known about the size of drops produced from this shattering. It must be concluded that the possibility or impossibility of steady detonations in a heterogeneous system is not established at this time and further research is required.

D. GEOMETRICAL EFFECTS ON DETONATION PROPAGATION

A few experiments were conducted in a segment of annular detonation tube designed to simulate the annular motor. This was a one-shot detonation utilizing pre-mixed hydrogen and oxygen and with provision for relief of the burned gases

through a continuous annular nozzle. Experiments with H₂-O₂ and with the nozzle blocked indicated that the detonation velocity on the centerline of the annulus was very close to the usual Chapman-Jouguet velocity and hence the velocity at the outer radius was greater and at the inner radius it was smaller. There was some curvature to the wave but the pressure gradient behind the wave seemed to give no important differences. In the cases of heterogeneous detonation the pressure gradient in the radial direction may be important in centrifuging the liquid drops. Experiments with the nozzle open yielded somewhat lower detonation velocities (approximately 7% for stoichiometric H₂-O₂ mixtures) due to the relief effect.

E. DETONATION VELOCITIES OF H₂-O₂ MIXTURES AT ELEVATED PRESSURES AND REDUCED TEMPERATURES

The detonation velocities of a range of H₂-O₂ mixture at pressures up to 15 atmospheres and temperatures down to 112°K were determined experimentally. This extended the range of existing experimental information. The experiments showed some meaningful disagreement with theoretical results obtained at these conditions. These effects are important in that they have strong influence on the maximum pressures realizable in the engine.

F. RESULTS OF TESTS IN THE LINEAR AND ANNULAR MOTOR

Considerable effort was spent in attempting to achieve a detonation wave (or waves) rotating continuously in one direction in an annular motor. Great difficulty was experienced in getting the wave to move in only one direction and it was only by employing the extreme measures of a diaphragm across the annular-chamber and a large baffle plate extending outside the chamber that the problem was solved. The linear motor was used to help solve this problem. However, having solved the problem of producing a detonation wave traversing the annulus in one direction for the first cycle, success was never achieved in obtaining sustained rotation after the first cycle. The wave was attenuated breaking the diaphragm and passing into the "fresh" charge. The reasons for this are believed to be among the following; (a) severe attenuation due to the discrete injector pattern, (b) insufficient mass flow rate into the motor, and (c) continuous burning after the passage of the first detonation wave.

As mentioned earlier, measurements of the pressure history behind the first detonation agreed well with theoretical predictions.

An interesting and surprising observation was that of a second accelerating pressure wave overtaking the detonation. Such phenomena could lead to the complicated interactions observed by Voitsekhovsky.

A very pertinent observation made was the rapidity with which a detonation could be developed from a spark in the highly turbulent flow field from the injectors. The time required (induction time) was an order of magnitude less than that required for the same gases pre-mixed and in a quiescent state. This may be significant to combustion instability in conventional motors.

G. GENERAL CONCLUSIONS

The major aim of this program was to operate a RDWE, measure appropriate performance parameters, compare the results to theoretical predictions where possible, and on the basis of this determine feasibility of the concept. This turned out to be a much more complicated and difficult task than that envisioned at the initiation of the study and as a result successful operation was never achieved. Accordingly, the question of feasibility cannot be definitely answered at this time. Nothing has been found that makes the concept not feasible but important questions (such as nozzle performance, actual overall performance, and detonation in heterogeneous mixtures) remain unanswered.

As mentioned in the introduction of this report, some work on the RDWE had been done at the University of Michigan prior to the initiation of this contract. The conclusion reached from those studies was that motor operation was successfully realized with multiple rotations of the detonation wave. This conclusion was based on Fastax camera records and Photocon pressure transducer measurements. When we consider the following facts, (1) the early tests utilized no channel blockage to prevent bi-directional initiation, (2) lower mass flows and 36 as compared to 72 injector pairs were utilized, and (3) every effort was made to duplicate the earlier runs with the same motor and same operating conditions but with better instrumentation (higher framing rate camera and higher frequency response, pressure transducers), it is difficult to believe that the motor could ever have been operated successfully. On the other hand no definite explanation exists for the seemingly consistent data first obtained.

Finally it is well to point out that many of the facets studied and experienced in this investigation are undoubtedly closely related to conventional rocket motor combustion instability problems.

H. RECOMMENDATIONS FOR FURTHER STUDY

It is believed that much is to be gained from further studies of rotating detonation waves in an annular chamber. While successful operation has not been achieved herein, nothing fundamental stands in the way of this accomplishment. Voitsekhovsky has achieved successful maintained detonations in the case of pre-mixed reactants. Further studies in the separate injection case could be

used to evaluate the RDWE concept. Also, the results would be of direct applicability to rocket motor combustion instability problems. It is recommended that initially the studies be confined to a gas-gas injection system and finally extended to the case where the fuel and/or oxidizer is in the form of liquid drops. Attention should be given to the initiation and propagation characteristics of detonation in a highly turbulent mixture. Fundamental studies of heterogeneous detonation should also be made.

REFERENCES

1. Nicholls, J. A., Wilkinson, H. R., Morrison, R. B., "Intermittent Detonation as a Thrust-Producing Mechanism," *Jet Propulsion*, May 1957.
2. Dunlap, R., Brehm, R. L., and Nicholls, J. A., "A Preliminary Study of the Application of Steady State Detonative Combustion of a Reaction Engine," *ARS Journal*, Vol. 28, No. 7, pp. 451-56, July 1958.
3. Sargent, W. H., and Gross, R. A., "Detonation Wave Hypersonic Ramjet," *ARS Journal*, Vol. 30, No. 6, 1960, pp. 543-549.
4. Spindler, C. L., Nunn, R. H., Krzycki, L. J., and Jenkins, H. Powell, Jr., "The Standing-Detonation-Wave Rocket Engine," presented at the Fourth JANAF Symposium, 6-8 November 1962, San Francisco, Calif.
5. Nicholls, J. A., et al, "The Feasibility of a Rotating Detonation Wave Rocket Motor," The Univ. of Mich., ORA Report 05179-1-P, Aug. 1962.
6. Nicholls, J. A., et al, "The Feasibility of a Rotating Detonation Wave Rocket Motor," The Univ. of Mich., ORA Report 05179-2-P, Dec. 1962.
7. Nicholls, J. A., et al, "The Feasibility of a Rotating Detonation Wave Rocket Motor," The Univ. of Mich., ORA Report 05179-3-P, Mar. 1963.
8. Nicholls, J. A., et al, "The Feasibility of a Rotating Detonation Wave Rocket Motor," The Univ. of Mich., ORA Report 05179-4-P, June 1963.
9. Nicholls, J. A., et al, "The Feasibility of a Rotating Detonation Wave Rocket Motor," The Univ. of Mich., ORA Report 05179-5-P, Sept. 1963.
10. Voitsekhovsky, B. V., "Maintained Detonations," *Soviet Physics Doklady*, 4, No. 6, Translated from *Doklady Akad. Nauk SSSR*, Vol. 129, No. 6, pp. 1254-56, Nov. -Dec. 1959.
11. Voitsekhovsky, B. V., *Zh. Prik. Mekhan. i Tekhn. Fiz.* (Journal of Applied Mechanics and Technical Physics) No. 3, 157-164 (1960). (A translation appears in Appendix A of this report)
12. Shapiro, A. H., The Dynamics and Thermodynamics of Compressible Fluid Flow, Vol. I, Chapter 8, The Ronald Press Co., New York, 1953.
13. Courant, R., and Friedrichs, K. O., Supersonic Flow and Shock Waves, Chapter III, Parts C and E, Interscience Publishers, Inc., New York, 1948.
14. Organick, E. I., A Computer Primer for the MAD Language, Ann Arbor, Michigan, 1961.
15. The University of Michigan Computing Center, Mess, (A collection of descriptions of available computer program subroutines), 20 January 1962.

REFERENCES (cont)

16. Scarborough, J. B., Numerical Mathematical Analysis, The Johns Hopkins Press, Fifth edition, Baltimore, 1962.
17. Zeleznik, F. J., and Gordon, S., "A General IBM 704 or 7090 Computer Program for Computation of Chemical Equilibrium Compositions, Rocket Performance, and Chapman-Jouguet Detonations," NASA TN D-1454, October 1962.
18. Zeleznik, F. J., and Gordon, S., "Calculation of Detonation Properties and Effect of Independent Parameters on Gaseous Detonations," ARS Journal, 32, 608 (1962).
19. Gordon, S., and McBride, B. J., "Theoretical Performance of Liquid Hydrogen with Liquid Oxygen as a Propellant," NASA Memo 5-21-59E, June 1959.
20. Williams, F. A., "Detonations in Dilute Sprays," Progress in Astronautics and Rocketry, Vol. 6, pp. 99-114, Academic Press, New York, 1962.
21. Williams, F. A., "Progress in Spray-Combustion Analysis," Eighth International Symposium on Combustion, The Williams and Wilkins Company, Baltimore, pp. 50-69, 1962.
22. Webber, W. F., "Spray Combustion in the Presence of a Travelling Wave," Eighth International Symposium on Combustion, pp. 1129-1140, The Williams and Wilkins Company, Baltimore, 1962.
23. Cramer, F. B., "The Onset of Detonation in a Droplet Combustion Field," Ninth International Symposium on Combustion, pp. 482-487, Academic Press, New York, 1963.
24. Williams, F. A., Ph. D. Thesis, Calif. Inst. of Tech., Pasadena, Calif., June 1958.
25. Williams, F. A., "Structure of Detonations in Dilute Sprays," The Physics of Fluids, Vol. 4, No. 11, Nov. 1961.
26. Burgoyne, J. H., and Chen, L., "The Effect of Drop Size on Flame Propagation in Liquid Aerosols," Roy. Soc. Proc. Series A, 225, 1954, pp. 375
27. Hinze, J. O., "Critical Speeds and Sizes of Liquid Globules," App. Sci. Res., pp. 273-288, 1949.
28. Dodd, K. N., "On the Disintegration of Water Drops by Shock Waves," Royal Aircraft Establishment Tech. Note No. M. S. 64, May 1960.

REFERENCES (cont)

29. Gordon, G. D., "Mechanism and Speed of Breakup of Drops," *J. of Applied Physics*, Vol. 30, No. 11, p. 1759, Nov. 1959.
30. Rabin, E., and Lawhead, R., "The Motion and Shattering of Burning and Nonburning Propellant Droplets," Rocketdyne, North American Aviation, AFOSR TN 59-129, Mar. 1959.
31. Cramer, F. B., "Shattering of Burning and Nonburning Propellant Droplets by Shock Waves," Rocketdyne, North American Aviation, Feb. 1958.
32. Hanson, A. R., Domich, E. G., and Adams, H. S., "An Experimental Investigation of Impact and Shock Wave Breakup of Liquid Drops," Univ. of Minn. Inst. of Tech., Dept. of Aero. Eng. Res. Report 125, Jan. 1956.
33. Lane, W. R., "Shatter of Drops in Streams of Air," *Ind. Eng. Chem.* 43, 1951.
34. Engel, O. G., "Fragmentation of Waterdrops in the Zone Behind an Air Shock," *J. of Res. NBS* 60, 1958.
35. Merrington, A. C., and Richardson, E. G., *proc. Phys. Soc. (London)* A 59, 1 (1947).
36. Hanson, A. R., and Domich, E. G., "The Effect of Liquid Viscosity on the Breakup of Droplets by Air Blast," Univ. of Minn., Inst. of Tech., Dept. of Aero. Eng. Res. Report 130, June 1956.
37. Lane, W. R., and Green, H. L., "The Mechanics of Drops and Bubbles," G. I. Taylor Anniversary Volume, Cambridge Univ. Press (1956).
38. Moyle, M. P., "The Effect of Temperature on the Detonation Characteristics of Hydrogen-Oxygen Mixtures," Ph. D. Thesis, The Univ. of Mich., (Industry Program Report IP-195), Dec. 1956.
39. Dabora, E. K., "The Influence of a Compressible Boundary in the Propagation of Gaseous Explosions," Ph. D. Thesis, The Univ. of Mich., (Industry Program Report IP-649), Dec. 1963.
40. Morrell, G., "Rate of Liquid Jet Breakup by a Transverse Shock Wave," NASA TN D 1728, May 1963.
41. Morrison, R. B., et al, "Equilibrium Temperature and Composition Behind a Detonation Wave," *Ind. Eng. Chem.*, Vol. 46, p. 1056, May 1954.
42. White, D. R., "Turbulent Structure of Gaseous Detonations," *Phys. Fl.*, Vol. 4, p. 465, 1961.

REFERENCES (cont)

43. Mirels, H., "The Wall Boundary Layer Behind a Moving Shock Wave," Boundary Layer Research, Symposium, Freiburg, Aug. 26-29, 1957, H. Gortler E., Springer Verlag.
44. Eckert, E. R. G., "Engineering Relations for Friction and Heat Transfer to Surfaces in High Velocity Flow," JAS, Vol. 22, No. 8, 1955.
45. Hartunian, R A , Russo, A L , and Marrone, P. V. , "Boundary Layer Transition and Heat Transfer in Shock Tubes," JAS, Vol. 27, Aug. 1960, p. 587.
46. "Tables of Selected Values of Chemical Thermodynamic Properties," NBS Series I, Vol I, Mar 1947-June 1959.
also see
Penner, S. S., Chemistry Problems in Jet Propulsion, Pergamon Press, New York, 1957.
47. Barrere, M , Rocket Propulsion, Elsevier, 1960.
48. Jaeger, J. C. , "Pulsed Surface Heating of a Semi-Infinite Solid," Quart. of Applied Math, Vol. XI, No. 1, (1953).
49. Phillips, R. L., private communication.
also see
"Development Studies of a Three Phase A-C Arc Heater," Proposal to ARL, Office of Aerospace Res. , U. S. Air Force, The Univ. of Mich. , ORA 62-371-Q, Oct. 1961.
50. Carslaw, H. S., and Jaeger, J. C. , Conduction of Heat in Solids, Second edition, Oxford Univ. Press, London.
51. Hayes, W. D. , and Probstein, R. F. , Hypersonic Flow Theory, Academic Press, New York, 1959, Chapter VIII.
52. Curran, A N , et al, "Analysis of Effects of Rocket-Engine Design Parameters on Regenerative-Cooling Capabilities of Several Propellants," NASA TN D-66, Sept. 1959.
53. Gealer, R. L. , "The Influence of High Pressure on the Properties of Hydrogen-Oxygen Detonation Waves, Ph D Thesis (Industry Program Report IP-295), The Univ. of Mich , June 1958
54. Fay, J A , "Two Dimensional Gaseous Detonations. Velocity Deficit," Physics of Fluids 2, 283 May-June 1959).

REFERENCES (cont)

55. Sommers, W. P., "The Interaction of a Detonation Wave with an Inert Boundary," Ph. D. Thesis, The Univ. of Mich., (Industry Program Report No. IP-501), Mar. 1961.
56. Oppenheim, A. K., Mason, N., and Wagner, H. G., "Recent Progress in Detonation Research and Its Relation to Rocket Propulsion," presented at AIAA Summer Meeting, Los Angeles, 1963.
57. Morrison, R. B., "A Shock Tube Investigation of Detonative Combustion," Univ. of Mich. Report UMM 97, Jan. 1952.
58. Jost, W., and Croft, H. O., Explosion and Combustion Processes in Gases, McGraw-Hill, p. 181, 1946 (p. 181)
59. Sievers, G. K., et al., "Theoretical Performance of Hydrogen-Oxygen Rocket Thrust Chambers," NASA Tech. Rept. R-111, 1961.

Appendix A

SPINNING MAINTAINED DETONATION*

B. V. Voitsekhovsky
(Novosibirsk)

Because of the high velocity of the propagation of detonation waves, usually reaching a few kilometers per second, the phenomenon of detonation is usually examined as a millimicrosecond process.

Over a prolonged period of time experiments have been undertaken to bring about a stationary detonation, that is—such a process in which the duration of the propagation of the detonation wave is in seconds or minutes depending on the amount of the burning mixture.

Efforts were directed for the most part, to the creation of a stream moving in a tube at the velocity of the detonation wave. The front of the detonation wave may be stopped relative to the observer when the opposing velocities of the stream and detonation are equal.

Among the various types of gaseous mixtures, greatest interest was placed on mixtures with a high heating value capability, possessing detonation velocities of about 3 km/sec. With such mixtures it is practically impossible to obtain a one-dimensional, maintained detonation because at velocities of 3 km/sec the gas would ignite on the walls of the nozzle ahead of the front of the detonation wave. In the work of Reference A1, the author states that he was able to stop the front of a detonation wave using a slightly lean hydrogen-air mixture having a velocity of detonation of 700 m/sec. At higher velocities the mixture ignited ahead of the front. If conditions in a given channel are such that the initial gaseous mixture enters at a velocity sufficiently high to continuously fill in the space ahead of the front of the detonation wave, then this phenomenon can be converted into a maintained state for any mixture having a high heating value.

In the work under consideration using an automatic shutter spanning the transverse section of the annular channel, the detonating process rotates in a clockwise direction at the moment of initiation.

In this way it was possible to bring about a maintained detonation in the annular channel with a duration of 1 - 1.5 sec.

*A translation of Reference 11 by William Whitney, Univ. of Mich.,
Office of Research Administration.

The arrangement of the apparatus in which the maintained detonation was obtained is shown in Figure A1. The front of the detonation wave is steadily propagated in one direction along the circumference of the annular channel. The transverse section of the channel is shown separately in Figure A2. The channel takes the form of an annular space between two walls, one of which is a steel plate. The outer rim of the annular channel has an inclined profile in order to diminish transverse oscillations. A straight profile would tend to reinforce transverse oscillations and cause the penetration of the detonation wave into the center of the plate and then to the gas reservoir containing the initial mixture. The other plate is made of transparent plastic. The supply and discharge of the gaseous mixture is accomplished through two apertures parallel to the channel and situated on opposite sides of its transverse section. The width of the apertures is somewhat smaller than the width of the channel. The initial gas mixture enters through one aperture while the products of the detonation escape out the other aperture. The gaseous mixture is introduced in a direction perpendicular to the direction of the propagation of the detonation front. To set up a maintained detonation it is necessary that the inlet gas be conducted in a radial direction from the center to the periphery because due to the rotary movement of the detonation front a flash-back of the flame upon meeting the inlet stream is less likely near the center than near the periphery. In the reverse direction of the flow of the gas (from the periphery to the center) a flash-back of the flame might occur in the initial reservoir even under lower pressures. The experiments were conducted using oxyacetylene mixtures. With less sensitive gas mixtures such as, for example, $2\text{H}_2 + \text{O}_2$, the probability of a flash-back of the detonation wave in the initial reservoir is lessened.

Ignition of the mixture at one of the points on the circumference in the annular channel is accomplished by a spark discharge between the electrode fastened to the transparent wall and the steel plate itself which is connected to the body of the apparatus. The shutter which is located near the point of ignition completely spans the transverse section of the channel. The shutter begins to open at the instant of ignition. Before the detonation wave is able to complete a single revolution, the shutter is fully open and allows the free flow necessary for the circulation of the detonating wave. In this way the rotary motion is established.

The rapid movement of the shutter is accomplished by means of a special explosive device. Before conducting the experiment the cylinder of this explosive device was filled with an explosive gaseous mixture. The body of the cylinder was made as light as possible and fastened to the shutter spanning the channel, the heavy portion of which is fastened securely. At the same time that the gaseous mixture is introduced into the channel a mixture is introduced into the cylinder. The shutter and the cylinder achieve an acceleration of $4 \times 10^6 \text{ m/sec}^2$. Special arrangements have to be made to prevent the detonation

wave from propagating in more than one direction from the point of ignition. The detonation waves impinge on the inner side of the annular channel at which point it is possible that the detonation waves could penetrate through the supplying nozzle to the reservoir containing the initial mixture. The problem of eliminating such flash-backs presents significant technical difficulties. It was solved by selecting a specially shaped supply nozzle and establishing the correct pressure regime.

In a short interval of time the collision of two opposing waves will generate a multiplication of the number of fronts creating a stable process of frequently colliding detonating waves. Under these conditions all the gas is burned in the detonating waves. This process in distinction to the maintained cyclic detonation is designated a maintained pulsating detonation inasmuch as the detonation waves effect frequent reciprocal motions in the channel. In order to study the pulsating maintained detonation a series of experiments were conducted in a section of the annular channel. To this end the annular channel was spanned in two places by radially arranged baffles. As might be expected the phenomenon in this configuration differed in no way from the pulsating maintained detonation in the closed annular channel. Exactly the same picture of a pulsating maintained detonation must be observed if a section of the circumference is straightened into a linear channel. In this case also a few detonation fronts will effect a reciprocal motion along the linear channel. A network formed by two groups of characteristics will be observed on a photorecord of such a process.

Up to this time we have observed maintained detonations in a linear channel either closed or unclosed. A maintained cyclic detonation may be observed only in a closed linear* channel.

A pulsating maintained detonation may be observed in both types of a linear channel, and also in between two plane surfaces if the inlet gaseous mixture is conducted through a large number of orifices perpendicular to one of the surfaces while the products of detonation are removed through corresponding orifices in the second surface.

In this case the only stable regime will be the following: the entire plane region will be divided into triangles and polygons by the detonating fronts continuously changing form as a result of the interaction of the fronts. The cells formed by the intersecting fronts do not differ in principle from those formed by transverse detonation waves in a normal detonation wave. The unreacted layer of gas compressed by the forward shock wave of a normal detonation

*Translator suspects author intended "annular" instead of "linear."

wave is equivalent to the layer of the unburned gaseous mixture in the space between the two surfaces.

It is essential to note the possibility of one other case of a plane pulsating maintained detonation. Imagine a solid cylinder with an end wall providing a large number of small apertures through which two components of the detonating mixtures pass separately. In this case a layer of gas capable of detonation may form along the supplying surface. If the depth of the layer thus formed exceeds a certain limit then detonation waves will begin to propagate along it in different directions forming a cellular pattern.

Any other type of pulsating maintained detonations will be unstable. For example, during a single ignition of the gas mixture at the center of the solid plate and the flow of the mixture through the surfaces it is impossible to create a stable detonation wave which periodically moves away from the center and is triggered anew by the converging shock wave reflected from the circumference. After a few pulsations a multiplication of the number of fronts occurs dividing the surface into a number of separate triangles and polygons.

The size of the cell must depend on the type of mixture and pressure according to the law applicable in the case of a defined size of the cells of a normal detonation wave.

A pulsating maintained detonation is accompanied by a collision of detonating waves resulting in the formation of local pressure peaks which might destroy the detonation chamber unless it has a sufficient margin of strength. A maintained cyclic detonation is characterized by the rotation of a few detonation fronts in one direction along a closed channel, thus the collision of detonating fronts is absent accounting for the rise in the initial pressure of the mixture.

Below we will examine exclusively the maintained cyclic detonation. In this connection the term maintained detonation should be considered to be maintained cyclic detonation.

In order to obtain a maintained detonation it is necessary to eliminate one of two fronts at the instant of ignition of the explosive mixture into the annular channel. This is comparatively easily achieved by the installation of a partial, fixed baffle in the channel near the point of ignition. A fixed baffle however does not always direct the detonation process in one direction. Occasionally there is a region where the detonation breaks through to the other side of the baffle creating several colliding fronts. A completely stable propagation of fronts in one direction is achieved by means of the above mentioned mechanical shutter which completely spans the transverse section of the channel.

The maintained detonation is photographed in the annular channel on a moving film through the upper transparent plate using a photorecorder situated above the plate. The photorecorder is arranged such that the optical axis of the objective coincides with the axis of the annular channel. The image of the annular channel falls within the limit of the film. As the front of the detonation wave is propagated along the circumference of the channel its image describes a cycloid on the moving film. A photorecord obtained in this way is shown in Figure A3. On this photorecord it is possible to see five separate filaments of a hypocycloid. The picture shows a five-headed, maintained detonation. Due to the fact that a maintained detonation is a prolonged process one revolution of the film drum is insufficient to capture the entire process. To increase the duration of recording we used a rotating photorecorder, the body of which rotates around the axis perpendicular to the axis of rotation of the film drum. The exposure is made from a distance great enough to record the phenomenon on a narrow path, the width of which is several times smaller than the width of the film. As a result of putting together two mutually perpendicular motions, the cycloid is recorded along a spiral on the cylindrical surface of the film drum. The beginning of the second motion occurs by means of an auxiliary explosion occurring at the instant of the ignition of the mixture. As a result of the explosion the body of the photorecorder receives a moment of momentum and starts turning at virtually constant velocity (to the extent of a small angle α) defined by the following expression

$$\operatorname{tg} \alpha/2 = b/2f$$

where b = width of the film, f = the focal length of the objective.

In Figure A4 a photorecord shows a few detonation fronts propagating in different directions and colliding with one another. It is possible to examine the correct periodicity of the colliding detonating waves.

To analyze the physical process accompanying the maintained detonation, we fix attention on some point in the annular channel. After a front of a detonation wave passes by this point a jump in pressure causes the burned mixture to be quickly forced out by the entering original mixture which occupies a wedge-shaped region curved along the annular channel with the vertex behind the front of a detonation wave and the base coinciding with the next detonation front. The arrangement of the fronts of a multiple-headed maintained detonation is shown in Figure A5. The projection $\Delta\ell$ of every front of the maintained detonation in the direction of the radius is equal to

$$\Delta\ell = \frac{\pi du}{Dn} \quad (1)$$

Here d = diameter of the annular channel, u = velocity of the inlet mixture, D = velocity of the maintained detonation, n = the number of fronts rotating around the circumference at any given time.

The value of $\Delta\ell$ does not depend on the velocity u of the inlet mixture. An increase in u leads to a proportional increase in the number of fronts. The value of $\Delta\ell$ and D entering in expression (1) remains constant.

It is essential to bear in mind that maintained detonations are as a rule multiple-headed and only at the very limit of the detonation process may a single detonation front be established. The photorecord in Figure A3 shows five fronts rotating in the same direction.

Other stable numbers of fronts may also be observed. In a multiple-headed maintained detonation the number of fronts establishes a limited maximum value and converges to a stable oscillation about a constant value. This characteristic of a maintained detonation is easily understood when it is remembered that the random damping of one front increases the width and thus the very stability of the remaining fronts. It is essential to recall that every front is the base of a wedge formed by the initial mixture. If the width of a front exceeds its limit then after a random reduction in the number of fronts, at least one front will reach the limiting width before the others thus leading to an increase in the number of fronts. In the opposite case when the number of fronts are generated with a width below the limiting value leading to a reduction of the number of fronts to the stable number.

Thus, a multiple-headed maintained detonation is a completely stable process.

The velocity of the propagation of the multi-headed maintained detonation is equal to the velocity of sound in the burned products. This remarkable characteristic of a maintained detonation enables us to decipher the structure of the detonation fronts.

The study of this characteristic leads naturally to the hypothesis that the energy used to introduce the gas mixture is transmitted to the head of the front along the edge of the burned gases. These sound waves are propagated along the edge adjacent to the cold gas. A refraction of the sound waves occurs at the contact surface with the formation of oblique shock waves in the cold gas. We will establish the system of coordinates at point K at which point the shock wave intersects (Figure A5) with the line of the contact discontinuity KM between the cold and the burned gases. Line KM represents the burning front which is moving at a low velocity relative to the gas. The meaning of the areas indicated by numerals is as follows I. - Region in which the cold, undisturbed gas flows, II. - Region occupied by the burned, undisturbed gas, III - Zone of rarefaction into the burned gas, IV. - Region behind the front of the oblique shock wave, V. - Region behind the front of the shock wave reflected from the inner wall of the annular channel.

The values relating to Zones I-V we will denote by the corresponding arabic numerals 1-5. In the system of coordinates under examination both in Zone I and in Zone II the gas flows at the speed of sound c_2 .

A wave of rarefaction is created in Zone III. The flow in this zone is defined by the Prandtl-Meyer hypothesis. Zone IV is the region of uniformity where the pressure and velocity are constant everywhere and equal to the corresponding values behind the front of the oblique shock wave KB. Front KD is assumed to be perpendicular to the streamlines. If the pressure p_3 behind the front KD is known then the angles between the fronts in the neighborhood of point K may be defined by solving the following equations:

$$p_4 = p_3 \left(\cos \sqrt{\frac{\gamma_2 - 1}{\gamma_2 + 1}} \phi \right)^{\Gamma} \quad \left(\Gamma = \frac{2\gamma_2}{\gamma_2 - 1} \right)$$

$$\chi = \phi + \arctg \left(\sqrt{\frac{\gamma_2 - 1}{\gamma_2 + 1}} \operatorname{ctg} \sqrt{\frac{\gamma_2 - 1}{\gamma_2 + 1}} \phi \right)$$

$$\frac{\frac{2}{\gamma_1 - 1} \left(1 - \frac{\gamma_2 \gamma_1 - 1}{\gamma_1 \gamma_2 - 1} \frac{\operatorname{tg}(\phi_1 - \theta)}{\operatorname{tg} \phi_1} \right)}{\frac{\gamma_2 + 1}{\gamma_2 - 1} \frac{\operatorname{tg}(\phi_1 - \theta)}{\operatorname{tg} \phi_1} - 1} = \frac{c_2^2}{c_1^2} \sin^2 \phi_1 \left(1 - \frac{\operatorname{tg}(\phi_1 - \theta)}{\operatorname{tg} \phi_1} \right), \quad (\theta = \chi - \frac{\pi}{2})$$

$$\chi = \angle AKD, \quad \gamma_2 = \gamma_3, \quad p_4 = \frac{2\rho_1}{\gamma_2 + 1} c_2^2 \sin^2 \phi_1$$

Here p_4 = pressure along the lines of the contact discontinuity AK and in area IV, ϕ = angle between the direction KD and the corresponding characteristic (ϕ is excluded from the first two equations); ϕ_1 = angle between direction of flow in Region I and the front of the oblique shock wave KB, θ = angle of deflection of the flow to shock wave KB; values p , χ , ϕ , θ , may be calculated expressing them through p_3 , c_1 , c_2 , γ_1 , γ_2 , γ_3 .

Taking into consideration that the velocity of sound c_2 is equal to 1.4 km/sec one may suppose that ignition will not be obtained on front KB. The transverse detonation waves, randomly arising along the front KB must immediately escape into the open area behind point K where they are dissipated. The reaction of the gas can take place at point B after the oblique shock wave KB is reflected from the solid wall.

The inner and outer walls of the annular channel were subjected to more severe action by the moving waves than the middle part. After every 5 or 6 experiments the upper transparent wall made of plastic acquired an erosion in the area indicated in Figure A2. It is characteristic that as a result of the action of the reflecting waves the inner and outer edges of the channel were eroded to a greater extent than the middle area.

We will construct two radial control surfaces normal to the annular channel, one ahead of the front of the detonation wave and the other behind at a distance equal to a few widths of the channel. Regarding these two control surfaces it is possible to write the equations of conservation mass, momentum, and energy. In composing the relations in distinction to the usual method, it is necessary to take into consideration the fact that mass and energy are distributed along the transverse section unequally and therefore the values in the equations pertain to the entire transverse section rather than a single section of the stream.

$$(h - \Delta\ell) \rho_2 c_2 + \Delta\ell \rho_1 c_2 = \rho_* v_* h = jk$$

$$hp_1 + (h - \Delta\ell) \rho_2 c_2^2 + \Delta\ell \rho_1 c_2^2 = p_* h + hp_* v_*^2$$

$$p_1 h c_2 + \epsilon_2 \rho_2 (h - \Delta\ell) c_2 + \epsilon_1 \rho_1 \Delta\ell c_2 + \frac{1}{2} \rho_2 c_2^3 (h - \Delta\ell) + \frac{1}{2} \rho_1 c_2^3 \Delta\ell =$$

$$p_* h v_* + \epsilon_* \rho_* h v_* + \frac{1}{2} \rho_* h v_*^3$$

The left side of the equation relates to the control surface ahead of the detonation front while the right side relates to the surface behind the front. The flow becomes homogeneous at the second control surface. In the last equation ϵ = internal energy of a unit of mass. The difference $\epsilon^* - \epsilon_1 = q$ is equal to the heat generated by the burning of a unit of mass of the original mixture.

In connection with the fact that the known velocity c_2 of the moving stream enters into the solution of the equations, it follows that it is possible to calculate the pressure at the second control surface. The detonation in the annular channel moves in such a way that if a quantity of heat is generated along front AB it will be distributed evenly along the entire section of the channel. In the given case the gas is converted from its original state to products of combustion not along the Hugoniot curve but along an adiabatic. The adiabatic corresponding to the products of detonation is situated parallel to and a small distance from the adiabatic for the initial mixture.

It is particularly essential to observe the process of eflux of the burned mixture in the annular channel. The burned mixture is conducted through a convergent aperture leading to the gas receiving tank where a pressure of 500-600 mm Hg-static is maintained. Firing of the apparatus establishes a shock impulse on the valve. All of the ignition spark discharges are united parallel to one another in the ignitor. The period of each discharge has a duration of 10^{-6} sec.

Under conditions where $C_1 \gg C_2 + C_3 + C_4 + \dots$ the charge on the capacitors C_2, C_3, \dots will increase to twice the original charge if it is not interrupted by a corresponding gap in the spark interval. After the opening of the valve, the flow of the inlet gaseous mixture proceeds under conditions of critical flow for which the expressions of velocity, density, and mass flow of the gaseous mixture have the following forms:

$$v_k = c_0 \sqrt{\frac{2}{\gamma + 1}}, \quad \rho_k = \rho_0 \left(\frac{2}{\gamma + 1} \right)^{\frac{1}{\gamma - 1}},$$

$$Q = v_k \rho_k s_1 = s_1 c_0 \rho_0 \left(\frac{2}{\gamma + 1} \right)^{\frac{\gamma + 1}{2(\gamma - 1)}}$$

Here s_1 is the minimum area of the inlet aperture.

The area of the exhaust aperture we will call s_2 . Then taking into consideration that the velocity of sound in the detonation channel is equal to D we have:

$$\rho_{2k} = \frac{Q}{s_2 v_{2k}}, \quad v_{2k} = D \sqrt{\frac{2}{\gamma + 1}}$$

$$\rho_{2k} = \frac{s_1 c_0 \rho_0}{s_2 D} \left(\frac{2}{\gamma + 1} \right)^{\frac{1}{\gamma - 1}}, \quad \rho_{20} = \rho_{2k} \left(\frac{2}{\gamma + 1} \right)^{\frac{1}{\gamma - 1}}$$

$$\rho_{20} = \frac{s_1 c_0 \rho_0}{s_2 D}$$

For the pressure in the annular channel we have.

$$\rho_{2_0} = \frac{\rho_{2_0}}{\gamma} D^2 = \frac{s_1 c_0 D \rho_0}{s_2^\gamma}, \quad p_{2_0} = \frac{s_1 D}{s_2 c_0} p_0 \quad (2)$$

The conditions of the critical flow at the minimum area of the supply aperture may be calculated in such a case if.

$$p_{2_0} < p_* = p_0 \left(\frac{2}{\gamma + 1} \right)^{\frac{\gamma}{\gamma - 1}} \quad (3)$$

where p_* = the critical pressure. From here substituting the value of p_0 from expression (2) we will have

$$p_{2_0} < p_{2_0} \frac{s_2 c_0}{s_1 D} \left(\frac{2}{\gamma + 1} \right)^{\frac{\gamma}{\gamma - 1}}, \quad \frac{s_1}{s_2} < \frac{c_0}{D} \left(\frac{2}{\gamma + 1} \right)^{\frac{\gamma}{\gamma - 1}}$$

During the experiment on the maintained detonation significant difficulty arose in connection with a flash-back of the flame into the supply reservoir. The flash-backs occurred when the initial pressure in the receiving tank exceeded 570 mm H_g-static. A decrease in the width of the aperture through which the unburned gas enters increases the upper limit of pressure under which a maintained detonation may be obtained. The shape of the transverse section of the annular channel is extremely important. The passage connecting the channel and the supply aperture must have a steep profile as shown in Figure A2. A maintained detonation is not obtainable in a channel having a smooth transition to the supply aperture inasmuch as any disturbance arising in the detonation channel is continually reinforced when it enters a smoothly tapering aperture the width of which is less than the width of the channel. A smooth passage from the inlet aperture to the channel would allow a supersonic flow to develop in the original mixture entering the channel. A great number of experiments using such smooth passages was conducted yet under all pressures a flash-back occurred while below a certain limit of pressure the detonation was extinguished.

The velocity of the propagation of a multi-headed maintained detonation as measured on the photorecorder (for example, Figure A3) reached 1.4 km/sec, a value equal to the velocity of sound in the products of combustion. If the course of the detonation is impaired in any way, for example by using an original mixture that approaches the limit of detonation or by varying the width of the channel, then the number of fronts will begin to decrease with the result

that the velocity of the front will approach the normal velocity as calculated according to the Chapman-Jouguet hypotheses.

Thus the velocity of the maintained detonation increases with a deterioration of the conditions of the flow. The velocity will vary within the limits of the velocity of sound in the burned products and the normal velocity of a detonation in the limiting mixture.

In every experiment the pressure in the supply reservoir decreased with the outflow of the mixture. Corresponding to this a decrease in the number of heads toward the end of the process was noticed on the photorecord along with a simultaneous increase in the velocity of detonation.

Concerning the external characteristics of the flame of a maintained detonation, it should be mentioned that this flame was of a blue-green color, and not yellow as in ordinary combustion.

Because of the instantaneous burning of the carbon atoms, no recombination into large groups is possible, and this evidently leads to a more complete burning of the explosive mixture.

A maintained detonation is accompanied by the production of monochromatic sound with a frequency n_f , where n is the number of fronts, and f is the frequency of rotation of each front.

Reference A1. Nicholls, Dabora and Gealer, "Studies in Connection with Stabilized Detonation Waves," Vopr Reactiv Tech. 1959, No. 11.

- 1 Annular Channel
- 2 Upper Transparent Wall
of the Annular Channel
Made of Plastic Glass
- 3 Photorecorder
- 4 Valve
- 5 Gas Supply Reservoir with
Initial Mixture
- 6 Tank Which Receives the
Burned Gas After Being
Initially Pumped Down to
the Correct Pressure
- 7 Direction of the Starting
Impulse
- 8 Central Channel Which Con-
ducts the Initial Mixture to
the Detonation Annulus
- 9 Exhaust Manifold

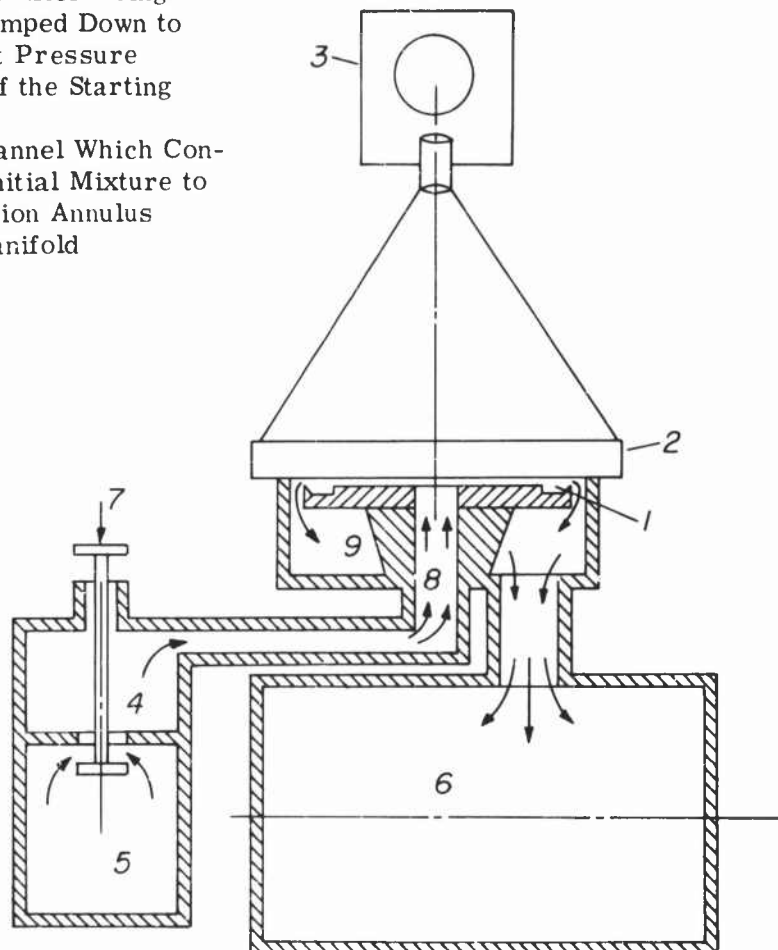


Figure A1. General Arrangement of the Apparatus in which a Maintained Cyclic Detonation Takes Place .

- 1 Annular Channel
- 2 Disk Made of Plastic Glass
- 3 Erosion Made in 3-4 Seconds by a Maintained Detonation
- 4 Steel Plate

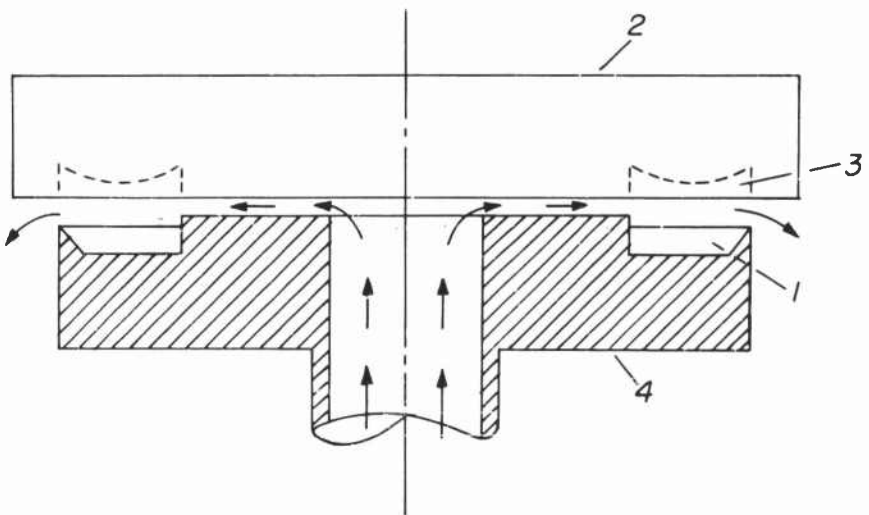


Figure A2. The Transverse Section of the Annular Detonation Channel.

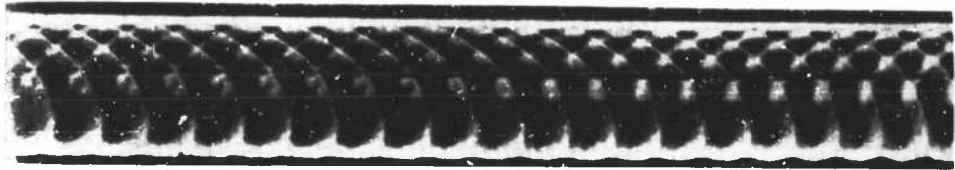


Figure A3. A Typical Photorecord of a Maintained Detonation .

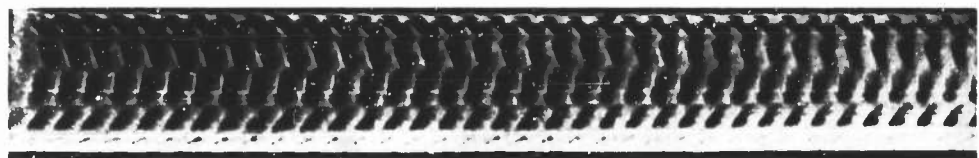


Figure A4. Photorecord of a Pulsating Maintained Detonation .

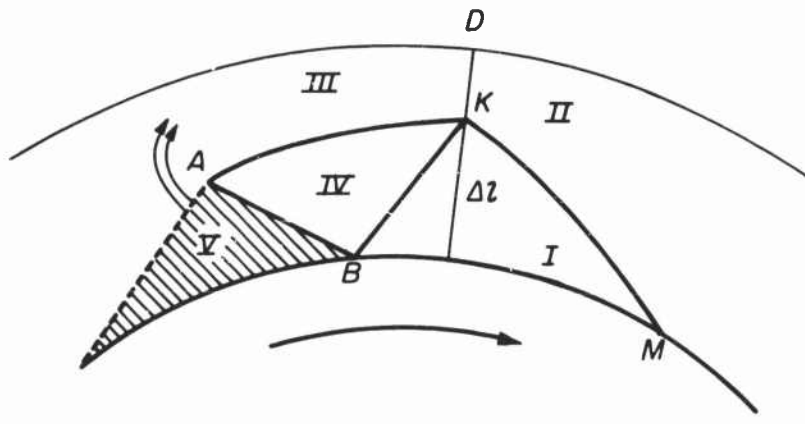


Figure A5. General Arrangement of the Distribution of Fronts in the Neighborhood of one of the Maintained Detonation Waves.

APPENDIX B. 1. COMPUTER PROGRAM FOR THE BLOCKED INJECTOR $(\bar{d}_p = 0)$ EQUATIONS

To facilitate the computation of M , \bar{v} , and \bar{P} as functions of $B\eta$ and γ the following was programmed.

```

$COMPILE MAD, EXECUTE, DUMP, PRINT OBJECT
      RSOLUTION OF THE BLOCKED INJECTOR CASE
      DIMENSION Y(9000),D(1),D(3)
      VECTOR VALUES D(1)=2,7,5
READ   READ FORMAT INPUT,K,DM,N
      READ FORMAT INPUT,K,DM,N
      WHENEVER K.LE.1., TRANSFER TO READ
      KK=(K+1.)/(K-1.)*SQRT.(2./(K-1.))
      KKK=N/(K-1.)
      THROUGH PETE, FOR J=0,1,J.G.N
      WHENEVER J.L.1
      Y(J,0)=0.
      Y(J,1)=1.
      OTHERWISE
      Y(J,1)=Y(J-1,1)+DM
      Y(J,0)=2./(K-1.)*(Y(J,1)-1.)-KK*ATAN.(SQRT.((K-1.)/2.)*
      1.(Y(J,1)-1.)/(1.+(K-1.)/2.*Y(J,1)))
      END OF CONDITIONAL
      Y(J,2)=Y(J,1)*SQRT.((K+1.)*5./(1.+(K-1.)/2.*Y(J,1).P.2))
      Y(J,3)=( (K+1.)/2. / (1.+(K-1.)/2.*Y(J,1).P.2)).P.KKK
      Y(J,4)=SQRT.((K+1.)/2.*Y(J,0))
      PRINT FORMAT OUTPUT,K,Y(0,0)...Y(N,4)
      TRANSFER TO READ
      INTEGER J,N
      VECTOR VALUES INPUT =$F7.3,E12.3,S1,I3*$_
      VECTOR VALUES COUTPUT =$S10,47HSOLUTION FOR THE BLOCKED INJECT
      OR CASE WITH K =,F7.3//S13,5H8*ETA,S9,1HM,S11,1HV,S11,1HP,S11
      2,5HM - 1/(S10,5F12.8)*$
      END OF PROGRAM
$DATA

```

<u>Program Symbol</u>	<u>Equivalent Engineering Symbol</u>
DM	ΔM (program input indicating the desired step size in M from one computation to the next)
K	γ
N	(program input, total number of computational steps)
Y(J, 0), B*ETA	$B\eta$
Y(J, 1), M	M
Y(J, 2), V	\bar{v}
Y(J, 3), P	\bar{P}
Y(J, 4), M-1	$M-1$ (approximate value)

Some computational results for $\gamma = 1.2$ are given in Table 2 and are plotted in Figure 1.

APPENDIX B. 2. COMPUTER PROGRAM FOR THE COMPLETE MIXING CASE PROBLEM

The following computer program was developed to solve numerically the problem of the complete mixing case equations.

```
$COMPILE MAD, EXECUTE, DUMP, PRINT OBJECT
      RRUNGE-KUTTA SOLUTION OF THE COMPLETE MIXING CASE
      DIMENSION Q(10),JC(5),Y(3),F(3),A(9000,D(1)),D(3)
      VECTOR VALUES D(1) = 2,10,8
      EXECUTE SETRKD.(N,Y(1),F(1),Q,X,H)
      N=3
READ      READ FORMAT INPUT ,ETAGO,DETA,C,L,K,KA,KB,G,TP,B,VW
          K2=TP+(K-1.)/2.*VW.P.2
          K1=B+G*(K*VW-(K+1.)/2.-K2)
          WHENEVER K1.LE.0.
          PRINT FORMAT NOGO, K1
          VECTOR VALUES NOGO =$20HDATA INCORRECT, K1 =,E15.8*$
          TRANSFER TO READ
          END OF CONDITIONAL
          THROUGH SAM, FOR I=0,1,I.G.7
SAM        A(0,I)=0.
          A(1,0)=ETAGO
          A(1,1)=SQRT.((K+1.)/2.*K1*ETAGO)
          A(1,2)=SQRT.(2./(K+1.)*K1*ETAGO)
          A(1,3)=K*A(1,2)
          X=A(1,0)
          THROUGH PETE, FOR I=1,1,I.G.3
PETE       Y(I)=A(1,I)
          THROUGH KATE, FOR I=1,1,I.G.5
KATE       JC(I)=0.
          LL=1
          M=1
CRAWL     WHENEVER X+C*X.LE.DETA
          H=C*X
          OR WHENEVER L.G.0
          H=C*DETA
          OR WHENEVER X+C*DETA.GE.1.
          H=1.-X
          L=M
          LL=0
          OTHERWISE
          H=C*DETA
          END OF CONDITIONAL
```

```

JOE
AA=VW/(Y(2)+1.)-1.
MM=1.+K*(Y(1)+1.)/2.*P.2
BB=(Y(1)+1.)/(Y(2)+1.)*P.2*K2-MM
MN=Y(1)*(Y(1)+2.)
MP=1.+K*(Y(1)+1.)*P.2
MC=(Y(2)+1.)*G/((1.-Y(3))*(Y(1)+1.))
F(1)=MM/MN*(B+(-1.+K*(Y(1)+1.)*P.2*AA-.5*MP*BB/MM)*MC)
F(2)=(Y(2)+1.)/MN*(B/(Y(1)+1.)+(-1.+K*(Y(1)+1.)*P.2*AA-BB)
*MC/(Y(1)+1.))
F(3)=K*(1.-Y(3))/MN*(B*(Y(1)+1.))+(-1.+((1.+K-1.)*(Y(1)+1.)*P.
1
1
WHENEVER RKDEQ.(0).E.1., TRANSFER TO JOE
M=M+1
THROUGH CARL, FOR I=1,1,I.G.3
A(M,I)=Y(I)
A(M-1,I+3)=F(I)
A(M,0)=X
WHENEVER L.L.1, TRANSFER TO CRAWL
WHENEVER M.LE.L, TRANSFER TO CRAWL
THROUGH DORA, FOR I=1,1,I.G.M
A(I,7)=A(I-1,7)+.5*(1.-A(I-1,7))*G*((A(I,2)+1.)/((1.-A(I,3))*A(I,1)+1.)*P.2)+(A(I-1,2)+1.)/((1.-A(I-1,3))*(A(I-1,1)+1.)*P.2)*(A(I,0)-A(I-1,0))
CONTINUE
WHENEVER LL.L.1
JC(2)=1.-KB*Y(2)
JC(1)=SQRT.(KB*(Y(2)+1.)/(KA*JC(2)))
JC(3)=Y(1)+1.
JC(4)=1.-Y(3)
JC(5)=((KB+1.)/2.+((KB-1.)/2.*KA+1.)/(KA-1.))*((Y(2)+1.)*P.2
1
1
-2.*((Y(2)+1.)*KA/KB*(KB+1.)/(KA+1.)))/A(M,7)
END OF CONDITIONAL
THROUGH ZAP, FOR I=1,1,I.G.3
A(M,I+3)=0.
PRINT FORMAT OUTPUT, K,KA,KB,TP,G,B,VW,A(0,0)...A(M,7)
PRINT FORMAT JUMP, JC(1)...JC(5)
TRANSFER TO READ
INTEGER I,L,LL,M,N
VECTOR VALUES INPUT = $S11,3E10.3,I3/S11,5E10.3/S11,2E10.3*$S
VECTOR VALUES OUTPUT=$S10,44HRUNGE-KUTTA SOLUTION, COMPLETE M
1IXING CASE //S10,3HK =,F7.3,S3,4HKA/,=,F7.3,S3,4HKB =,F7.3,
2S3,4HTP.,=,E10.3//S10,3HG =,F7.3,S3,4H B =,F7.3,S3,4HVW =,E10.
33//S15,1HX,S9,5HM - 1,S7,5HV - 1,S7,5H1 - P,S8,2HF1,S8,2HF2,
4S8,2HF3,S8,2HML/(S10,4F12.8,3E10.3,F10.6)*$*
VECTOR VALUES JUMP = $S10,5HM1J =,F9.5,S3,5HP1J =,F8.5,S3,
16HM1DE =,F9.5,S3,6HP1DE =,F8.5,S3,6HQBAR =,E12.5*$*
END OF PROGRAM
$DATA

```

Program SymbolEquivalent Engineering Symbol

K, KA, KB	γ
G	G
\bar{T}_p	\bar{T}_p
B	B
VW	\bar{V}_w
A(J, 0), X	η
A(J, 1), M-1	M-1
A(J, 2), V-1	$\bar{v}-1$
A(J, 3), 1-P	$1-\bar{P}$
A(J, 4), F(1)	$f_1/(M-1)$
A(J, 5), F(2)	$f_2/(M-1)$
A(J, 6), F(3)	$f_3/(M-1)$
A(J, 7), MU	μ
MIDE	M_1 (calculated from the differential equations)
MIJ	M_1 (calculated from the jump conditions)
PIDE	P_1 (calculated from the differential equations)
PIJ	P_1 (calculated from the jump conditions)
QBAR	\bar{Q}

The problem solution for G = 1, $\bar{T}_p = .0743$ (propellant injected at ambient temperature) and $\gamma = 1.25$ appears in Table 3 and Figure 2.

APPENDIX B. 3. COMPUTER PROGRAM FOR THE GASEOUS, NO-MIXING CASE PROBLEM

The following computer program was developed to solve numerically the problem of the gaseous no mixing case equations.

```
$COMPILE MAD, EXECUTE, DUMP, PRINT OBJECT
      RRUNGE-KUTTA SOLUTION OF THE NO MIXING CASE
      EXECUTE SETRKD,LN,Y(1),F(1),Q,X,H
      DIMENSION Q(10),JC(4),Y(3),F(3),A(9000,D(1)),D(3)
      VECTOR VALUES D(1)=2,18,16
      DIMENSION YS(2),E(100)
      INTEGER I,M,N,END,J,WW
      G=1.
      TP=270./6625.2
      KA=1.5
      KB=1.15
      CPA=KA/KB*(KB-1.)/(KA-1.)*1.258
      N=2
      E(1)=.001
      E(2)=.005
      E(3)=.01
      E(4)=.02
      E(5)=.05
      THROUGH SAM, FOR I=1,1,I,G.19
      K=I
      SAM
      READ FORMAT INPUT, B,VW
      VECTOR VALUES INPUT = $S10,F10,6,F10.6*
      HP=(KA-1.)/(KB-1.)*CPA*TP+(KA-1.)/2.*VW.P.2
      A(0,0)=0.
      A(0,1)=VW*SQRT.((KB-1.)/((KA-1.)*CPA*TP))
      A(0,2)=1.
      A(0,3)=1.
      A(0,4)=0.
      A(0,5)=VW
      A(0,6)=1.
      A(0,7)=0.
      A(0,8)=VW-1.
      A(0,9)=TP
      A(0,10)=1.
      A(0,11)=KA/KB*(KB-1.)/((KA-1.)*CPA*TP)
      A(0,12)=1.
      A(0,13)=0.
      A(0,14)=1.
      A(0,15)=1.
      X=.0001
      Y(1)=KB/(KA*A(0,1))*(1.+(KA-1.)/2.*A(0,1).P.2)*SQRT.(2./(KB+1
      1.)*(B-G/(A(0,11)*VW))*X)
      Y(2)=SQRT.((KB+1.)/2.*(B-G/(A(0,11)*VW))*X)
      M=0
      J=0
      END=0
      WW=0
```

```

RAK      WHENEVER RAK, .E.1., TRANSFER TO JOE
        H=E(M+1)-X
        M=M+1
        OTHERWISE
        H=.1*X
        J=1
        END OF CONDITIONAL
JOE      MA=Y(1)+A(0,1)
        MB=Y(2)+1.
        MMA=1.+((KA-1.)/2.*MA.P.2
        MMB=1.+((KB-1.)/2.*MB.P.2

        ZI=SQRT.(HP/MMA)/MA*(2./(KB+1.)*MMB).P.(KB/(KB-1.))*KB/KA*G*X
        VA=MA*SQRT.(HP/MMA)
        RA=KA/KB*MMA/HP*((KB+1.)/2.*MMB).P.(KB/(KB-1.))
        MPA=1.+((KA-1.)*MA.P.2
        MPB=1.+((KB-1.)*MB.P.2
        DD=ZI*(KB*MB.P.2/(KA*MA.P.2)*MPA-MPB)-Y(2)*(Y(2)+2.)
        F(1)=MA*MMA*(KB*MB.P.2/(KA*MA.P.2)*(G/RA/VA-B/MB)-(VW-VA)/VA*
        1G/RA/VA*(MPB+Y(2)*(Y(2)+2.)/ZI))/DD
        F(2)=MR*MMB*(G/RA/VA-B/MB-(VW-VA)/VA*G/RA/VA*MPA)/DD
WHENEVER RKDEQ(.0).E.1., TRANSFER TO JOE
WHENEVER J.E.0
        A(M,0)=X
        A(M,1)=Y(1)+A(0,1)
        A(M,2)=Y(2)+1.
        OTHERWISE
        J=0
        END OF CONDITIONAL
WHENEVER M.L.24.AND.END.L.1, TRANSFER TO RAK
THROUGH WHO, FOR I=1,1,I.G.M
MMA=1.+((KA-1.)/2.*A(I,1).P.2
MMB=1.+((KB-1.)/2.*A(I,2).P.2
A(I,3)=((KB+1.)/2./(1.+(KB-1.)/2.*A(I,2).P.2)).P.(KB/(KB-1.))
A(I,4)=SQRT.(HP/MMA)/A(I,1)/A(I,3)*KB/KA*G*A(I,0)
A(I,5)=A(I,1)*SQRT.(HP/MMA)
A(I,6)=A(I,2)*SQRT.((KB+1.)/2./(1.+(KB-1.)/2.*A(I,2).P.2))
A(I,7)=VW-A(I,5)
A(I,8)=VW-A(I,6)
A(I,9)=(KB-1.)/(KA-1.)/CPA*HP/(1.+(KA-1.)/2.*A(I,1).P.2)
A(I,10)=(KB+1.)/2./(1.+(KB-1.)/2.*A(I,2).P.2)
A(I,11)=KA/KB*MMA/HP*A(I,3)
A(I,12)=A(I,3)/A(I,10)
A(I,13)=A(I,11)*A(I,5)*A(I,4)
A(I,14)=A(I,12)*A(I,6)*(1.-A(I,4))
A(I,15)=A(I,13)+A(I,14)
SS=KA/KB*(KB+1.)/(KA+1.)
JC(1)=SS+SQRT.(SS.P.2-2./((KA+1.)*HP)
JC(2)=1.-KB*(JC(1)-1.)
WHENEVER JC(2).LE.0.
        VW=1
        JC(3)=0.
        OTHERWISE
        JC(3)=SQRT.(KB/KA*JC(1)/JC(2))
END OF CONDITIONAL

```

```

JC(4)=(KB+1.)/2-(KB-1.)/(KA-1.)*HP
N=2
PRINT FORMAT TITLE, G,TP,KA,KB,CPA,B,VW
PRINT FORMAT HEAD
PRINT FORMAT OUTPUT, A(0,0)...A(24+END,15)
WHENEVER WW.F.1
PRINT FORMAT NOGOOD, JC(2)
VECTOR VALUES NOGOOD = $S5,19HDATA NO GOOD, P1J =,E12.5*$
END OF CONDITIONAL
PRINT FORMAT JUMP,JC(1)...JC(4)
TRANSFER TO READ
VECTOR VALUES TITLE = $1H1,S9,30HSOLUTION TO THE NO MIXING CAS
1E/S10,3HG =,F8.5,S3,4HTP =,F8.5,S3,4HKA =,F8.5,S3,4HKB =,
2F8.5,S3,5HCPA =,F8.5/S10,3HB =,F8.5,S3,4HVW =,F8.5*$
VECTOR VALUES HEAD = $S2,3HETA,S4,2HMA,S6,2HMB,S6,1HP,S7,2HZI,
1S5,2HVA,S5,2HVB,S5,3HVAA,S4,3HVBA,S4,2HTA,S5,2HTB,S4,4HRHOA,S
23,4HRHOB,S3,4HRVZA,S3,4HRVZB,S3,4HMDOT*$*
VECTOR VALUES OUTPUT = $(S1,F5.3,4F8.5,11F7.4)*$*
VECTOR VALUES JUMP = $S10,6HVA1J =,F8.5,S3,5HP1J =,F7.5,S3,
16HMA1J =,F8.5,S3,6HQBAR =,F8.5*$*
END OF PROGRAM
$DATA

```

<u>Program Symbol</u>	<u>Equivalent Engineering Symbol</u>
G	G
\bar{T}_p	\bar{T}
KA	γ_A
KB	γ_B
CPA	\bar{C}_{P_A}
B	B
VW	\bar{V}_w
A(J, 0), ETA, X	η
A(J, 1), MA	M_A
A(J, 2), MB	M_B
A(J, 3), P	\bar{P}
A(J, 4), ZI	ξ

<u>Program Symbol</u>	<u>Equivalent Engineering Symbol</u>
A(J, 5), VA	\bar{v}_A
A(J, 6), VB	\bar{v}_B
A(J, 7), VAA	$\bar{v}_A a$
A(J, 8), VBA	$\bar{v}_B a$
A(J, 9), TA	\bar{T}_A
A(J, 10), TB	\bar{T}_B
A(J, 11), RHφA	ρ_A
A(J, 12), RHφB	ρ_B
A(J, 13), RVZA	$\rho_A \bar{v}_A \xi$
A(J, 14), RVZB	$\rho_B \bar{v}_B (1-\xi)$
A(J, 15), MDφT	\dot{m}
VALJ	\bar{v}_A (calculated from jump conditions)
PIJ	\bar{P}_1 (calculated from jump conditions)
MAIJ	M_{A_1} (calculated from jump conditions)
QBAR	\bar{Q}

Problem solutions for (a) $G = 1$, $\bar{T}_p = 0.081$ ($\bar{T}_p \approx 540^0R$), $\bar{C}_{P_A} = 0.54968$, $\gamma_A = 1.401$, and $\gamma_B = 1.15$ and (b) $G = 1$, $\bar{T}_p = 0.04075$, $\bar{C}_{P_A} = 0.49226$, $\gamma_A = 1.5$ and $\gamma_B = 1.15$ appear in Tables 4 and 5 and Figures 3 and 4, respectively.

APPENDIX B. 4. COMPUTER PROGRAM FOR THE LIQUID-GASEOUS NO-MIXING CASE PROBLEM

The following computer program was developed to solve numerically the problem of the liquid-gaseous no-mixing case.

```
$COMPILE MAD, EXECUTE, DUMP, PRINT OBJECT
      RRUNGE-KUTTA SOLUTION OF THE NO MIXING CASE
      EXECUTE SETRKD=(N,Y(1),F(1),Q,X,H)
      DIMENSION Q(10),JC(4),Y(3),F(3),A(9000,D(1)),D(3)
      VECTOR VALUES D(1)=2,18,16
      DIMENSION YS(2),F(100)
      INTEGER I,M,N,END,J,WW
      XG=2./3.
      MWG=2.016
      MWL=32.
      G=MWG*XG/(MWG*XG+MWL*(1.-XG))
      TP=270./6625.2
      KA=1.5
      KB=1.15
      CPA=KA/KB*(KB-1.)/(KA-1.)*1.258*12.011/2.016
      N=2
      E(1)=.001
      E(2)=.005
      E(3)=.01
      E(4)=.02
      E(5)=.05
      THROUGH SAM, FOR I=1,1,I.G.19
      K=I
      SAM
      READ      E(I+5)=(1.+K)*.05
      READ FORMAT INPUT, B,VW
      VECTOR VALUES INPUT = $S10,F10.6,F10.6*$
      HP=(KA-1.)/(KB-1.)*CPA*TP+(KA-1.)/2.*VW*P.2
      A(0,0)=0.
      A(0,1)=VW*SQRT.((KB-1.)/((KA-1.)*CPA*TP))
      A(0,2)=1.
      A(0,3)=1.
      A(0,4)=0.
      A(0,5)=VW
      A(0,6)=1.
      A(0,7)=0.
      A(0,8)=VW-1.
      A(0,9)=TP
      A(0,10)=1.
      A(0,11)=KA/KB*(KB-1.)/((KA-1.)*CPA*TP)
      A(0,12)=1.
      A(0,13)=0.
      A(0,14)=1.
      A(0,15)=1.
      X=.0001
      Y(1)=KB/(KA*A(0,1))*(1.+(KA-1.)/2.*A(0,1)*P.2)*SQRT.(2./(KB+1
      1.)*(B-G/(A(0,11)*VW))*X)
      Y(2)=SQRT.((KB+1.)/2.*(B-G/(A(0,11)*VW))*X)
      M=0
      J=0
      END=0
      WW=0
```

```

RAK      WHENEVER 1.1*X.GE.E(M+1)
H=E(M+1)-X
M=M+1
OTHERWISE
H=.1*X
J=1
END OF CONDITIONAL
JOE      MA=Y(1)+A(0,1)

MB=Y(2)+1.
MMA=1.+((KA-1.)/2.*MA.P.2)
MMB=1.+((KB-1.)/2.*MB.P.2)
ZI=SQRT.(HP/MMA)/MA*(2./((KB+1.)*MB).P.(KB/(KB-1.))*KB/KA*G*X
VA=MA*SQRT.(HP/MMA)
RA=KA/KB*MMA/HP*((KB+1.)/2./MMB).P.(KB/(KB-1.))
MPA=1.+((KA-1.)*MA.P.2
MPB=1.+((KB-1.)*MB.P.2
DD=ZI*(KB*MB.P.2/(KA*MA.P.2)*MPA-MPB)-Y(2)*(Y(2)+2.)
F(1)=MA*MMA*(KB*MB.P.2/(KA*MA.P.2)*(G/RA/VA-B/MB)-(VW-VA)/VA*
1G/RA/VA*(MPB+Y(2)*(Y(2)+2.)/ZI))/DD
F(2)=MB*MMB*(G/RA/VA-B/MB-(VW-VA)/VA*G/RA/VA*MPA)/DD
WHENEVER RKDEQ.(0).E.1.,TRANSFER TO JOE
WHENEVER J.E.0
A(M,0)=X
A(M,1)=Y(1)+A(0,1)
A(M,2)=Y(2)+1.
OTHERWISE
J=0
END OF CONDITIONAL
WHENEVER M.L.24.AND.END.L.1,TRANSFER TO RAK
THROUGH WHO, FOR I=1,1,I G.M
MMA=1.+((KA-1.)/2.*A(I,1).P.2
MMB=1.+((KB-1.)/2.*A(I,2).P.2
A(I,3)=((KB+1.)/2./*(1.+(KB-1.)/2.*A(I,2).P.2)).P.(KB/(KB-1.))
A(I,4)=SQRT.(HP/MMA)/A(I,1)/A(I,3)*KB/KA*G*A(I,0)
A(I,5)=A(I,1)*SQRT.(HP/MMA)
A(I,6)=A(I,2)*SQRT.((KB+1.)/2./*(1.+(KB-1.)/2.*A(I,2).P.2))
A(I,7)=VW-A(I,5)
A(I,8)=VW-A(I,6)
A(I,9)=(KB-1.)/(KA-1.)/CPA*HP/(1.+(KA-1.)/2.*A(I,1).P.2)
A(I,10)=(KB+1.)/2./*(1.+(KB-1.)/2.*A(I,2).P.2)
A(I,11)=KA/KB*MMA/HP*A(I,3)
A(I,12)=A(I,3)/A(I,10)
A(I,13)=A(I,11)*A(I,5)*A(I,4)
A(I,14)=A(I,12)*A(I,6)*(1.-A(I,4))
A(I,15)=A(I,13)+A(I,14)
SS=KA/KB*(KB+1.-KA*(1.-G)*VW)/(KA+1.)/G
JC(1)=SS+SQRT.(SS.P.2-2./*(KA+1.)*HP)
JC(2)=1.-KB*(G*JC(1)+(1.-G)*VW-1.)
WHENEVER JC(2).LE.0.
WW=1
JC(3)=0.
OTHERWISE
JC(3)=SQRT.(KB/KA*G*JC(1)/JC(2))
END OF CONDITIONAL
WHO

```

```

JC(4)=(KB+1.)/2.-(KB-1.)/(KA-1.)*HP
N=2
PRINT FORMAT TITLE, G,TP,KA,KB,CPA,B,VW
PRINT FORMAT HEAD
PRINT FORMAT OUTPUT, A(0,0)....A(24+END,15)
WHENEVER WW.E.1
PRINT FORMAT NOGOOD, JC(2)
VECTOR VALUES NOGOOD = $S5,19HDATA NO GOOD, P1J =,E12.5*$
END OF CONDITIONAL
PRINT FORMAT JUMP,JC(1)....JC(4)
TRANSFER TO READ
VECTOR VALUES TITLE = $1H1,S9,30HSOLUTION TO THE NO MIXING CASE
1E/S10,3HG =,F8.5,S3,4HTP =,F8.5,S3,4HKA =,F8.5,S3,4HKB =,
2F8.5,S3,5HCPA =,F8.5/S10,3HB =,F8.5,S3,4HVW =,F8.5*,
VECTOR VALUES HEAD = $S2,3HETA,S4,2HMA,S6,2HMB,S6,1HP,S7,2HZI,
1S5,2HVA,S5,2HVB,S5,3HVAA,S4,3HVBA,S4,2HTA,S5,2HTB,S4,4HRHOA,S
23,4HRHOB,S3,4HRVZA,S3,4HRVZB,S3,4HMDOT*$*
VECTOR VALUES OUTPUT = $(S1,F5.3,4F8.5,11F7.4)*$*
VECTOR VALUES JUMP = $S10,6HVA1J =,F8.5,S3,5HP1J =,F7.5,S3,
16HMA1J =,F8.5,S3,6HQBAR =,F8.5*$*
END OF PROGRAM

```

\$DATA

<u>Program Symbol</u>	<u>Equivalent Engineering Symbol</u>
XG	x_G
MWG	G
MWL	L
G	G
\bar{T}_p	\bar{T}_p
KA	γ_A
KB	γ_B
CPA	$\bar{C}_p A$
B	B
VW	\bar{V}_w
A(J, 0), ETA, X	η
A(J, 1), MA	M_A
A(J, 2), MB	M_B

<u>Program Symbol</u>	<u>Equivalent Engineering Symbol</u>
A(J, 3), P	\bar{P}
A(J, 4), ZI	ξ
A(J, 5), VA	\bar{v}_A
A(J, 6), VB	\bar{v}_B
A(J, 7), VAA	\bar{v}_A^a
A(J, 8), VBA	\bar{v}_B^a
A(J, 9), TA	\bar{T}_A^a
A(J, 10), TB	\bar{T}_B^a
A(J, 11), RHφA	$\bar{\rho}_A$
A(J, 12), RHφB	$\bar{\rho}_B$
A(J, 13), RVZA	$\bar{\rho}_A \bar{v}_A \xi$
A(J, 14), RVZB	$\bar{\rho}_B \bar{v}_B (1-\xi)$
A(J, 15), MDφT	\dot{m}
VALJ	\bar{v}_{A_1} (calculated from jump conditions)
PLJ	\bar{P}_1 (calculated from jump conditions)
MAIJ	M_{A_1} (calculated from jump conditions)
QBAR	\bar{Q}_1

The numerical solution of this problem was not carried to completion.

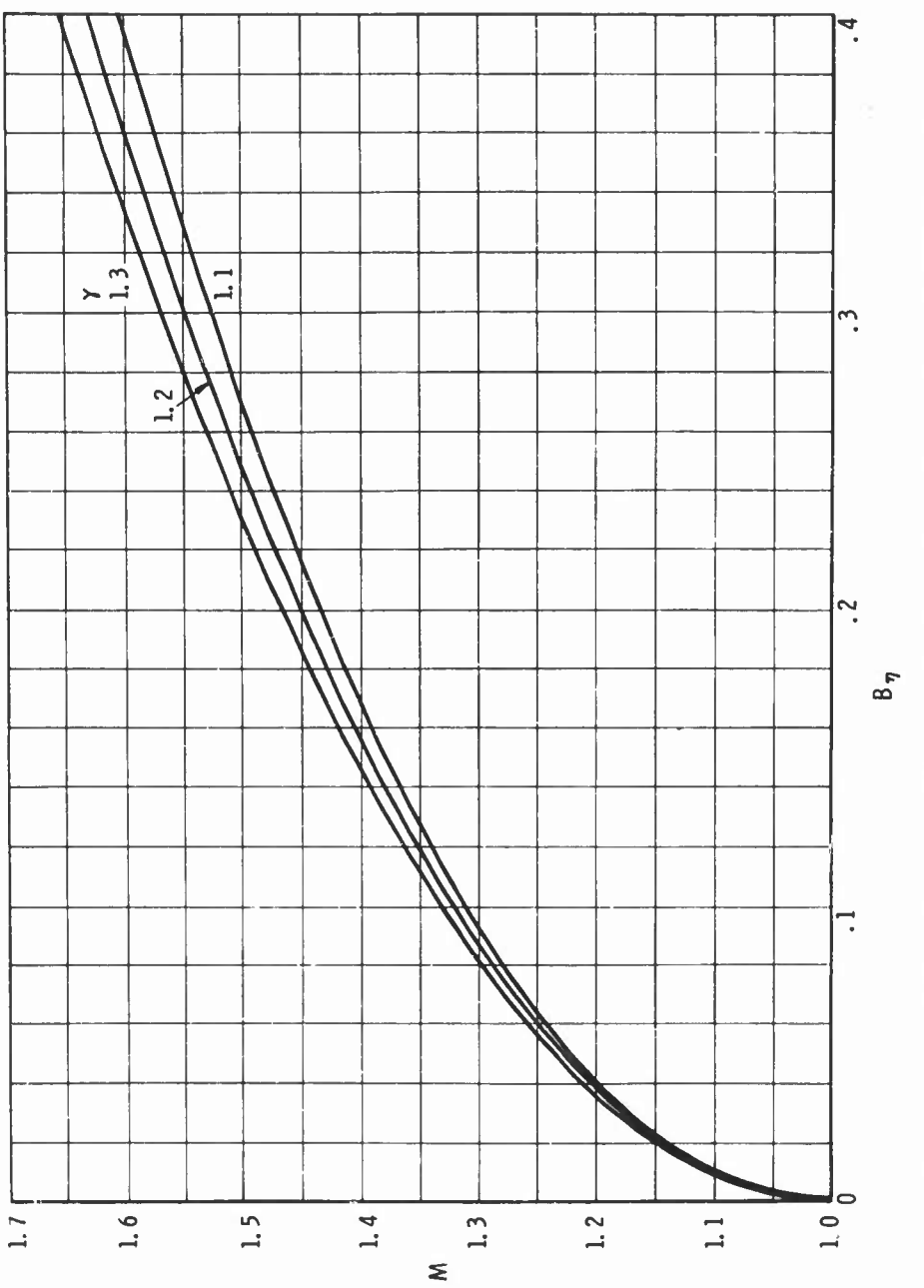


Figure 1(a). Mach Number, M , as a Function of the B_η Product for the Case of a Blocked Injector ($d\dot{m}_p = 0$)

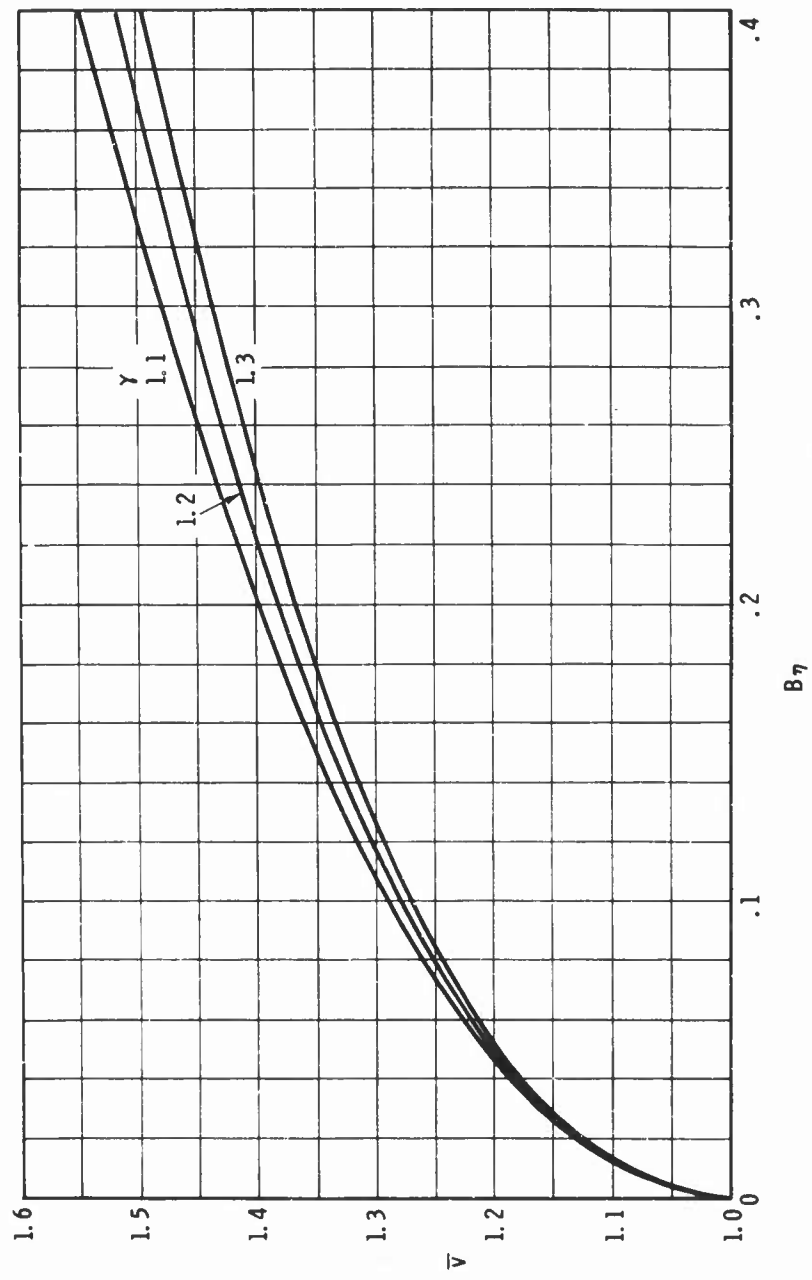


Figure 1(b). Dimensionless Velocity, \bar{v} , as a Function of the B_7 Product for the Case of a Blocked Injector ($d_m = 0$)

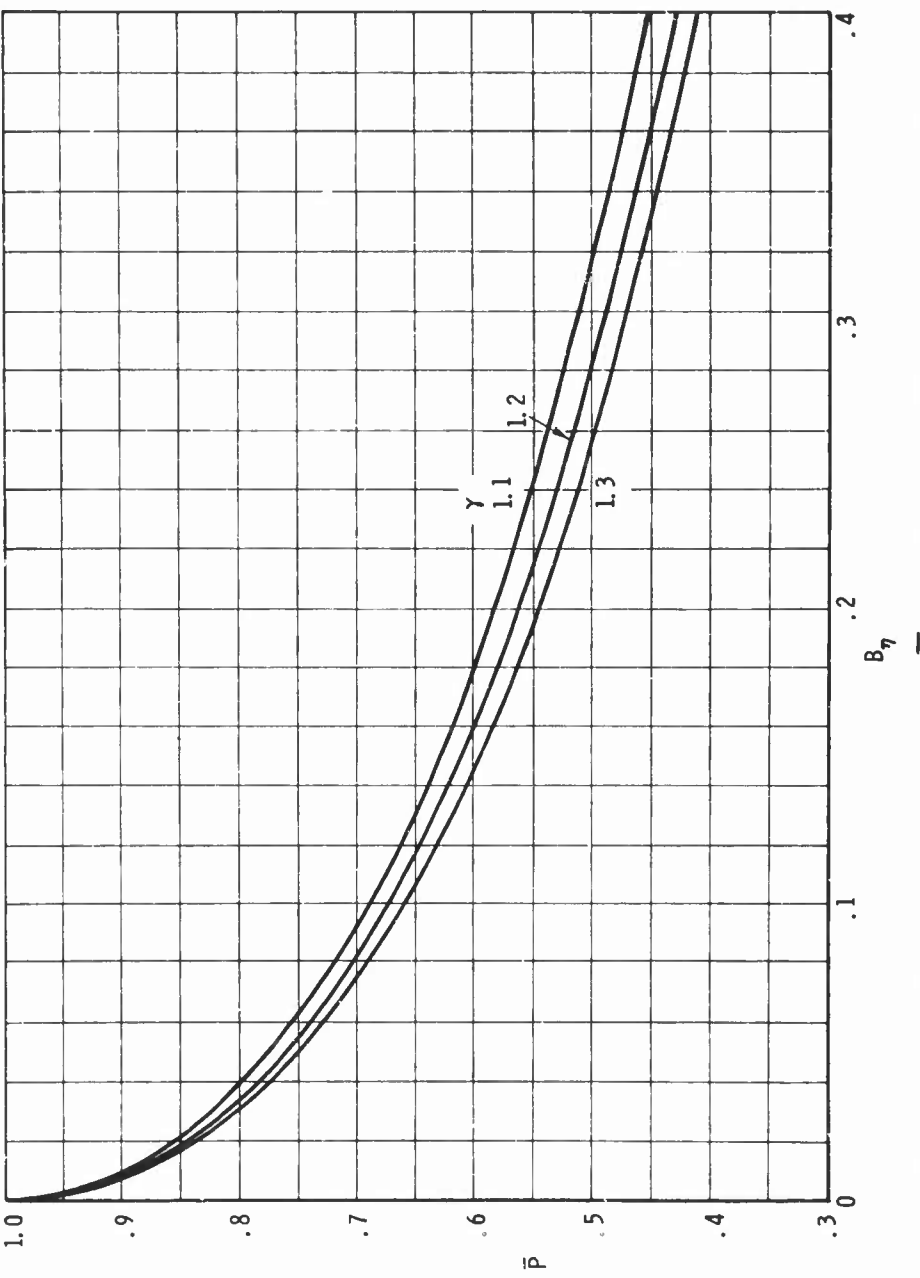


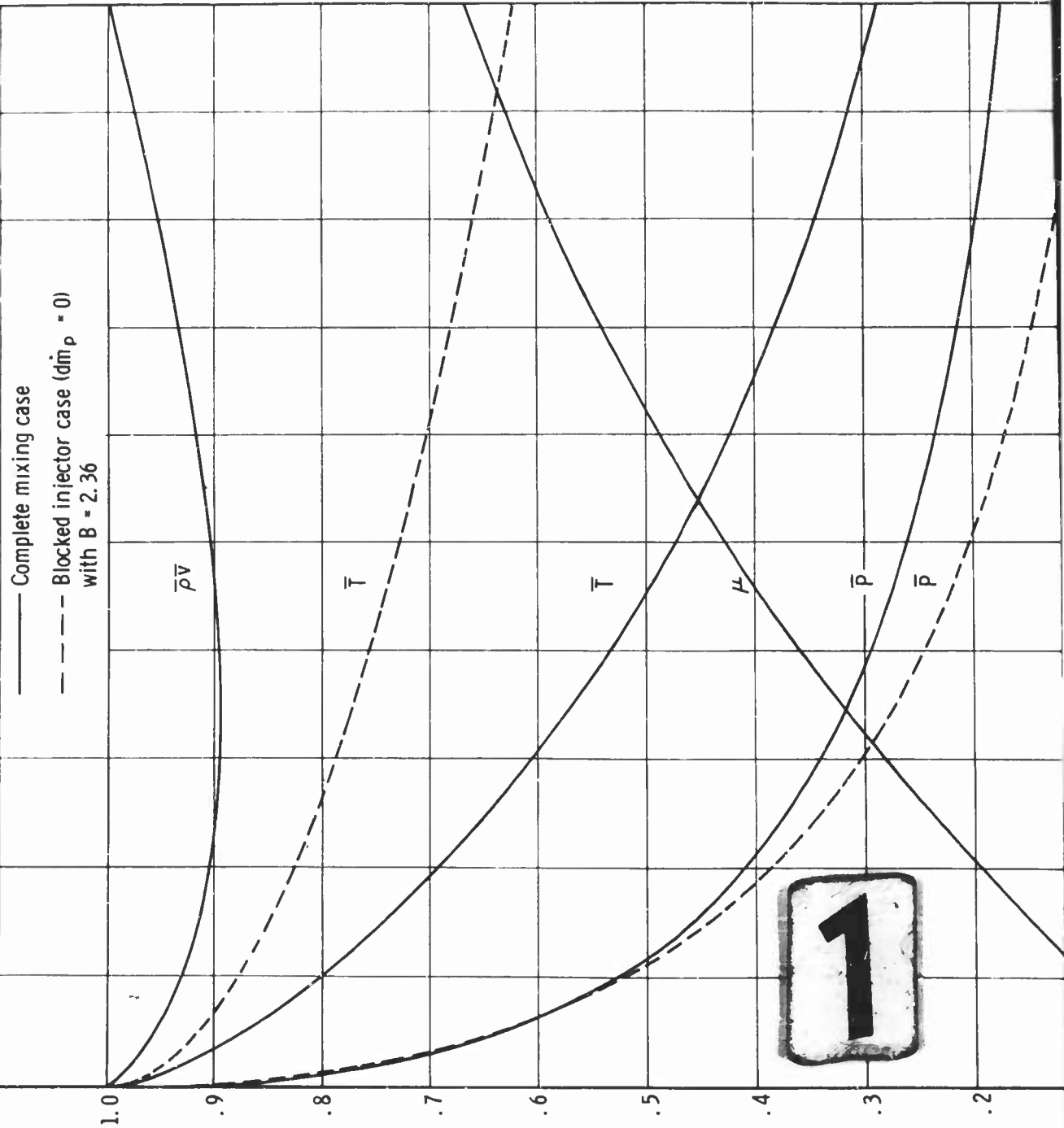
Figure 1(c). Dimensionless Pressure, \bar{P} , as a Function of the $B\eta$ Product for the Case of a Blocked Injector ($\text{dim}_p = 0$)

Solution to the complete mixing case obtained numerically on the IBM 7090 Digital Computer for:

$$\begin{aligned} G &= 1.0 \\ Y &= 1.25 \\ \bar{T}_p &= 0.0743 \end{aligned}$$

The dependent parameters satisfying both the differential equations and the hydrodynamic jump conditions are:

$$\begin{aligned} B &= 2.36 \\ \frac{V_w}{V_p} &= 1.55 \\ \bar{Q} &= 0.741 \end{aligned}$$



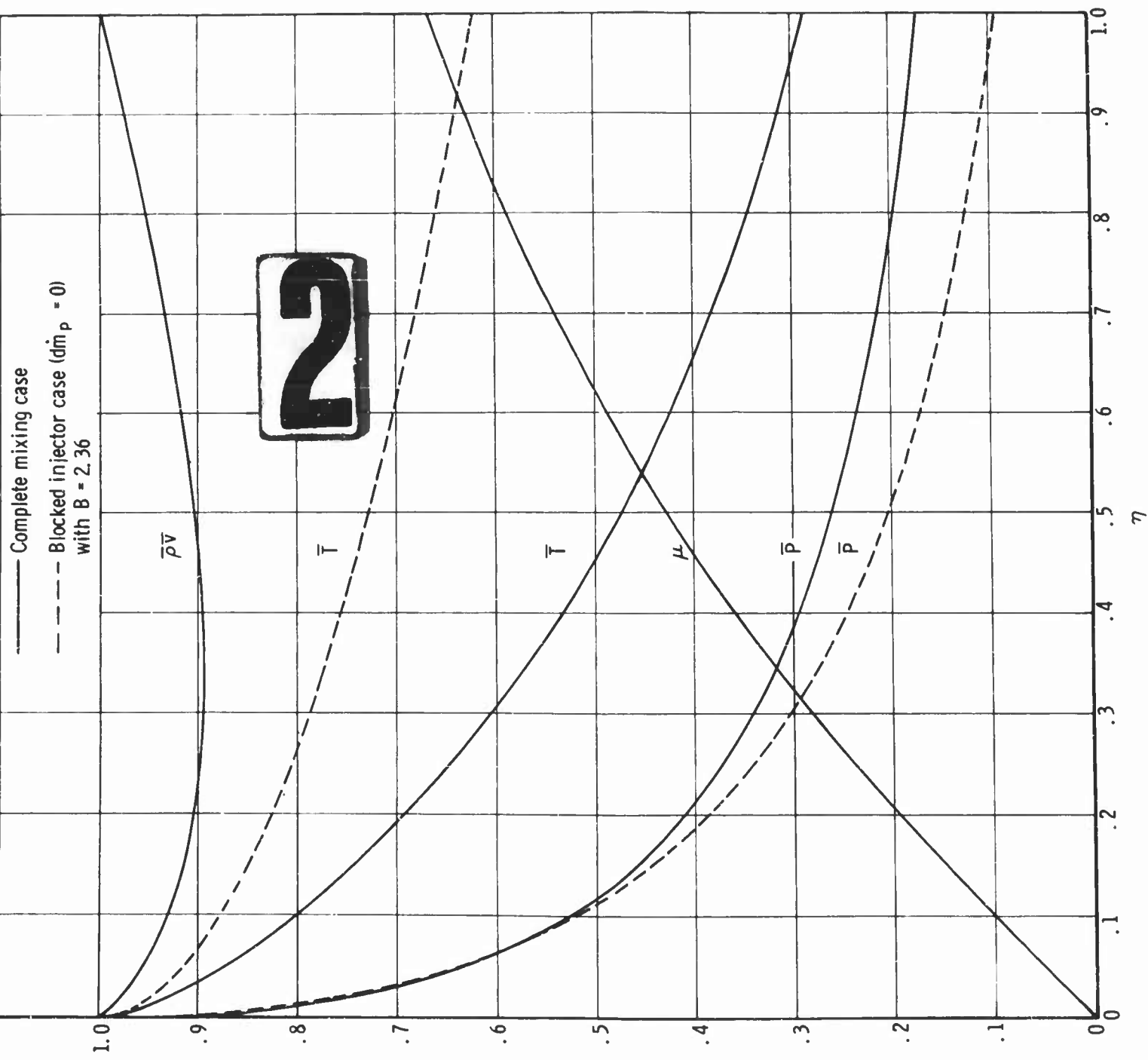


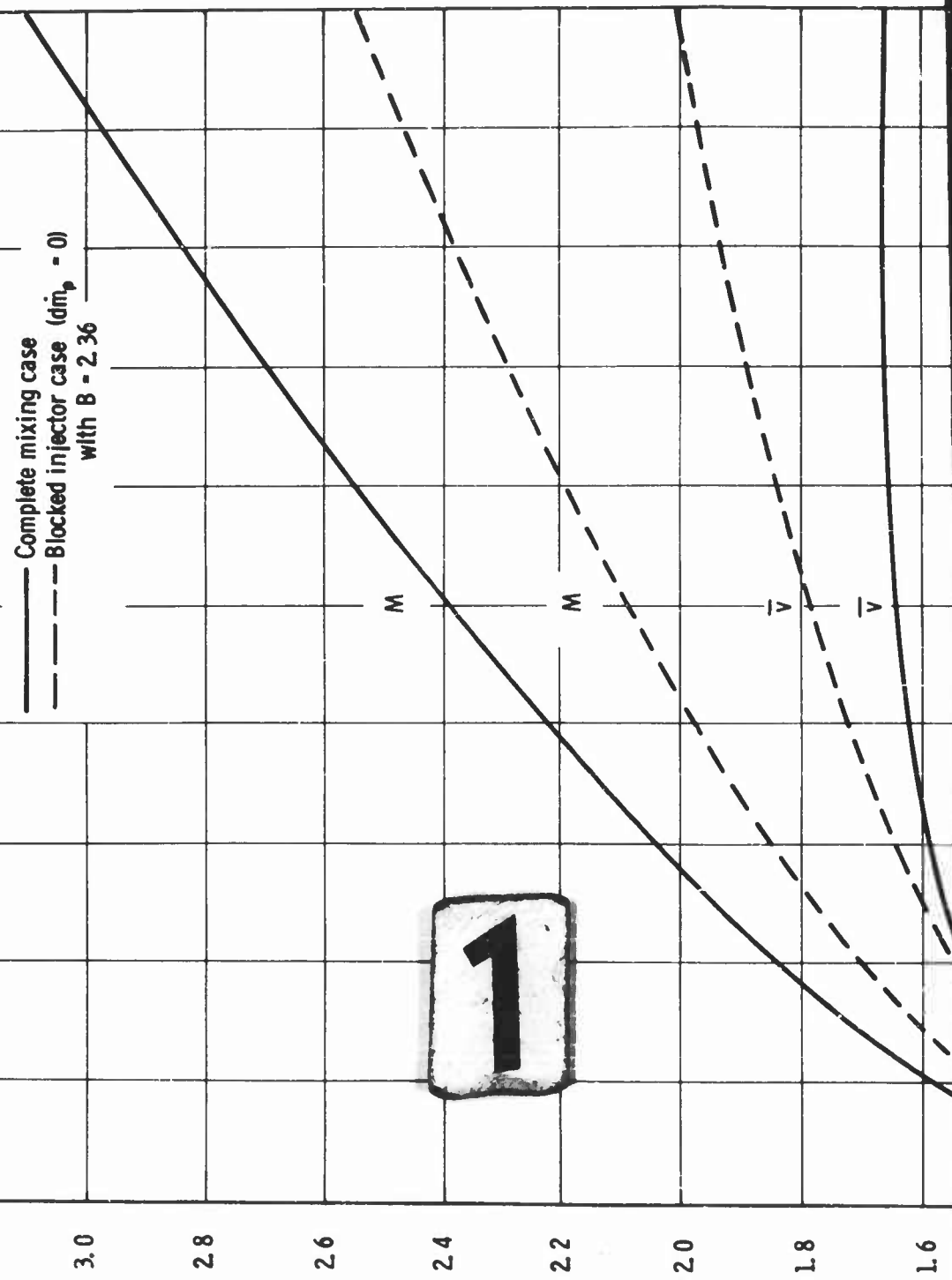
Figure 2(a). Dimensionless Properties \bar{P} , \bar{T} , $\bar{\rho}v$, and μ as Functions of the Dimensionless Circumferential Coordinate, η

Solution to the complete mixing case obtained numerically on the IBM 7090 Digital Computer for:

$$\begin{aligned} G &= 1.0 \\ \gamma &= 1.25 \\ \bar{T}_p &= 0.0743 \end{aligned}$$

The dependent parameters satisfying both the differential equations and the hydrodynamic jump conditions are:

$$\begin{aligned} B &= 2.36 \\ \bar{V}^* &= 1.55 \\ \bar{Q} &= 0.741 \end{aligned}$$



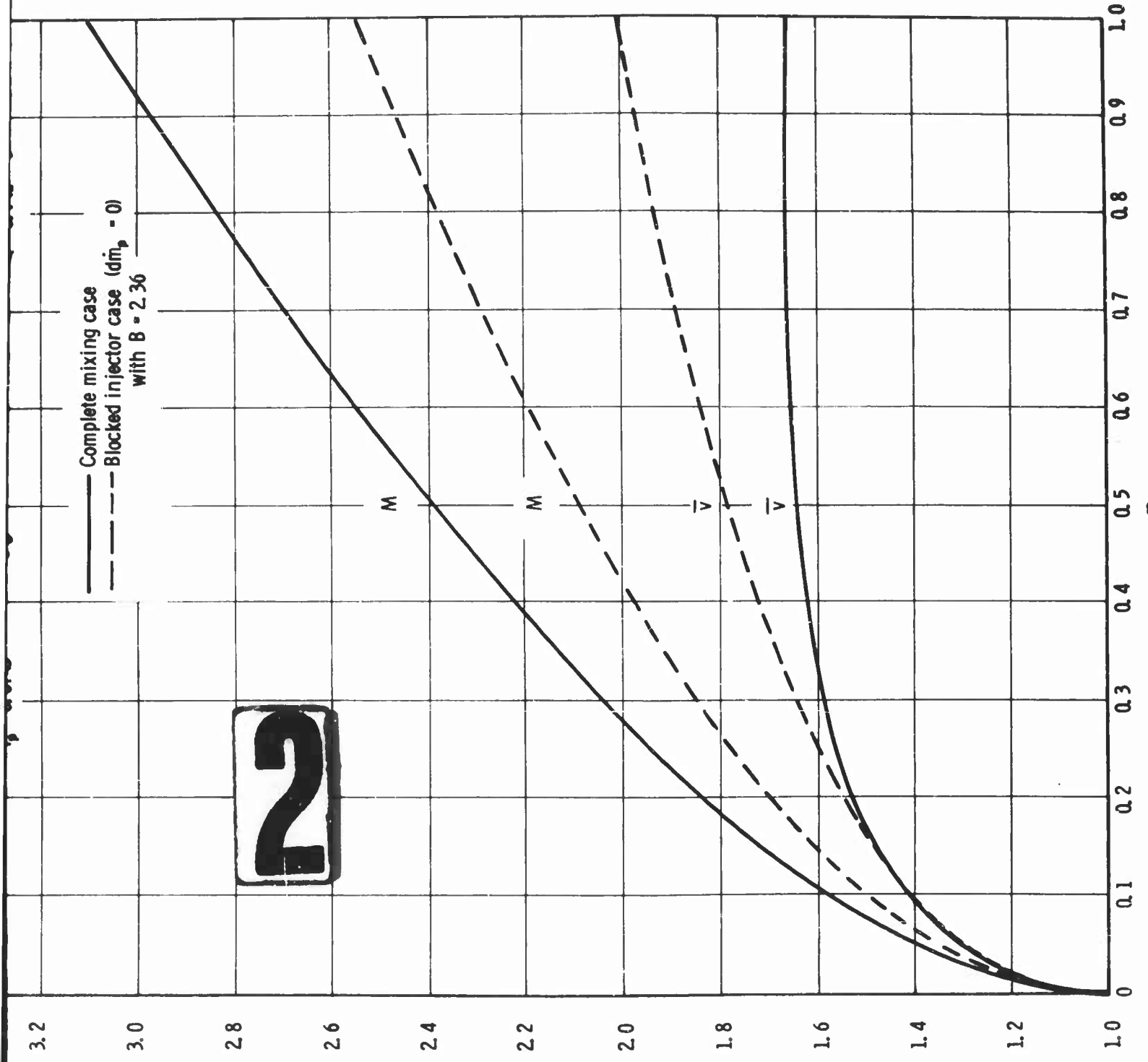


Figure 2(b). Mach Number, M , and Dimensionless Velocity, \bar{v} , as a Function of the Dimensionless Circumferential Coordinate, η

The dependent parameters satisfying both the differential equations and the hydrodynamic jump conditions are:

Solution to the no mixing case:

$$\begin{aligned}G &= 1.0 \\ \bar{T}_P &= 0.081 \\ \gamma_A &= 1.401 \\ \gamma_B &= 1.15 \\ \bar{C}_{P_A} &= 0.5497\end{aligned}$$

$$\begin{aligned}B &= 5.76 \\ \bar{V}_W &= 1.797 \\ \bar{Q} &= 0.788\end{aligned}$$

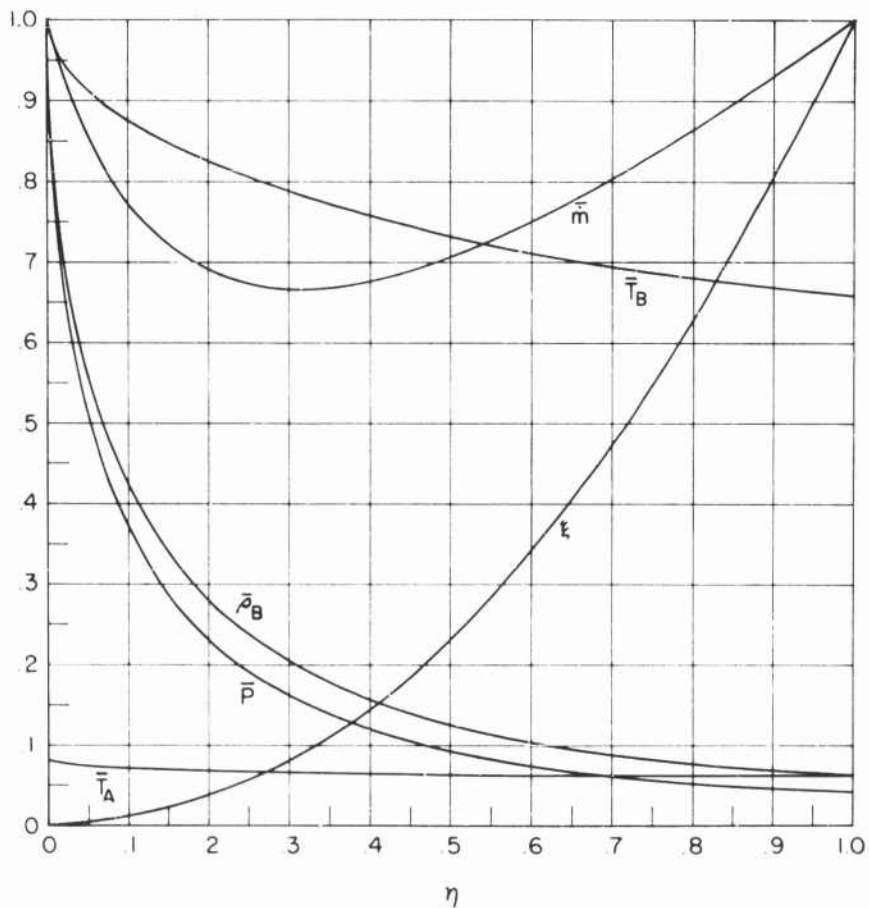


Figure 3(a). Dimensionless Properties \bar{P} , \bar{T}_A , \bar{T}_B , $\bar{\rho}_B$, ξ , and \bar{m} as Functions of The Dimensionless Circumferential Coordinate, ξ , For $\bar{T}_P = 537^0R$, Gaseous No Mixing Case.

Solution to the no mixing case:

The dependent parameters satisfying both the differential equations and the hydrodynamic jump conditions are:

$$G = 1.0$$

$$B = 5.76$$

$$\bar{T}_P = 0.081$$

$$\bar{V}_W = 1.797$$

$$\gamma_A = 1.401$$

$$\bar{Q} = 0.788$$

$$\gamma_B = 1.15$$

$$\bar{C}_{PA} = 0.5497$$

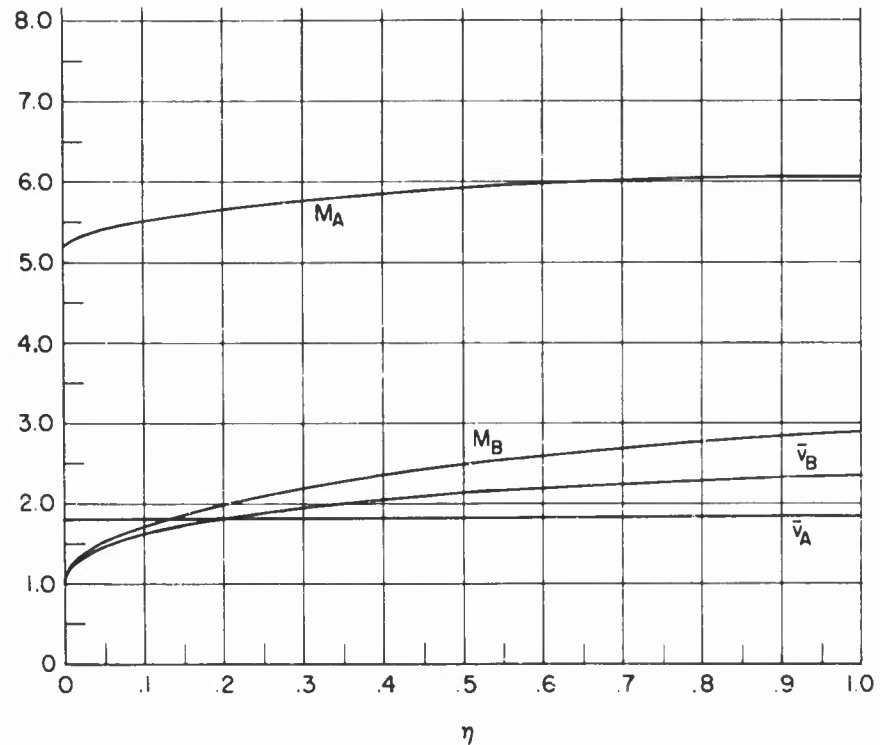


Figure 3(b). Dimensionless Properties M_A , M_B , \bar{v}_A , \bar{v}_B as Functions of the Dimensionless Circumferential Coordinate, η , for $T_P = 537^{\circ}\text{R}$, Gaseous No Mixing Case.

The dependent parameters satisfying both the differential equations and the hydrodynamic jump conditions are:

Solution to the no mixing case:

$$\begin{aligned} G &= 1.0 \\ \bar{T}_P &= 0.04075 \\ \gamma_A &= 1.5 \\ \gamma_B &= 1.15 \\ \bar{C}_{P_A} &= 0.4923 \end{aligned}$$

$$\begin{aligned} B &= 7.608 \\ \bar{V}_W &= 1.8303 \\ \bar{Q} &= 0.8037 \end{aligned}$$

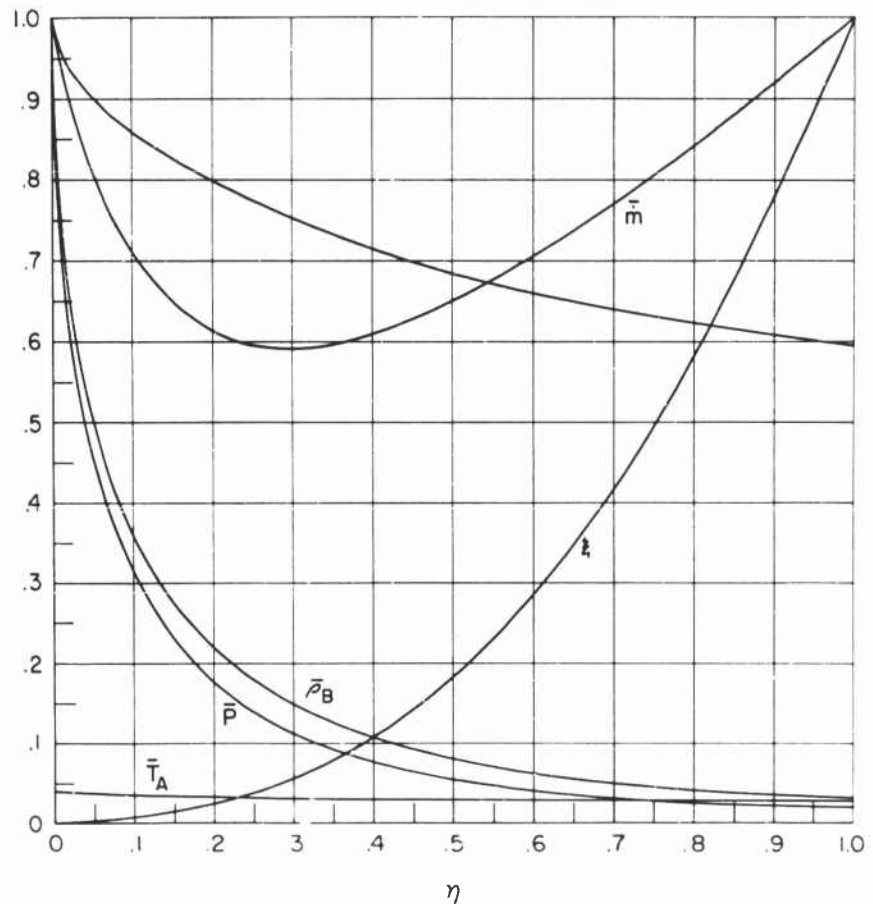


Figure 4(a). Dimensionless Properties \bar{P} , \bar{T}_A , \bar{T}_B , $\bar{\rho}_B$, ξ , and \bar{m} as Functions of the Dimensionless Circumferential Coordinate, η , for $\bar{T}_P = 270^{\circ}\text{R}$, Gaseous No Mixing Case.

The dependent parameters satisfying both the differential equations and the hydrodynamic jump conditions are:

Solution to the no mixing case:

$$G = 1.0$$

$$\bar{T}_P = 0.04075$$

$$\gamma_A = 1.5$$

$$\gamma_B = 1.15$$

$$C_{PA} = 0.4923$$

$$B = 7.608$$

$$\bar{v}_W = 1.8303$$

$$\bar{Q} = 0.8037$$

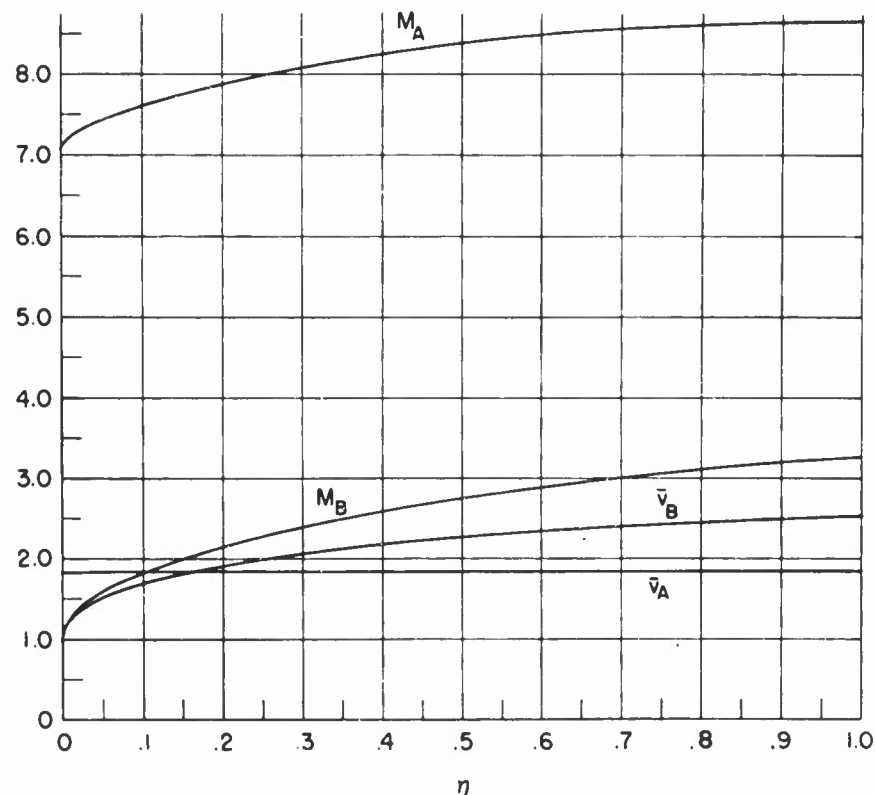


Figure 4(b). Dimensionless Properties M_A , M_B , \bar{v}_A , \bar{v}_B as Functions of the Dimensionless Circumferential Coordinate, η , for $\bar{T}_P = 270^{\circ}\text{R}$, Gaseous No Mixing Case.

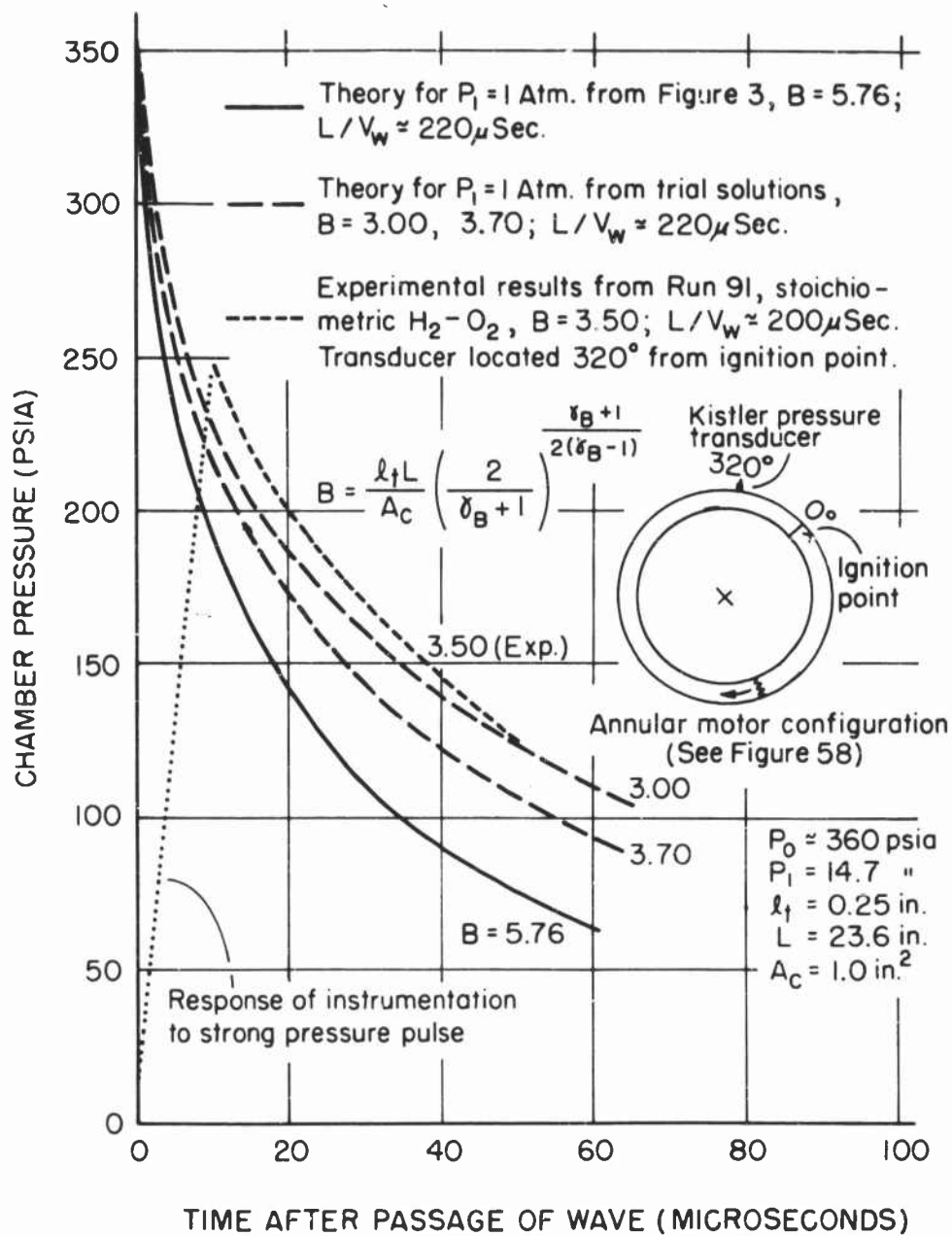


Figure 5. Theoretical Results Compared with an Experimental Pressure-Time History for the Passage of the Initial Detonation Wave.

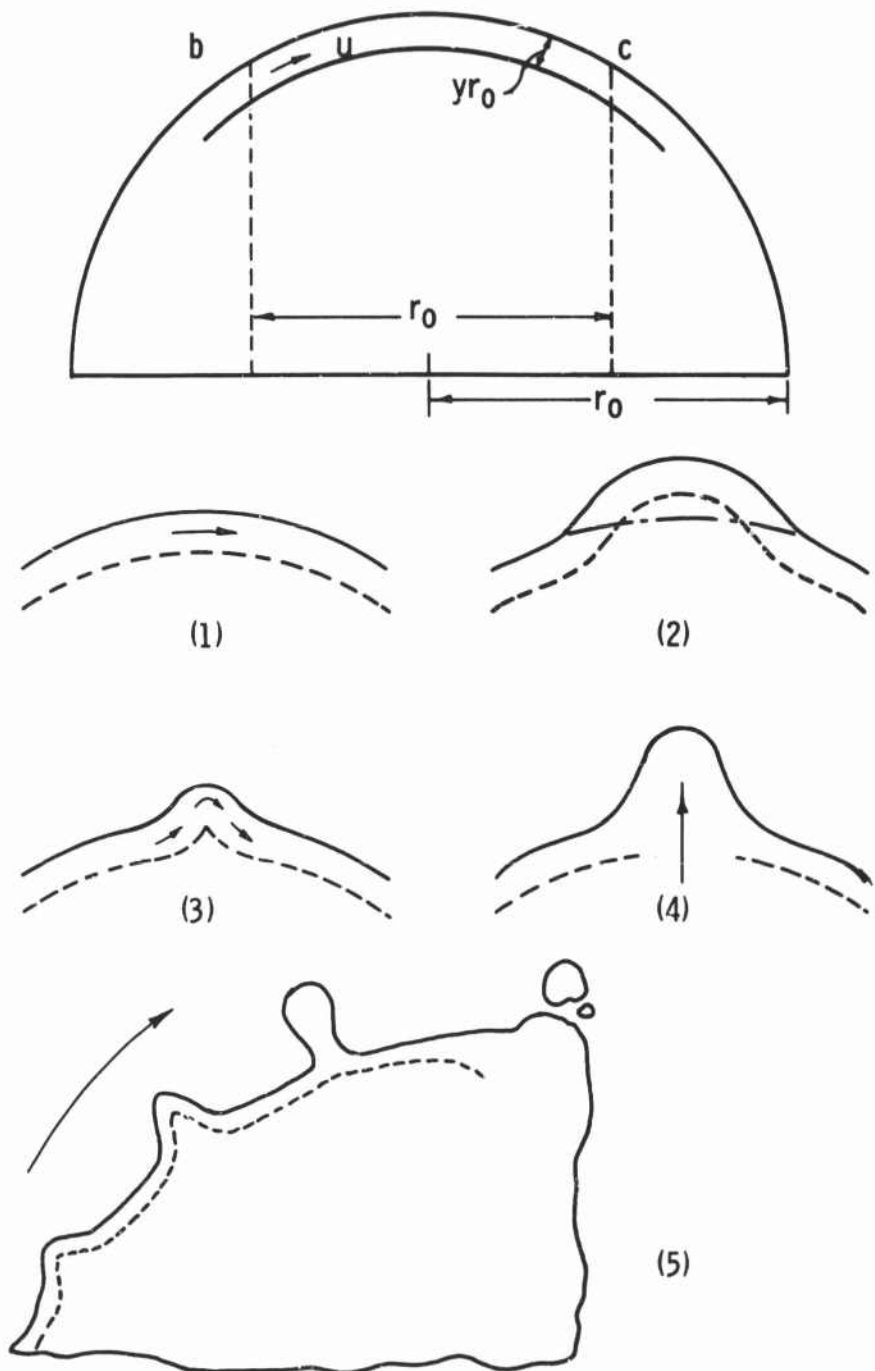


Figure 6(a). Schematic Process for Shear Type Breakup.

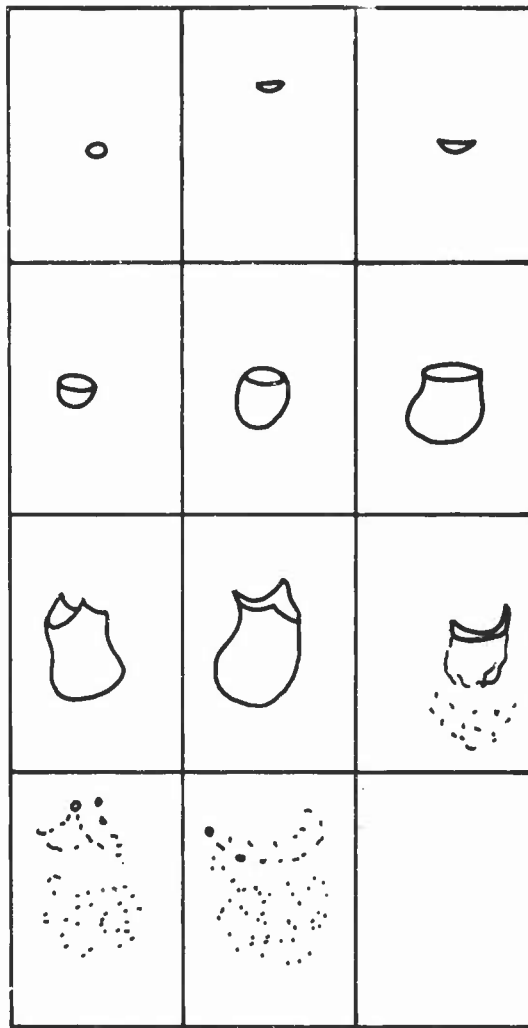


Figure 6(b). Schematic Process of Bag Type Breakup.

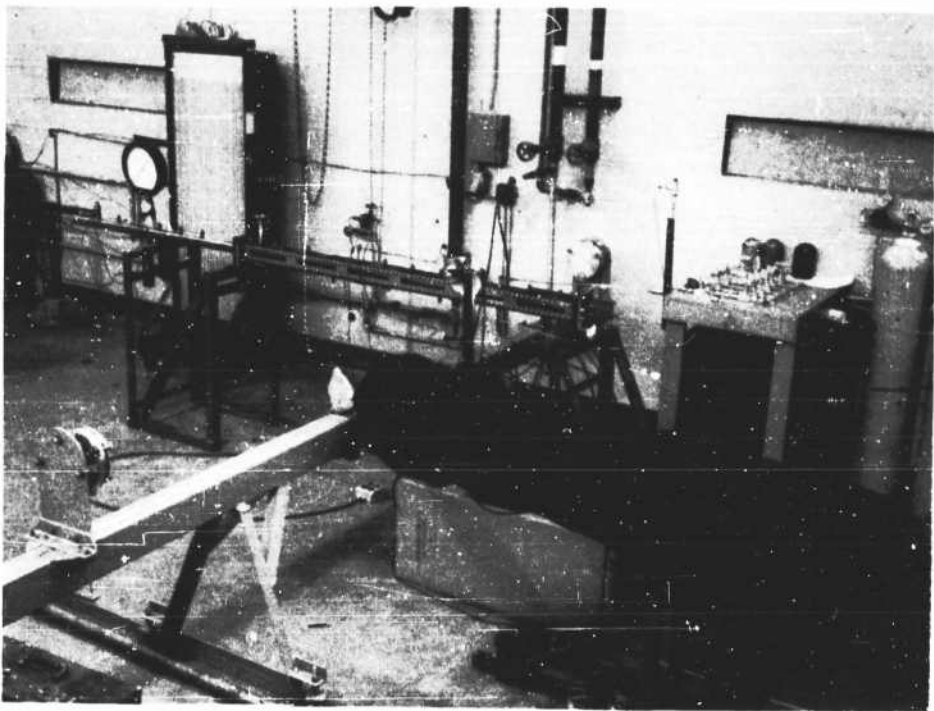


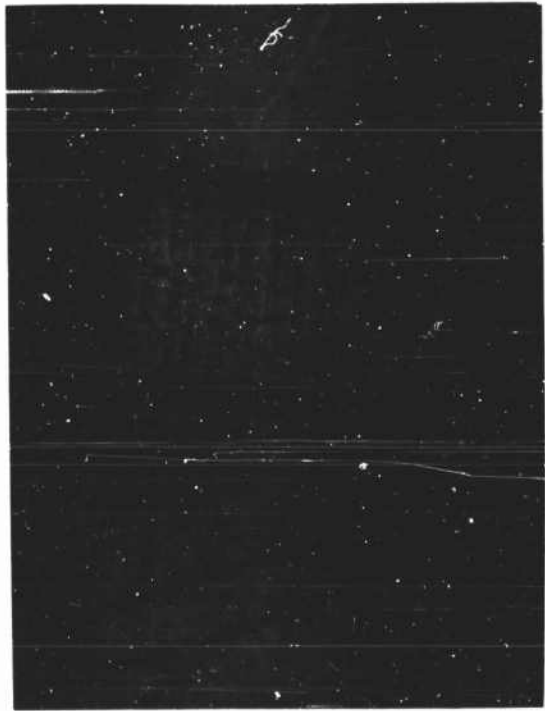
Figure 7. Photograph of the Test Setup for Detonation-Droplet Interaction Studies.



0



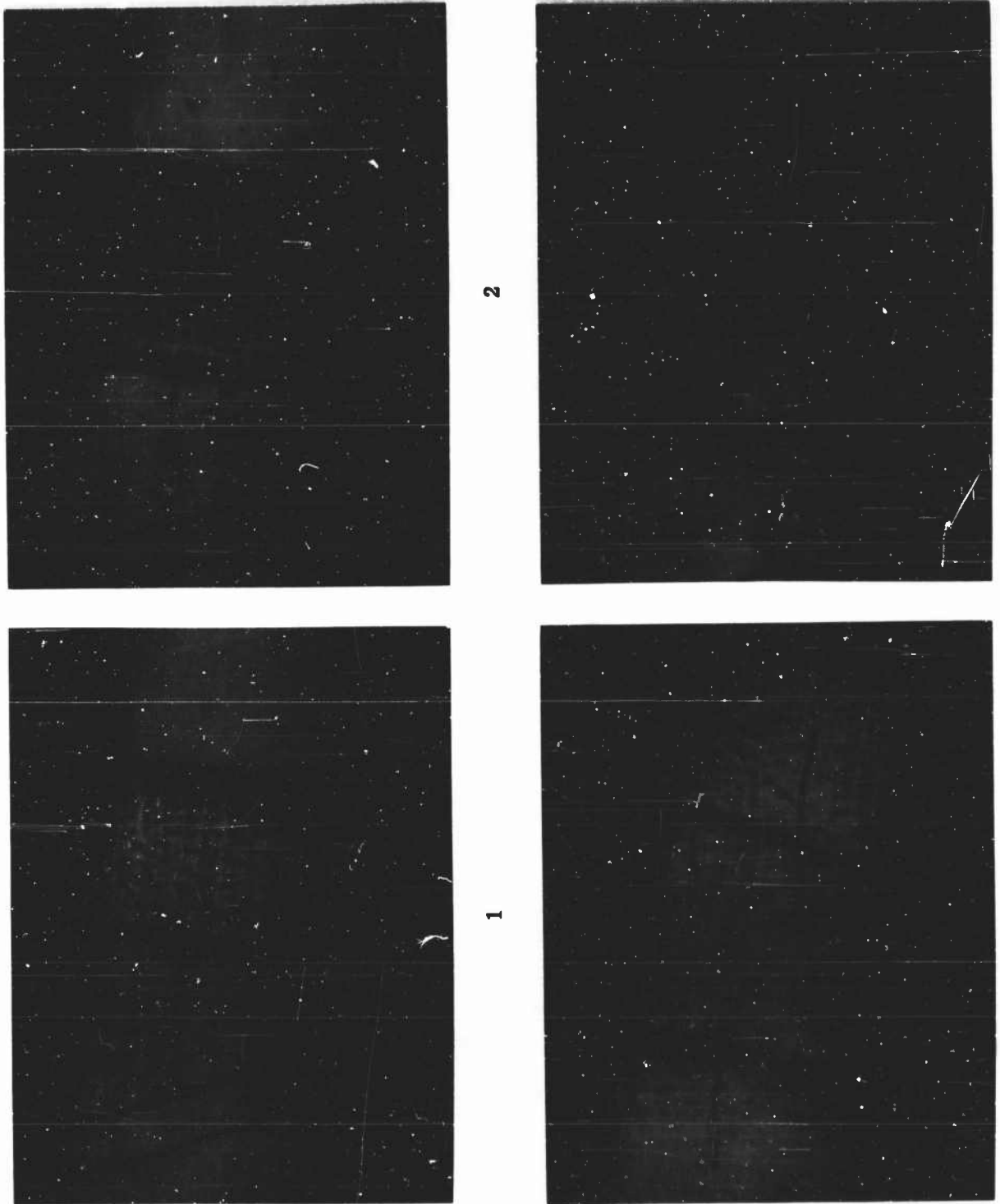
2

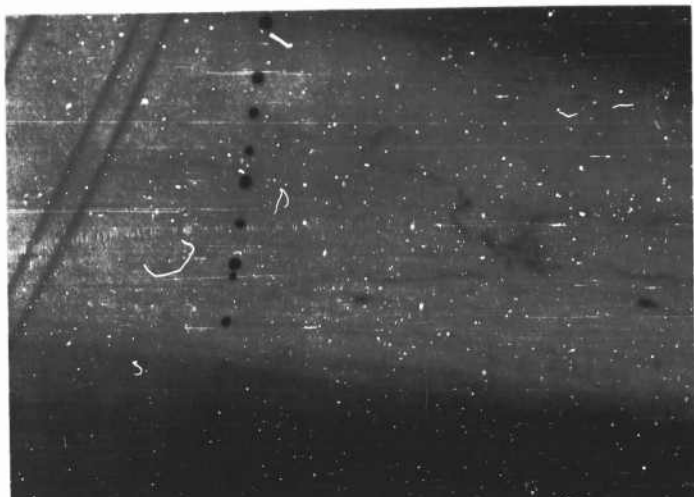


1

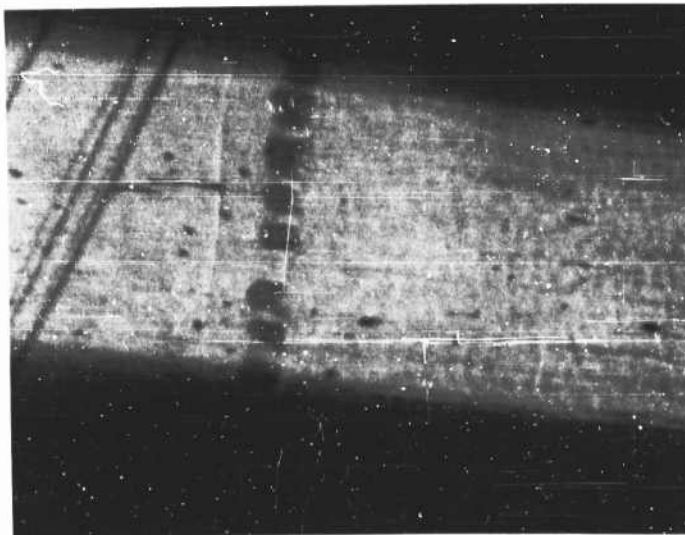


Figure 8. Schlieren Photographs of the Shattering of H_2O Droplets Behind H_2-O_2
Detonation Waves ($X_{H_2} \approx .70$) (0) Undisturbed Droplet Row (1000 μ Diameter)





(a)



(b)

Figure 9. Schlieren Photographs of the Shattering of
 H_2O Droplets Behind H_2-O_2 Detonation Waves
 $(X_{H_2} \approx .67)$.

- (a) Undisturbed Droplet Row (220-580 μ Diameter)
(Retouched)
- (b) Shattered Droplets 11-12 μ -sec After Passage of
Wave

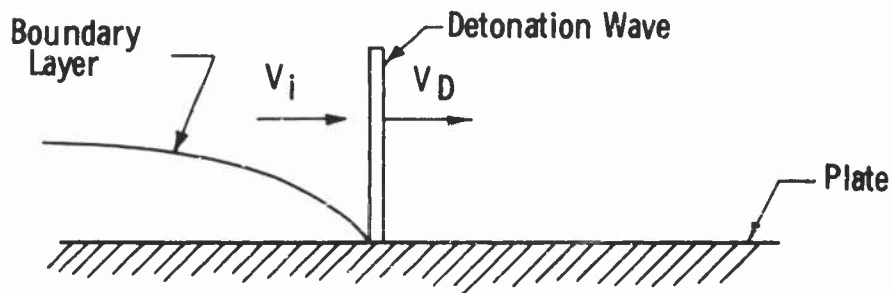


Figure 10. Detonation Moving Over a Flat Plate.

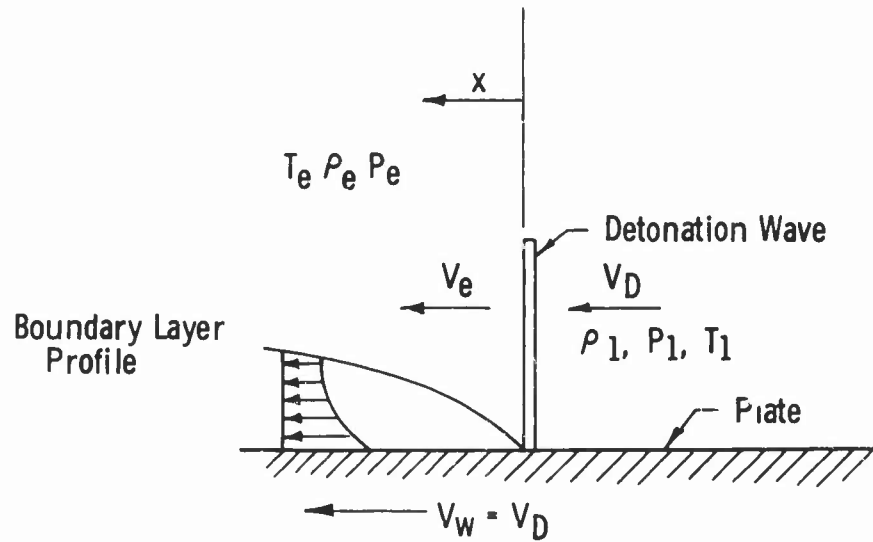


Figure 11. Coordinate System for Heat Transfer Analysis.

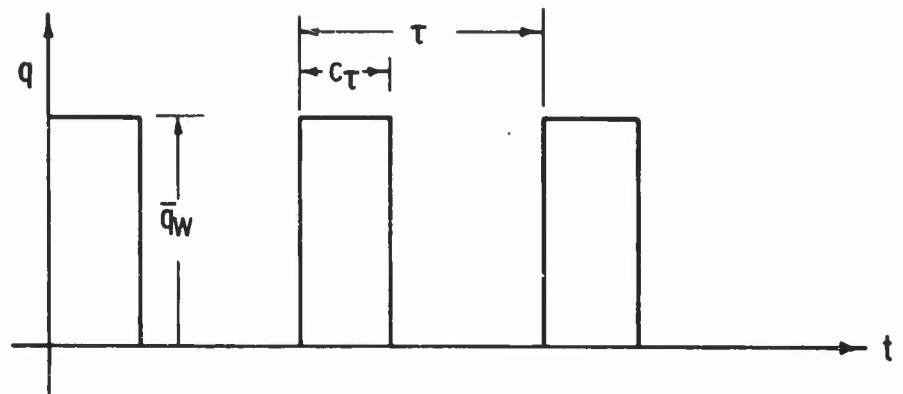


Figure 12. Square Pulse Approximation of Surface Heat Flux.

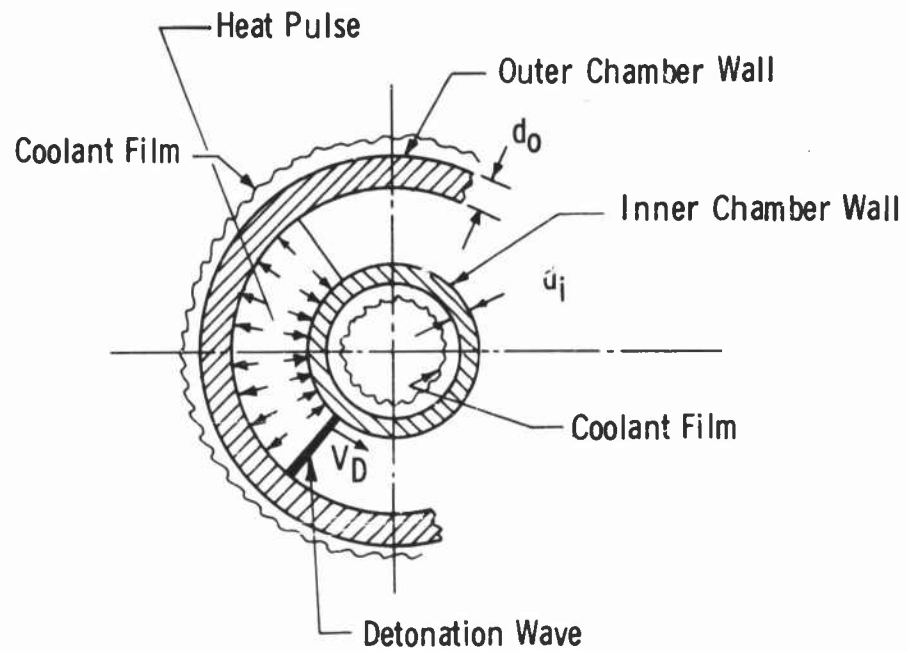


Figure 13. Theoretical Heat Transfer Model—Rotating Detonation Wave Engine.

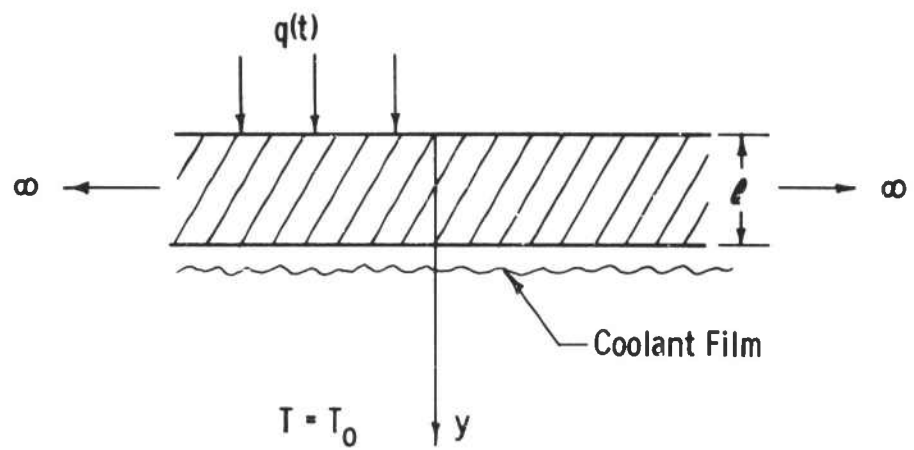


Figure 14. One Dimensional Conduction Model.

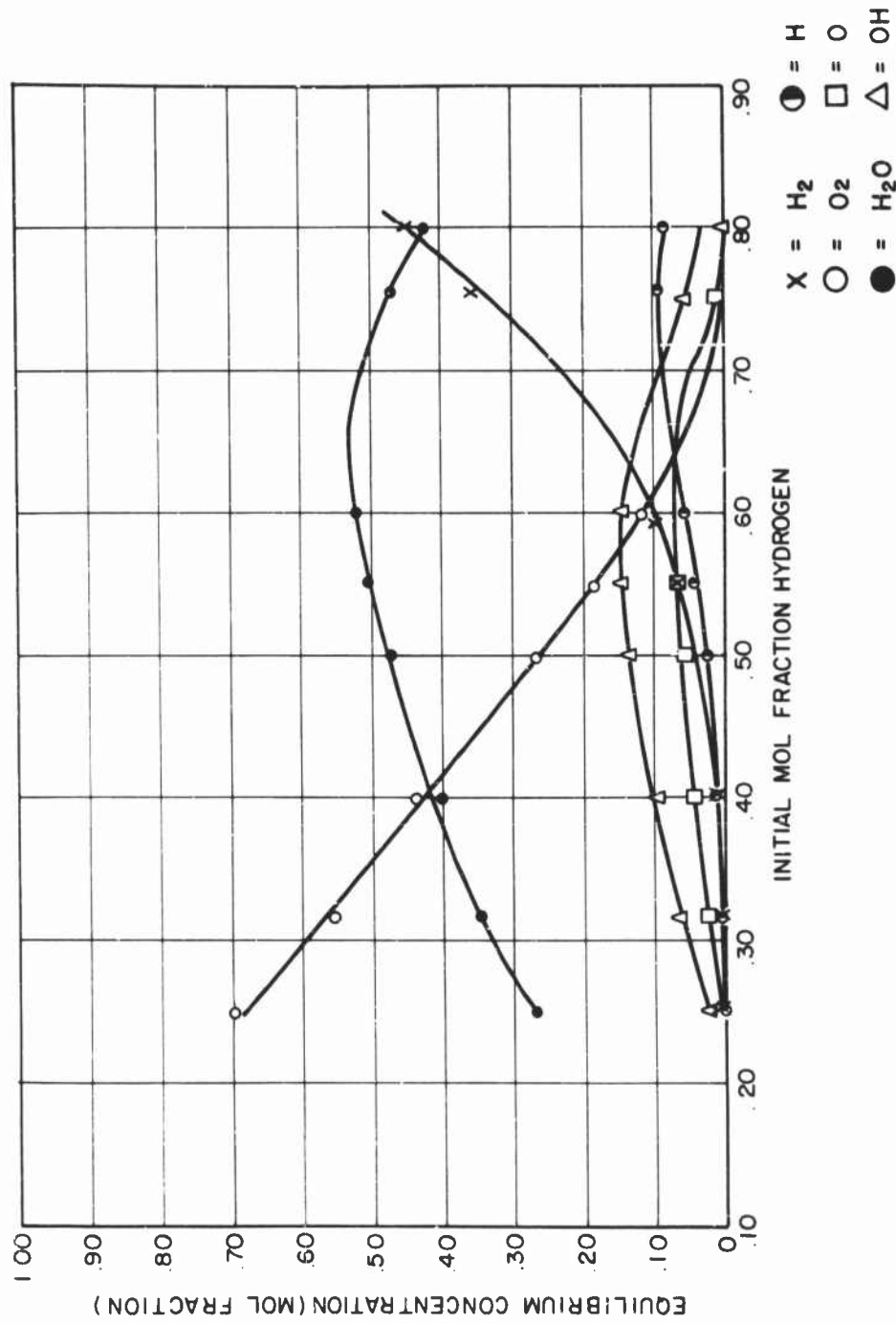


Figure 15. Equilibrium Concentration Versus Initial Hydrogen Content Behind H₂-O₂ Chapman-Jouguet Detonations. Initial Temperature = 300°K; Initial Pressure = 1 Atm.

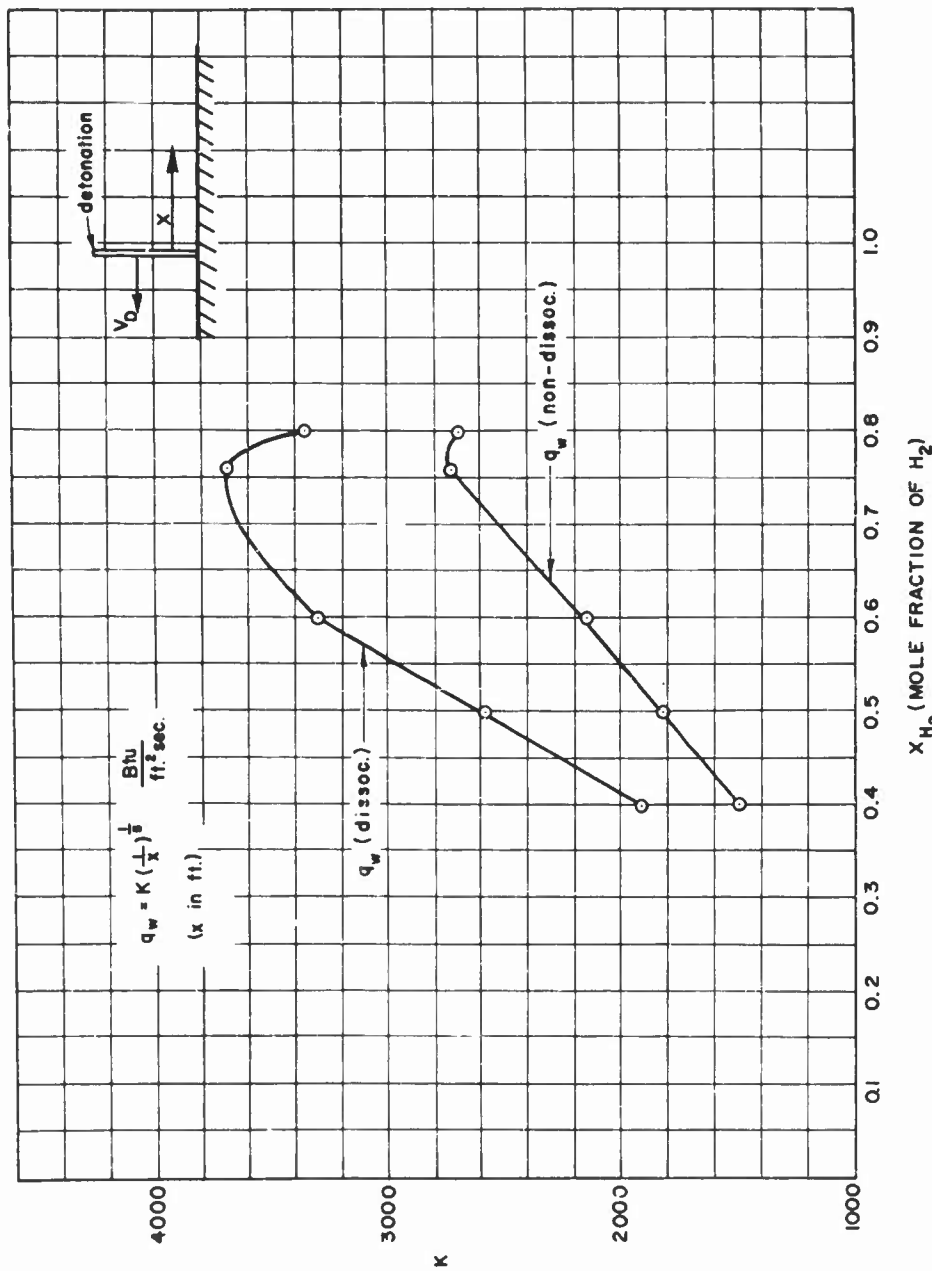


Figure 16. Heat Flux to the Wall of the Rotating Detonation Wave Engine Versus Mixture Ratio With and Without Dissociative Recombination.

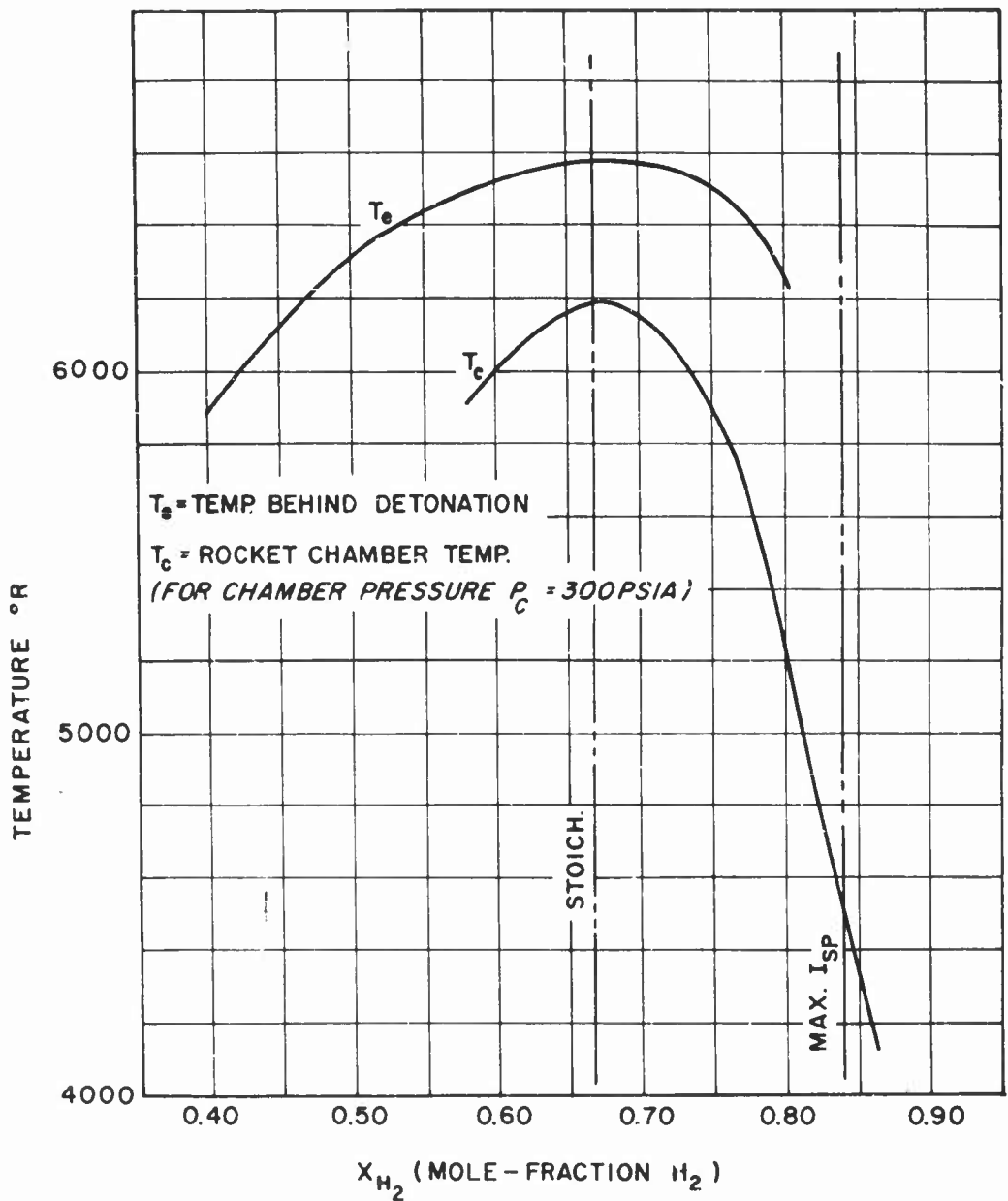


Figure 17. H_2 - O_2 Chapman-Jouquet Detonation and Combustion Chamber Temperature as a Function of Mixture Ratio.

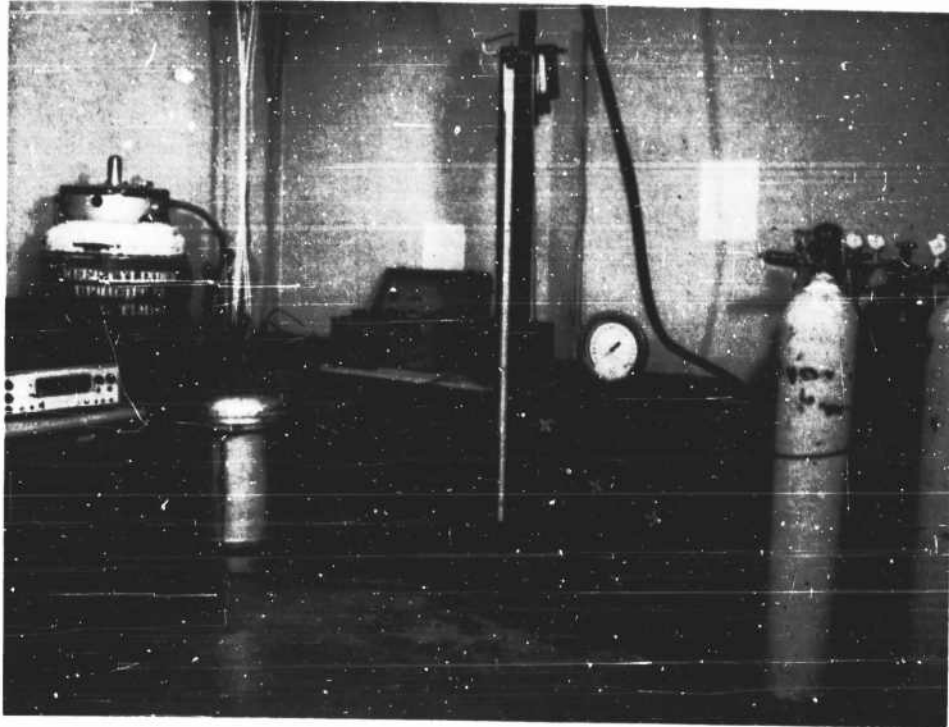


Figure 18. Photograph of the Test Setup for the Measurement of the Temperature and Pressure Effects on Hydrogen-Oxygen Detonation Velocities.

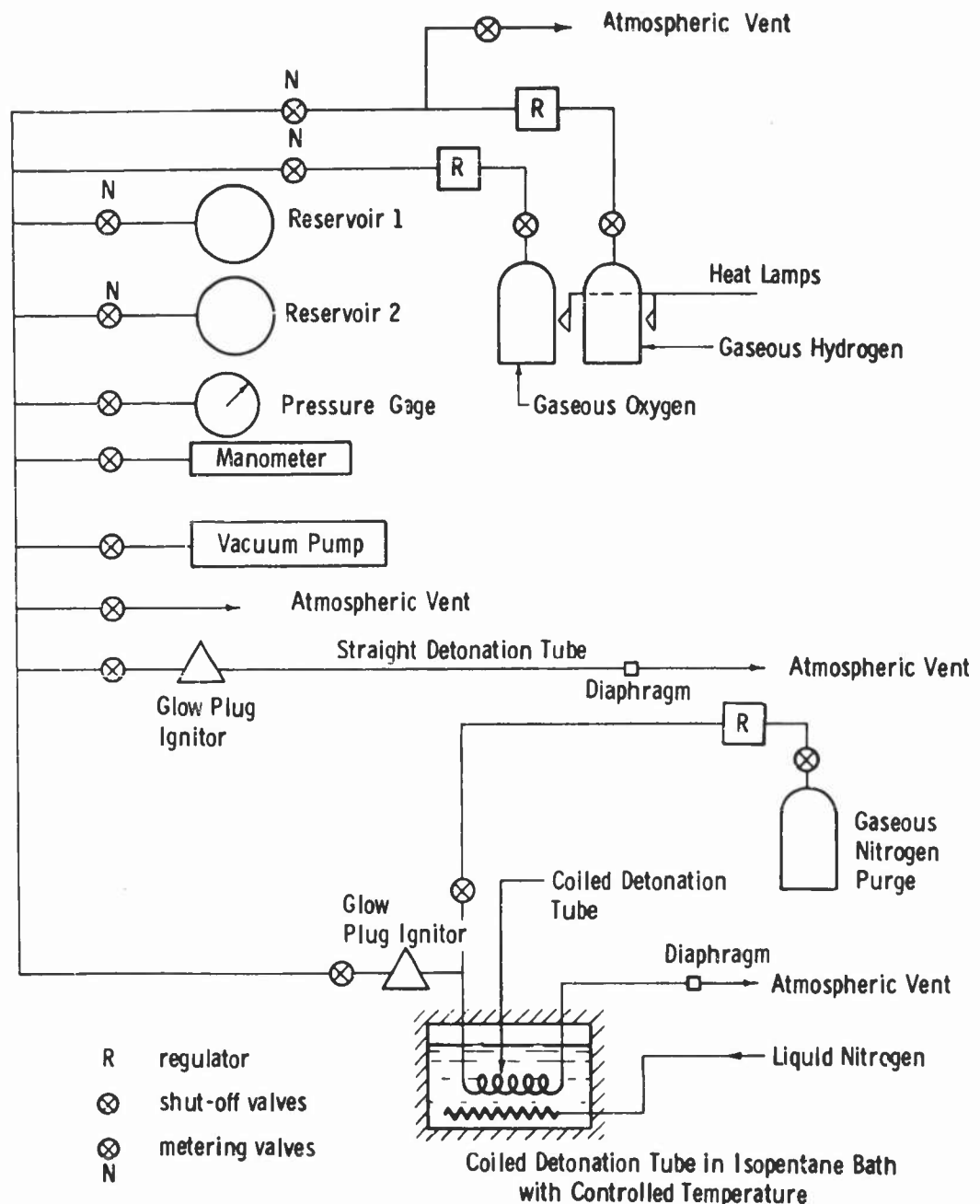


Figure 19. Schematic View of the Test Setup for the Measurement of the Temperature and Pressure Effects on Hydrogen-Oxygen Detonation Velocities.

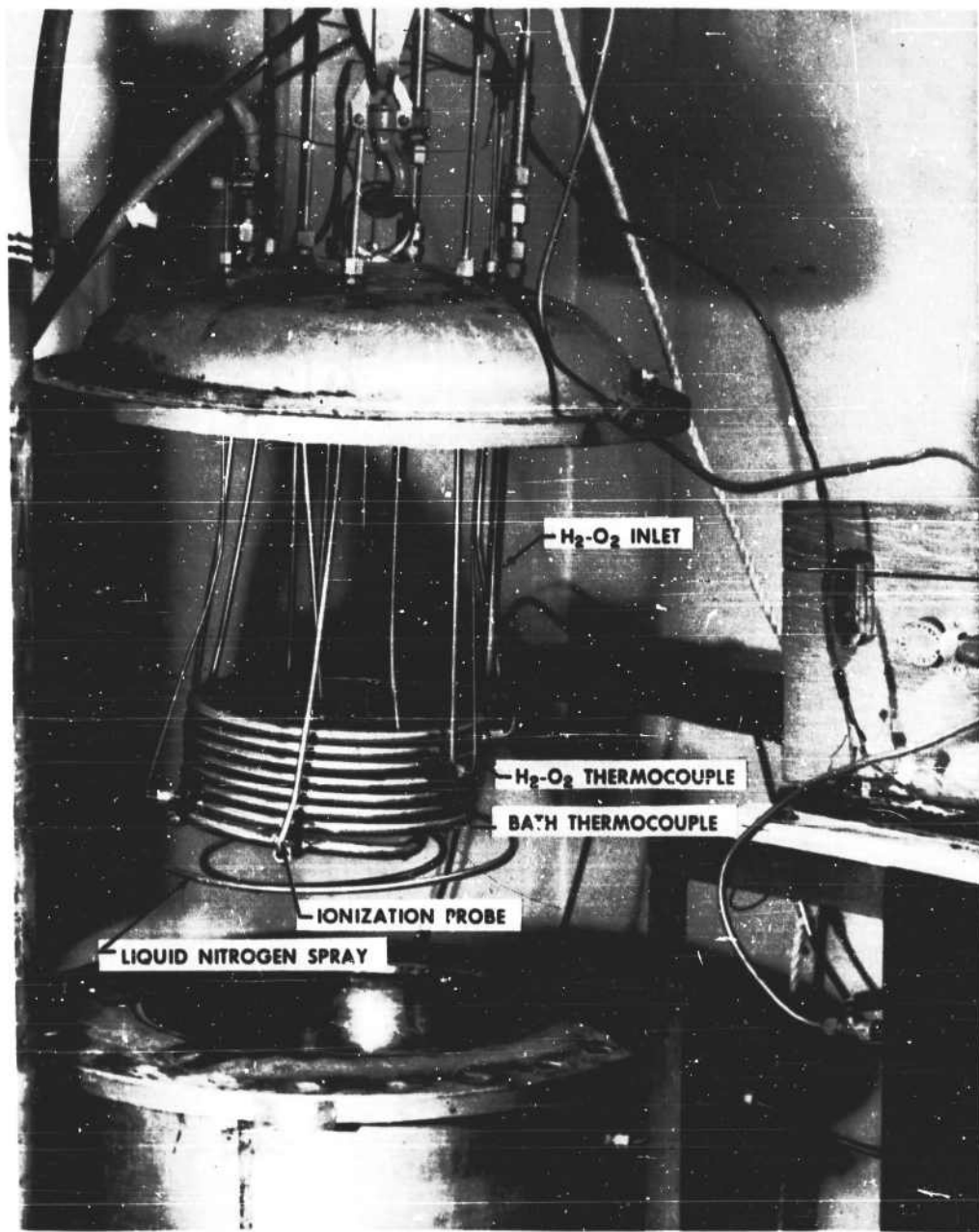


Figure 20. Photograph of the Coiled Detonation Tube and the Low-Temperature Vessel.

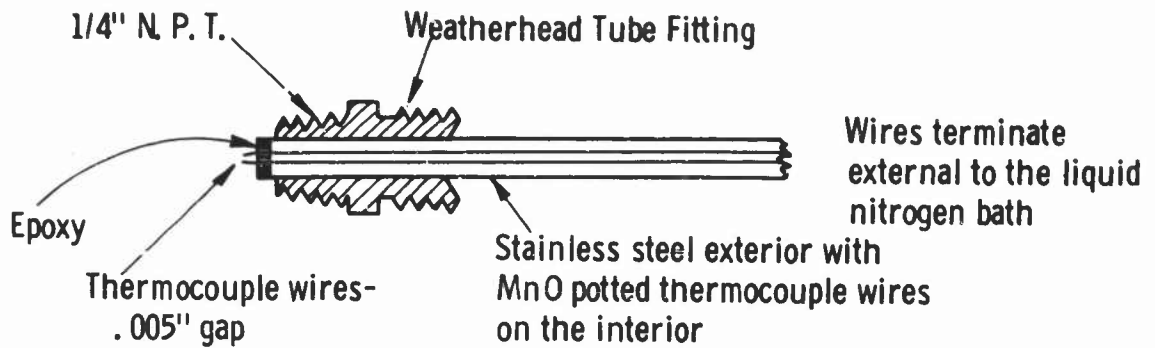


Figure 21. Schematic View of the Ionization Probe for Detonation Velocity Measurements.

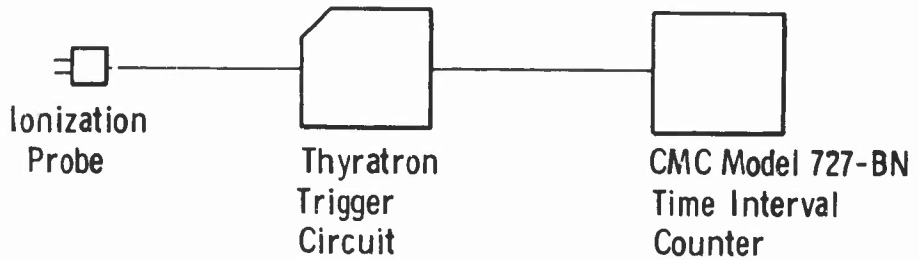


Figure 22. Schematic View of the System for Detonation Velocity Measurements.

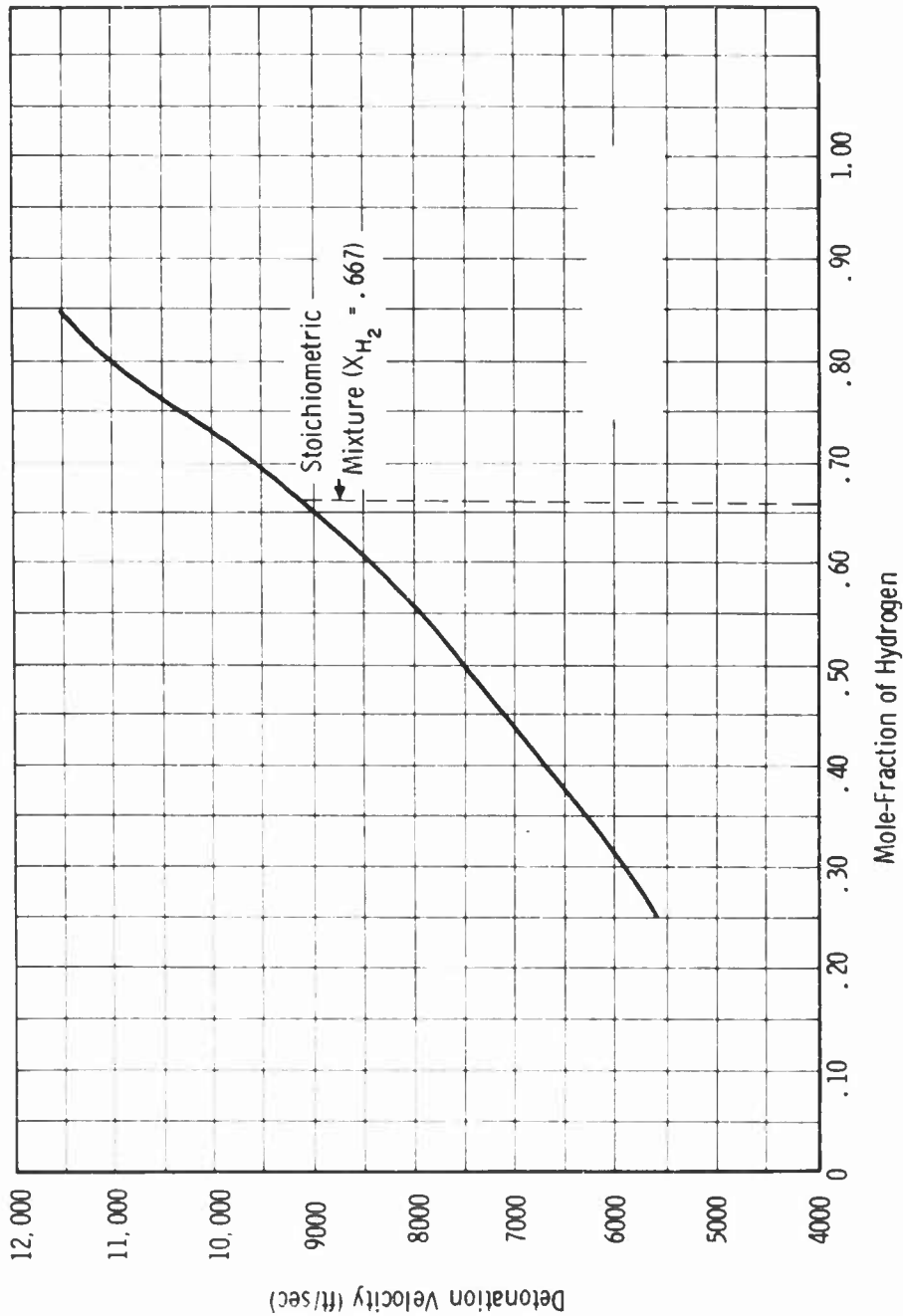


Figure 23. Experimental Detonation Velocity, U_D , of Hydrogen-Oxygen Detonations as a Function of the Mole-Fraction of Hydrogen (X_{H_2}) from Data Obtained by Moyle³⁸.

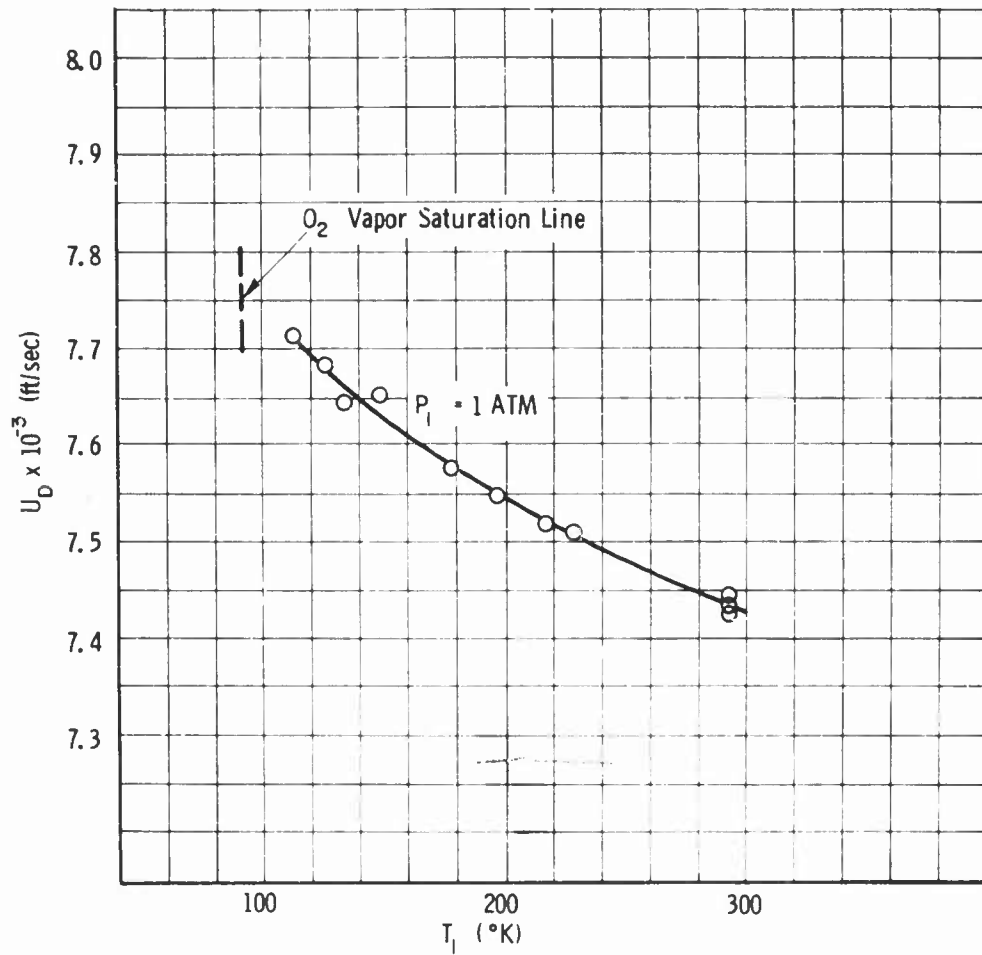


Figure 24. Experimental Detonation Velocity, U_D , of Hydrogen-Oxygen Detonations as a Function of the Initial Temperature, T_1 , for $X_{H_2} = 0.500$.

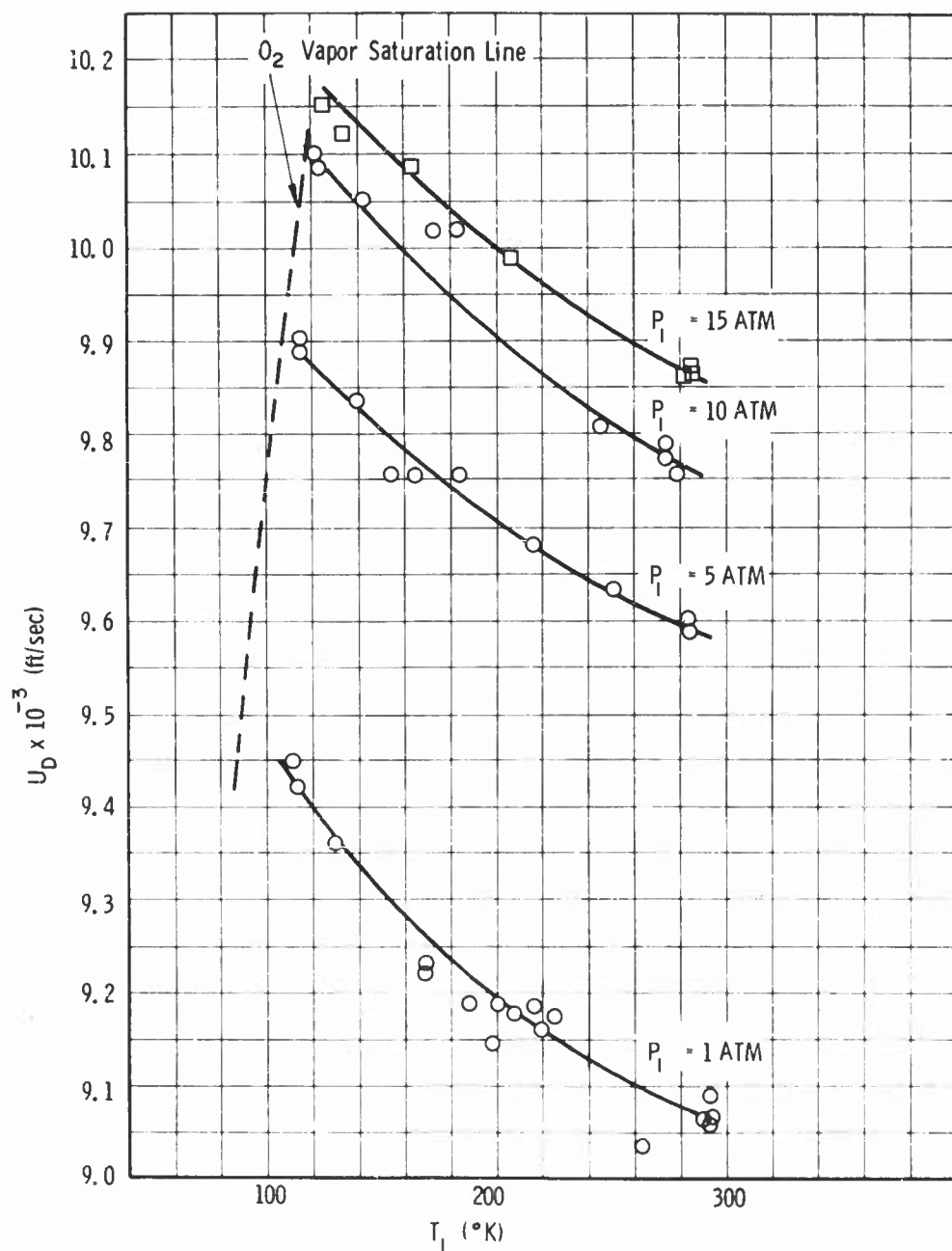


Figure 25. Experimental Detonation Velocity, U_D , of Hydrogen-Oxygen Detonations as a Function of the Initial Temperature, T_1 , for $X_{H_2} = 0.667$

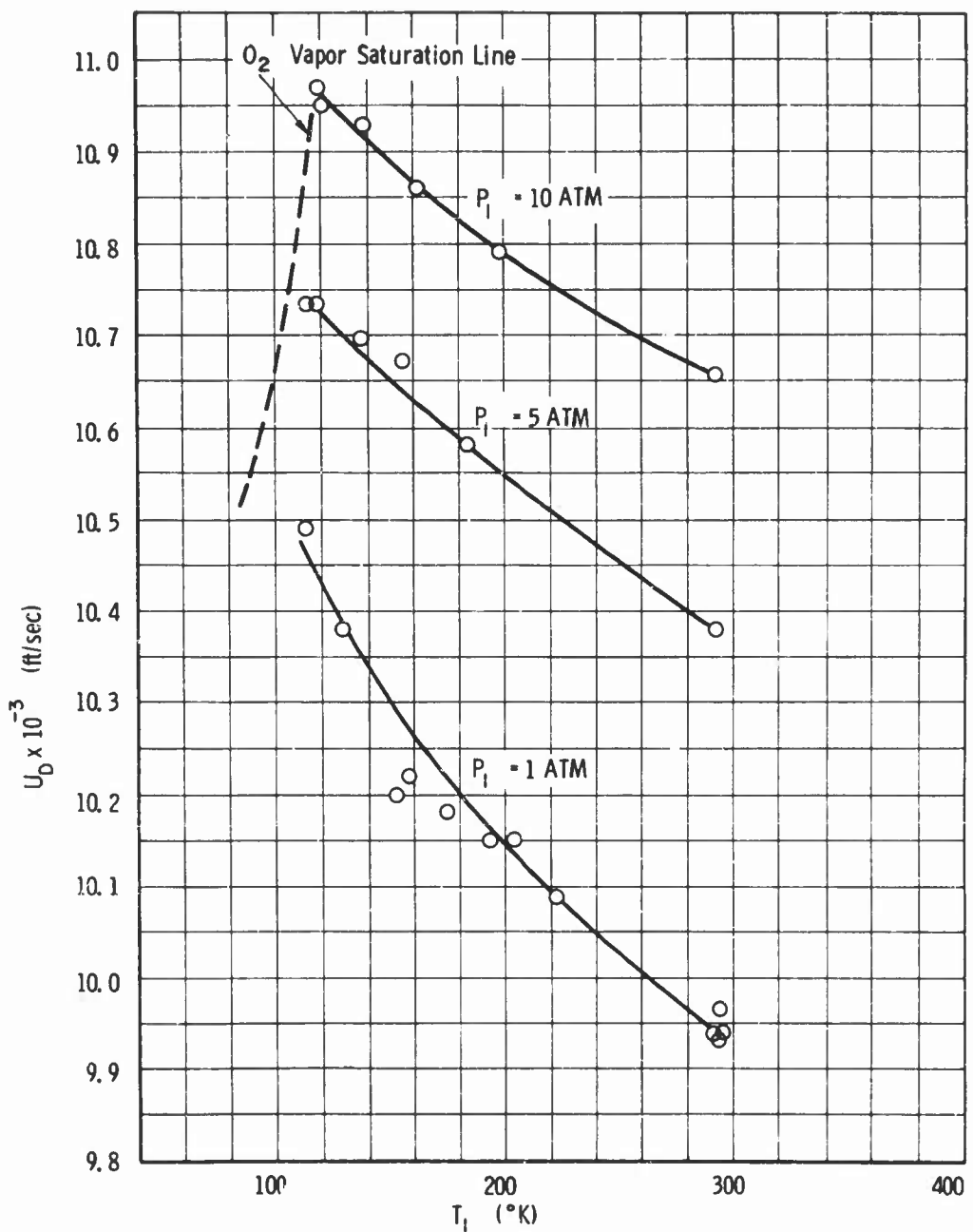


Figure 26. Experimental Detonation Velocity, U_D , of Hydrogen-Oxygen Detonations as a Function of the Initial Temperature, T_1 , for $X_{H_2} = 0.730$

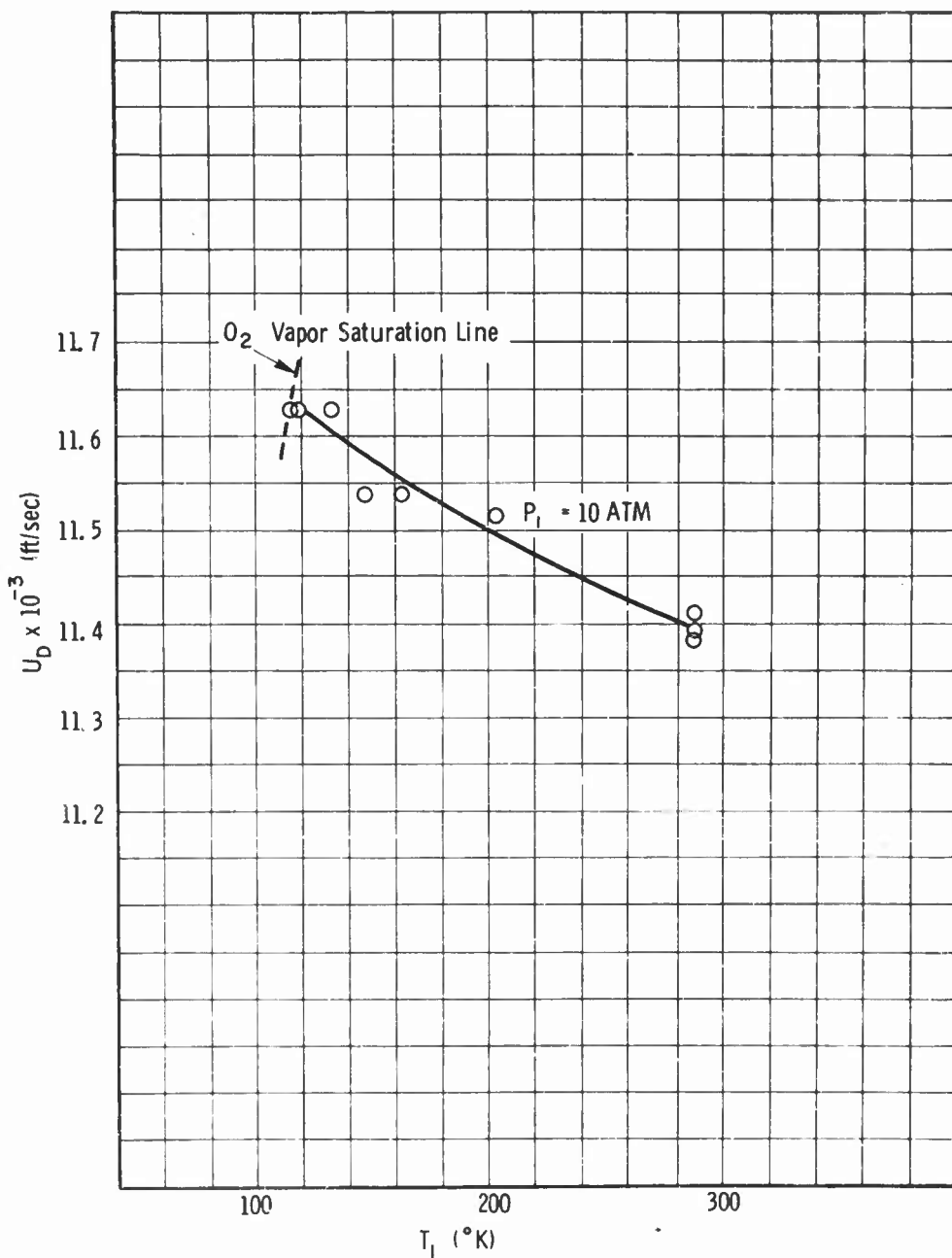


Figure 27. Experimental Detonation Velocity, U_D , of Hydrogen-Oxygen Detonations as a Function of the Initial Temperature, T_1 , for $X_{H_2} = 0.800$

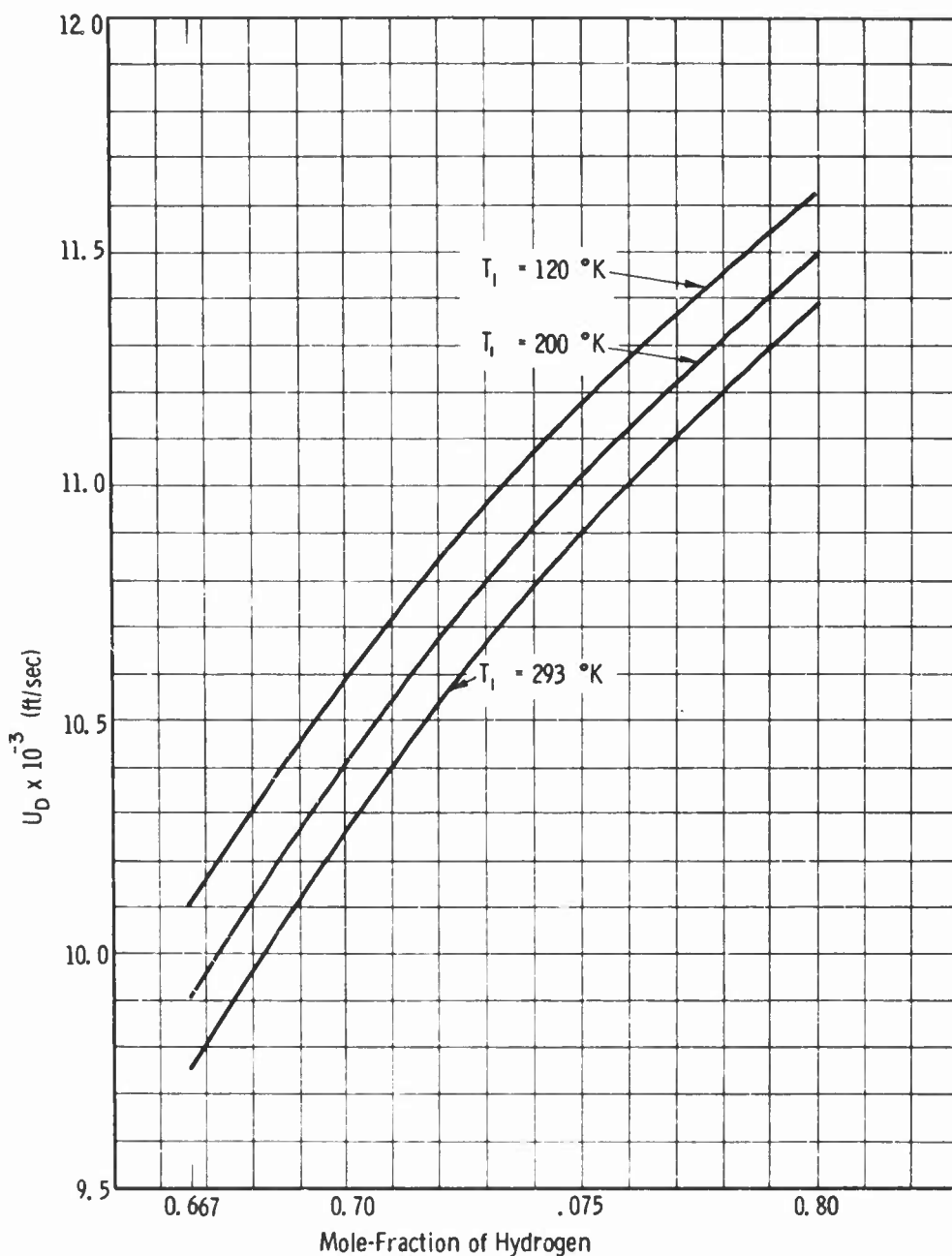


Figure 28. Experimental Detonation Velocity, U_D , of Hydrogen-Oxygen Detonations as a Function of the Mole-Fraction of Hydrogen, X_{H_2} , for Initial Pressure, $P_1 = 10$ Atmospheres.

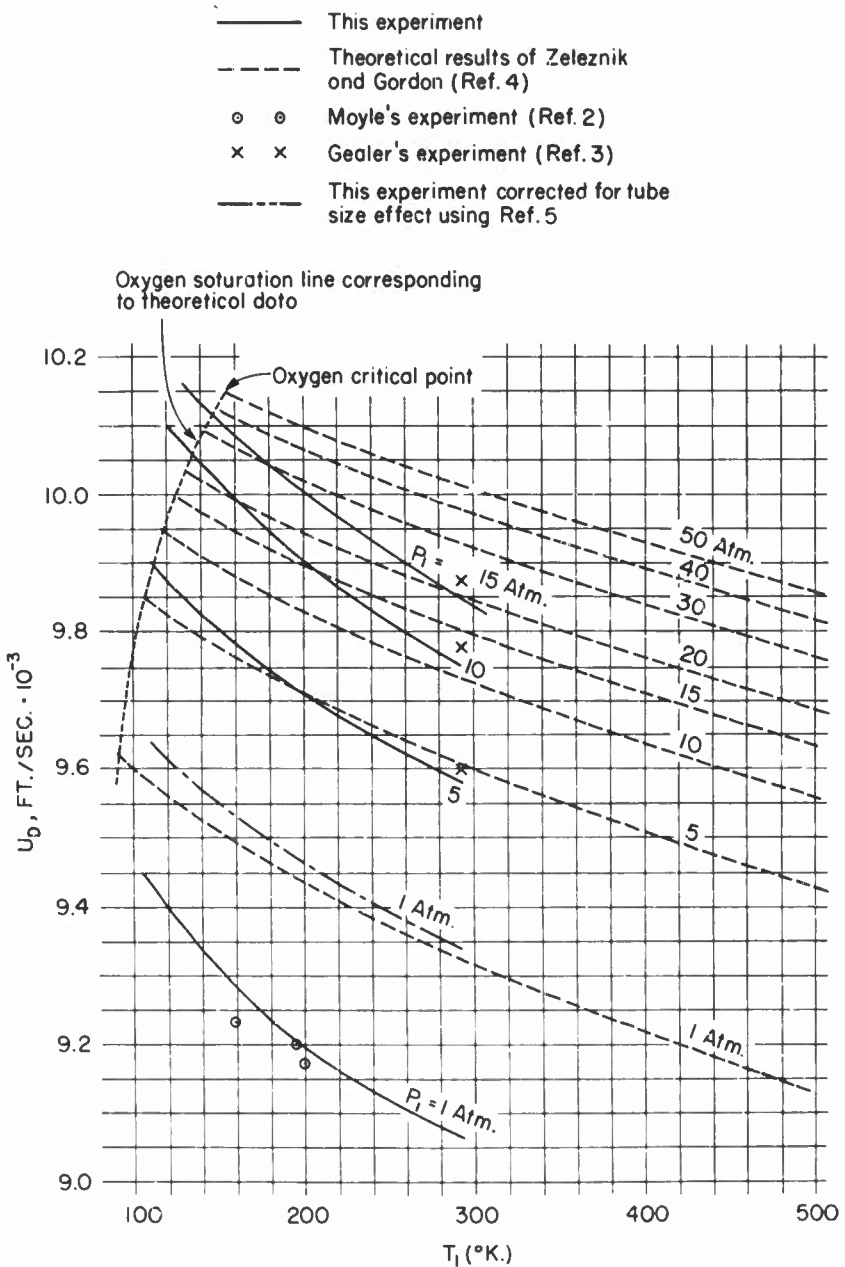


Figure 29. Comparison of Experimental Detonation Velocity, U_D , as a Function of Initial Temperature, T_1 , at Various Initial Pressures, P_1 , With Results of Other Investigators for Stoichiometric ($X_{H_2} = .667$) $H_2 - O_2$ Mixtures

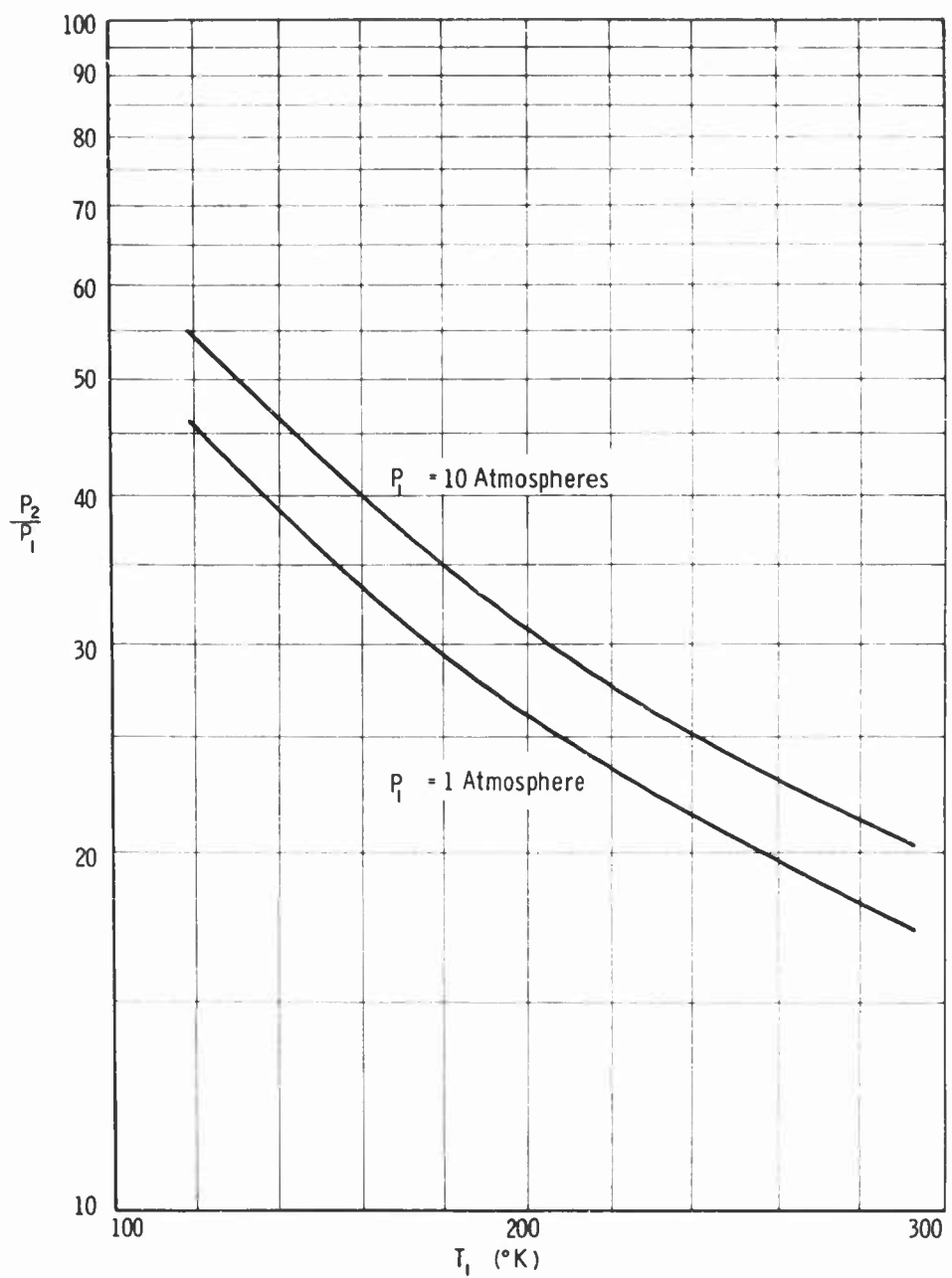


Figure 30. Log of the Detonation Pressure Ratio, P_2/P_1 (obtained from experimental detonation velocity measurements) as a Function of the Initial Temperature, T_1 , for Stoichiometric ($X_{H_2} = .667$) H_2-O_2 Mixtures.

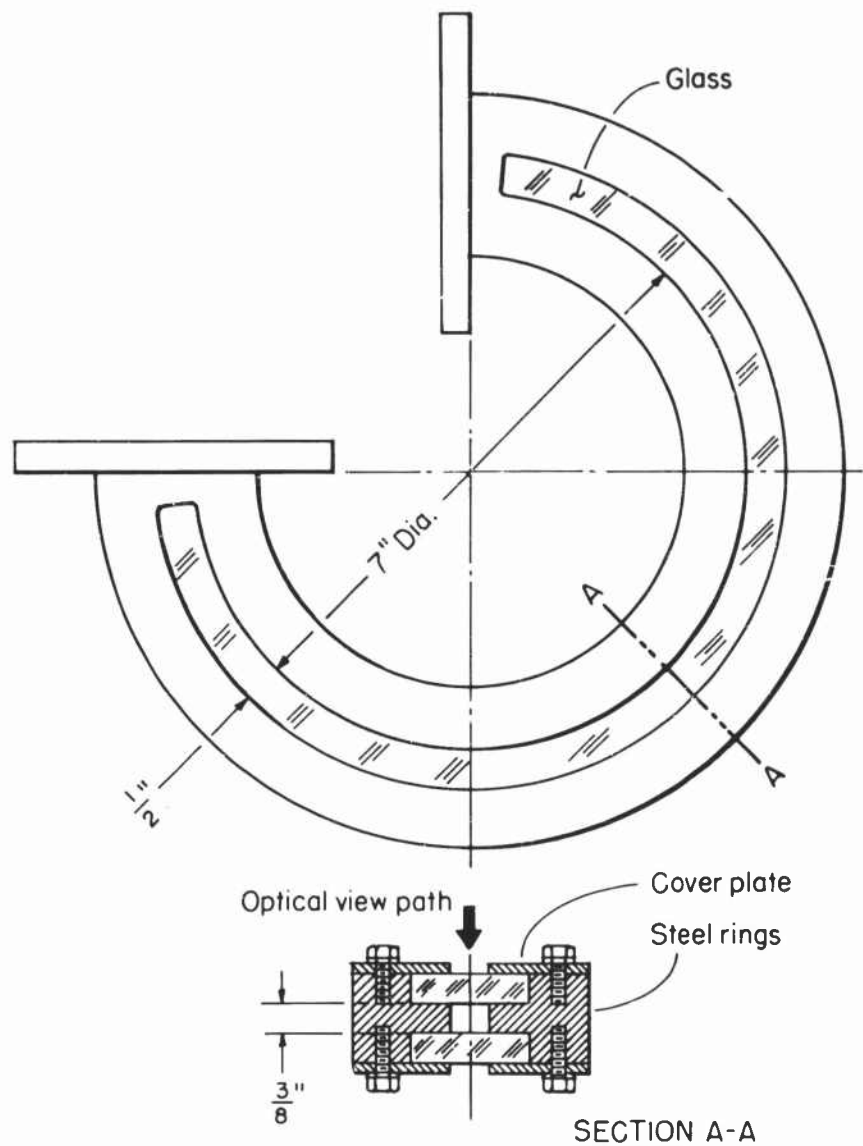


Figure 31. Schematic Drawing of the Curved Detonation Tube Section with Solid Walls.



Figure 32. Photograph of the Curved Detonation Tube Section with Solid Walls.

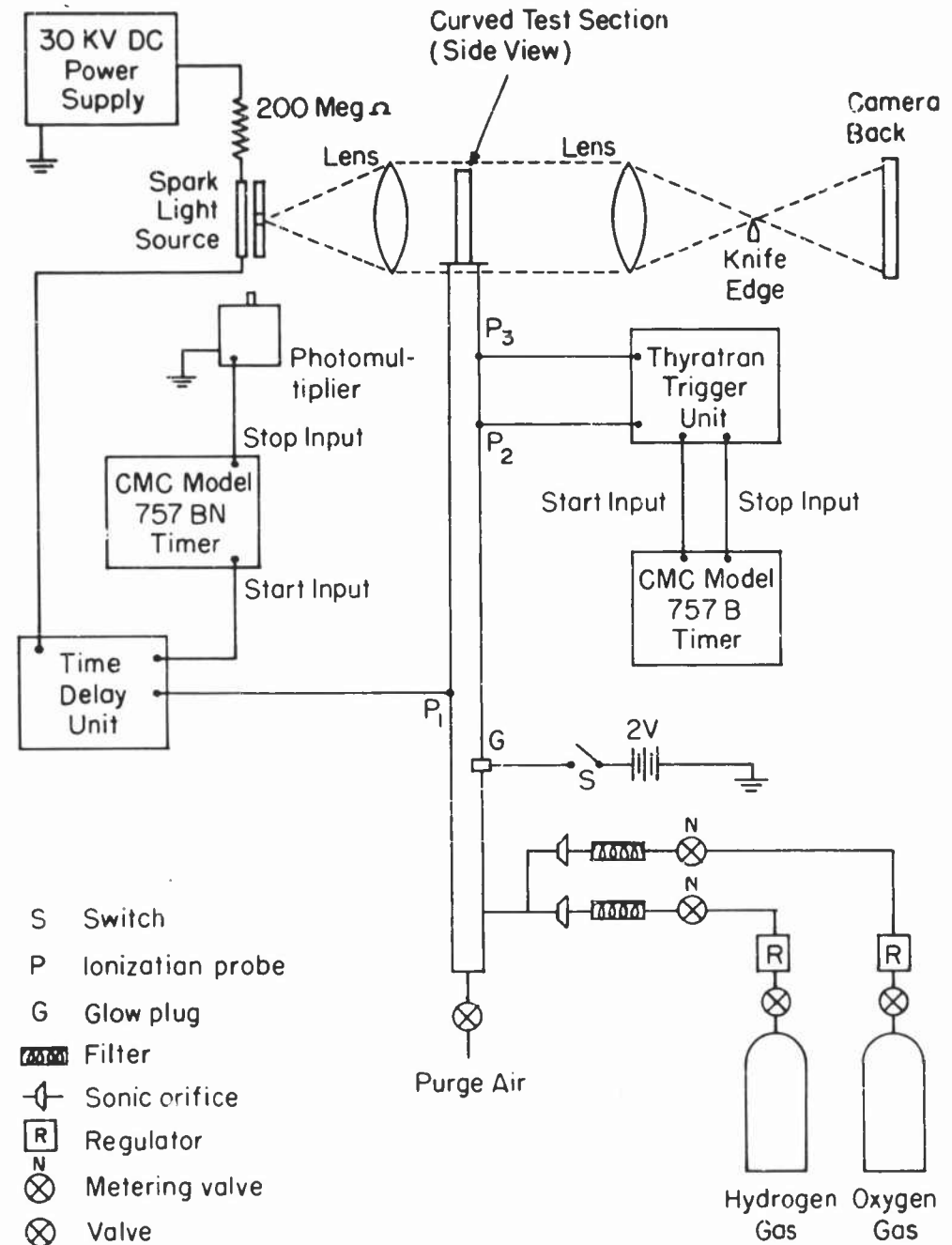


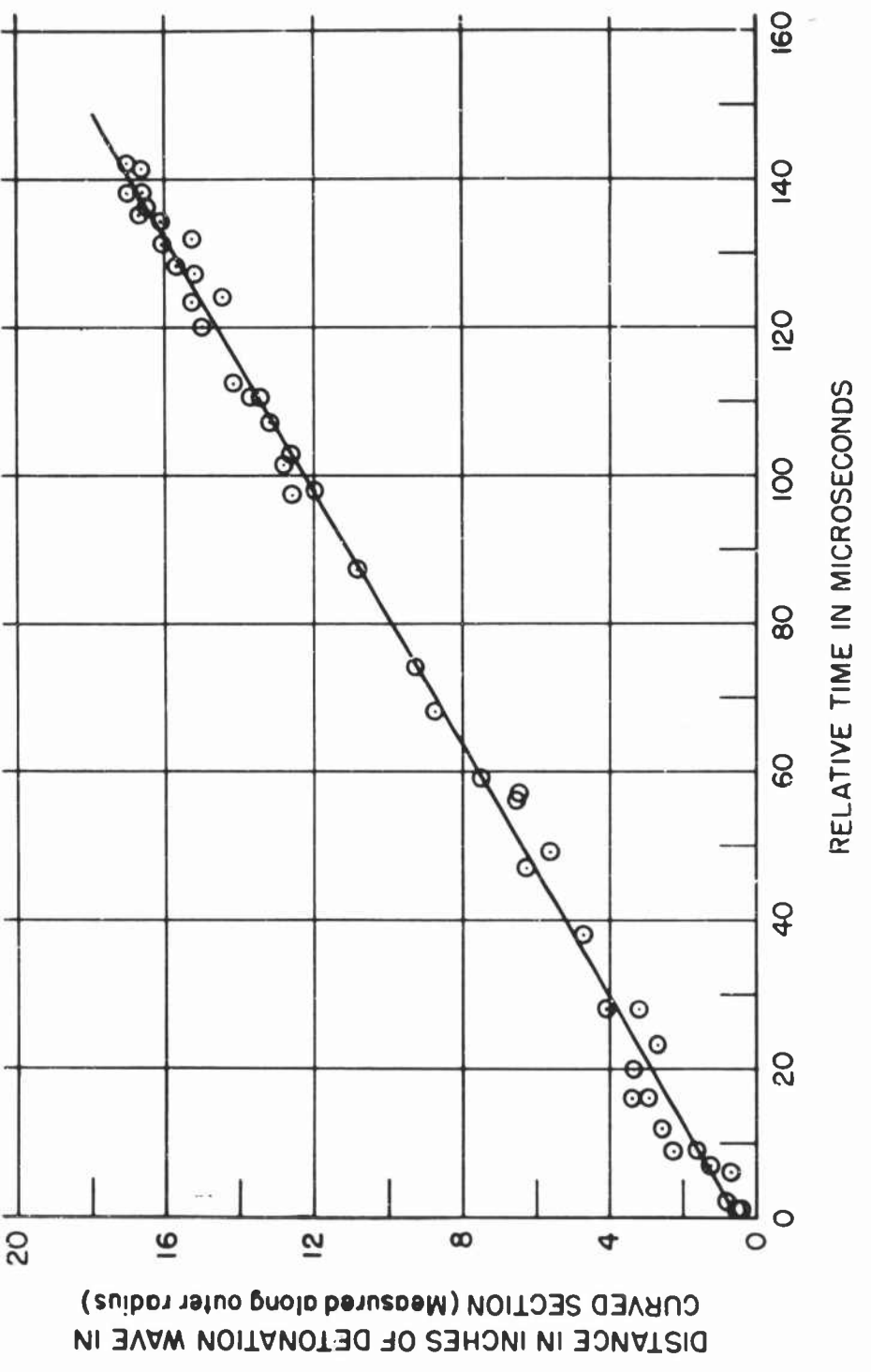
Figure 33. Schematic Diagram of the Basic Experimental System for Studying Detonation Waves in Curved Channels.



Figure 34(a). Schlieren Photograph of a Stoichiometric H₂-O₂ Detonation Wave in a Curved Channel Utilizing a Thin, Nitrocellulose Membrane for Inward Radial Relief Employing a Flowing System.



Figure 34(b). Schlieren Photograph of a Stoichiometric H₂-O₂ Detonation Wave in a Curved Channel with Complete Solid Wall Confinement Employing a Flowing System.



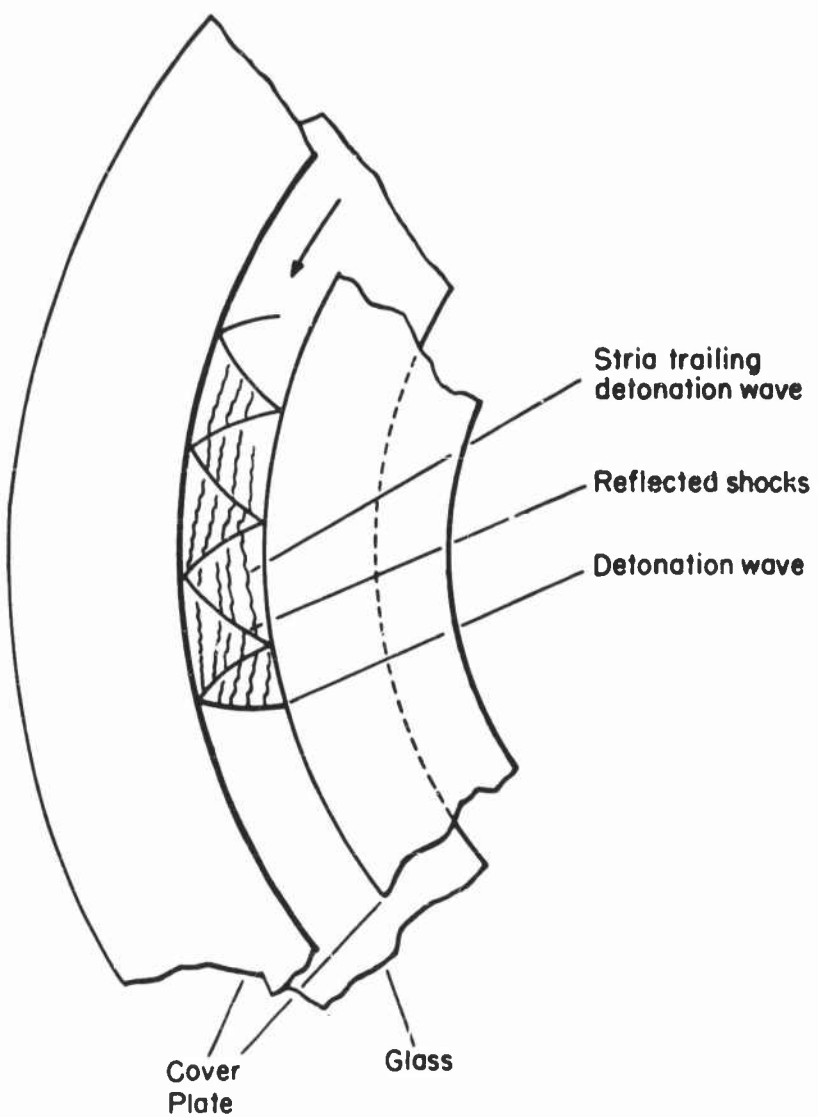


Figure 36. Interpretive Sketch of a Stoichiometric $\text{H}_2\text{-O}_2$ Detonation Wave in a Curved Channel with Complete Solid Wall Confinement.

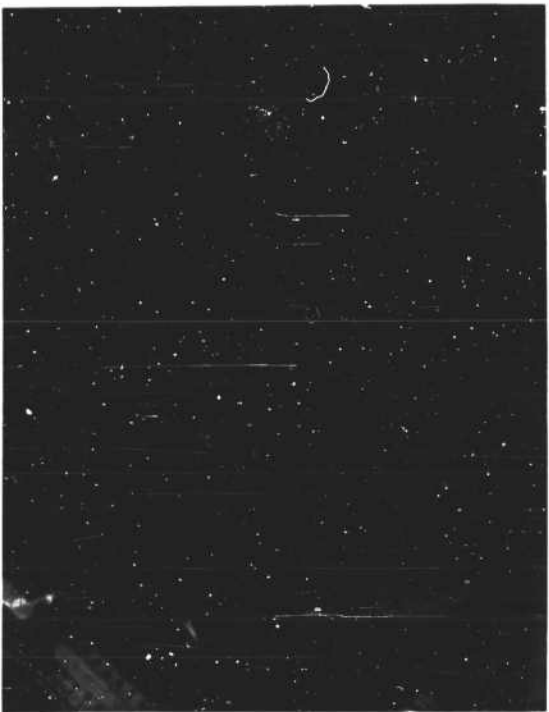


Figure 37. Schlieren Photograph of a Stoichiometric H₂-O₂ Detonation Wave in a Curved Channel with the Inner Wall Removed Employing a Flowing System.

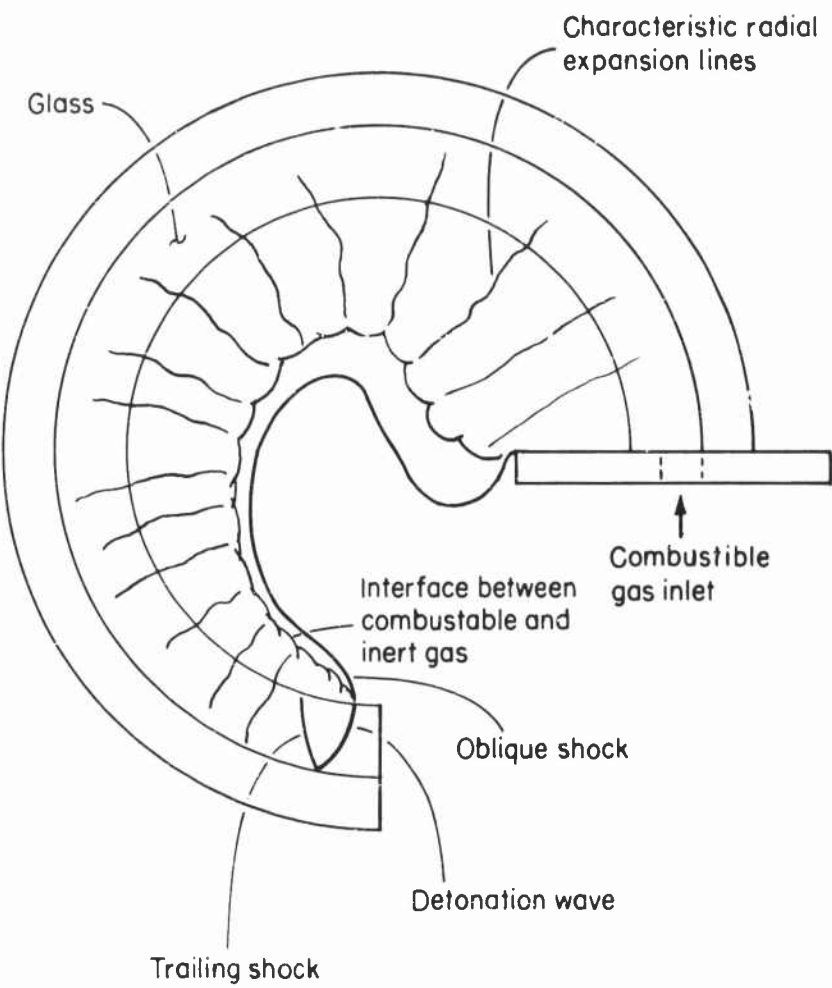


Figure 38. Interpretive Sketch of a Stoichiometric $\text{H}_2\text{-O}_2$ Detonation Wave in a Curved Channel with the Inner Wall Removed Employing a Flowing System.

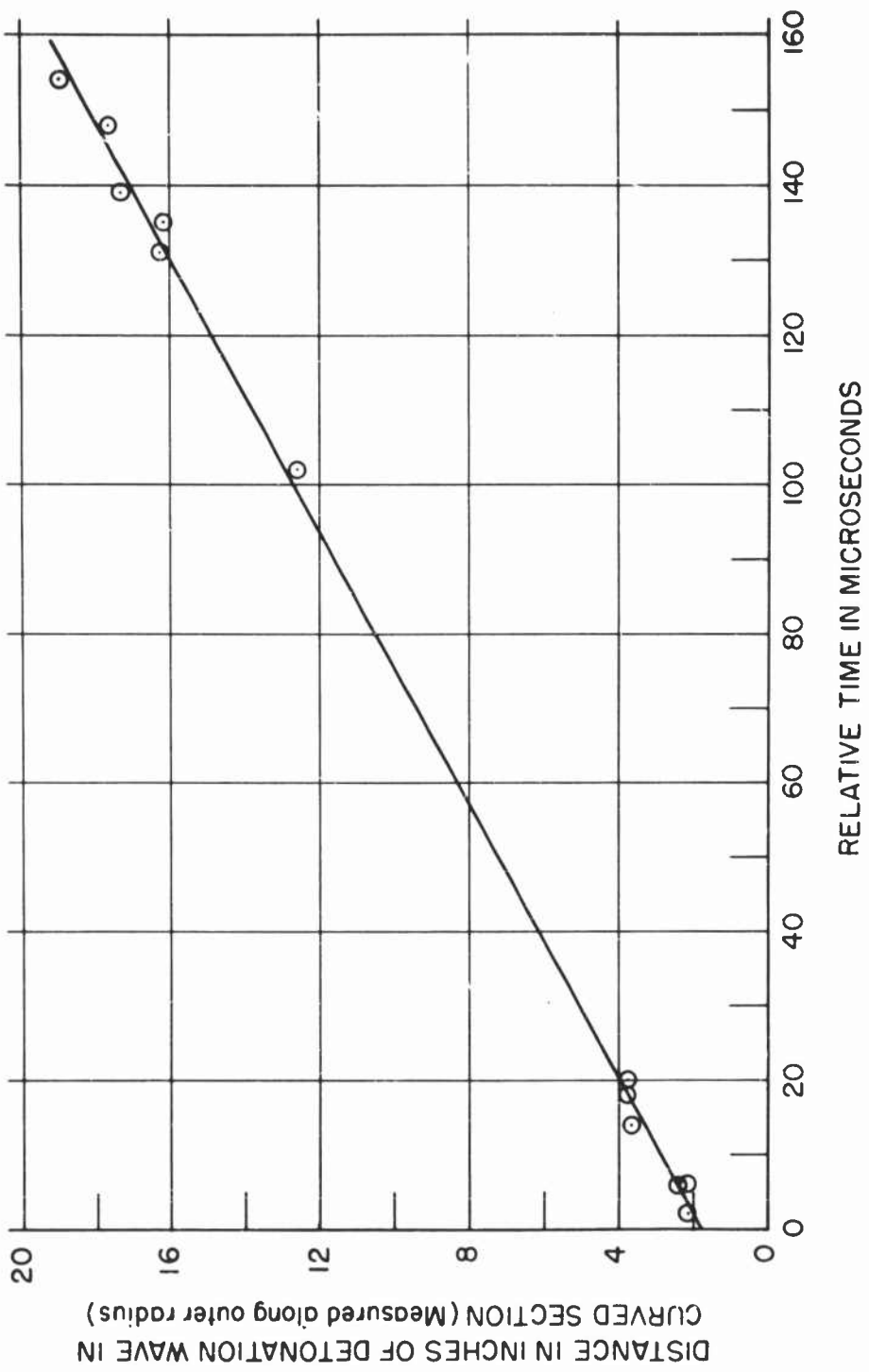


Figure 39. Position Versus Relative Time of Stoichiometric H₂-O₂ Detonation Waves Along the Outer Radius of the Curved Channel with Inner Wall Removed Employing a Flowing System.

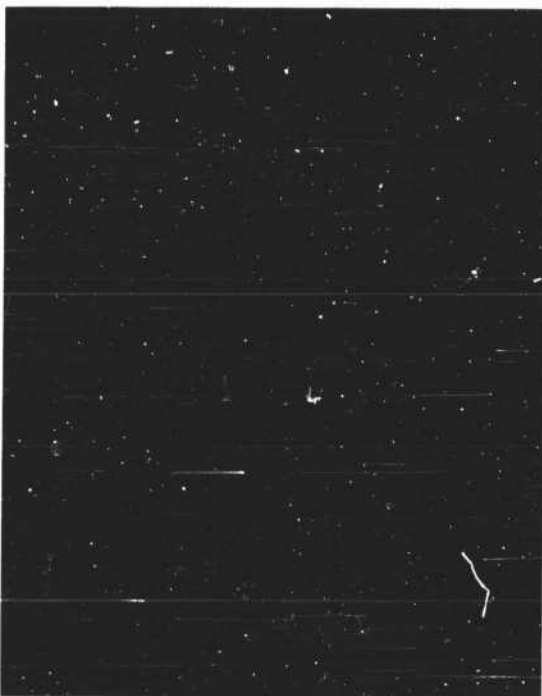


Figure 40. Schlieren Photograph of a Stoichiometric H₂-O₂ Detonation Wave in a Curved Channel with One Window Removed (Relief in the Axial Direction).

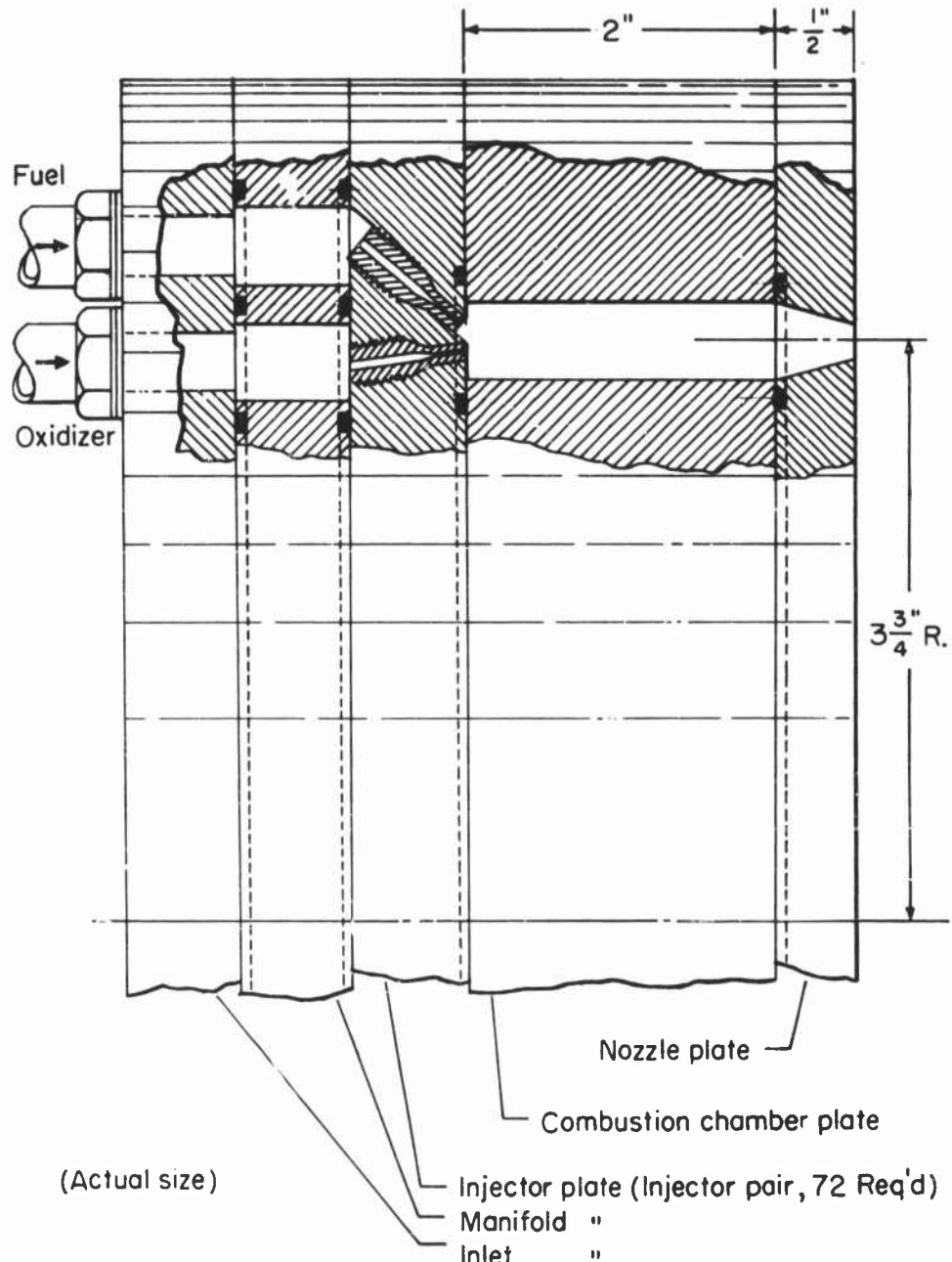


Figure 41. Schematic Drawing of Annular Motor.

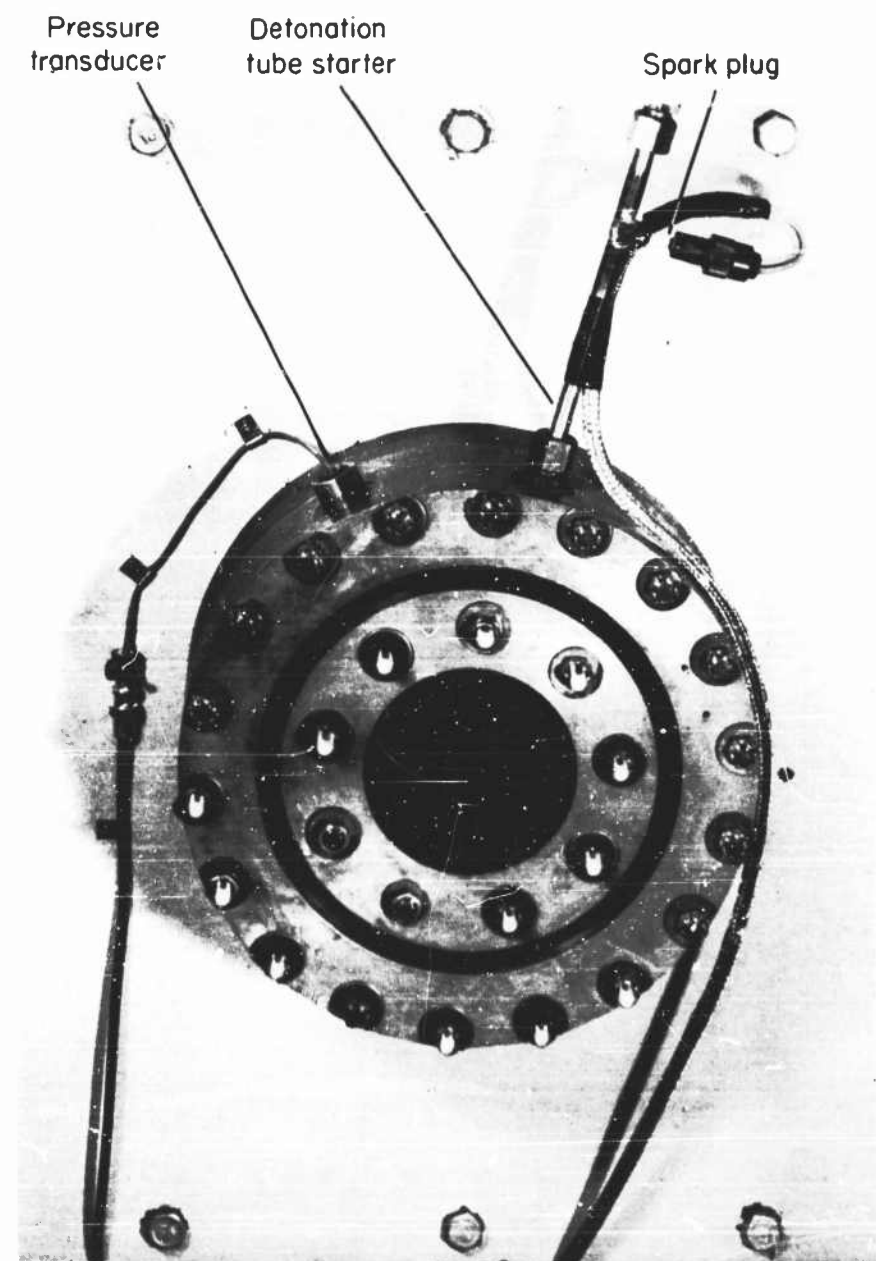
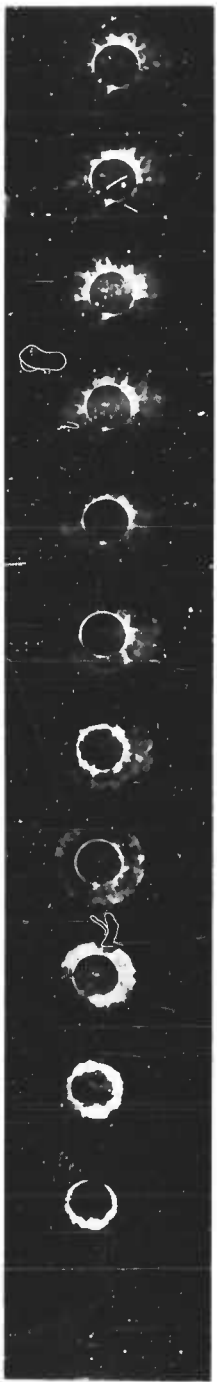


Figure 42. Photograph of Downstream End of Annular Motor.



(a) Spark Ignition with No Channel Blockage.



(b) Spark Ignition with Complete Channel Blockage
(Using 1/8 inch Thick Steel Plate).

Figure 43. High Speed Photographs of Colliding Detonation Waves in Annular Motor Taken by 8 mm Fastax Camera.
 $X_{H_2} = 2/3$, Framing Rate - 14,000 PPS.

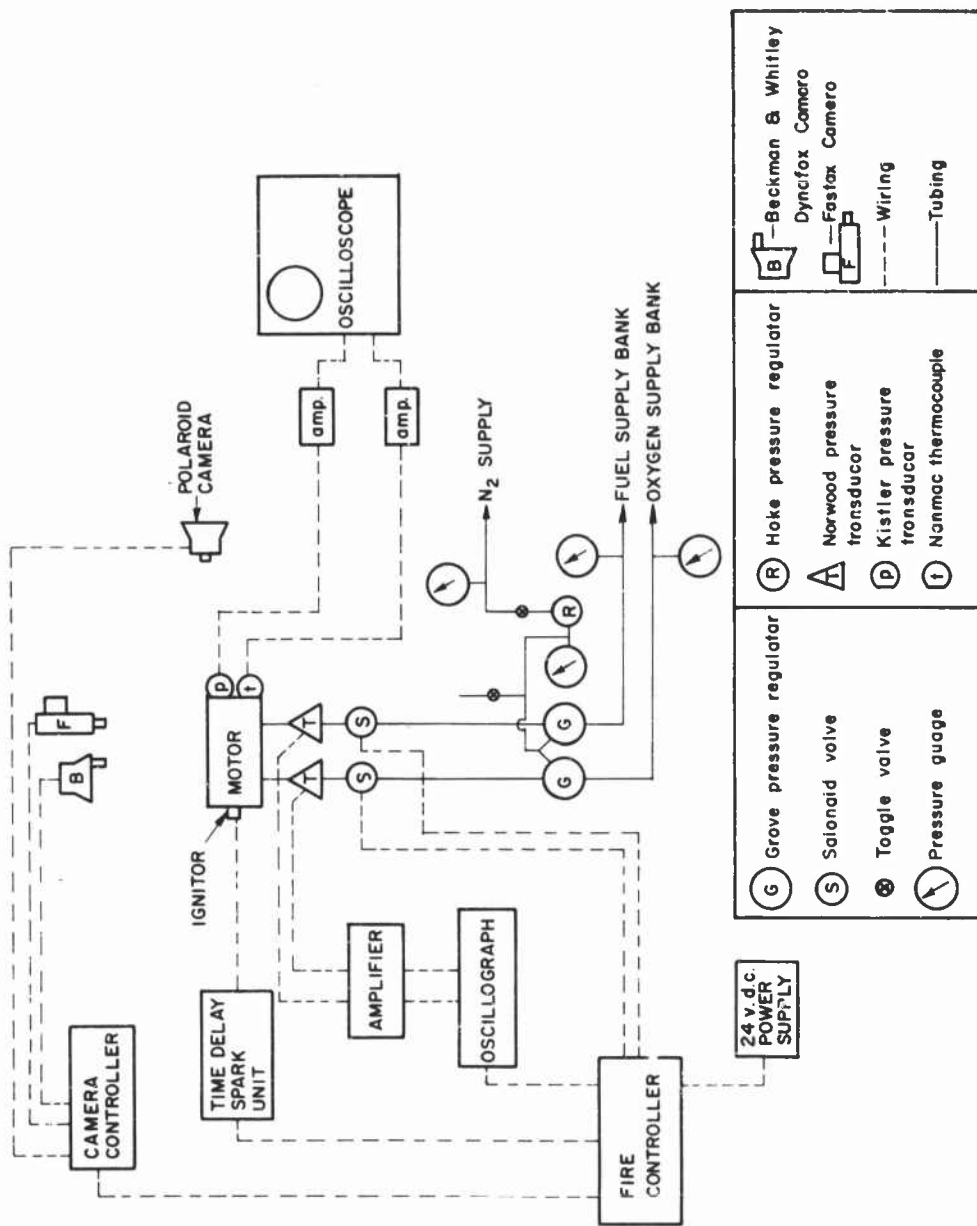


Figure 44. Schematic Diagram of Propellant Feed System and Instrumentation.

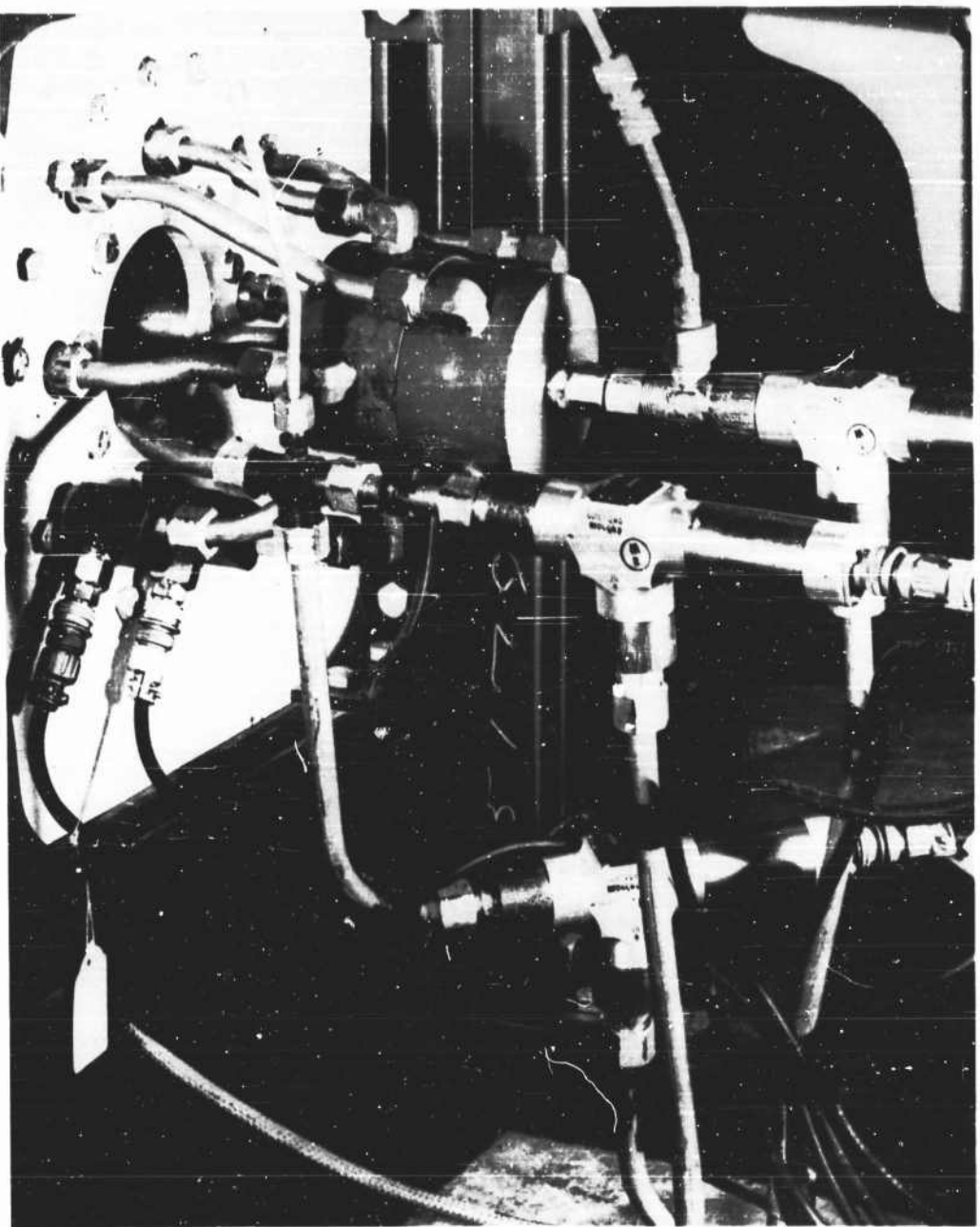


Figure 45. Photograph of Solenoid Valves and Injector Manifold Arrangement.

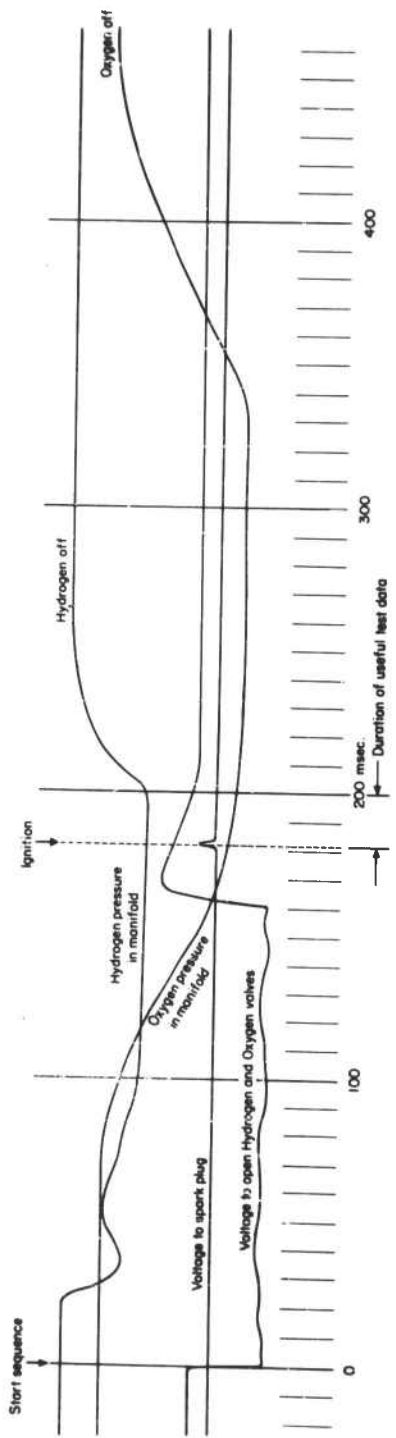
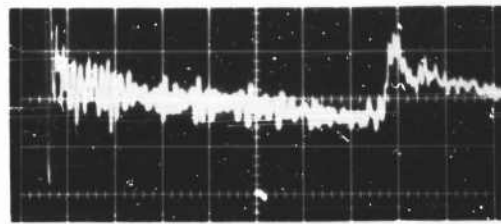
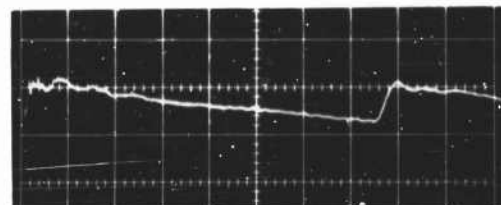


Figure 46. Typical Oscillograph Record Sequence of Events.

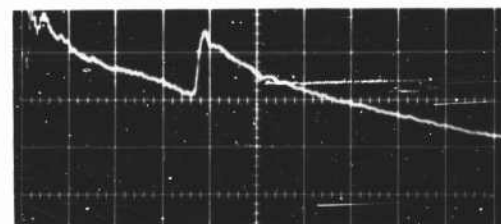
(a) Un-modified signal
50 μ sec/cm, 100 mv/cm



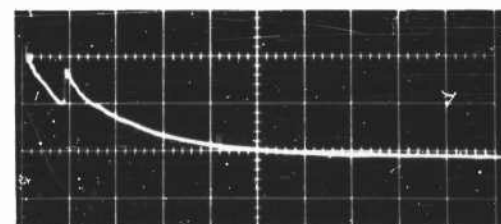
(b) Signal damped and filtered
50 μ sec/cm, 100 mv/cm



(c) Signal damped and filtered
100 μ sec/cm, 50 mv/cm



(d) Signal damped and filtered
500 μ sec/cm, 100 mv/cm



Note:

Transducer flush mounted in 1/2" x 1/4" detonation tube with .0005" scatch tape over end. One atmosphere detonation of 40% Hydrogen - 60% Oxygen. Peak pressure theoretically 250 psi. Manufacturers sensitivity .405 pCb/psi. Charge amplifier setting 5mv/pCb.

Result:

Sensitivity for damped and filtered signal .160 pCb.

Figure 47. Calibration of Kistler 603 Pressure Transducer in Detonation Tube.

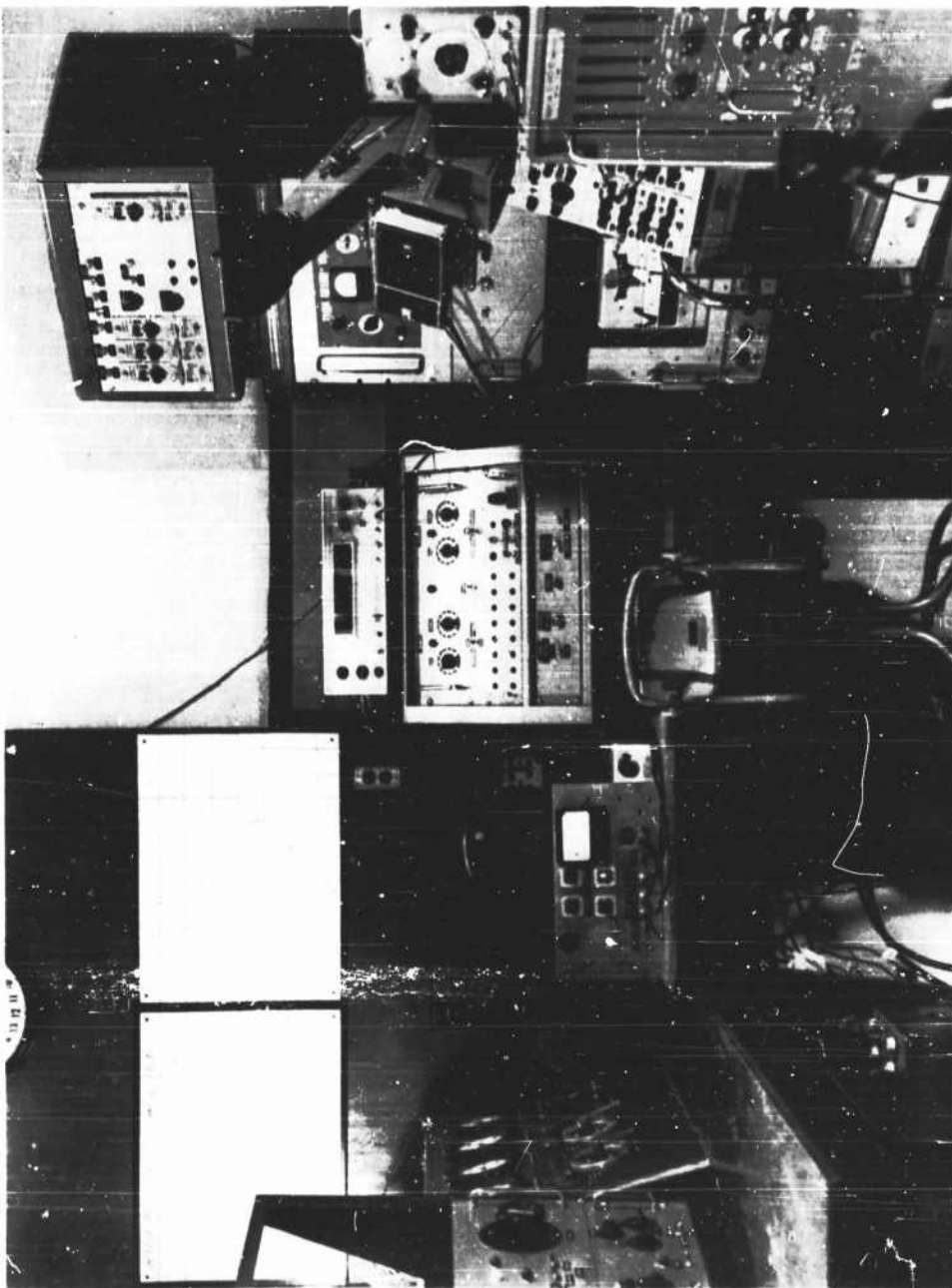


Figure 48. Photograph of Instrumentation Setup Outside Test Cell.

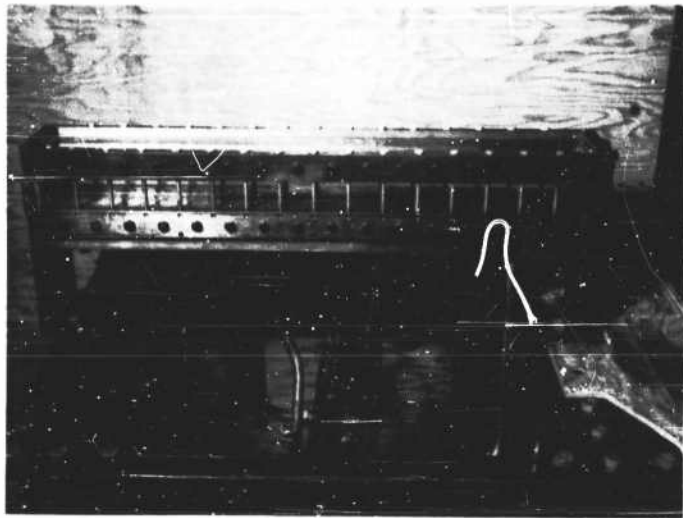


Figure 49. Photograph of the Linear Motor on the Test Stand.

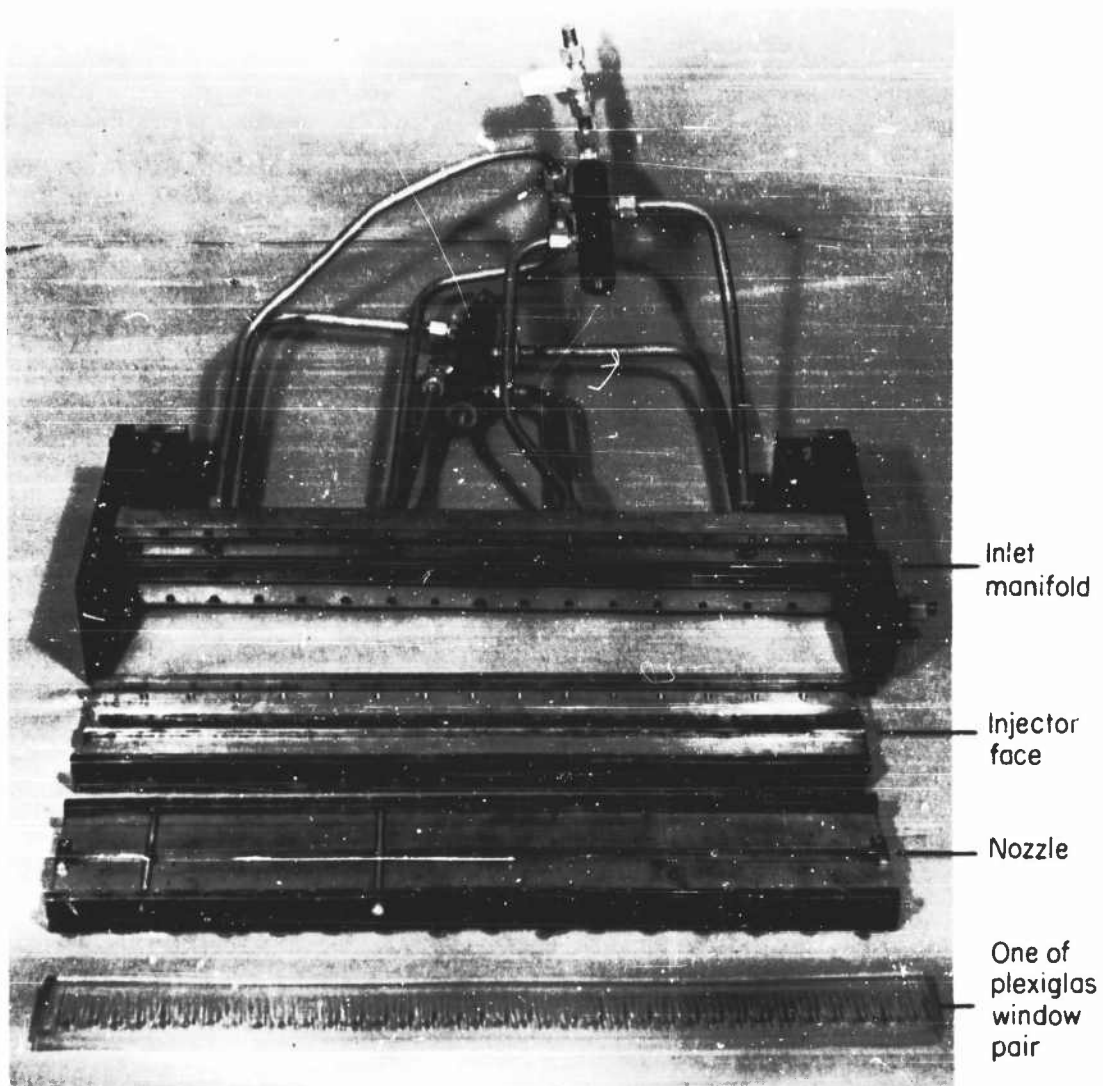


Figure 50. Photograph of the Components of the Linear Motor.

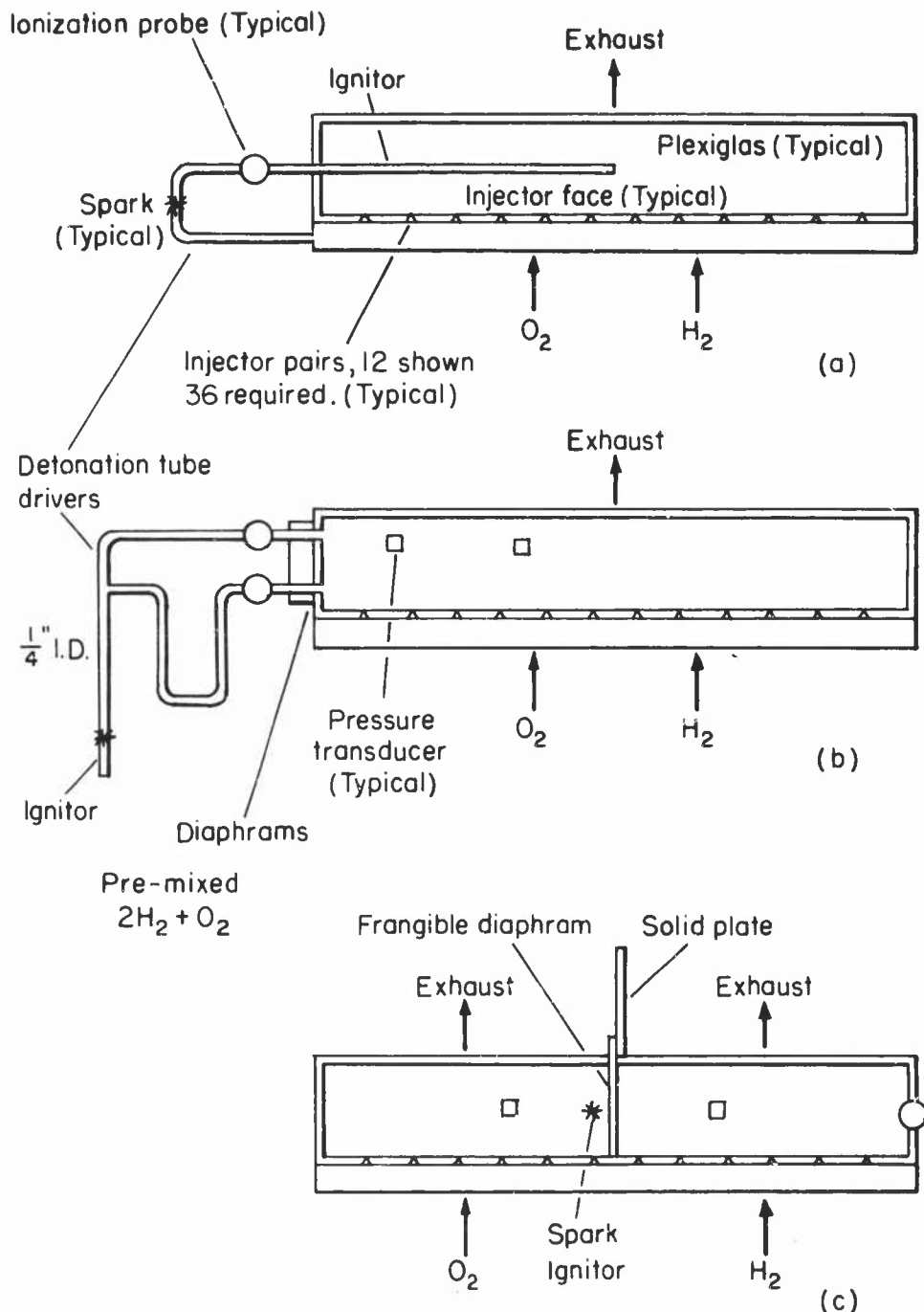
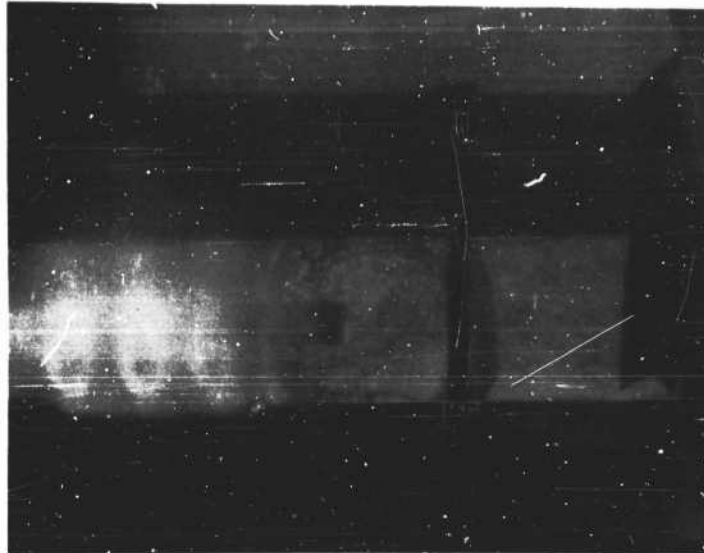


Figure 51. Schematic Drawing of Test Configurations for the Linear Motor.



Input Data:

H₂ Manifold Pressure: 1,000 psi

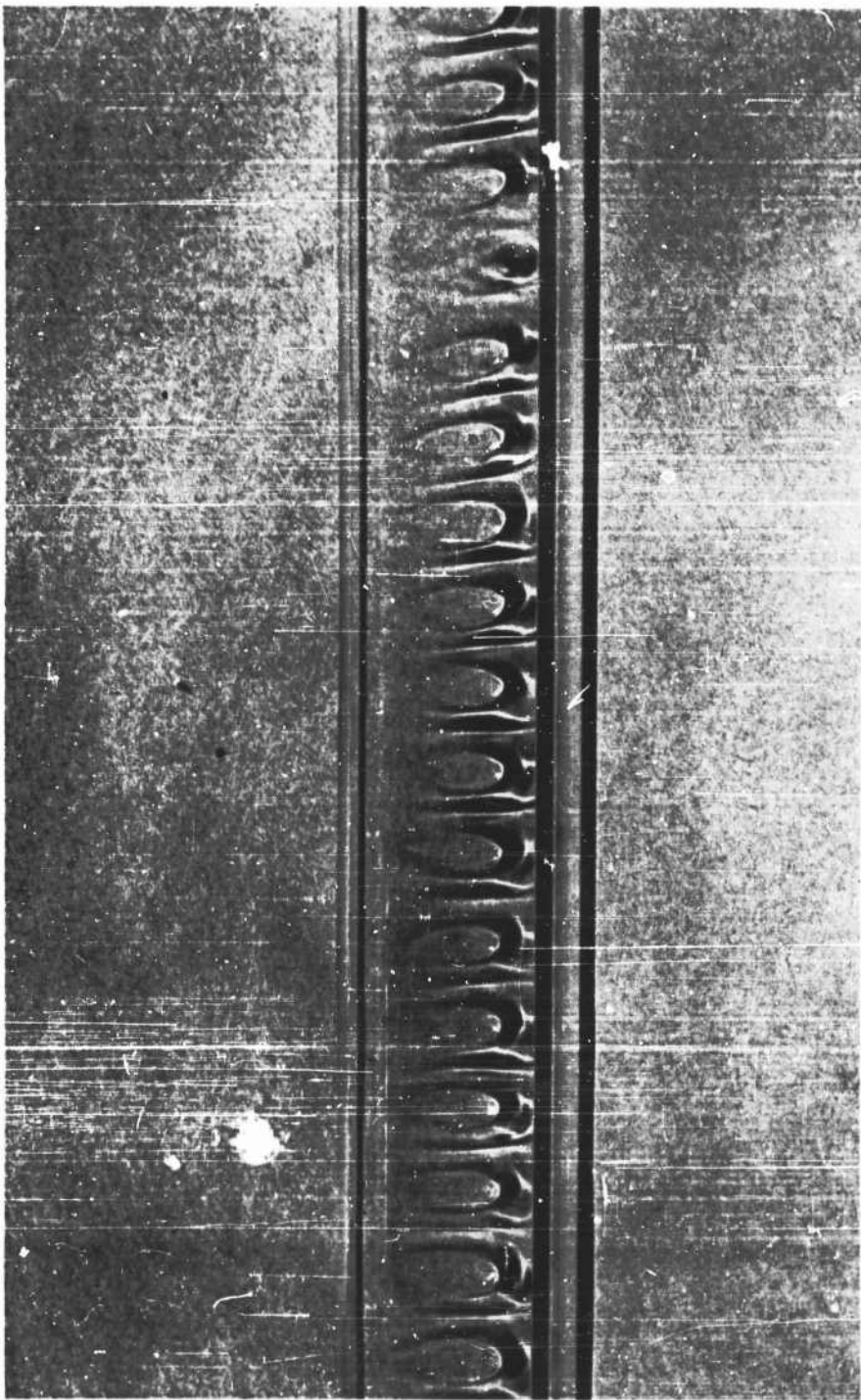
O₂ " " "

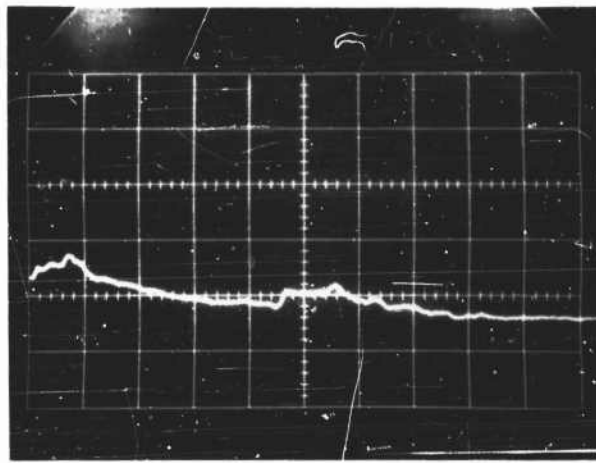
Mixture Ratio: 0.67 %, Mole Fraction Hydrogen

Nominal Mass Flow: 0.36 l.b.s. Propellant Per Second

Figure 52. Spark Schlieren Photograph of Test in Linear Motor Configuration (a).

Figure 53. Photograph of Plexiglas Window from Linear Motor after Test.



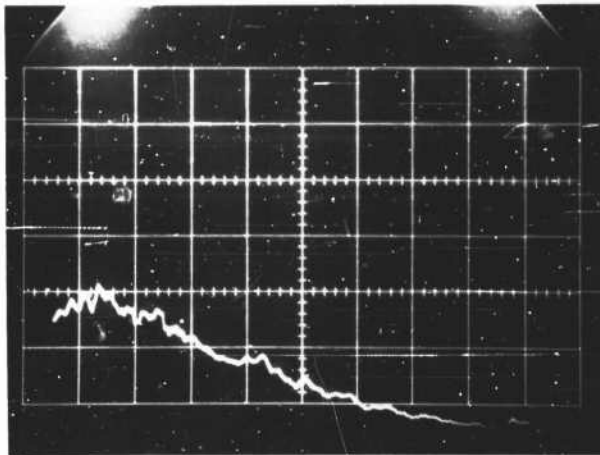


Horizontal Scale: 50 μ sec./cm.

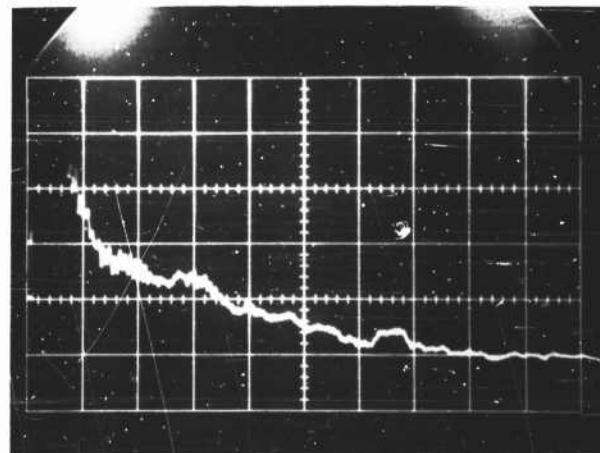
Vertical Scale: 0.5 Volts/cm.

Transducer located 1 3/4 inches from starter face and
7/8 inch from injector.

Figure 54. Pressure Recording of Starter Tube Fired into
Stagnant Air-Linear Motor.



(a) Transducer 1 3/4 inches from starter



(b) Transducer 7 1/4 inches from starter

Horizontal Scale : 50 μ sec./cm.
Vertical Scale : 0.5 Volts/cm.
Hydrogen Manifold Pressure: 1,000 psi
Oxygen " " 1,000 psi
Nominal Mass Flow: 0.46 Lbs./sec.
Mixture Ratio: 0.67 % H₂ by Volume

Figure 55. Pressure Recording of Linear Motor Configuration (b) Tests 15 and 16.

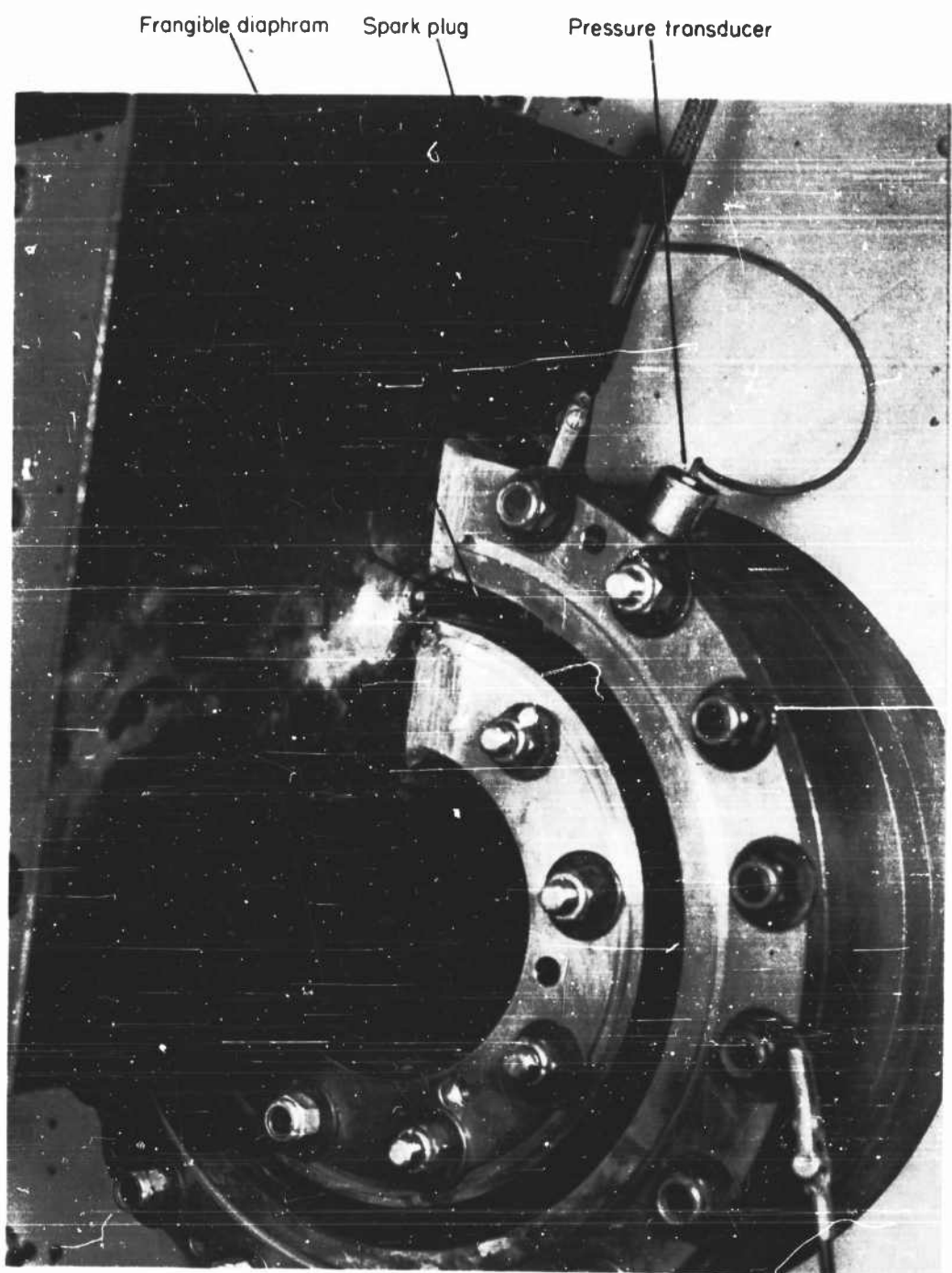
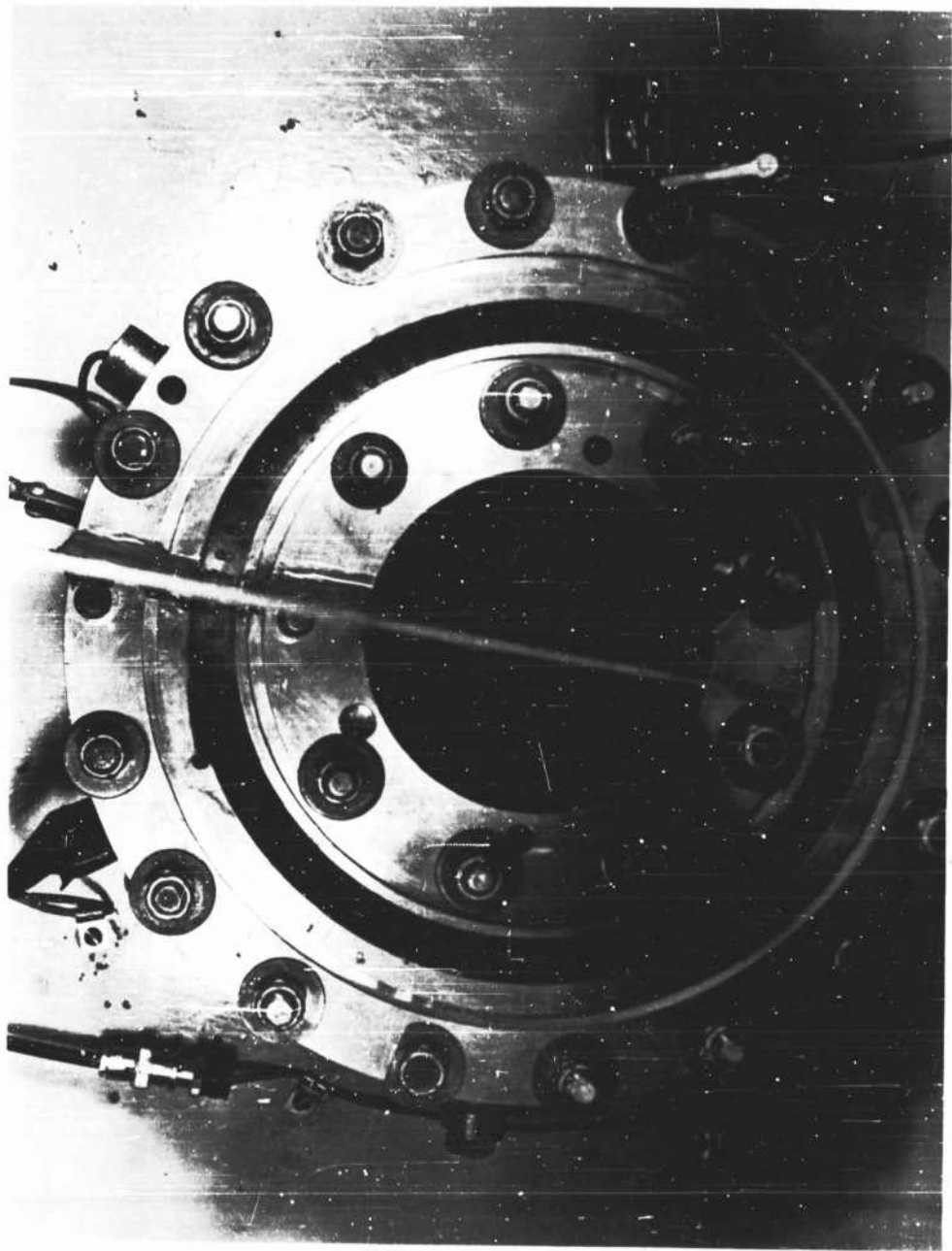


Figure 56. Photograph Showing Diaphragm in Annular Motor.

Figure 57. Photograph of Nozzle End of Annular Motor.



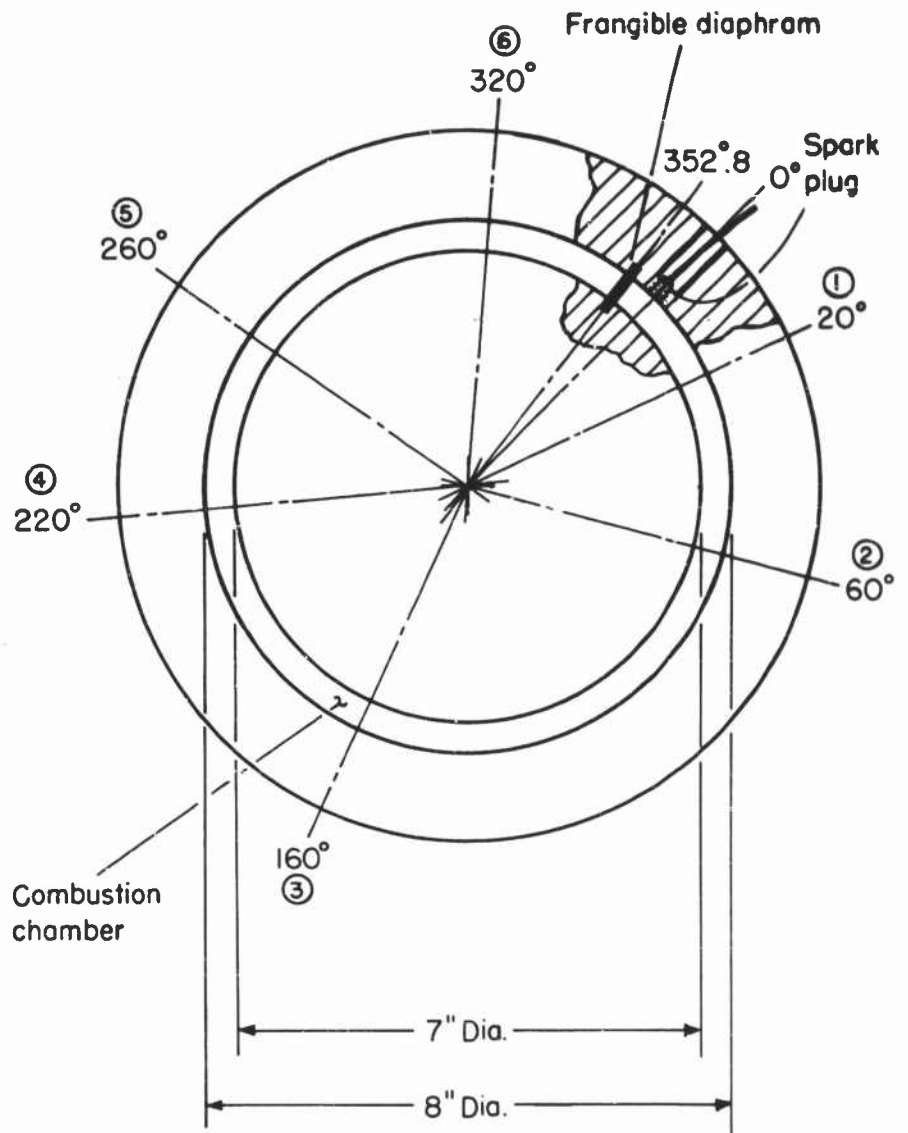
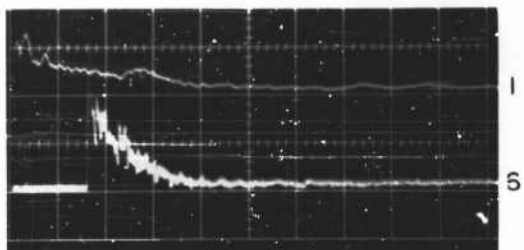
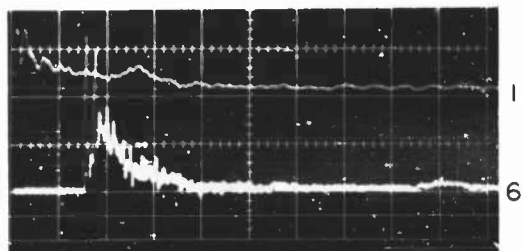


Figure 58. Station Locations for Pressure Transducers in Annular Motor.

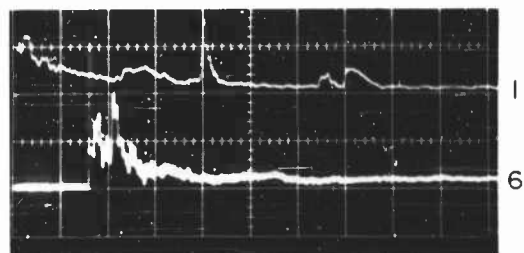
Run No. 151
 Horizontal scale 100 μ sec/cm
 Vertical scale 125 ~ psi/cm
 Fuel manifold pressure 1300 psi
 O₂ manifold pressure 1275 psi
 Nominal mass flow 1.15 lbs/sec
 Nominal mixture ratio 66.2 % fuel by vol.
 Diaphragm thickness .001 in



Run No. 154
 Horizontal scale 100 μ sec/cm
 Vertical scale 125 ~ psi/cm
 Fuel manifold pressure 1360 psi
 O₂ manifold pressure 1350 psi
 Nominal mass flow 1.22 lbs/sec
 Nominal mixture ratio 66.6 % fuel by vol.
 Diaphragm thickness .001 in



Run No. 156
 Horizontal scale 100 μ sec/cm
 Vertical scale 125 ~ psi/cm
 Fuel manifold pressure 1680 psi
 O₂ manifold pressure 1330 psi
 Nominal mass flow 1.23 lbs/sec
 Nominal mixture ratio 71.9 % fuel by vol.
 Diaphragm thickness .001 in



Run No. 160
 Horizontal scale 100 μ sec/cm
 Vertical scale 125 ~ psi/cm
 Fuel manifold pressure 1620 psi
 O₂ manifold pressure 1310 psi
 Nominal mass flow 1.21 lbs/sec
 Nominal mixture ratio 71.2 % fuel by vol.
 Diaphragm thickness .001 in

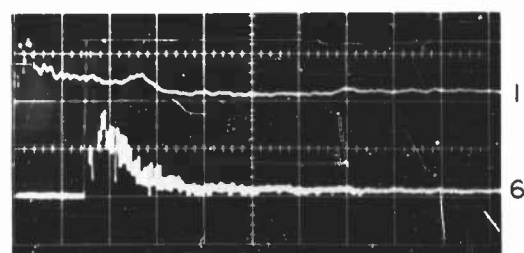
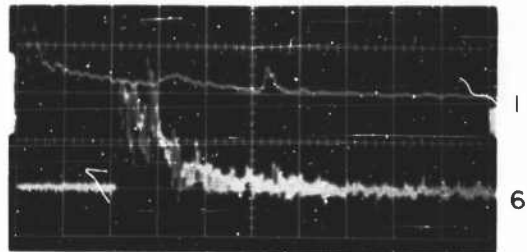
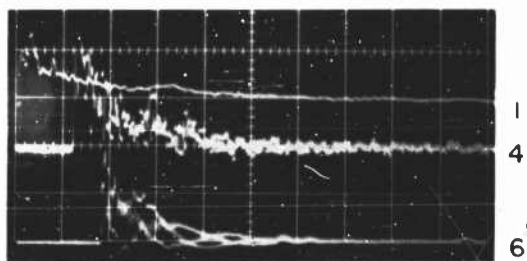


Figure 59. Pressure Recordings of Annular Motor Tests, Hydrogen-Oxygen,
 $A_c/A_t = 2.0$.

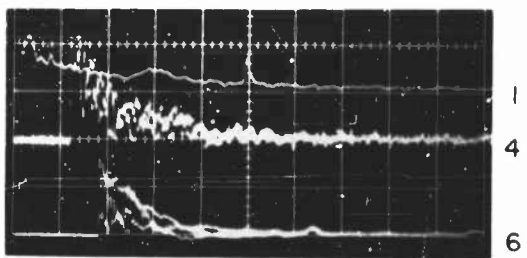
Run No. 166
 Horizontal scale 100 μ sec/cm
 Vertical scale 125 ~ psi/cm
 Fuel manifold pressure 600 psi
 O₂ manifold pressure 1265 psi
 Nominal mass flow 1.08 lbs/sec
 Nominal mixture ratio 48.7 % fuel by vol.
 Diaphragm thickness .001 in



Run No. 173
 Horizontal scale 100 μ sec/cm
 Vertical scale 125 ~ psi/cm
 Fuel manifold pressure 840 psi
 O₂ manifold pressure 1215 psi
 Nominal mass flow 1.06 lbs/sec
 Nominal mixture ratio 58.2 % fuel by vol.
 Diaphragm thickness .001 in



Run No. 174
 Horizontal scale 100 μ sec/cm
 Vertical scale 125 ~ psi/cm
 Fuel manifold pressure 820 psi
 C₂ manifold pressure 1210 psi
 Nominal mass flow 1.05 lbs/sec
 Nominal mixture ratio 57.6 % fuel by vol.
 Diaphragm thickness .001 in



Run No. 175
 Horizontal scale 100 μ sec/cm
 Vertical scale 125 ~ psi/cm
 Fuel manifold pressure 720 psi
 O₂ manifold pressure 1210 psi
 Nominal mass flow 1.04 lbs/sec
 Nominal mixture ratio 54.3 % fuel by vol.
 Diaphragm thickness .001 in

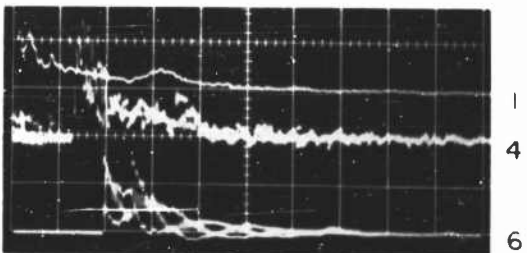
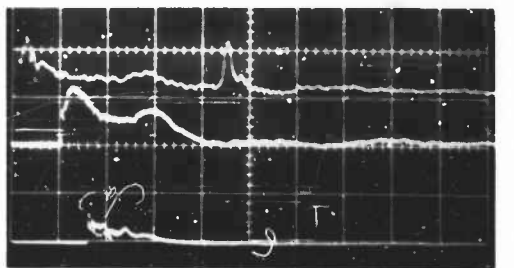


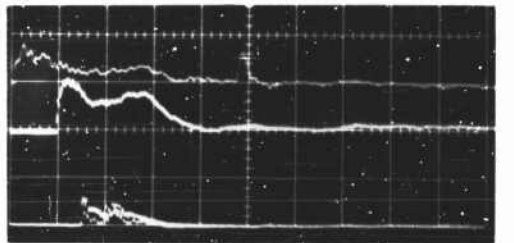
Figure 59. Concluded.

Run No. 205
 Horizontal scale 100 μ sec/cm
 Vertical scale 125 ~ psi/cm
 Fuel manifold pressure 1640 psi
 O₂ manifold pressure 1360 psi
 Nominal mass flow 1.25 lbs/sec
 Nominal mixture ratio 70.5 % fuel by vol.
 Diaphragm thickness .001 in

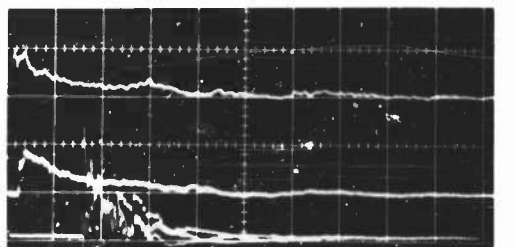


Run No. 206

(Typical)



Run No. 217
 Horizontal scale 100 μ sec/cm
 Vertical scale 125 ~ psi/cm
 Fuel manifold pressure 1230 psi
 O₂ manifold pressure 1275 psi
 Nominal mass flow 1.14 lbs/sec
 Nominal mixture ratio 65.9 % fuel by vol.
 Diaphragm thickness .001 in



Run No. - 219

(Typical)

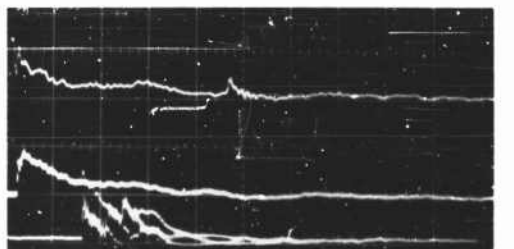
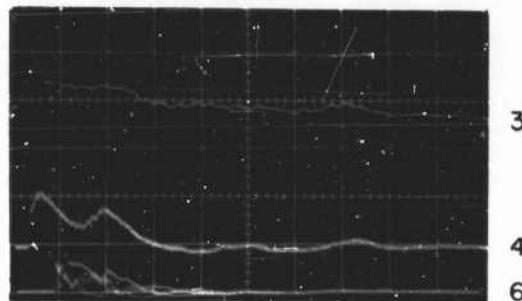


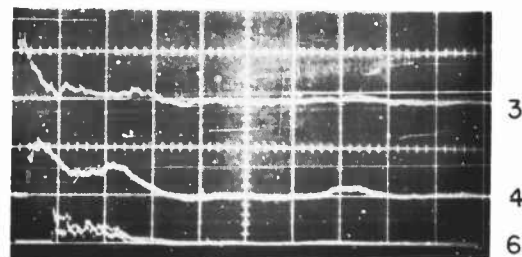
Figure 60. Pressure Recordings of Annular Motor Tests, Hydrogen-Oxygen,
 $A_c/A_t = 1.0$.

Run No. 209
Horizontal scale 100 μ sec/cm
Vertical scale 125 ~ psi/cm
Fuel manifold pressure 1280 psi
 O_2 manifold pressure 1280 psi
Nominal mass flow 1.15 lbs/sec
Nominal mixture ratio 67.0 % fuel by vol
Diaphragm thickness .125 in



Run No. 210

(Typical)



Run No. 211

(Typical)

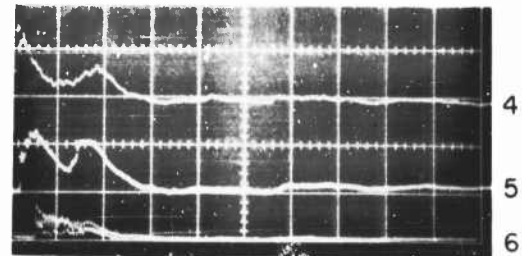


Figure 60. Continued.

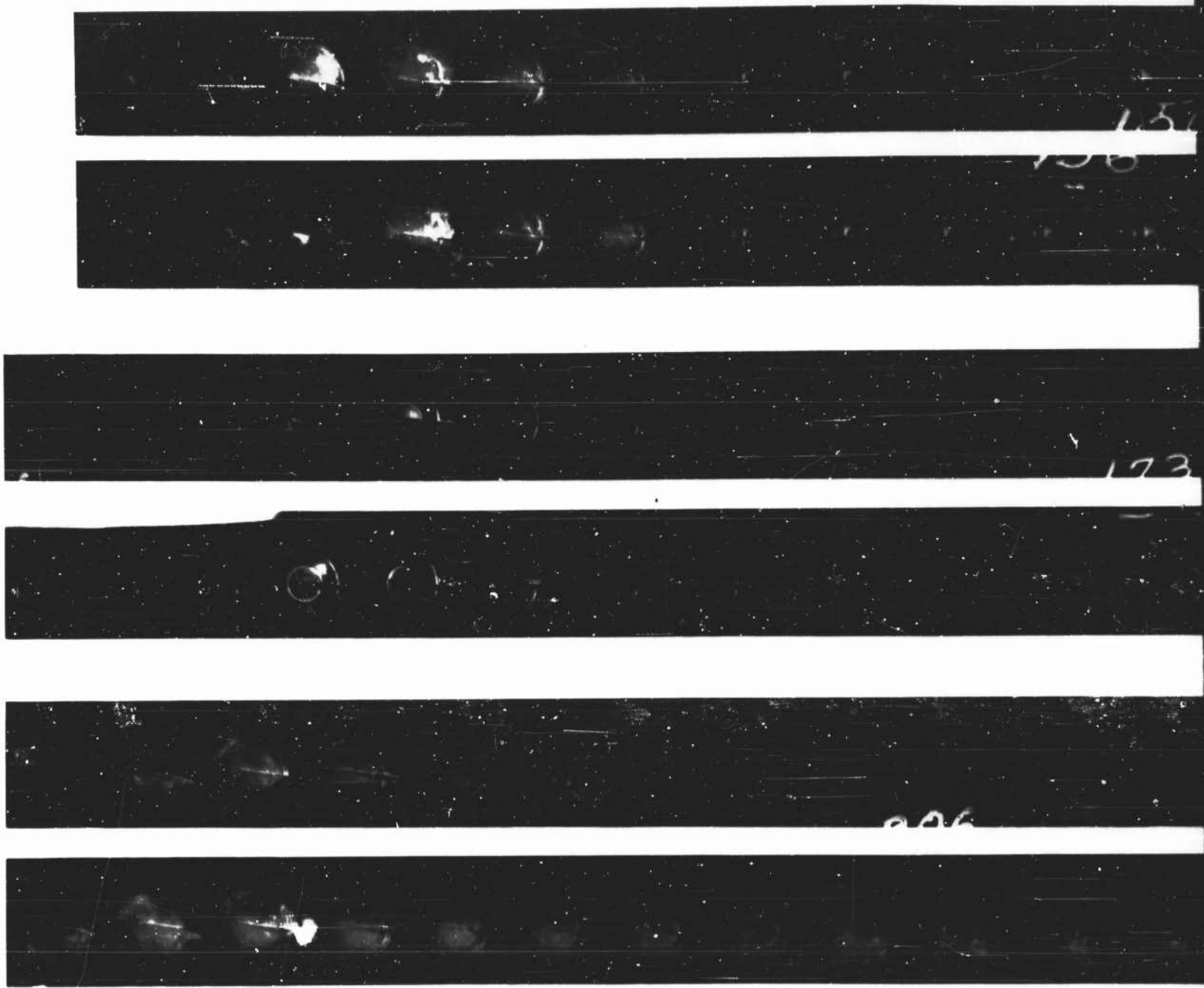
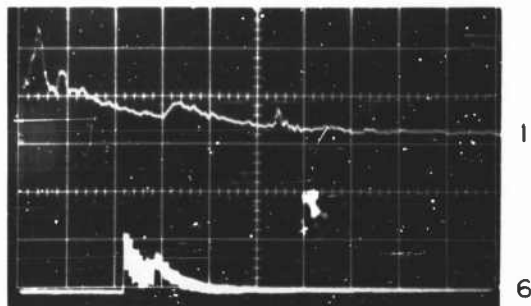


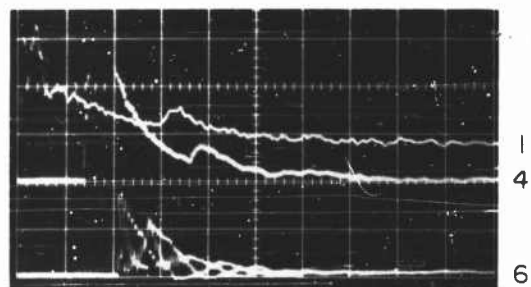
Figure 61. High Speed Photographs of Annular Motor Tests, Hydrogen-Oxygen.

1

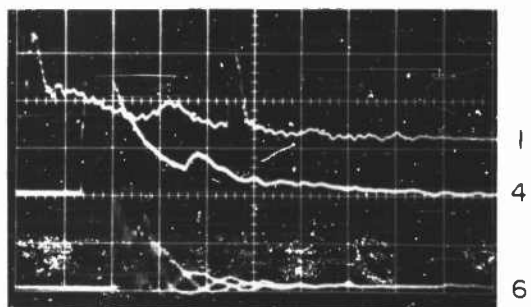
Run No. 182
 Horizontal scale 100 μ sec/cm
 Vertical scale 125 ~ psi/cm
 Fuel manifold pressure 720 psi
 O₂ manifold pressure 1165 psi
 Nominal mass flow 1.13 lbs/sec
 Nominal mixture ratio 29.7 % fuel by vol.
 Diaphragm thickness .002 in



Run No. 196
 Horizontal scale 100 μ sec/cm
 Vertical scale 125 ~ psi/cm
 Fuel manifold pressure 1040 psi
 O₂ manifold pressure 1320 psi
 Nominal mass flow 1.35 lbs/sec
 Nominal mixture ratio 34.8 % fuel by vol.
 Diaphragm thickness .002 in



Run No. 197
 Horizontal scale 100 μ sec/cm
 Vertical scale 125 ~ psi/cm
 Fuel manifold pressure 1140 psi
 O₂ manifold pressure 1320 psi
 Nominal mass flow 1.38 lbs/sec
 Nominal mixture ratio 36.8 % fuel by vol.
 Diaphragm thickness .002 in



Run No. 198

(Typical)

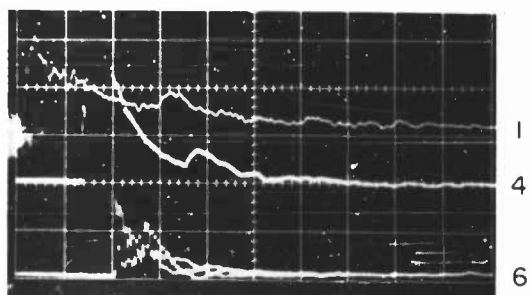
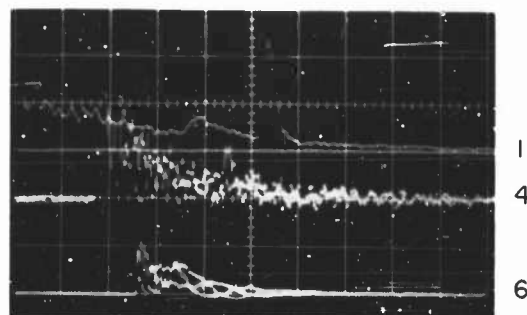
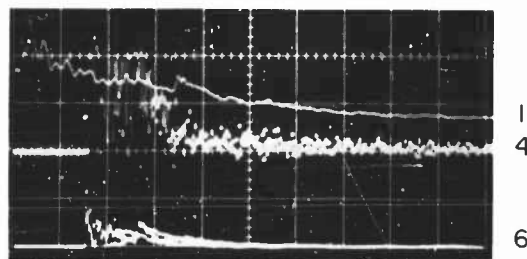


Figure 62. Pressure Recordings of Annular Motor Tests, Methane-Oxygen,
 $A_c/A_t = 2.0$.

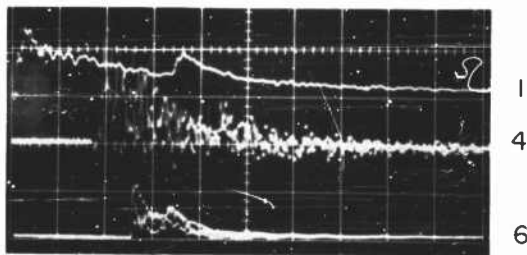
Run No. 189
 Horizontal scale 100 μ sec/cm
 Vertical scale 125 ~ psi/cm
 Fuel manifold pressure 440 psi
 O₂ manifold pressure 1425 psi
 Nominal mass flow 1.26 lbs/sec
 Nominal mixture ratio 17.4 % fuel by vol.
 Diaphragm thickness .0015 in



Run No. 190
 Horizontal scale 100 μ sec/cm
 Vertical scale 125 ~ psi/cm
 Fuel manifold pressure 500 psi
 O₂ manifold pressure 1425 psi
 Nominal mass flow 1.28 lbs/sec
 Nominal mixture ratio 17.1 % fuel by vol.
 Diaphragm thickness .0015 in



Run No. 191
 Horizontal scale 100 μ sec/cm
 Vertical scale 125 ~ psi/cm
 Fuel manifold pressure 400 psi
 O₂ manifold pressure 1425 psi
 Nominal mass flow 1.25 lbs/sec
 Nominal mixture ratio 16.1 % fuel by vol.
 Diaphragm thickness .001 in



Run No. 192
 Horizontal scale 100 μ sec/cm
 Vertical scale 125 ~ psi/cm
 Fuel manifold pressure 260 psi
 O₂ manifold pressure 1410 psi
 Nominal mass flow 1.20 lbs/sec
 Nominal mixture ratio 11.2 % fuel by vol.
 Diaphragm thickness .001 in

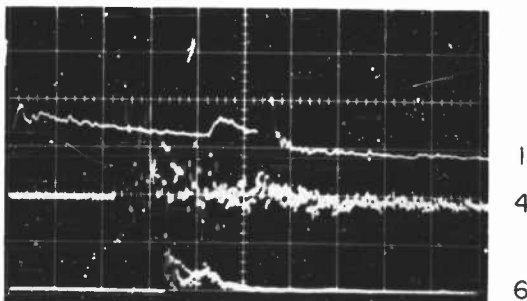
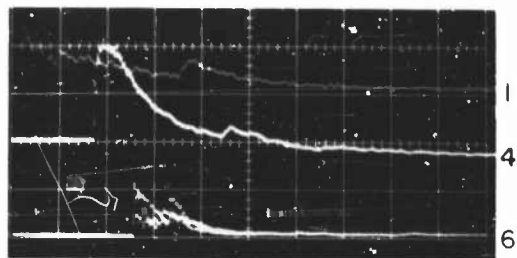
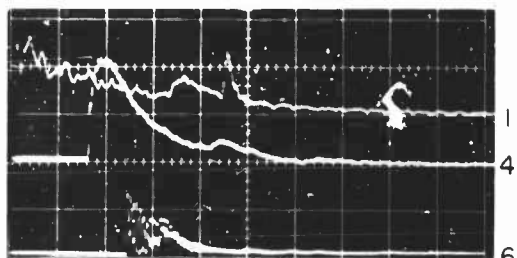


Figure 62. Continued.

Run No. 193
 Horizontal scale 100 μ sec/cm
 Vertical scale 125 ~ psi/cm
 Fuel manifold pressure 390 psi
 O₂ manifold pressure 1350 psi
 Nominal mass flow 1.19 lbs/sec
 Nominal mixture ratio 16.5 % fuel by vol.
 Diaphragm thickness .0015 in



Run No. 194
 Horizontal scale 100 μ sec/cm
 Vertical scale 125 ~ psi/cm
 Fuel manifold pressure 490 psi
 O₂ manifold pressure 1345 psi
 Nominal mass flow 1.21 lbs/sec
 Nominal mixture ratio 20.0 % fuel by vol.
 Diaphragm thickness .0015 in



Run No. 195
 Horizontal scale 100 μ sec/cm
 Vertical scale 125 ~ psi/cm
 Fuel manifold pressure 500 psi
 O₂ manifold pressure 1350 psi
 Nominal mass flow 1.22 lbs/sec
 Nominal mixture ratio 20.2 % fuel by vol.
 Diaphragm thickness .0015 in

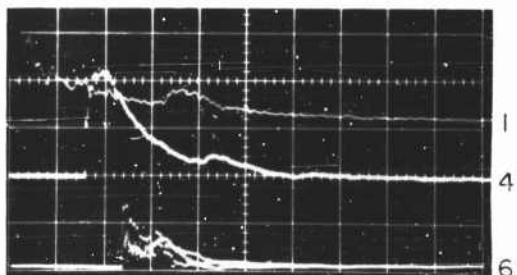
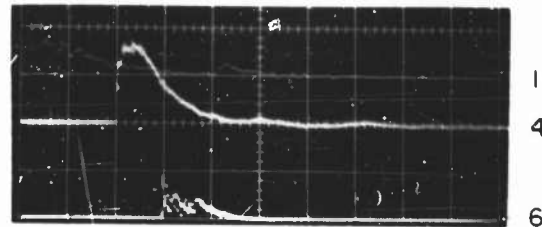
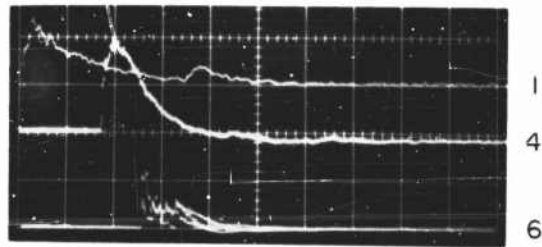


Figure 62. Concluded.

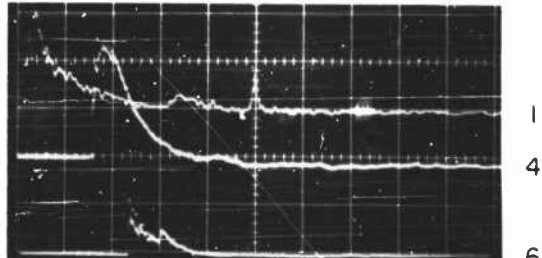
Run No. 199
 Horizontal scale 100 μ sec/cm
 Vertical scale 125 ~ psi/cm
 Fuel manifold pressure 350 psi
 O₂ manifold pressure 1330 psi
 Nominal mass flow 1.16 lbs/sec
 Nominal mixture ratio 15.3 % fuel by vol.
 Diaphragm thickness .0015 in



Run No. 200
 Horizontal scale 100 μ sec/cm
 Vertical scale 125 ~ psi/cm
 Fuel manifold pressure 400 psi
 O₂ manifold pressure 1310 psi
 Nominal mass flow 1.16 lbs/sec
 Nominal mixture ratio 17.2 % fuel by vol.
 Diaphragm thickness .0015 in



Run No. 201
 Horizontal scale 100 μ sec/cm
 Vertical scale 125 ~ psi/cm
 Fuel manifold pressure 600 psi
 O₂ manifold pressure 1275 psi
 Nominal mass flow 1.18 lbs/sec
 Nominal mixture ratio 24.4 % fuel by vol.
 Diaphragm thickness .0015 in



Run No. 203
 Horizontal scale 100 μ sec/cm
 Vertical scale 125 ~ psi/cm
 Fuel manifold pressure 440 psi
 O₂ manifold pressure 1380 psi
 Nominal mass flow 1.22 lbs/sec
 Nominal mixture ratio 17.9 % fuel by vol.
 Diaphragm thickness .0015 in

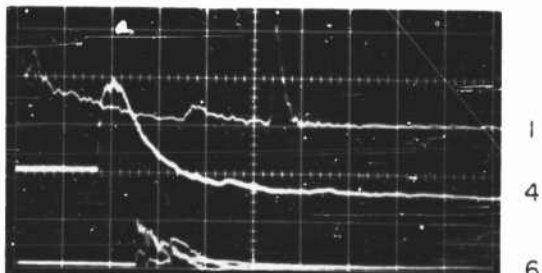


Figure 63. Pressure Recordings of Annular Motor Tests, Methane-Oxygen,
 $A_c/A_t = 1.0$.

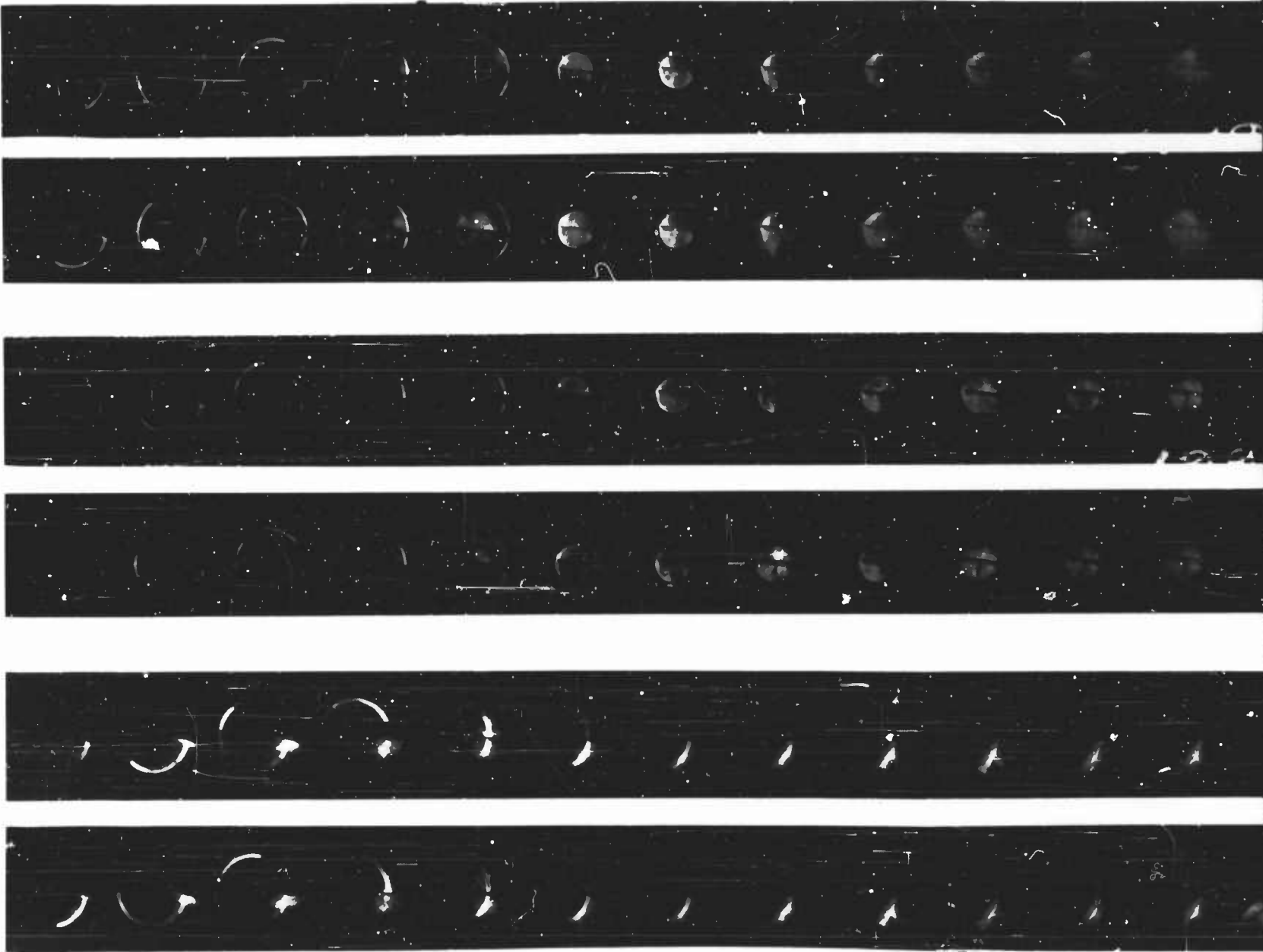


Figure 64. High Speed Photographs of Annular Motor Tests, Methane-Oxygen.



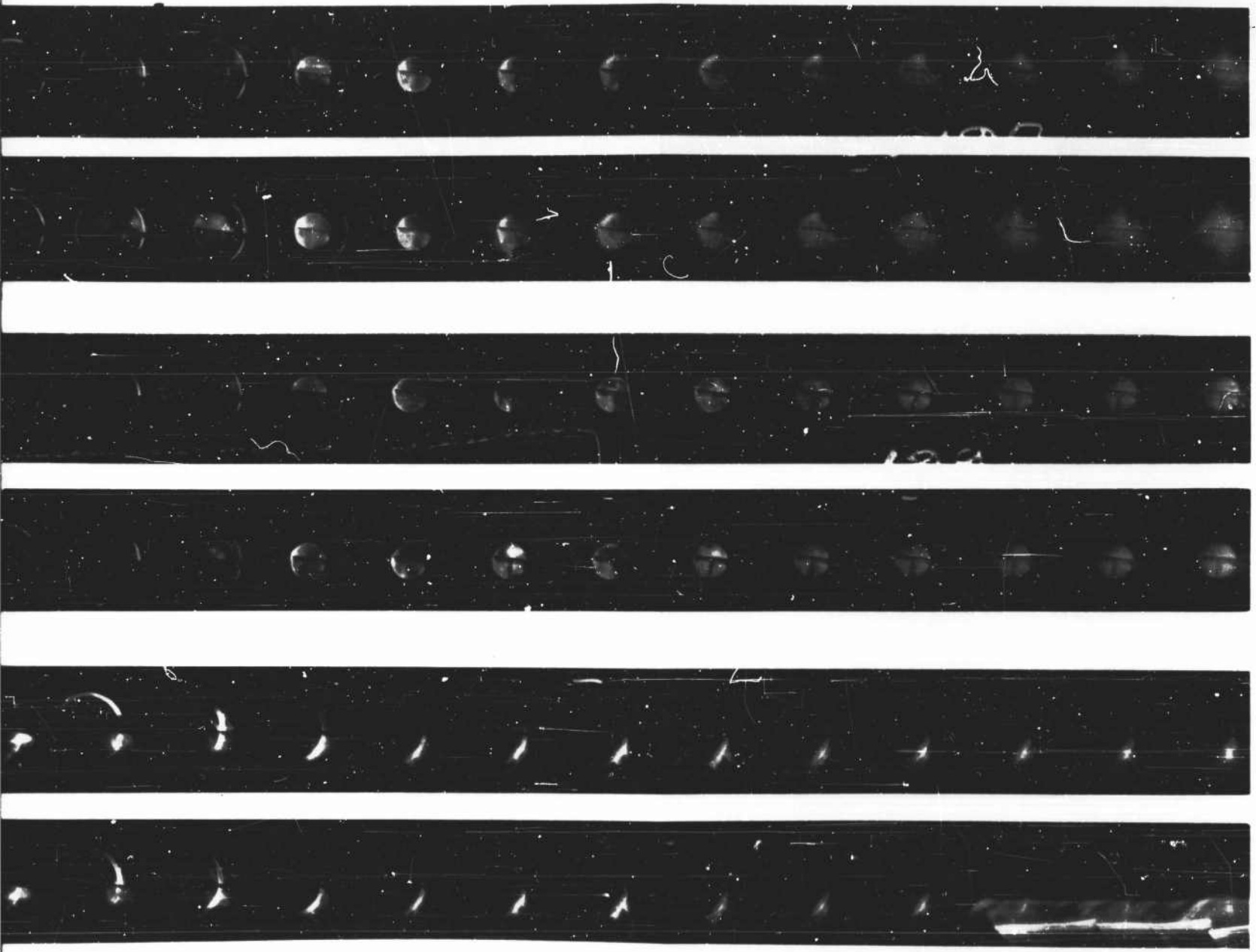


Figure 64. High Speed Photographs of Annular Motor Tests, Methane-Oxygen.



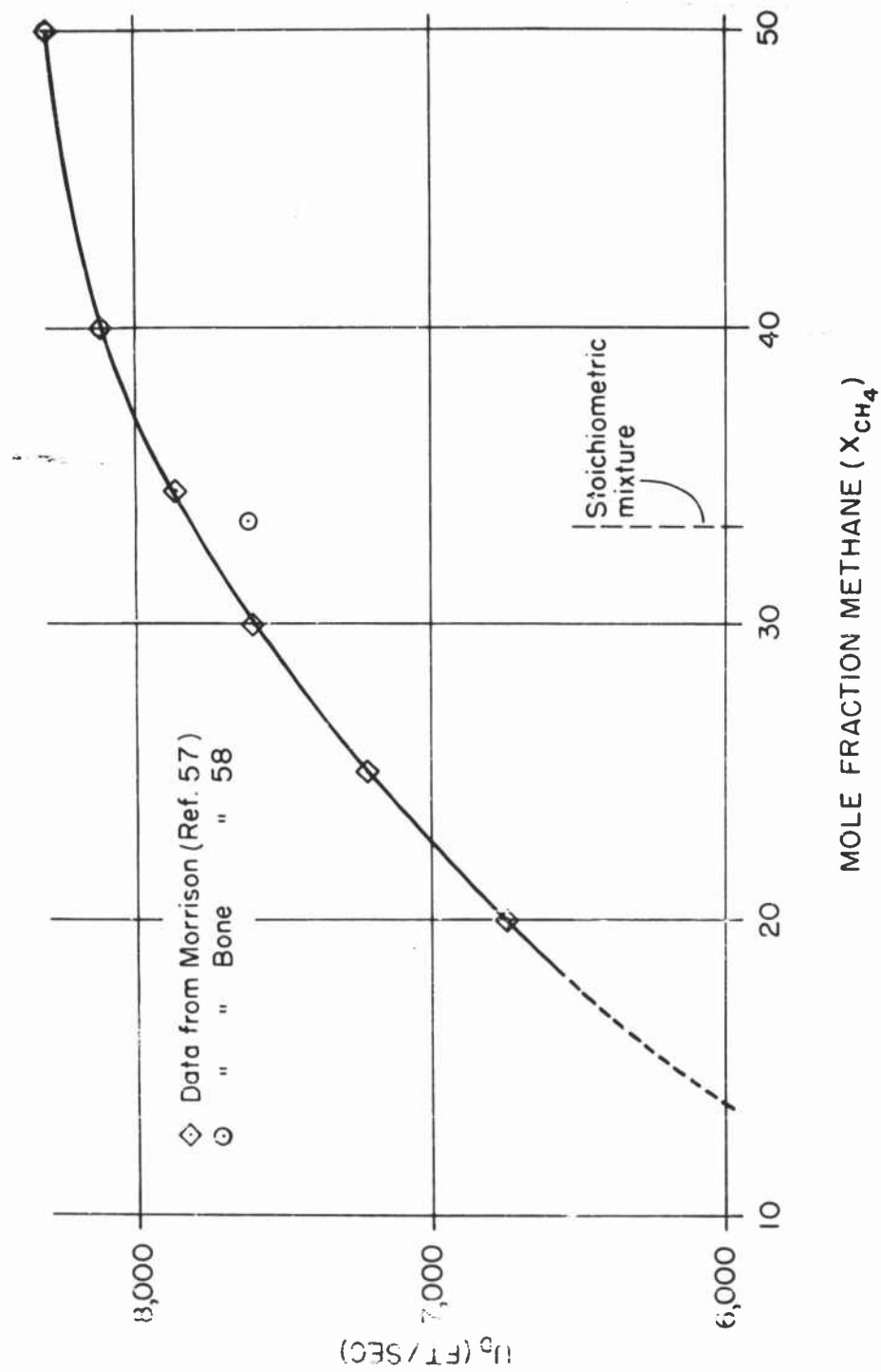


Figure 65. Chapman-Jouguet Detonation Velocity for Methane-Oxygen in Closed Tube.

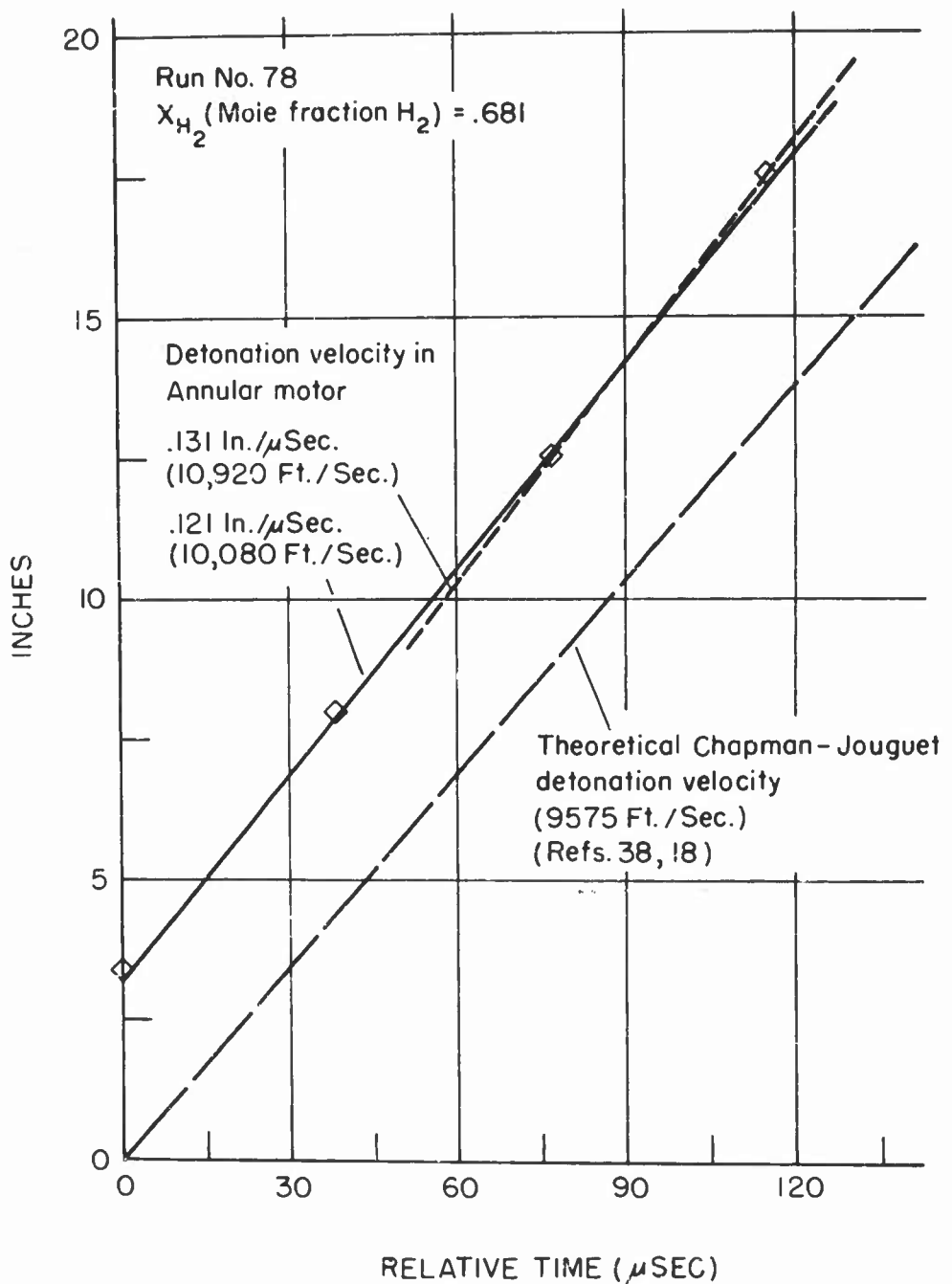


Figure 66. Displacement Versus Time Plots for Initial Detonation Wave in Annular Motor, Hydrogen-Oxygen.

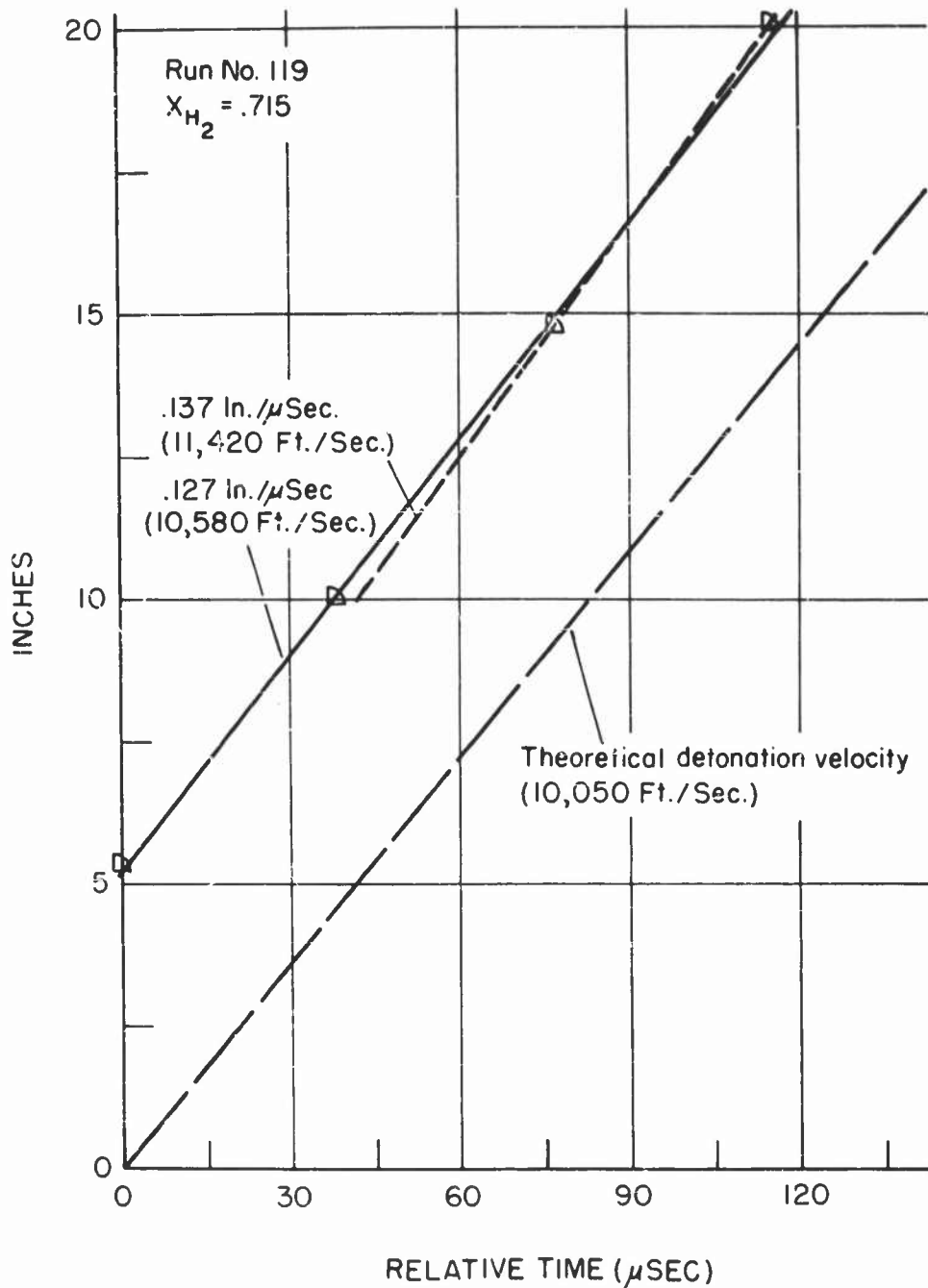


Figure 66. Continued.

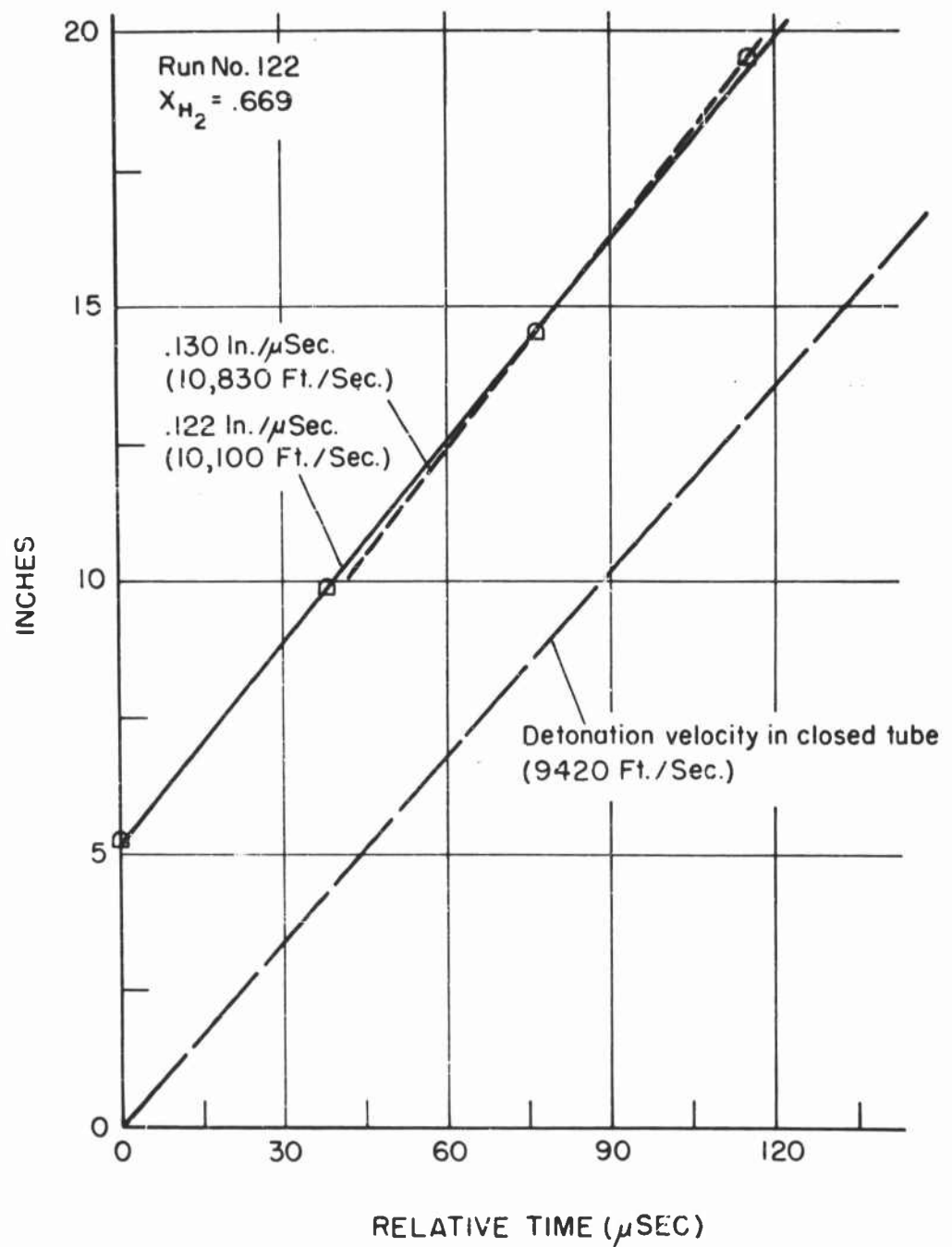


Figure 66. Continued.

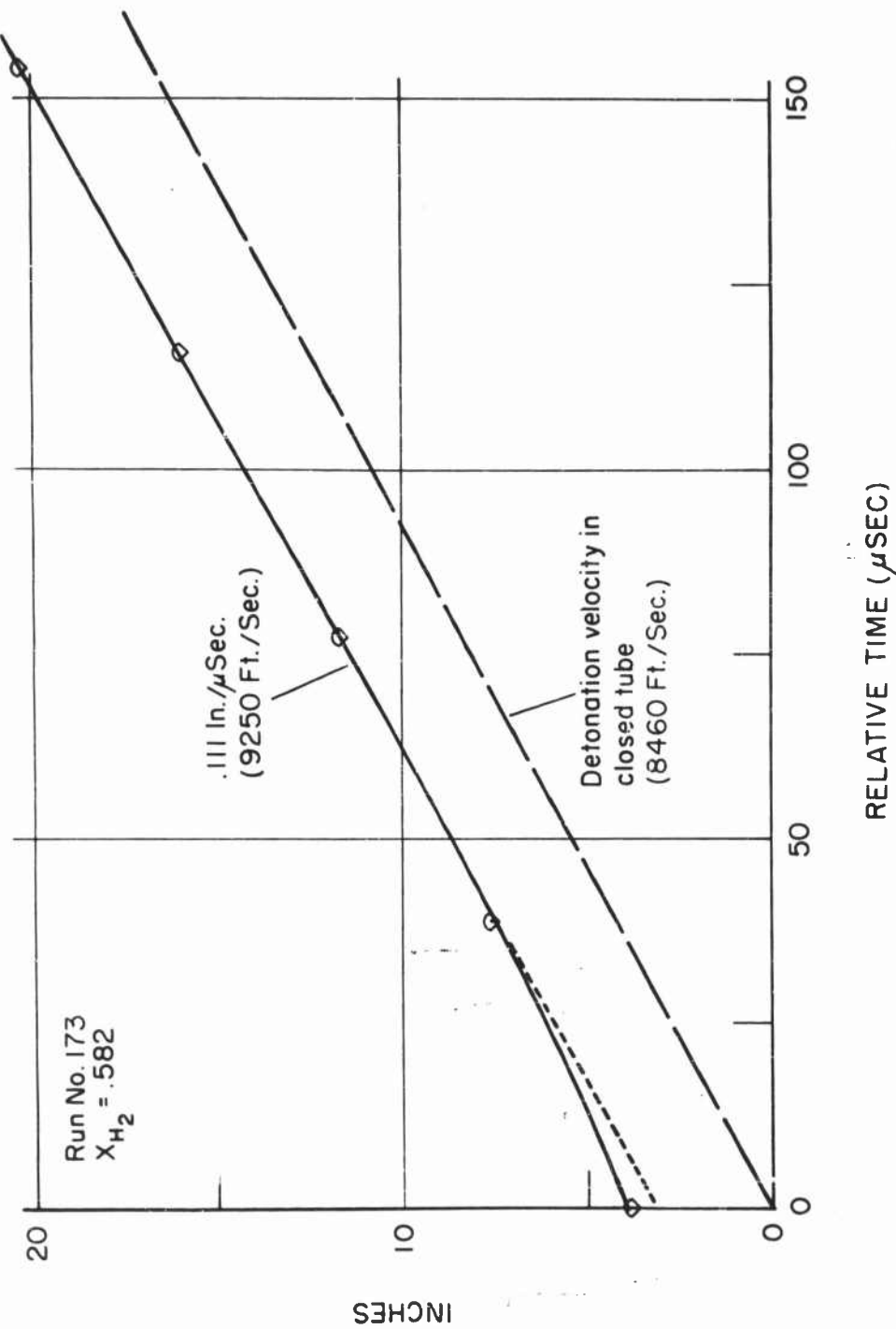


Figure 66. Continued.

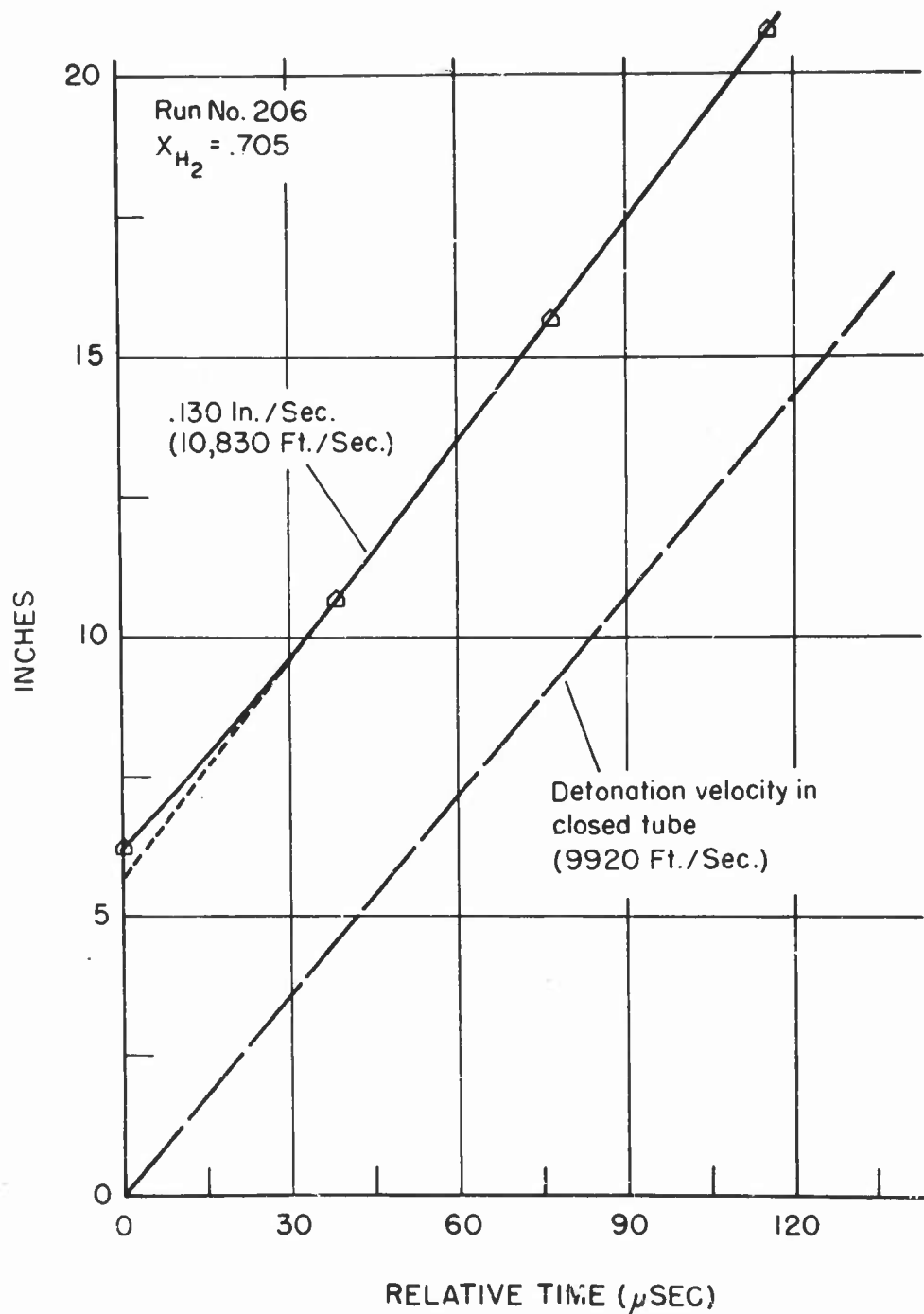


Figure 66. Concluded.

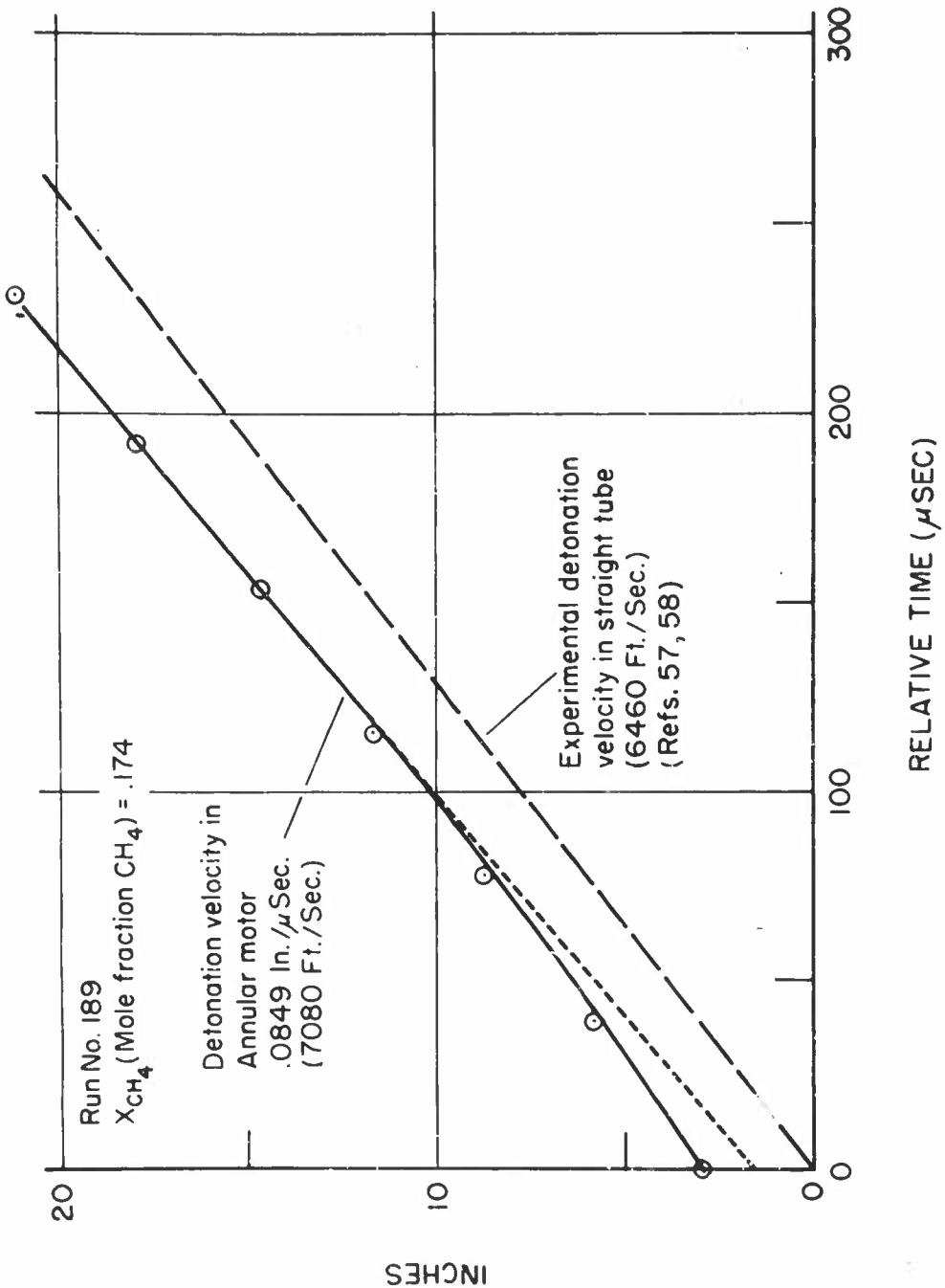


Figure 67. Displacement Versus Time Plots for Initial Detonation Wave in Annular Motor, Methane-Oxygen.

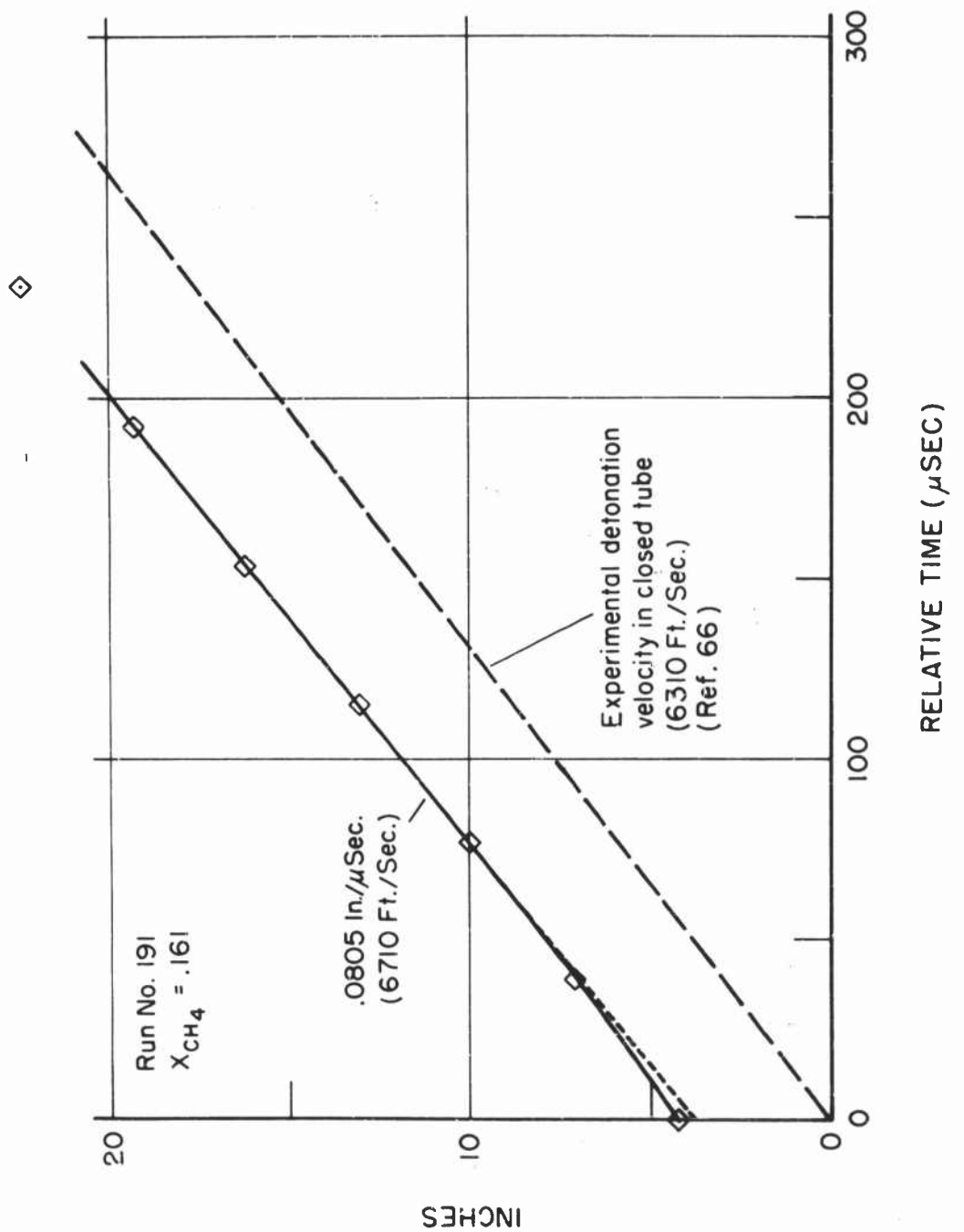


Figure 67. Contin'd.

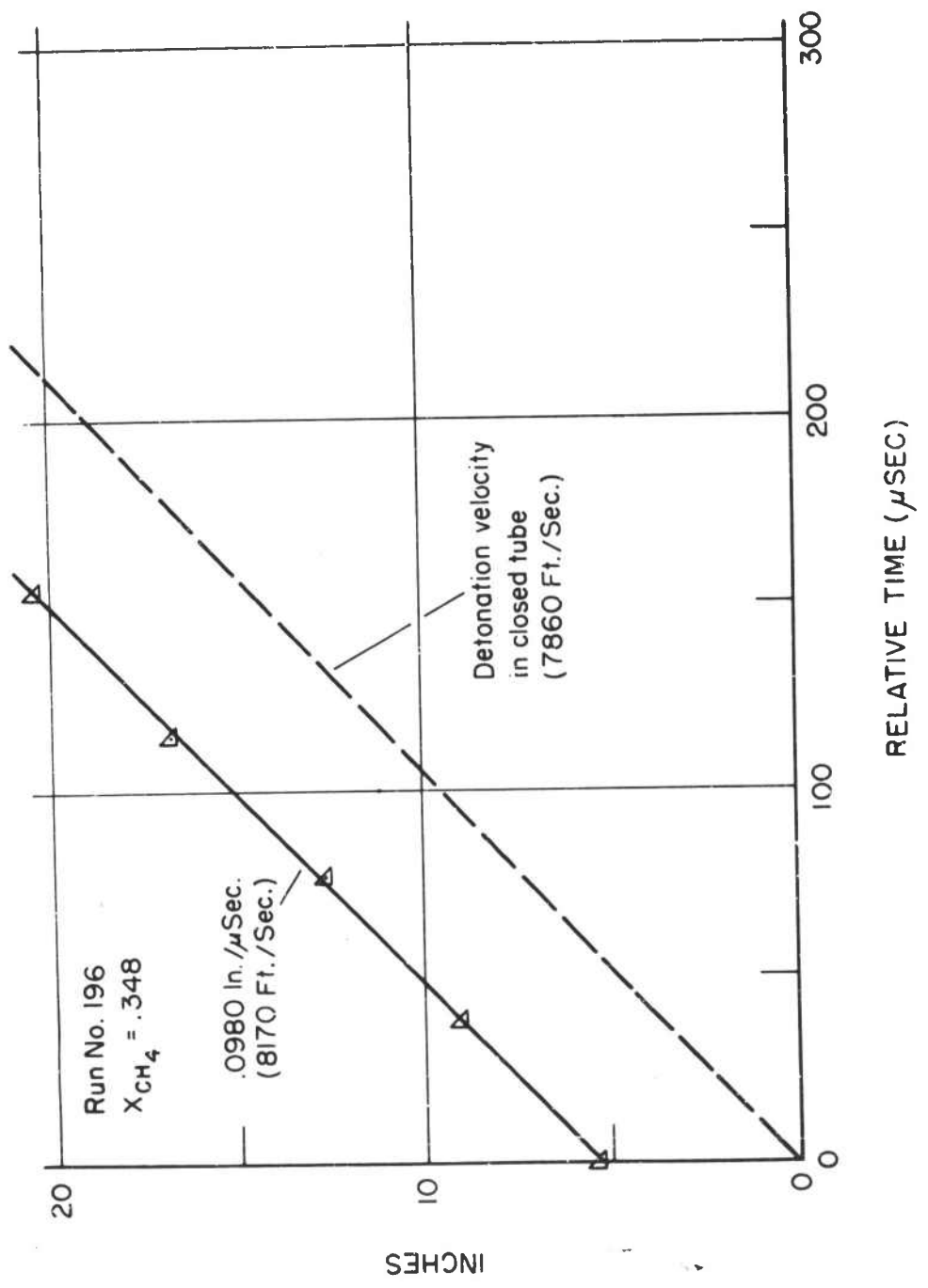


Figure 67. Continued.

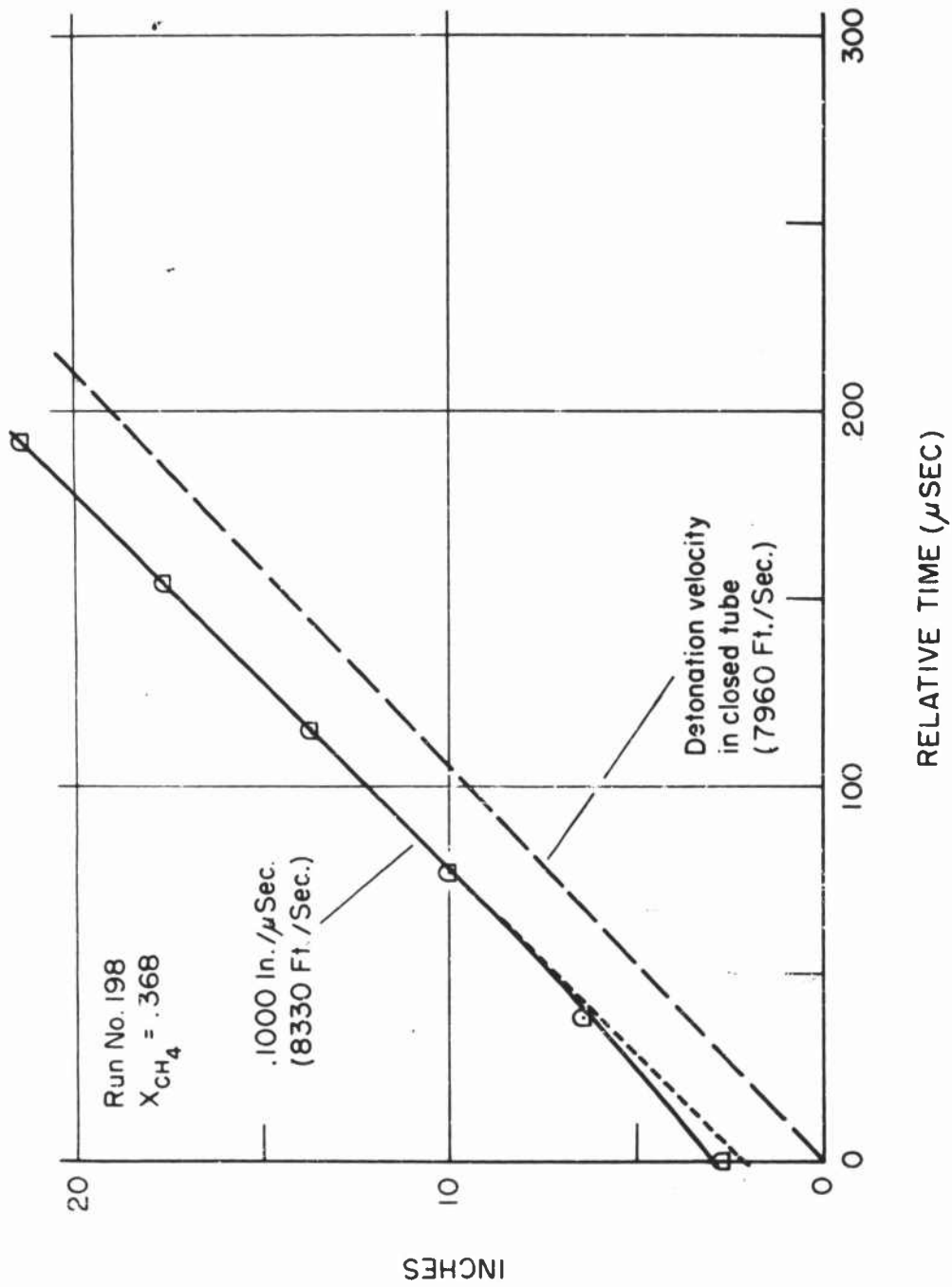


Figure 67. Continued.

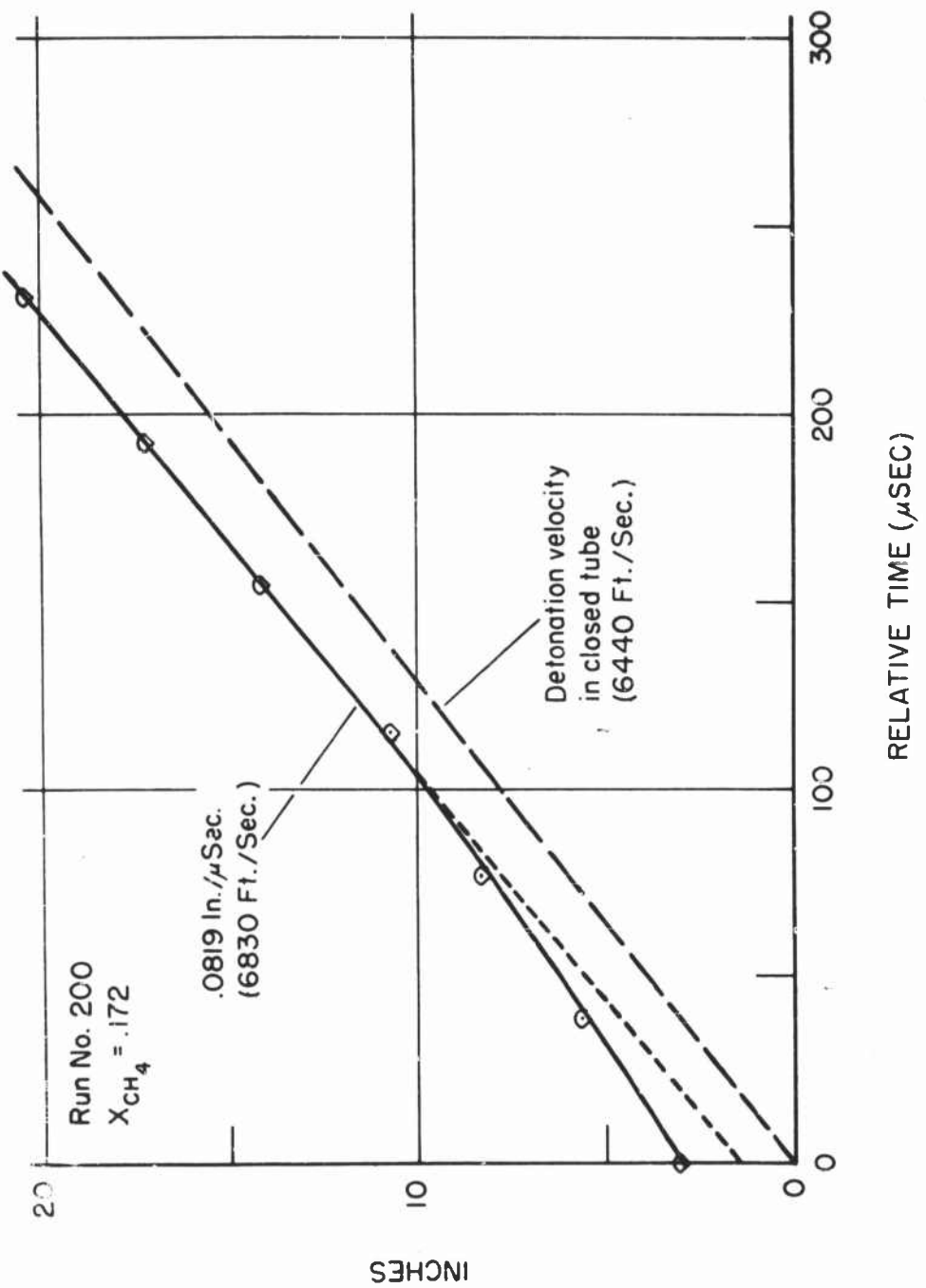


Figure 67. Continued.

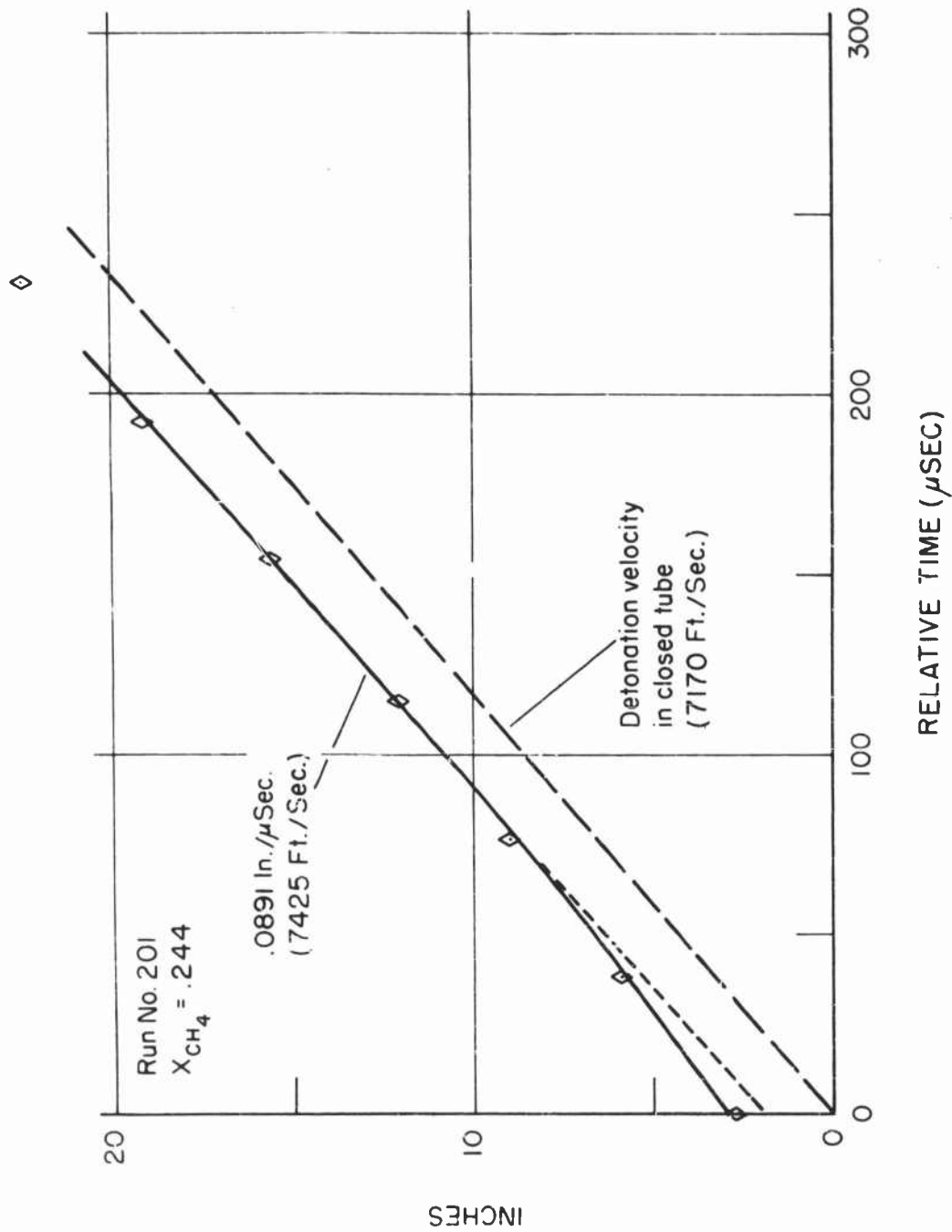


Figure 67. Concluded.

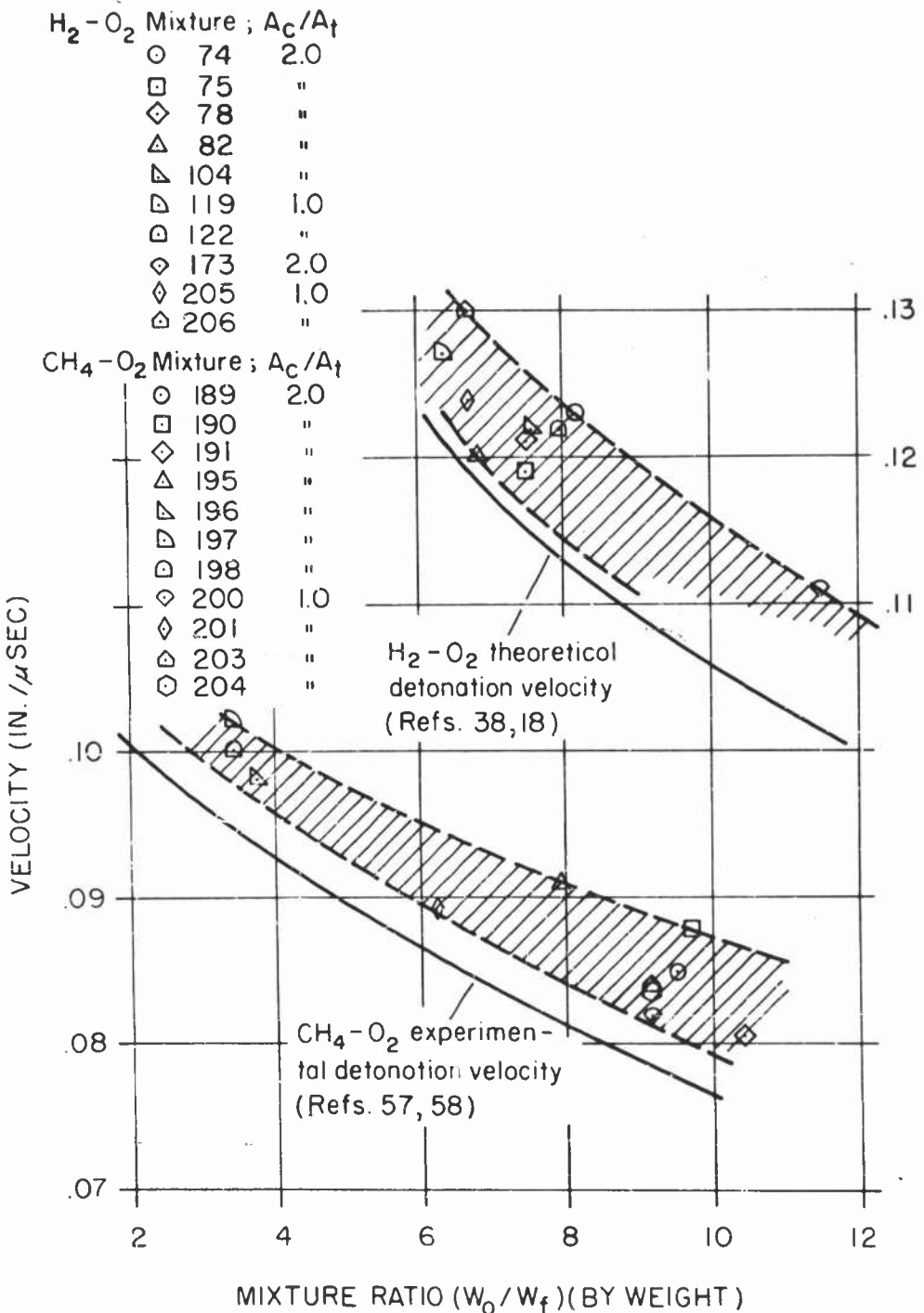


Figure 68. Summary of Initial Detonation Wave Velocity Versus Mixture Ratio in Annular Motor.

DISTRIBUTION LIST

	No. of Copies
Scientific and Technical Information Facility P. O. Box 5700 Bethesda, Maryland 20014 ATTN: NASA Representative (SAK/DL)	3
Nat'l. Aeronautics & Space Admin. Lewis Research Center 21000 Brookpark Road Cleveland 35, Ohio ATTN: Library	1
Office of the Director of Defense Research and Engineering Washington 25, D.C. ATTN: D. B. Brooks Office of Fuels & Lubricants	1
Commander Aeronautical Research Laboratory Wright-Patterson AFB, Ohio ATTN: ARC, Mr. Karl Scheller	1
Aeronautical Systems Division Wright-Patterson AFB, Ohio ATTN: ASRCEE-1	1
Air Force Systems Command Andrews AFB Washington 25, D.C. ATTN: SCTAP	1
Commander AFSC Foreign Technology Division Wright-Patterson AFB, Ohio ATTN: FTD (TD-E3b)	1
Defense Documentation Center Cameron Station Alexandria, Virginia 22314	10

DISTRIBUTION LIST (Continued)

	No. of Copies
Aeronautical Systems Division Wright-Patterson AFB, Ohio ATTN: ASNRPP	1
Commander Air Force Flight Test Center Edwards AFB, California ATTN: Tech. Library Code FTOOT	1
Commanding General Aberdeen Proving Ground Maryland ATTN: Ballistic Res. Lab. CRDBG-BLI	1
Commander U.S. Army Ord. Missile Command Redstone Arsenal, Alabama ATTN: Technical Library	1
Commanding Officer Picatinny Arsenal Liquid Rocket Propulsion Laboratory Dover, New Jersey ATTN: Technical Library	1
Bureau of Naval Weapons Department of the Navy Washington 25, D.C. ATTN: RMMP-24	2
Bureau of Naval Weapons Department of the Navy Washington 25, D.C. ATTN: RMMP-4	1
Commander Naval Ordnance Laboratory White Oak Silver Spring, Maryland ATTN: Dr. J. R. Holden	1

DISTRIBUTION LIST (Continued)

	No. of Copies
Commander U.S. Naval Ordnance Test Station China Lake, California ATTN: Code 45	3
Director (Code 6180) U.S. Naval Research Lab. Washington 25, D.C. ATTN: H. W. Carhart	1
Department of the Navy Office of Naval Research Washington 25, D.C. ATTN: Power Branch-Code 429	1
Commanding Officer ONR Branch Office 103C East Green Street Pasadena, California	1
Superintendent U.S. Naval Postgraduate School Naval Academy Monterey, California	1
Commanding Officer U.S. Naval Underwater Ordnance Sta. Newport, Rhode Island ATTN: W. W. Bartlett	1
Aerojet-General Corp. P. O. Box 296 Azusa, California ATTN: M. Grenier, Librarian	1
Aerojet-General Corporation Sacramento Plants, P. O. Box 1947 Sacramento 9, California ATTN: R. G. Weitz Head, Tech. Info. Office	2

DISTRIBUTION LIST (Continued)

	No. of Copies
Aeronutronic Division of Ford Motor Company Ford Road Newport Beach, California ATTN: Library	1
Aeroprojects, Inc. West Chester, Pennsylvania ATTN: W. Tarpley	1
Armour Research Foundation Illinois Inst. of Technology Chicago, Illinois ATTN: C. K. Hersh, Chemistry Division	1
Atlantic Research Corporation Edsall Road & Shirley Highway Alexandria, Virginia	1
Bell Aerosystems Box 1 Buffalo 5, New York ATTN: T. Reinhardt	1
General Electric Company Aerotermochimistry Unit Combustion Applied Research Mail Stop No. H-52, Cincinnati 15, Ohio ATTN: G. G. Kutzko, Manager	2
Jet Propulsion Laboratory 4800 Oak Grove Drive Pasadena 3, California ATTN: I. E. Newlan, Chief Reports Group	1
Liquid Propellant Information Agency Applied Physics Laboratory The Johns Hopkins University 8621 Georgia Avenue Silver Spring, Maryland	3

DISTRIBUTION LIST (Continued)

	No. of Copies
Marquardt Corp. 16555 Saticoy Street Box 2013-South Annex Van Nuys, California	1
New York University Dept. of Chem. Engineering New York 53, New York ATTN: P. F. Winternitz	1
Princeton University Project Squid Forrestal Research Center Princeton, New Jersey ATTN: Librarian	1
Purdue University Lafayette, Indiana ATTN: M. J. Zucrow	1
Reaction Motors Division Thiokol Chemical Corp. Denville, New Jersey ATTN: Library	1
Rocketdyne North American Aviation, Inc. 6633 Canoga Avenue Canoga Park, California ATTN: J. Silverman	2
Space Technology Labs. P. O. Box 95001, Airport Station Los Angeles 45, California ATTN: James R. Dunn	1
General Dynamics/Convair San Diego 12, California ATTN: Engrg. Library K. G. Blair, Ch. Librn. Mail Zone 50-03	1

DISTRIBUTION LIST (Continued)

	No. of Copies
Aerospace Corp. P. O. Box 95085 Los Angeles 45, California ATTN: Dr. D. H. Loughridge Dir. Applied Res. Management	2
United Technology Corp. P. O. Box 358 Sunnyvale, California ATTN: Technical Library	1
Hattelle Memorial Institute 505 King Avenue Columbus 1, Ohio ATTN: Reports Library, Room 6A	1
E. I. duPont de Nemours & Co. Explosives Department Eastern Laboratory P. O. Box B Gibbstown, New Jersey	1
United Aircraft Corp. Pratt & Whitney, Fla. Res. & Dev. Ctr. P. O. Box 2691 W. Palm Beach, Florida ATTN: Library	1
Polytechnical Institute of Brooklyn 335 Jay Street Brooklyn 1, New York ATTN: Dr. V. D. Agosta	1
United Aircraft Corporation Corporation Library 400 Main Street East Hartford, Connecticut ATTN: Dr. David Rix	1

DISTRIBUTION LIST (Concluded)

No. of Copies

University of California
ATTN: A. K. Oppenheim
Berkeley, California

1

Massachusetts Institute of Technology
Dept. of Mechanical Engineering
ATTN: Prof. T. Y. Toong
Cambridge 39, Massachusetts

1

Dept. of Aeronautical & Astronautical Engineering
ATTN. Prof. Loren E. Bollinger
Ohio State University
Columbus, Ohio

1

Final Report:
Air Force Flight Test Center
6593d Test Group (Development)
Edwards, California
ATTN: DGRR

10